The Pennsylvania State University

The Graduate School

Graduate Program in Acoustics

GRATING LOBE REDUCTION IN TRANSDUCER ARRAYS THROUGH STRUCTURAL FILTERING OF SUPERCRITICAL PLATES

A Thesis in

Acoustics

by

Brian Eric Anderson

Submitted in Partial Fulfillment
of the Requirements
for the Degree of

Doctor of Philosophy

December 2006

The thesis of Brian Eric Anderson was reviewed and approved* by the following:

W. Jack Hughes
Professor of Acoustics, Emeritus
Senior Scientist
Thesis Advisor
Chair of Committee

Courtney B. Burroughs
Associate Professor of Acoustics, Emeritus

Stephen A. Hambric
Associate Professor of Acoustics
Senior Research Associate

Nadine Barrie Smith
Associate Professor of Bioengineering

Anthony A. Atchley
Professor of Acoustics
Head of the Graduate Program in Acoustics

*Signatures are on file in the Graduate School

ABSTRACT

The effect of placing a structural acoustic filter between the water medium and the transducer elements of an array is investigated, in this thesis, to help reduce undesirable grating lobes. A plate is mounted to transducer elements with a thin decoupling polyurethane layer between the transducers and the plate. The plate acts as a radiation/incidence angle filter to pass energy at angles near normal incidence, but suppress energy at large incidence angles. The plate must possess a very high bending stiffness while maintaining low mass to achieve optimal results. Grating lobe reduction is achieved at the expense of limiting the available steering of the main lobe. Within this steer angle limit the main lobe beams can be steered as normal while the grating lobe level is reduced by the plate's angular filtering. The insertion of a plate structural filter provides an inexpensive and easily implemented approach to extend usable frequency bandwidth with reduced level grating lobes, without increasing the number of array elements. Even though some data matches theory well, a practical material has yet to be found that possesses optimal material properties. To the author's knowledge, this thesis represents the first attempt to advantageously utilize a plate to provide angular dependent sound transmission filtering above the plate's critical frequency (the supercritical frequency region).

Theoretical analysis, numerical analysis, and extensive experimental results have been performed and a comparison will be presented in this thesis. The angular dependence of sound transmission through a plate is reviewed, followed by design considerations to optimize a plate for angular filtering. The optimal thickness for a plate

depends on the plate's material properties. Equivalent circuit modeling and finite element modeling was applied, and is compared to. Extensive experimental results conducted with bars and a plate will be shown. Good agreement with theory and modeling is achieved for an alumina bar bonded to transducer elements.

TABLE OF CONTENTS

LIST OF FIGURES

LIST OF TABLES

ACKNOWLEDGEMENTS

First and foremost I need to thank my loving wife Angela who has supported me in my efforts and helped me through the hard times. From the meals brought up to campus to the highly uncertain work schedule she has always been my biggest support.

Thanks to my son Travis who would eventually stop crying every morning I left for school, and provided lots of fun every evening to relieve my sometimes stressed mind.

Thanks to my parents who provided financial support to get me to this point, by paying for all of my undergraduate schooling. They also provided love and encouragement along the way. My father offered advice and suggestions on my project as he is a structural vibrations engineer himself.

Thanks are due to Dr. Hughes, who took me on as a graduate student when things in his personal life were hard and uncertain. He could have easily passed on me due to his situation, but instead he chose to give me a chance. I thank him for his professional advice as well as his very helpful personal advice along the way. Dr. Hughes was very flexible and willing to let me try new things, even if he knew they would fail, so that I could learn for myself by experience.

Thanks go to Dr. Burroughs, Dr. Hambric, and Dr. Smith who assisted me with questions and provided a thought provoking comprehensive exam.

Thanks to Paul Bednarchik for getting the project started and creating the initial numerical model in ANSYS. Paul also helped many times with questions about ANSYS and many other items.

Thanks to Chuck Allen, Jared Beltowski, Dan Charles, Steve Conlin, Bob Dashem, Steve Garrett, Mark Geleskie, Greg Granville, Larry Horner, Doug Markley, Rich Meyer, Tom Montgomery, Ryan Scott, Eric Strauch, Mike Thibeault, Bill Thomas, Steve Thompson, Pete Tussey, Dave Van Tol, and Mark Wilson and for their various roles in assisting with efforts on this project and in other matters.

A special thank you goes to The Pennsylvania State University, the PSU College of Engineering, the Audio Engineering Society, David Drumheller at the Office of Naval Research, and Richard Stern of the ARL for providing funding support respectively through: a University Graduate Research Fellowship, a College of Engineering Fellowship, AES Educational Foundation Award, ONR research funding support, and Exploratory and Foundational Research Program funding. These sources of funding not only supported myself, but also supported my wife, my two year old son, and my son who will arrive this December.

Chapter 1

INTRODUCTION

1.1 Background

Arrays of transducer elements are often used to channel sound radiation into specific directivity patterns. According to traditional array theory, the usable frequency bandwidth of any given array of elements is limited according to its element spacing (1, p. 185), (2, p. 166), (3, pp. 503-504). The optimal element spacing d is typically set equal to half the center frequency wavelength λ. Thus, the resulting array may be operated below and above the center frequency, within certain limitations. Below the center frequency, the radiated beam widens and approaches an omni-directional beam pattern. Above the center frequency, the radiated beam narrows. At frequencies greater than or equal to twice that of the center frequency, grating lobes appear in the radiated beam pattern as duplicates of the main beam of sound energy (i.e., duplicates in radiation level, but not in the direction radiated). These undesirable grating lobes result from an aliasing effect due to the discrete nature of an array of elements and the regular spacing of elements. The above discussion assumes that the pattern is in a direction normal to the plane of the array. An array may also be used to steer sound radiation in different directions. When an array is steered, the grating lobe(s) will appear in the beam pattern at frequencies lower than twice the center frequency. A typical beam pattern for an 8-element array (array shown vertically), with $d/\lambda = 1.016$ and a steering angle of 15° may

be found in Fig. 1.1. The grating lobe is located at -46°. The other lobes are natural, unavoidable side lobes.

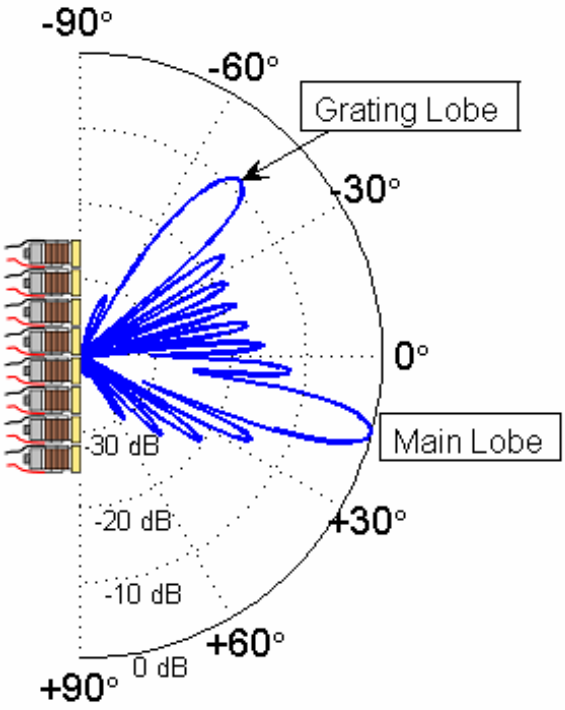

Fig. 1.1. Beam pattern (in dB relative to peak pressure, versus angle in degrees) for an 8-element point source array with $d/\lambda = 1.016$ and the array steered to 15°. The main beam is steered to 15° and the resulting grating lobe is located at -46°.

Grating lobes in radiation beam patterns cause operational confusion for technology that relies on arrays. In a transmit condition, grating lobes cause an array to transmit sound energy into unintended directions. In a receive condition, grating lobes prevent an array's ability to detect the direction of incoming sound energy. However, larger frequency bandwidth allows higher resolution and greater ranging capabilities in SOund NAvigation and Ranging (SONAR) applications, where both transmit and receive conditions are used. If a technique could be developed in which grating lobes can be eliminated or suppressed, it would provide a tremendous advancement for SONAR

applications and potentially other research areas such as ultrasound, and audio sound reinforcement.

1.2 Literature on Grating Lobe Reduction

There have been many different attempts to reduce or eliminate grating lobes in radiation patterns in SONAR array applications and in medical ultrasound array applications. SONAR arrays are often designed for high source level output in a narrow frequency band and are not traditionally used in the broad frequency range as that used in the ultrasound community. Consequently, the majority of studies involving grating lobe reduction have traditionally come from the ultrasound community. The most commonly used techniques, aimed at grating lobe reduction in directivity patterns, attempt to break up the regular element spacing or regular element size which gives rise to grating lobes. Current techniques of reducing grating lobes include: sparse element spacing, annular rings of elements, use of adjacent staggered arrays, pseudo random continuous wave (CW) signals, and exploitation of harmonic imaging.

A sparse, or aperiodic, layout of elements means that the element spacing is not fixed and often means that the element spacing is random. A sparse layout of elements may be achieved for various different array geometries. The sparse layout of elements serves to break up the regular spacing of elements which gives rise to grating lobes. Some techniques utilize a random subset of elements in a regular spaced array by deactivating elements for transmit and/or undersampling the elements in the array for receive. Techniques which use different subsets of elements on transmit and receive

provide increased grating lobe reductions relative to those which utilize the same subset of elements for both transmit and receive. However, deactivating elements and/or undersampling the array decreases the array's sensitivity and provides relatively minimal reduction in the grating lobe. Sparse arrays were proposed by von Ramm *et al* in 1975 (4) and the technique was extended to 2-D arrays by Smith *et al* in 1991 (5). Several others have addressed this technique and provided improvements incorporating other grating lobe reduction techniques (6)-(17).

Annular layouts of elements possess spatial diversity and therefore result in decreased grating lobe levels relative to rectangular grids of elements. An additional advantage of annular arrays is that the axial symmetry of annular arrays provides regularity in the radiated field distribution. Annular array layouts are typically specific to the ultrasound community due to their function of providing focusing. A number of authors have proposed annular element layouts and discussed their performance in grating lobe reductions (18)-(22).

Some research on reducing grating lobe levels has focused on arranging two-dimensional arrays so that grating lobes of adjacent line arrays add out of phase and cancel each other. The staggering of adjacent line arrays results in a decrease in the effective element spacing which is equivalent to increasing the frequency at which grating lobes are generated. The staggered array configuration works well for a unidirectional array but grating lobe level reduction is not achievable in all directions with a planar 2-D array. Hildebrand and Posakony patented a method, for two-dimensional arrays, where adjacent line arrays contain different numbers of elements (23). Talman and Lockwood investigated staggering techniques with different element

spacings in adjacent line arrays (24). Later, Pompei and Wooh proposed another staggered array configuration for rectangular, diamond, and circular elements (25).

Techniques to reduce grating lobes by varying the input signals, from the standard sinusoidal signal to pseudorandom phase-modulated continuous wave, CW, signals have been proposed by Dupenloup *et al* (26)-(28). CW signals require the transducer to operate continuously which is a critical issue for SONAR transducers and requires lower power output (due to thermal failure limitations) relative to pulsed signals (with a fixed duty cycle).

Bouakaz *et al* proposed a unique grating lobe reduction technique, which they refer to as selective harmonic imaging (29). The technique exploits nonlinear acoustics phenomena through the utilization of harmonic frequency analysis. Their work states that grating lobes produce almost no harmonic energy, whereas the main lobe generates a considerable amount of harmonic energy. Thus harmonic imaging should not suffer from grating lobes as much as the fundamental frequency imaging.

There are many existing arrays currently used by the U. S. Navy that have no practical means for reducing their grating lobes. None of the methods mentioned above are practical solutions to retrofit onto existing Navy array systems. The methods mentioned above either require different element geometries than that of existing Navy array systems, or require impractical modifications to the input signals. A practical technique is needed, which directly eliminates grating lobes, that could be retrofitted onto existing array designs. Grating lobe reduction would provide these existing arrays with better ranging capabilities and larger frequency bandwidth and therefore better image resolution compared to existing array capabilities.

1.3 Grating Lobe Plate Technique

The proposed technique for grating lobe level reduction presents an entirely different approach to the problem than any other proposed method. An extremely stiff and lightweight plate, operated at frequencies above its critical frequency, is placed in front of the transducer array to provide a radiation angle filter (or incidence angle filter) achieved through exploitation of the coincidence effect (a sound and structure interaction principle). Sound energy will pass through the plate at normal incidence and radiation angles less than the coincidence angle, attenuated somewhat due to the mass of the plate. Sound energy at large radiation angles, greater than the coincidence angle, will be attenuated due to the stiffness of the plate. If the plate's material properties and geometry are designed appropriately and the array is operated within certain constraints, then grating lobe levels may be greatly reduced while main lobes are passed by the radiation angle filter. The insertion of a plate would provide a very inexpensive and easily implemented approach to eliminating grating lobes without increasing the number of array elements. The concept could be retrofit onto existing Navy array systems. The concept could also be applied to many other array applications.

This thesis merges theory from two different fields in acoustics: acoustics of transducer arrays and structural acoustics, by presenting a passive structural filtering method, aimed at reducing the levels of grating lobes. Both fields in acoustics have developed a bias against investigation of such a technique. In transducer array design, it is commonly accepted that one should avoid cross-coupling neighboring transducers. In structural acoustics, is has been stated by a well respected author that, regarding the use

of plates, “in marine applications, frequencies greater than the critical frequency are rarely of practical importance (30, p. 154).” The technique forces transducer elements of an array to drive a plate and thus one might suspect that this technique would fail due to cross-coupling of transducer elements. In addition this technique exploits sound and structural interaction effects which occur only above the plate’s critical frequency.

The idea behind this technique was developed as an extension of the work by Hutto (31), Grosh (32), and Phillips (33).

1.4 Brick Wall Structural Filter

The best that a passive structural filter could do is to eliminate grating lobes while not affecting the main lobe. In digital signal processing, the best case filter is referred to as a “brick wall” filter, which describes a filter that perfectly passes all energy in the desired region(s) (called the pass band) while perfectly attenuating all energy in the undesired region(s) (called the stop band). An inherent limitation in a passive structural filter is that the main lobe must always be at a shallower angle (closer to normal incidence) than the grating lobe to ensure that the first grating lobe is not passed while the main lobe is not affected (perfect filter). The brick wall structural filter establishes limits on achievable grating lobe filtering and will be discussed in Sections 2.13 and 3.8.

1.5 Outline

The chapters of this thesis will proceed as follows. Chapter 2 discusses array theory and grating lobes in detail. Chapter 3 discusses sound and structure interaction theory used to model the angular dependence of the structural filtering and to design an optimal plate. Chapters 4 and 5 describe equivalent circuit modeling and numerical modeling of the grating lobe plate technique, respectively. Chapter 6 discusses experimental techniques used in this study, along with results. Chapter 7 summarizes the results from analytical and experimental studies. Chapter 8 provides conclusions and recommendations for further work.

Chapter 2

ARRAY THEORY AND DESIGN

2.1 Introduction

This chapter presents the derivation involved to obtain the directivity function of a point source array. The derivation is followed with an introduction to array steering, amplitude shading, single element directivity, baffle directivity, grating lobes, extension to planar arrays, the continuous source line array, reciprocity, beamwidth, and array design. The concept of an ideal, passive, radiation/incidence angle filter is then introduced. At the conclusion of this chapter are array performance plots displaying drive inputs versus resulting receive and amplitude outputs.

2.2 One-Dimensional Point Source Line Array

Much of the following discussion has been adapted from Albers (1, pp. 181-188), Blackstock (3, pp. 502-503), and Kinsler, Frey *et al* (34, pp. 195-197).

A point source is an infinitesimally small vibrating sphere in space in which all portions of the sphere vibrate in phase. The beam pattern of a point source is omni-directional (no angular dependence).

A line array is defined as a line of point sources. Consider a line array of N point sources equally spaced a distance d apart. Figure 2.1 displays the geometrical layout (a) for an odd-numbered line array of point sources and (b) for an even-numbered

line array of point sources. The following derivation will assume all point sources have equal amplitudes and all vibrate in phase. Also, the derivation is restricted to a 2-D plane.

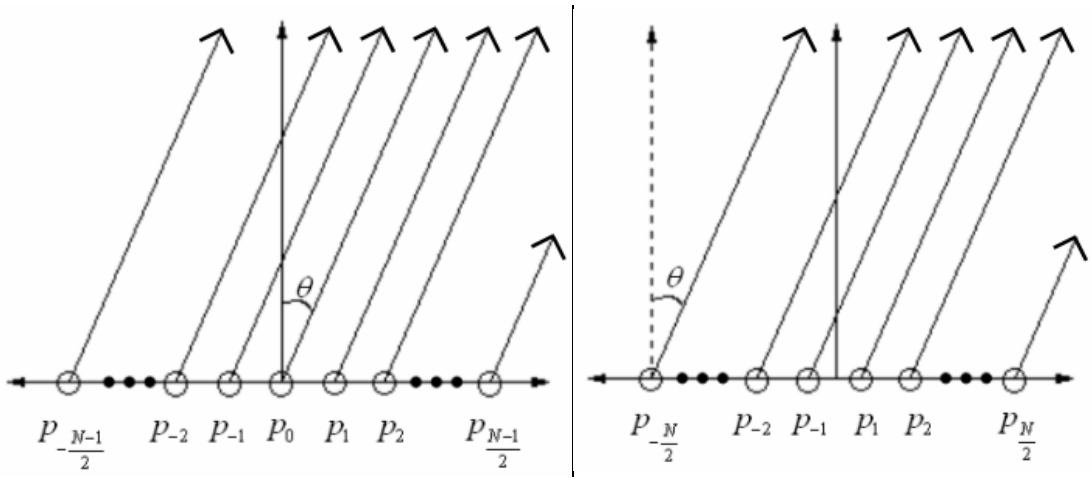

Fig. 2.1. Geometrical layouts for two line arrays of point sources. Open arrows represent directions of acoustic rays from point sources. (**a**) An odd-numbered array (right plot). (**b**) An even-numbered array (left plot). The shorter arrow lines in each drawing do not physically mean anything since the arrows indicate direction only.

The pressure at a field point located at a radial distance r, and at an angle θ from a point source located at the origin is

$$p_0(r,\theta,t) = \frac{A}{r} e^{j(\omega t - kr)}, \tag{2.1}$$

where A is the point source pressure magnitude, j is the complex number $\sqrt{-1}$, ω is the angular frequency, and k is the acoustic wavenumber. Each point source in the array is assumed to be far enough away from the field point such that the angles between the directions of each point source's ray and the direction normal to the array are all equal to θ. An assumption is also made such that the distances between each point source and the field point are equivalent for each of the amplitude terms. These two assumptions

lumped together are generally referred to as the far-field assumption. The far-field assumption means that the pressure due to each neighboring point source differs by a constant phase amount ϕ, where

$$2\phi = kd\sin\theta\,. \tag{2.2}$$

For an odd-numbered array, the pressure due to the source designated p_{-1} is

$$p_{-1} = \frac{A}{r}e^{j(\omega t - kr - 2\phi)} = p_0 e^{-j2\phi}\,. \tag{2.3}$$

The pressure due to the source designated p_{-2} is

$$p_{-2} = p_0 e^{-j4\phi}\,. \tag{2.4}$$

The pressure due to the source designated $p_{-\frac{N-1}{2}}$ is

$$p_{-\frac{N-1}{2}} = p_0 e^{-j(N-1)\phi}\,. \tag{2.5}$$

The total pressure at the field point is the sum of the contribution from each point source:

$$p = p_0\left(e^{-j(N-1)\phi} + ... + e^{-j4\phi} + e^{-j2\phi} + 1 + e^{j2\phi} + e^{j4\phi} + ... + e^{j(N-1)\phi}\right). \tag{2.6}$$

The term $e^{j(N-1)\phi}$ is then factored out of Eq. (2.6)

$$p = p_0 e^{j(N-1)\phi}\left(1 + e^{-j2\phi} + e^{-j4\phi} + ... + e^{-j2(N-1)\phi}\right). \tag{2.7}$$

The terms in the parentheses of Eq. (2.7) may be simplified using the following geometric progression equality

$$1 + x + x^2 + x^4 + ... + x^{N-1} = \frac{1 - x^N}{1 - x}, \tag{2.8}$$

where $x = e^{-j2\phi}$. Use of the equality for Eq. (2.7) results in Eq. (2.10)

$$p = p_0 \frac{e^{jN\phi}}{e^{j\phi}} \frac{1-e^{-j2N\phi}}{1-e^{-j2\phi}} = p_0 \frac{e^{jN\phi} - e^{-jN\phi}}{e^{j\phi} - e^{-j\phi}} = p_0 \frac{\sin(N\phi)}{\sin\phi} \tag{2.9}$$

$$p(r,\theta,t) = \frac{A}{r} e^{j(\omega t - kr)} \frac{\sin\left(\frac{N}{2} kd \sin\theta\right)}{\sin\left(\frac{1}{2} kd \sin\theta\right)}. \tag{2.10}$$

For an even-numbered array, there is no point source at the origin, but the pressures due to each point source may be expressed in terms of a point source at the origin, as if there were one located at the origin. The pressure due to the source designated p_{-1} is

$$p_{-1} = \frac{A}{r} e^{j(\omega t - kr - \phi)} = p_0 e^{-j\phi}. \tag{2.11}$$

The pressure due to the source designated p_{-2} is

$$p_{-2} = p_0 e^{-j3\phi}. \tag{2.12}$$

The pressure due to the source designated $p_{-\frac{N}{2}}$ is

$$p_{-\frac{N}{2}} = p_0 e^{-j(N-1)\phi}. \tag{2.13}$$

The total pressure at the field point is then the sum of the contribution from each point source is

$$p = p_0 \left(e^{-j(N-1)\phi} + \ldots + e^{-j3\phi} + e^{-j\phi} + e^{j\phi} + e^{j3\phi} + \ldots + e^{j(N-1)\phi}\right). \tag{2.14}$$

The term $e^{j(N-1)\phi}$ is factored out of Eq. (2.14) and the same summation as found in Eq. (2.7) results

$$p = p_0 e^{j(N-1)\phi}\left(1 + e^{-j2\phi} + e^{-j4\phi} + ... + e^{-j2(N-1)\phi}\right). \tag{2.15}$$

Thus the expression for the total pressure due to an even-numbered array is also equivalent to Eq. (2.10).

At $\theta = 0$, Eq. (2.10) reduces to

$$p(r,0,t) = \frac{NA}{r} e^{j(\omega t - kr)} \tag{2.16}$$

Thus the angular dependence of Eq. (2.10), or directivity function, $H(\theta)$, may be normalized to separate the axial expression in Eq. (2.16) from the directivity function

$$H(\theta) = \frac{1}{N} \frac{\sin\left(\frac{Nkd}{2}\sin\theta\right)}{\sin\left(\frac{kd}{2}\sin\theta\right)}. \tag{2.17}$$

The absolute value of the directivity function is often plotted to show the angular dependence of the pressure field, often referred to as a radiation pattern or receive pattern. This allows amplitude comparison of positive and negative side lobes simultaneously. The directivity function of Eq. (2.17) has a maximum value of 1.0 at $\theta = 0$. It should be noted here that the term directivity function is used to describe the mathematical expression for angular dependence, while the term directivity pattern is used to describe the plot of a directivity function and/or a plot of angular dependence obtained experimentally.

2.3 Phase Shading for Array Steering

In array applications it is desirable to steer sound in a known direction, or a known steer angle, θ_0, without actually rotating the array physically. This may be accomplished by introducing a consecutively increasing electronic phasing, or time delay, across the line array. This time delay, τ_0, of

$$\tau_0 = \frac{d \sin\theta_0}{c}, \tag{2.18}$$

where c is the speed of sound in the fluid, can be applied to each point source

$$p(r,\theta,t) = \sum_{i=1}^{N} \frac{A_i}{r_i} e^{j(\omega(t - i\tau_0) - kr_i)}. \tag{2.19}$$

The consecutively increasing time delay is independent of drive frequency, thus the steer angle does not change as frequency is changed. Again, assuming that all point source amplitudes are equal $A_i = A$, and through utilization of the above geometric progression equality the directivity function becomes

$$H(\theta,\theta_0) = \frac{1}{N} \frac{\sin\left[\frac{Nkd}{2}(\sin\theta - \sin\theta_0)\right]}{\sin\left[\frac{kd}{2}(\sin\theta - \sin\theta_0)\right]}. \tag{2.20}$$

It is important to note that the width of the main lobe increases as the main lobe is steered from 0° (broad side) to 90° (end fire). See Appendix A, Section A.1, for MATLAB code which generates the directivity pattern for an array.

2.4 Amplitude Shading for Side Lobe Reduction

Amplitude shading, sometimes called apodization, is a means by which the amplitudes of the point sources are adjusted in a manner such that side lobes are reduced in level (grating lobe levels are not reduced). The inherent tradeoff in amplitude shading is that side lobes are reduced at the expense of widening the main lobe and grating lobe(s). Amplitude shading spatially modifies the velocity amplitudes of the array and is analogous to windowing time domain waveforms in digital signal processing applications. A commonly used method for amplitude shading was proposed by Dolph (35) which utilizes Tschebyscheff polynomials and provides the narrowest main lobe width for a specified reduced side lobe level. Dolph's method is referred to as the Dolph-Tschebyscheff method and is the only type of amplitude shading used in this thesis. See Appendix A, Section A.3, for MATLAB code which generates the required shading coefficients.

2.5 Single Element Directivity

A simple source, or a source of finite size, is any vibrating object where the radiated acoustic wavelength λ is much larger than the geometrical size of the object; a simple source is said to be acoustically small. A simple source is a source in which sound radiates equally in all directions, creating an omni-directional pattern. All exterior portions of the source must vibrate in phase and the size of the source must be much smaller than the radiated acoustic wavelength. As the frequency increases, and the acoustic wavelength approaches the size of the source, the pattern becomes more

directional. Point source array theory is strictly theoretical, but is valid if the sources can be considered simple sources. As this approximation ceases to hold true, the "First Product Theorem" must be used (sometimes referred to as the "Product Theorem"). This theorem states (36):

> *The directivity function of an array of N identical size and shape sources (or receivers), which are oriented the same, is equal to the product of the directivity function of any one of them times the directivity function of an array of N point sources (or receivers) positioned with the same center-to-center spacing and with the same relative amplitudes and phases as the original sources (or receivers).*

For a square shaped source housed in an infinite rigid baffle the single element directivity function, in a direction perpendicular to the plane of the baffled source, is

$$H(\theta) = \frac{\sin\left(\frac{1}{2}ka\sin\theta\right)}{\frac{1}{2}ka\sin\theta}, \tag{2.21}$$

where a represents the length of the side of the source (34, p. 177). See Appendix A, Section A.2, for MATLAB code which computes a single element directivity pattern.

2.6 Baffle Directivity

In practical array systems, sources are not housed in infinite baffles. Typically the infinite baffle single element directivity function is used and then a baffle directivity correction is applied. The baffle directivity not only depends on its geometrical shape but also depends on the impedance of the baffle. In addition, if neighboring rigid piston

sources are moving they create what is referred to as mutual impedance. An in-depth analysis of baffle directivity is beyond the scope of this thesis, though experimentally obtained baffle directivity patterns are found in Appendix B. In this thesis baffle directivity will be referred to account for the difference between a point source array directivity pattern possessing single element directivity, and experimentally determined directivity patterns of actual arrays. Mutual impedance effects will be lumped into baffle impedance.

2.7 Grating Lobes

Analysis of Eq. (2.20) reveals multiple poles, or angular locations of maximum amplitude, other than the main lobe located at θ_0, which occur when the denominator goes to zero and are located at

$$\theta_m = \sin^{-1}\left[\sin\theta_0 + m\left(\frac{2\pi}{kd}\right)\right], \tag{2.22}$$

where θ_m are the poles, and m is the grating lobe integer $m = \pm 1, \pm 2, \pm 3, \ldots$. These poles are called grating lobes. The first grating lobe, θ_{GL}, assuming positive steering, occurs at $m = -1$,

$$\theta_{GL} = \sin^{-1}\left[\sin\theta_0 - \left(\frac{2\pi}{kd}\right)\right]. \tag{2.23}$$

The frequency at which the acoustic wavelength equals twice the source spacing,

$$\lambda = 2d, \tag{2.24}$$

is referred to as the design frequency,

$$f_0 = \frac{c}{2d}. \tag{2.25}$$

The directivity pattern of an array operating at the design frequency will only possess a grating lobe peak when steered to 90°, or end fire. At twice the design frequency, a grating lobe peak will always appear in the directivity pattern, with grating lobes at each end fire direction when unsteered; this frequency is referred to as the grating lobe frequency or aliasing frequency. Figure 2.2 indicates the locations of the grating lobe peaks versus the ratio of operation frequency to design frequency (the design frequency ratio) and steer angle. Figure 2.2 could be mirrored about the 0° steer angle for negative steer angles. As an example of how to use Fig. 2.2, consider a frequency of 2 times the design frequency and a steer angle of 15°, a grating lobe will be found at -46°.

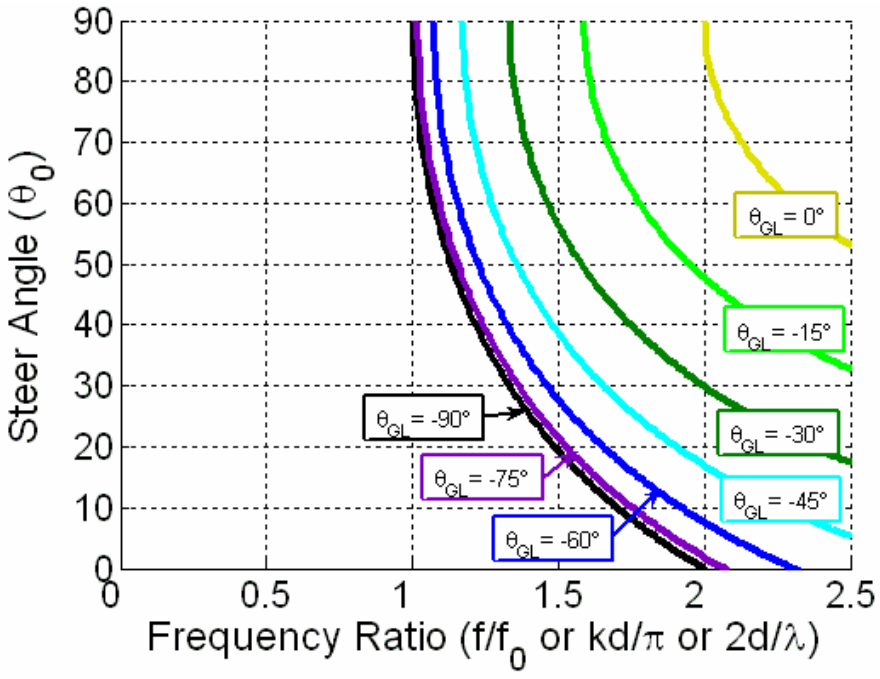

Fig. 2.2. Grating lobe angular location versus design frequency ratio and steer angle. The contour lines represent the resulting grating lobe angular location for $m = -1$ grating lobes.

2.8 Two-Dimensional Planar Arrays

The directivity function for a two-dimensional planar array may be found using the "Second Product Theorem." This theorem states (36):

> *The directivity function of a planar velocity distribution of the form* $u(x,y)=u_0 f(x)g(y)$ *is equivalent to the product of the directivity functions of the two perpendicular line sources, one lying along the x-direction with the velocity distribution* $f(x)$ *and the other lying along the y-direction with the velocity distribution* $g(y)$.

Thus, the directivity functions in the directions x and y may be multiplied since they are orthogonal, meaning that the directivity patterns in each direction are independent.

2.9 Continuous Source Line Array

Consider a point source array of aperture length L. As the spacing between the point sources, d, decreases to zero (meaning that the number of point sources, N, increases towards infinity), the velocity distribution along L transitions from point sources at discrete locations to a continuous function line source. The expression for the far field directivity function of a continuous line source (34, p. 177) is

$$H(\theta)=\frac{\sin\left(\frac{1}{2}kL\sin\theta\right)}{\frac{1}{2}kL\sin\theta}. \tag{2.26}$$

The directivity function for a steered continuous line source steered to θ_0 would then be

$$H(\theta) = \frac{\sin\left[\frac{1}{2}kL(\sin\theta - \sin\theta_0)\right]}{\frac{1}{2}kL(\sin\theta - \sin\theta_0)}. \qquad (2.27)$$

2.10 Reciprocity

One aspect of the principle of reciprocity states that the directivity patterns of a given transducer at the same distance r are the same whether it is used as a receiver or as a transmitter (37, p. 378). This principle does not apply to transducer transmit and receive frequency responses since transduction ratios (ratio of one form of energy to another) are different for transmit and receive. Appendix C gives directivity patterns experimentally obtained in transmit and receive conditions for the same with-bar array verifying reciprocity for a bar placed in front of a transducer array.

2.11 Beamwidth

The beamwidth, BW, of a transducer or an array is a measure of how wide the single element directivity or main lobe is. A pattern whose amplitude is independent of angle is called an omni-directional pattern and has a beamwidth of 360°. Beamwidth is an angular measurement of the width of a peak measured at some specified decibel value down from the peak value and specified, for example, as the -3, -6, or -10 dB beamwidth.

2.12 Array Design

Design of a line array often begins with selection of the design frequency. Once the design frequency is chosen, the source spacing is often chosen such that

$$d = \frac{\lambda_0}{2} = \frac{c}{2 f_0}, \tag{2.28}$$

where λ_0 is the acoustic wavelength in air corresponding to the design frequency f_0. A half wavelength spacing between consecutive elements is very typical but in general the selection of element spacing depends on the steering requirements and number of sources N. For a fixed element spacing, as the number of sources is increased (assuming the aperture is allowed to vary), the beamwidth narrows while the angular location of the grating lobe is unchanged. The angular location of a grating lobe is governed by the ratio of the source separation and the wavelength, and the amount of steering introduced. Figure 2.3 displays the inherent main lobe -3 dB beamwidth for an unsteered array versus design frequency ratio and the number of sources.

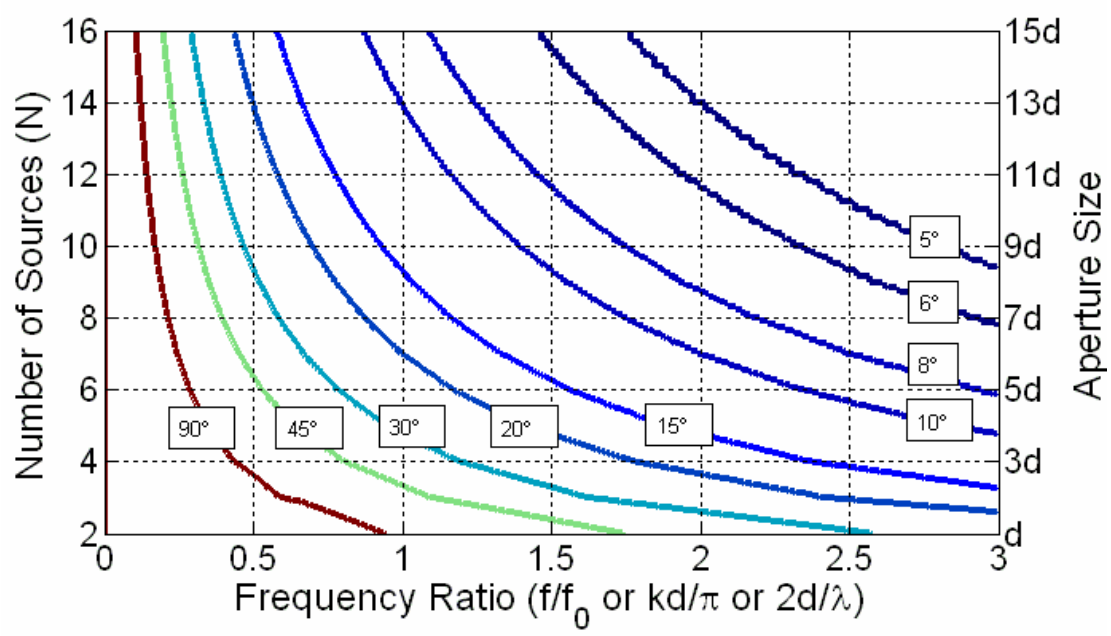

Fig. 2.3. Array design plot of -3 dB beamwidth of main lobe for an unsteered array versus design frequency ratio and the number of sources.

2.13 Ideal Passive Filter

As explained in Section 1.4, a brick wall filter, which filters out the grating lobe at a larger angle than the filter cutoff while passing the main lobe at a shallower angle than the cutoff, is the theoretical optimum passive filter. The limit of this filter, then, is when an array is operated such that the grating lobe angle equals the negative of the main lobe angle. This grating lobe mirror angle θ_{GLM} may be solved by substituting $\theta_{GLM} = -\theta_{GL} = \theta_0$ into Eq. (2.23),

$$\theta_{GLM} = \sin^{-1}\left[\frac{c}{2d}\frac{1}{f}\right]. \tag{2.29}$$

The $m = -1$, 90° grating lobe angle curve from Fig. 2.2 along with the angular dependence of the grating lobe mirror angle are plotted in Fig. 2.4.

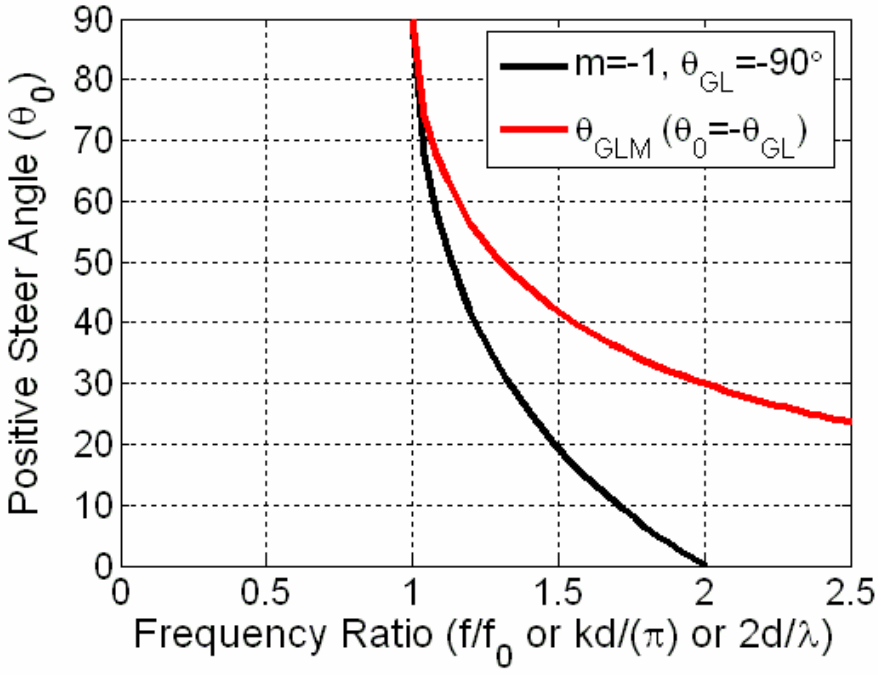

Fig. 2.4. Frequency and steer angle dependence of the angle of first encountered grating lobe ($m = -1$) and the grating lobe mirror angle where $\theta_0 = \theta_{GL}$.

2.14 Theoretical Directivity Pattern Surface Plots

Visualization of the directivity function of an array versus steer angle and receive angle, or angle of incidence, allows one to determine grating lobe locations and therefore steer angle limits.

The directivity pattern plot at 50 kHz, found in Fig. 2.5, is reviewed as an example to point out features commonly seen in these plots. A directivity pattern may be found as a vertical line cross section in each of the plots. The broadside, or unsteered,

directivity pattern is a vertical line at a steer angle of 0°, as denoted in Fig. 2.5. The 15° steered, directivity pattern is a vertical line at a steer angle of 15°. The $m = -1$ grating lobe is the long red-colored, curved ridge, in the angular plot, which runs from a steer angle of 0° and a receive angle of -90° to a steer angle of 90° and a receive angle of 0°. The $m = 1$ grating lobe ridge is a mirror ridge of the $m = -1$ grating lobe (mirrored and reversed about the main lobe). The horizontal line at 0° represents normal incidence for the peak in every vertical line pattern. The horizontal valleys located at receive angles of about ±90° are due to the first null from the single element directivity function.

The main lobe, always at a value of 0 dB, is denoted by the dashed black line which runs diagonally across the plot. Steered directivity patterns are also vertical lines at the appropriate steer angle. One may count the six side lobe ridges expected between the main lobe ridge and the grating lobe ridge. An N element array will have $N - 2$ side lobes. One may note the expected widening of the main lobe at large steer angles, particularly at lower frequencies.

For practical reasons, patterns are often steered only to ±30°. Therefore, to ease comparison analyses, the steer angle axis of the directivity pattern surface plots (other than the one found in Fig. 2.5) have been limited to ±30°. To simplify the analysis, only directivity pattern surface plots at 25 and 50 kHz will be presented. The standard theoretical directivity patterns, in unsteered and 15° steered conditions, at 25 and 50 kHz, may be found in the figures contained in Section 7.2.

The unshaded directivity functions plotted in the surface plots in Figs. 2.6-2.7 were each generated at 25 and 50 kHz, noted in the figure title, by steering the array from -30° to +30°. The angular directivity pattern may be found as a vertical line cross section

in each of the plots. The pattern is normalized with respect to its main lobe value for each steer angle. Color in Figs. 2.6-2.7 represents directivity pattern amplitude and the colorbar on the right of each subplot denotes the dB amplitude values corresponding to the various colors displayed. White colored portions indicate that the actual value is below -40 dB. The plots, obtained purely from theory, in Figs. 2.6-2.7 represent an array with $d = 1.164"$, $a = 1.148"$, and $f_0 = 25\,\text{kHz}$, which quantities match the arrays used in the experiments (see Chapter 6). See Appendix A, Section A.4, for MATLAB code which generates these plots.

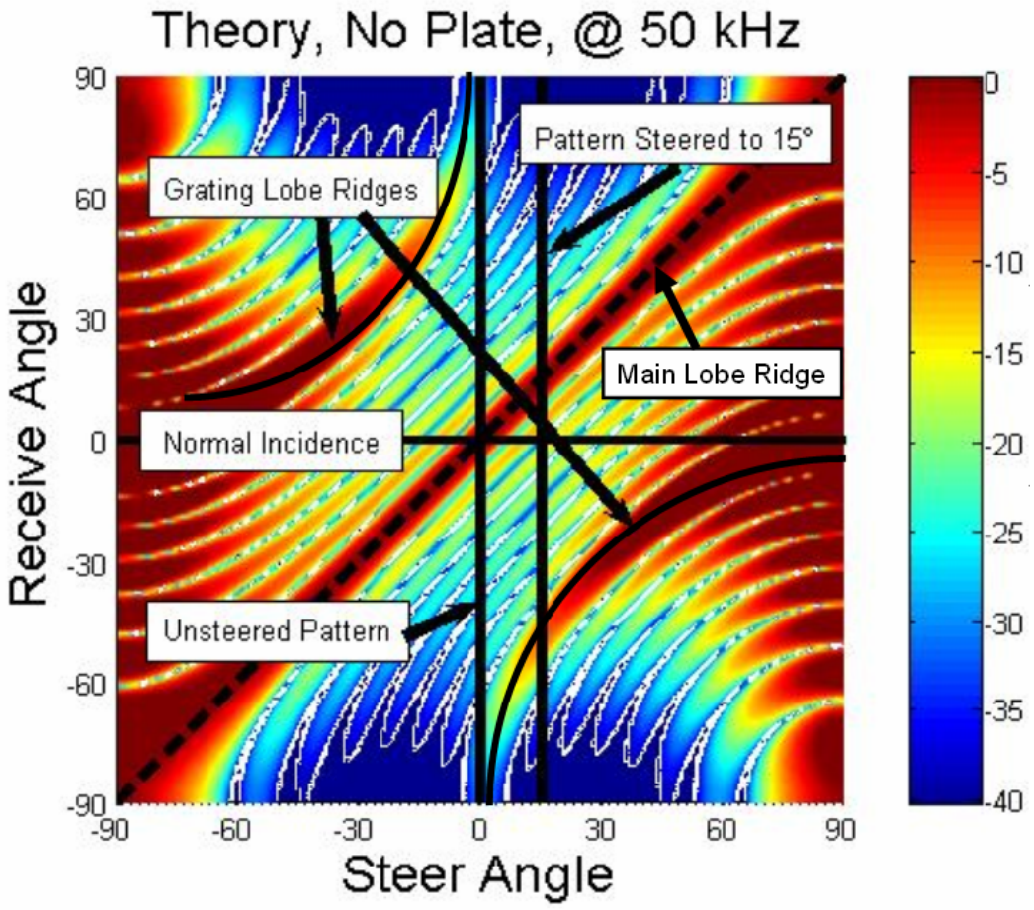

Fig. 2.5. Receive angle versus steer angle directivity pattern surface plot for the theoretical array driven at 50 kHz.

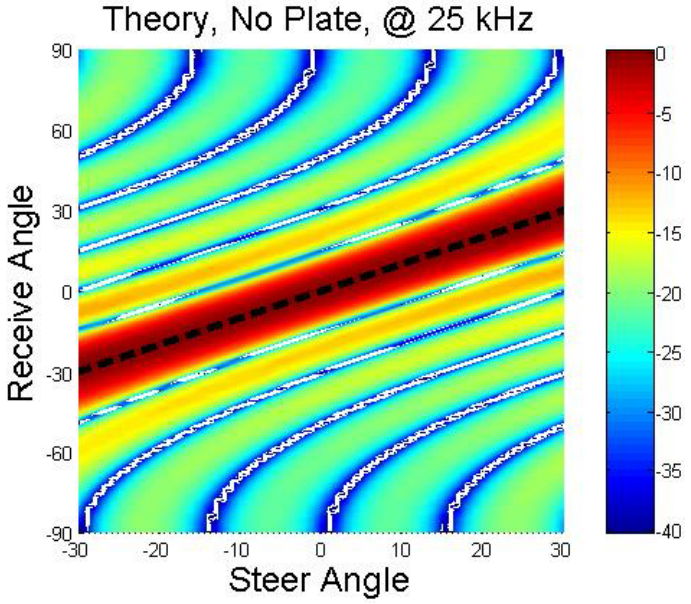

Fig. 2.6. Receive angle versus steer angle directivity pattern surface plot for the theoretical array driven at 25 kHz. Steer angle axis has been limited to ease analysis and to represent the region of practical interest. No grating lobes are present, as expected.

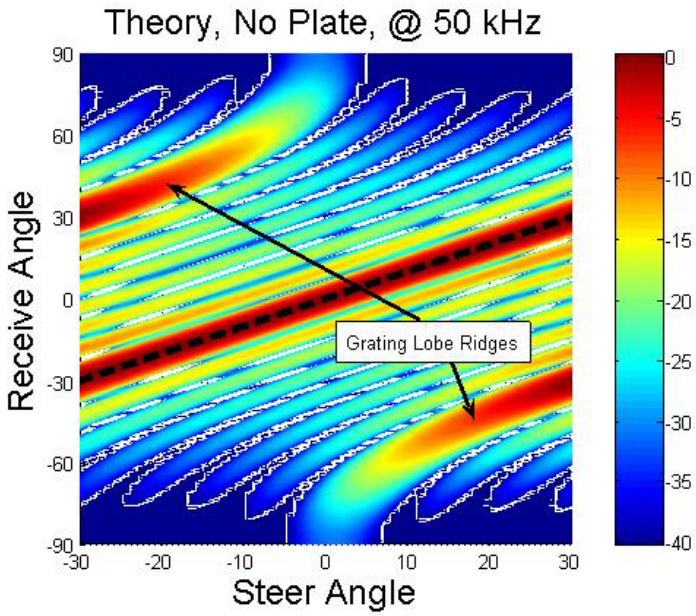

Fig. 2.7. Receive angle versus steer angle directivity pattern surface plot for the theoretical array driven at 50 kHz. Steer angle axis has been limited to ease analysis and to represent the region of practical interest. Grating lobe ridges are found at the expected angular locations.

Chapter 3

STRUCTURAL RADIATION AND TRANSMISSION THEORY

3.1 Introduction

This chapter will discuss common types of structural waves found in plates. An expression for the impedance of an unbounded flexible plate will be developed. The sound radiation from transverse waves will then be discussed. This will be followed by a development of expressions governing the sound intensity transmission through an unbounded flexible plate. The idea of structural filtering of supercritical plates will be presented along with a discussion of plate design. The predicted filtering performance of bars and a plate which are used in the experimental measurements of this thesis will conclude this chapter.

3.2 Structural Waves

Three common types of structural waves will be considered in this section, longitudinal, shear, and bending waves. All three types of waves can generate sound radiation. In structures, the longitudinal wave speed is the fastest, followed by the shear wave speed, and finally the bending wave speed (though the bending wave speed eventually approaches the shear wave speed as frequency increases). Of these three types of waves, only the bending wave speed is frequency dependent or dispersive.

3.2.1 Longitudinal Waves

A longitudinal wave propagates in the direction of its corresponding compressions and rarefactions. The longitudinal wave speed, c_L, is governed by the structure's Young's modulus, E, and its density, ρ_P, and is given by

$$c_L = \sqrt{\frac{E}{\rho_P}}. \tag{3.1}$$

Longitudinal waves create transverse motion due to the Poisson effect where contraction in one direction produces extension in the other orthogonal directions. Longitudinal wave speed is frequency independent.

3.2.2 Shear Waves

A transverse wave propagates in a direction perpendicular to its corresponding compressions and rarefactions. A shear wave is a specific type of a transverse wave, in which cross sections through the thickness of a plate or bar remain parallel. The shear wave speed, c_S, is governed by the structure's Young's modulus, E, its density, ρ_P, and its Poisson's ratio, σ, and is given by

$$c_S = \sqrt{\frac{E}{2\rho_P(1+\sigma)}} = \sqrt{\frac{G}{\rho_P}}. \tag{3.2}$$

where G is defined as the shear modulus. Shear wave speed is frequency independent.

3.2.3 Bending Waves

A bending wave is also a transverse wave, in which cross sections through the thickness of a plate or bar are not parallel. The bending wave speed, c_B, is dispersive and is governed by the structure's Young's modulus, E, its density, ρ_P, its Poisson's ratio, σ, and its thickness, h, and is given (for low frequencies) by

$$c_B = \sqrt{\omega\sqrt{\frac{Eh^2}{12\rho_P\left(1-\sigma^2\right)}}} = \sqrt{\omega\sqrt{\frac{D}{m}}}\,, \tag{3.3}$$

$$D = \frac{Eh^3}{12\left(1-\sigma^2\right)}, \tag{3.4}$$

$$m = \rho_P h\,, \tag{3.5}$$

where ω is the angular frequency, D is the bending stiffness of the plate, and m is the mass per unit area of the plate. Equation (3.3) is based on Bernoulli-Euler theory and does not include shear deformation and rotary inertia effects. As frequency increases towards infinity, the bending wave speed in Eq. (3.3) also goes towards infinity. An infinite wave speed is never actually reached in plates. When the following frequency inequality relationship holds:

$$\omega > \omega_T = \frac{c_B}{h}\,, \tag{3.6}$$

where ω_T is the Timoshenko angular frequency, the effects due to shear deformation and rotary inertia are necessary to accurately predict the bending wave speed. The bending

wave speed asymptotically approaches the value of the shear wave speed, and is no longer dispersive in frequency as frequency approaches infinity.

3.3 Unbounded Flexible Plate Impedance

An unbounded flexible plate may be modeled to possess a certain bending stiffness D, mass m, and damping η. The deflection, $\hat{\xi}$, of such a plate in the transverse direction to the plane of the plate subject to a distributed pressure field $\hat{p}$ is given by the following differential equation,

$$D\frac{\partial^4 \hat{\xi}}{\partial x^4} + m\frac{\partial^2 \hat{\xi}}{\partial t^2} = \hat{p}. \tag{3.7}$$

The deflection, $\hat{\xi}$, is assumed to possess the following form,

$$\hat{\xi} = \xi e^{j(\omega t - \tilde{\kappa} x)}, \tag{3.8}$$

where ξ is the displacement magnitude, ω is the angular frequency of oscillation, and $\tilde{\kappa}$ is the structural wavenumber. The structural wavenumber may be defined, for small damping ($\eta << 0.1$), as a complex quantity to include the damping loss factor η in the plate structure

$$\tilde{\kappa} = \kappa\left(1 - \frac{j\eta}{4}\right) = \frac{\omega}{c_P}\left(1 + \frac{j\eta}{4}\right), \tag{3.9}$$

where c_P is the transverse wave speed in the plate. Substitution of Eq. (3.8) into Eq. (3.7) results in the following equation (after discarding second order and higher ordered damping terms),

$$D\kappa^4(1-j\eta)\hat{\xi} - m\omega^2\hat{\xi} = \hat{p}\,. \tag{3.10}$$

The specific acoustic impedance $\tilde{z}_{SP}$ of the plate structure for transverse deflections is

$$\tilde{z}_{SP} = \frac{\hat{p}}{\hat{v}} = \frac{\hat{p}}{j\omega\hat{\xi}} = \frac{1}{\omega}D\eta\kappa^4 - \frac{j}{\omega}\left(D\kappa^4 - m\omega^2\right), \tag{3.11}$$

where $\hat{v}$ is the mechanical transverse velocity of the plate structure.

3.4 Sound Radiation by Transverse Waves

If an unbounded flexible plate supports a traveling wavenumber, κ, in the x direction, it will create acoustic plane waves in the fluid media on both sides of the plate. These plane waves will have nodes and antinodes corresponding to those found in the structural waves. The matching of the sound and structural waves may be expressed as follows

$$\frac{\kappa}{k} = \sin\theta\,, \tag{3.12}$$

$$\frac{c}{c_P} = \sin\theta\,, \tag{3.13}$$

$$\frac{\lambda}{\lambda_P} = \sin\theta\,, \tag{3.14}$$

where k is the acoustic wavenumber, c is the fluid sound speed, λ is the acoustic wavelength, λ_P is the wavelength in the plate and θ is the angle of incidence (normal incidence is defined as 0°). Note that Eqs. (3.12)-(3.14) produce real angles only when

the left-hand sides of these expressions are less than or equal to 1. One may also notice that pistonic motion of the plate corresponds to an infinite structural sound speed in the x direction and sound radiation purely in the z direction (normal to the plate). A plot of the relationship found in Eq. (3.13) is shown in Fig. 3.1. The curve in Fig. 3.1 shows the angle at which sound will radiate from a plate supporting a structural wave which is traveling faster than the speed of sound in the fluid. If the structural wave is slower than the fluid sound speed it will not radiate at a forward angle, $|\theta| \leq 90°$. Steering an array of transducers to radiate at a certain angle effectively creates an imaginary wave traveling in the plane of the array. Therefore, all forward steer angles correspond to supersonic traveling waves in the plane of the array.

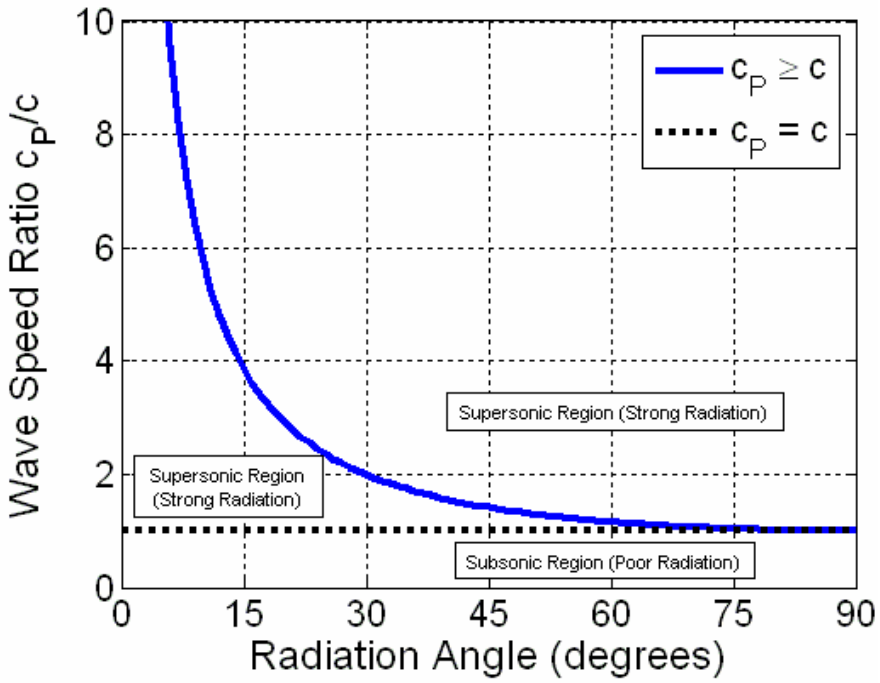

Fig. 3.1. Sound radiation angle resulting from a transverse structural wave versus the sound speed ratio of the structural wave speed to the fluid sound speed. Supersonic waves occur when $c_P > c$, while subsonic waves occur when $c_P < c$.

When the structural wave speed is greater than the fluid sound speed (super sonic), the generated acoustic plane wave will radiate well. When the structural wave speed is less than the fluid sound speed (sub sonic), the generated acoustic plane wave will radiate poorly. When the two sound speeds are equal, a maximum in the radiation efficiency occurs. Figure 3.2 gives an illustration of sound radiation by a super sonic structural wave. The principle of acoustic reciprocity applies to a structure radiating sound. Thus the reverse analogy where sound waves generate structural waves also behaves as described in this section.

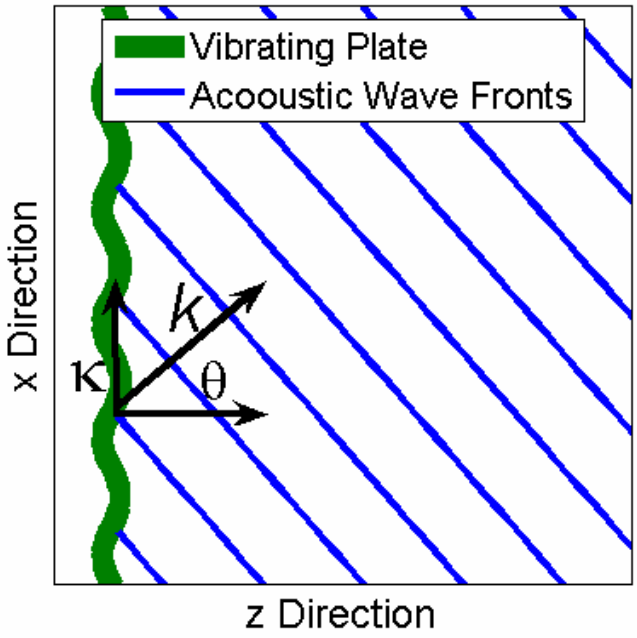

Fig. 3.2. Drawing depicting sound radiation by an unbounded flexible plate. The sound speeds of the fluid medium and the plate have been chosen arbitrarily such that $c_P > c$.

3.5 Transmission through an Unbounded Flexible Plate

The derivation in this section has been adapted from Fahy, (30, pp. 149-159) and (38, pp. 320-328). The specific acoustic impedance, $\tilde{z}_{SF}$, for a normal incidence plane wave incident upon an unbounded rigid plate, at the fluid plate interface, is given by

$$\tilde{z}_{SF}(0) = 2\rho c, \tag{3.15}$$

where ρ is the density of the fluid medium, and c is the speed of sound in the fluid medium. As the angle of incidence, θ, is varied from normal incidence, the impedance increases according to the following equation

$$\tilde{z}_{SF}(\theta) = 2\rho c \sec\theta. \tag{3.16}$$

In both Eq. (3.15) and Eq. (3.16), the factor of two arises from the pressure doubling effect of a plane wave incident on a rigid surface.

For the case of plane wave transmission through an unbounded flexible plate, the fluid media on either side of the plate may possess different material properties as shown in Fig. 3.3 (where the subscript numbers 1 and 2 correspond to incident and transmitted portions of space). Refraction of the direction of the transmitted waves is apparent in Fig. 3.3 due to the differing sound speeds in the incident and transmitted fluid media.

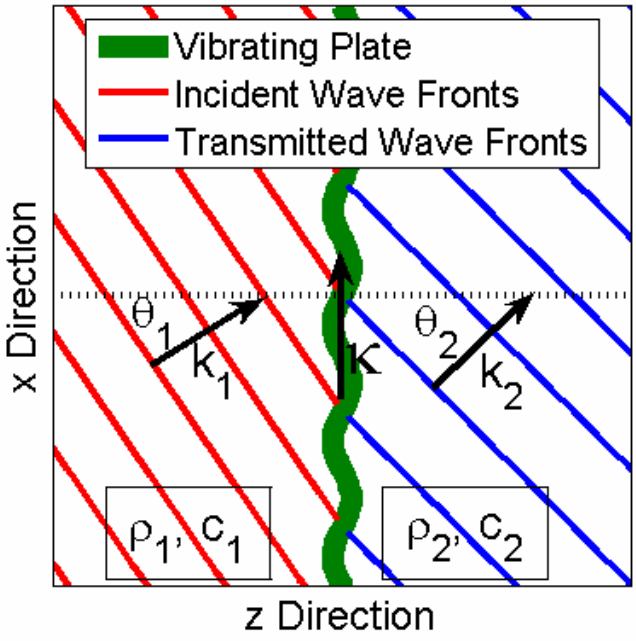

Fig. 3.3. Drawing depicting refracted transmission through an unbounded flexible plate. The sound speeds of the fluid media have been chosen arbitrarily such that $c_1 > c_2$.

The incident plane wave pressure, $\hat{p}_1$, may be expressed as

$$\hat{p}_1 = \tilde{p}_1 e^{j(\omega t - k_1 z - k_1 \sin\theta_1 x)}, \tag{3.17}$$

where $\tilde{p}_1$ is the incident pressure amplitude, k_1 is the incident acoustic wavenumber, θ_1 is the angle of incidence, x is the displacement in the x direction, and z, the displacement in the z direction, does not include the boundary surface. At the boundary, the incident pressure is commonly referred to as the blocked incident pressure, $\hat{p}_{B1}$, described by

$$\hat{p}_{B1}\left(x, z = 0^-, t\right) = 2\tilde{p}_1 e^{j(\omega t - k_1 \sin\theta_1 x)}. \tag{3.18}$$

The transmitted plane wave pressure, $\hat{p}_2$, and blocked transmitted pressure, $\hat{p}_{B2}$, may be expressed in a similar fashion to the respective equations for incident pressures,

$$\hat{p}_2 = \tilde{p}_2 e^{j(\omega t - k_2 z - k_2 \sin\theta_2 x)}, \tag{3.19}$$

$$\hat{p}_{B2}\left(x, z = 0^+, t\right) = 2\tilde{p}_2 e^{j(\omega t - k_2 \sin\theta_2 x)}, \tag{3.20}$$

where $\tilde{p}_2$ is the transmitted pressure amplitude, k_2 is the transmitted acoustic wavenumber, and θ_2 is the transmitted angle.

The normal incidence intensity transmission coefficient, $\tau_{\theta_1=\theta_2=0}$, is given by

$$\tau_{\theta_1=\theta_2=0} = \frac{\left|\dfrac{\tilde{p}_2}{2\tilde{z}_{SF2}(\theta_2 = 0)}\right|^2}{\left|\dfrac{\tilde{p}_1}{2\tilde{z}_{SF1}(\theta_1 = 0)}\right|^2} = \frac{\left|\dfrac{\tilde{p}_2}{2\rho_2 c_2}\right|^2}{\left|\dfrac{\tilde{p}_1}{2\rho_1 c_1}\right|^2} = \frac{\left|\tilde{p}_2\right|^2}{\left|\tilde{p}_1\right|^2}\frac{\rho_1 c_1}{\rho_2 c_2}, \tag{3.21}$$

where ρ is the fluid density, c is the fluid sound speed and the numbers 1 and 2 correspond to the incident and transmitted fluid media respectively. At angles other than normal incidence, and when the fluid media have different sound speeds, refraction must be taken into account according to Snell's law,

$$\frac{\sin\theta_1}{c_1} = \frac{\sin\theta_2}{c_2}. \tag{3.22}$$

Thus the intensity transmission coefficient, τ, for any general angle of incidence, must include the refraction relationship

$$\tau = \frac{\left|\dfrac{\tilde{p}_2}{2\tilde{z}_{SF2}}\right|^2}{\left|\dfrac{\tilde{p}_1}{2\tilde{z}_{SF1}}\right|^2} = \frac{\left|\dfrac{\tilde{p}_2}{2\rho_2 c_2 \sec\theta_2}\right|^2}{\left|\dfrac{\tilde{p}_1}{2\rho_1 c_1 \sec\theta_1}\right|^2} = \frac{\left|\tilde{p}_2\right|^2}{\left|\tilde{p}_1\right|^2}\frac{\rho_1 c_1}{\rho_2 c_2}\frac{\sec\theta_1}{\sec\theta_2}. \tag{3.23}$$

Equation (3.22) may be solved for $\sin\theta_2$ and substituted into Eq. (3.23) (with the use of the trigonometric identity ($\sin^2\theta + \cos^2\theta = 1$) to remove the dependence on θ_2,

$$\tau = \frac{\left|\tilde{p}_2\right|^2}{\left|\tilde{p}_1\right|^2}\frac{\rho_1 c_1}{\rho_2 c_2}\left[\frac{1-\left(\dfrac{c_2}{c_1}\sin\theta_1\right)^2}{1-\sin^2\theta_1}\right]^{\frac{1}{2}}. \tag{3.24}$$

If the fluid media on both sides of the unbounded plate are the same (sound speeds and densities must be equal, not just an impedance match), then Eq. (3.24) reduces to

$$\tau = \frac{\left|\tilde{p}_2\right|^2}{\left|\tilde{p}_1\right|^2}. \tag{3.25}$$

Normal to the surface of the plate, the acoustic particle velocity equals that of the mechanical velocity of the plate. The incident pressure amplitude may be expressed in terms of the mechanical velocity of the plate through an impedance relation given by

$$2\tilde{p}_1 = \left(\tilde{z}_{SP} + \tilde{z}_{SFT}\right)\tilde{v}, \tag{3.26}$$

where $\tilde{z}_{SFT}$ is the total specific acoustic impedance including the incident and transmitted fluid media $\tilde{z}_{SF1}$ and $\tilde{z}_{SF2}$ respectively. $\tilde{z}_{SFT}$ may also be expressed in terms of each individual fluid media

$$\tilde{z}_{SFT} = \tilde{z}_{SF1} + \tilde{z}_{SF2} = \rho_1 c_1 \sec\theta_1 + \rho_2 c_2 \sec\theta_2. \tag{3.27}$$

The transmitted pressure amplitude may be expressed in terms of the mechanical velocity of the plate through an impedance relation given by

$$\tilde{p}_2 = \tilde{z}_{SF2}\tilde{v} = \rho_2 c_2 \sec\theta_2 \tilde{v} = \frac{2\tilde{z}_{SF2}}{\tilde{z}_{SP} + \tilde{z}_{SF1} + \tilde{z}_{SF2}}\tilde{p}_1 . \tag{3.28}$$

Equation (3.28) may be used to expand Eq. (3.24) as follows

$$\tau = \left|\frac{2\tilde{z}_{SF2}}{\tilde{z}_{SP} + \tilde{z}_{SF1} + \tilde{z}_{SF2}}\right|^2 \frac{\rho_1 c_1}{\rho_2 c_2}\left[\frac{1-\left(\frac{c_2}{c_1}\sin\theta_1\right)^2}{1-\sin^2\theta_1}\right]^{\frac{1}{2}} . \tag{3.29}$$

Equation (3.29) may be expanded further to include the impedance expressions found in Eq. (3.11) and Eq. (3.27)

$$\tau = \left|\frac{2\rho_2 c_2 \sec\theta_2}{\frac{1}{\omega}D\eta\kappa^4 - \frac{j}{\omega}\left(D\kappa^4 - m\omega^2\right)... \\ ... + \rho_1 c_1 \sec\theta_1 + \rho_2 c_2 \sec\theta_2}\right|^2 \frac{\rho_1 c_1}{\rho_2 c_2}\left[\frac{1-\left(\frac{c_2}{c_1}\sin\theta_1\right)^2}{1-\sin^2\theta_1}\right]^{\frac{1}{2}} . \tag{3.30}$$

The square bracketed term in Eq. (3.30) models refraction of a wave from one medium to the other. If the two fluid media are the same (or are close enough), then refraction may be ignored and Eq. (3.30) simplifies to

$$\tau = \left|\frac{2\rho c \sec\theta}{\frac{1}{\omega}D\eta\kappa^4 - \frac{j}{\omega}\left(D\kappa^4 - m\omega^2\right) + 2\rho c \sec\theta}\right|^2 . \tag{3.31}$$

Application of the squared absolute value operators in Eq. (3.31) along with substitution of Eq. (3.12) results in

$$\tau = \frac{\left(2\rho c \sec\theta\right)^2}{\left[2\rho c \sec\theta + \frac{D}{\omega}\eta k^4 \sin^4\theta\right]^2 + \left[m\omega - \frac{D}{\omega}k^4 \sin^4\theta\right]^2}. \tag{3.32}$$

See Appendix A, Section A.5, for MATLAB code which plots Eq. (3.32). The transmission loss, TL, defined as

$$TL = 10\log_{10}\left(\frac{1}{\tau}\right), \tag{3.33}$$

for Eq. (3.32) is

$$TL = \begin{bmatrix} 10\log_{10}\left[\left(2\rho c \sec\theta + \frac{D}{\omega}\eta k^4 \sin^4\theta\right)^2 + \left(m\omega - \frac{D}{\omega}k^4 \sin^4\theta\right)^2\right] \\ \ldots - 10\log_{10}\left[\left(2\rho c \sec\theta\right)^2\right] \end{bmatrix}. \tag{3.34}$$

At normal incidence Eq. (3.32) reduces to

$$\tau_{\theta=0} = \frac{1}{\left[\frac{m\omega}{2\rho c}\right]^2 + 1}. \tag{3.35}$$

3.6 Sound Radiation/Incidence Angle Filter

A plate may be designed such that the angular dependence of the transmission provides an advantageous radiation/incidence angle filter. When the transverse wave speed in the plate c_P is less than the fluid wave speed, a subsonic plate, Eq. (3.32) may be approximated to be equivalent to the normal incidence transmission coefficient, Eq. (3.35), which also corresponds to the well known transmission mass law. If c_P is greater than the fluid wave speed, a super sonic plate, then a complex angular dependence

may be seen in the transmission coefficient. Figure 3.4 shows a sample plot of the transmission angular dependence for a supersonic plate using Eq. (3.32).

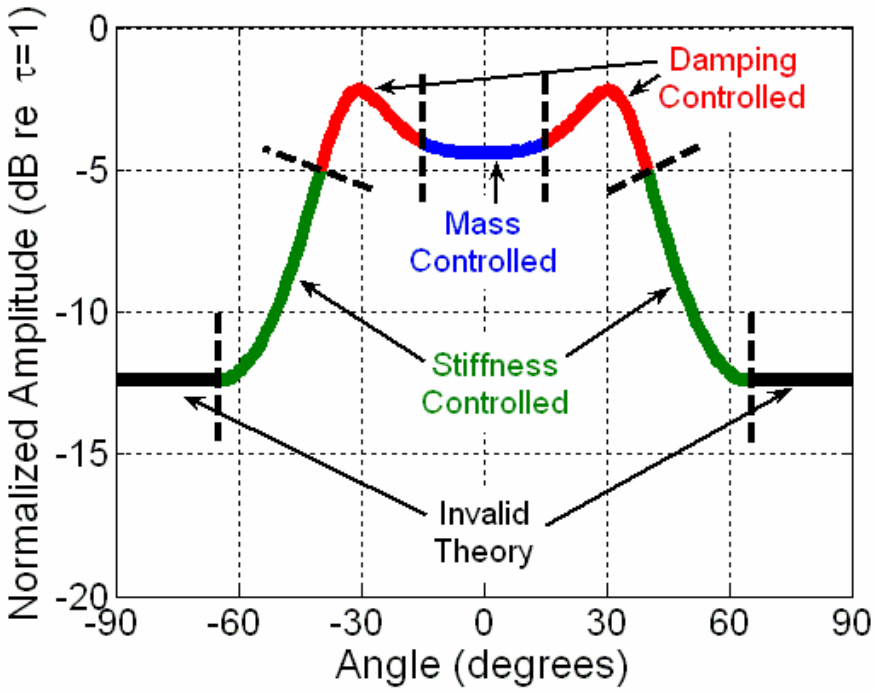

Fig. 3.4. Sample plot of transmission in dB versus angle through an unbounded flexible plate at a fixed frequency. The material properties of the plate and fluid media have been chosen such that $c_P > c$. The dashed lines separate various "controlled" regions.

The mass-controlled region of the plot in Fig. 3.4 may be approximated using the equation for mass law transmission coefficient (see Eq. (3.35)). The peak in the plot in Fig. 3.4, is due to the coincidence condition. The frequency-dependent coincidence condition is defined where the structural wave speed equals the fluid wave speed of the pressure component in the plane of the structure (or $c_P = c\sin\theta$). The angle of the peak, called the coincidence angle, θ_{CO}, is governed by

$$\sin^2\theta_{CO} = \frac{c^2}{\omega}\sqrt{\frac{m}{D}}. \qquad (3.36)$$

The θ_{CO} occurs when the imaginary part of the plate's impedance equals zero (or when the bracketed expression on right-hand-side of the denominator of Eq. (3.32) equals zero) and is proportional to the arcsine of the inverse square root of frequency. At θ_{CO}, Eq. (3.32) simplifies to

$$\tau(\theta_{CO}) = \frac{1}{\left(1 + \frac{\eta m \omega}{2\rho c}\sqrt{1 - \frac{c^2}{\omega}\sqrt{\frac{m}{D}}}\right)^2}. \tag{3.37}$$

When no damping is present in the plate the transmission coefficient equals one at θ_{CO} (perfect transmission at θ_{CO}). Many structural materials, including the ones tested in this thesis, possess very small loss factors; for this reason the loss factor is set to zero when plotting Eq. (3.32) in this thesis. The stiffness controlled region of the transmission coefficient expression occurs when the stiffness terms begin to dominate. The transmission coefficient expression in Eq. (3.32) returns to a value of 1.0 (perfect transmission) at end-fire or 90°. Fahy comments that (30, pp. 157-158):

> *… and performing the integration from 0° to 78°. Theories of sound transmission through panels of finite area, … provide evidence to support omission of waves close to grazing incidence in the case of a bounded panel.*

The reason for the selection of a cutoff of 78° is unclear. Inspection of many different filter shapes for various materials reveals that the minimum of these filters, before heading back up to a transmission coefficient of 1.0, is about 65°. In nearly all filter shapes, 78° is just after the minimum and is a couple dB higher than the minimum. In

this thesis, it is assumed that the filter dependence beyond 65° is at the same level at the value at 65° or at a decreased value.

3.7 Material and Geometry Considerations for Optimum Plate Design

Figure 3.5 shows various materials versus their mechanical properties of density and Young's modulus (39, p. 418). Red colored dots represent approximate material properties for the plates and bars used. From right to left, the dots represent aluminum honeycomb (AH) , pine wood (PW), and alumina (AA). These red dots are also represented in Figs. 3.6-3.8.

The coincidence or filter angle may be set to any desired value, within some limits (40, p. 172, Fig. 6.6), at a specific frequency. Once this coincidence condition is chosen plate design follows according to the discussion below. For practical reasons in this thesis, the desired coincidence angle is chosen to be 30° at 50 kHz (approximately twice the design frequency for the arrays used in this thesis) and the Poisson ratio is fixed at 0.30. The optimum thickness, $h_{Optimum}$, may then be calculated for any material using Eqs. (3.4), (3.5), and (3.36),

$$h_{Optimum} = \frac{{c_B}^2}{\omega}\sqrt{\frac{12\rho_P\left(1-\sigma^2\right)}{E}}\,. \tag{3.38}$$

From Eq. (3.13), a fixed coincidence angle of 30° forces the bending wave speed to be 3000 m/s, if the speed of sound in water is taken to be 1500 m/s. A plot of the optimum thickness values for various Young's moduli and densities is found in Fig. 3.6.

The filtering performance of a plate may partly be characterized by the pass band transmission loss and by the relative stop band transmission loss. The frequency response of the plate filtering is also important to characterize a plate's performance and will be covered in Chapter 4. The transmission coefficient in the pass band is the transmission coefficient at normal incidence. The transmission loss in the pass band, TL_{PB}, is calculated using Eq. (3.35),

$$TL_{PB} = 10\log_{10}\left(\frac{1}{\tau_{\theta=0}}\right) = 10\log_{10}\left(\left[\frac{m\omega}{2\rho c}\right]^2 + 1\right). \tag{3.39}$$

A plot of the pass band transmission loss versus material properties is found in Fig. 3.7. The pass band transmission loss for the example in Fig. 3.4 is about 4 dB.

The relative stop band transmission loss, TL_{RSB}, is defined as the difference between the pass band transmission level, TL_{PB}, and the minimum of the filter at 65° (see Section 3.6),

$$TL_{RSB} = TL_{PB} - \min\left[TL(\theta)\right] = TL_{PB} - TL(65°). \tag{3.40}$$

A plot of the relative stop band transmission loss versus material properties may be found in Fig. 3.8. The relative stop band transmission loss for the example in Fig. 3.4 is about $-4-(-12)=8$ dB.

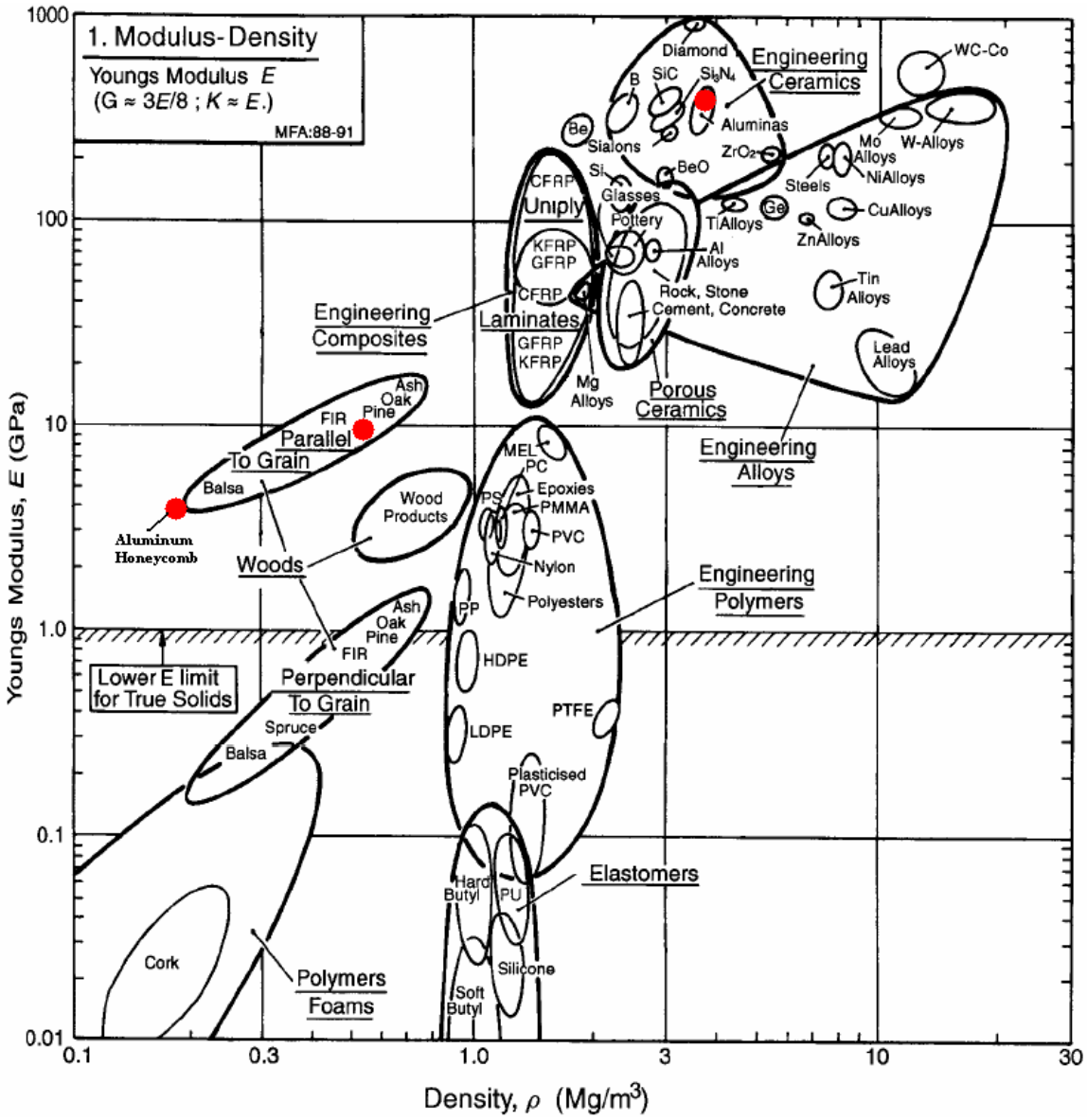

Fig. 3.5. Plot of Young's modulus versus density for various materials (39). From left to right, red dots represent aluminum honeycomb, pine wood, and alumina.

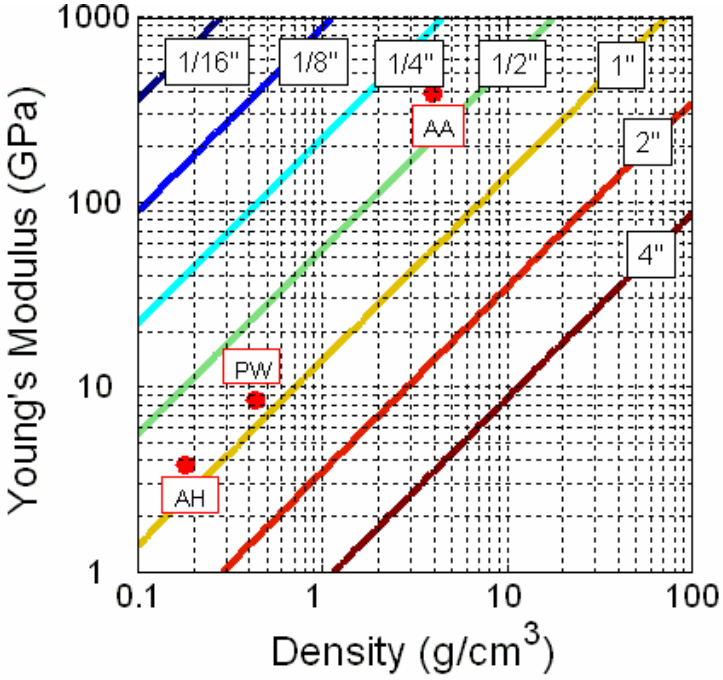

Fig. 3.6. Optimum thickness for plate filtering versus Young's modulus and density. From left to right, red dots represent aluminum honeycomb, pine wood, and alumina.

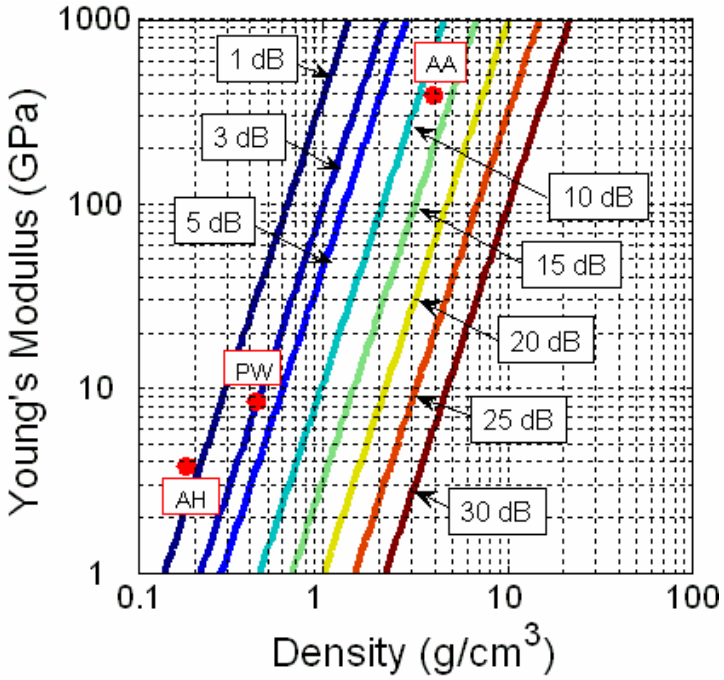

Fig. 3.7. Pass band transmission loss for an optimum thickness plate versus Young's modulus and density. From left to right, red dots represent aluminum honeycomb, pine wood, and alumina.

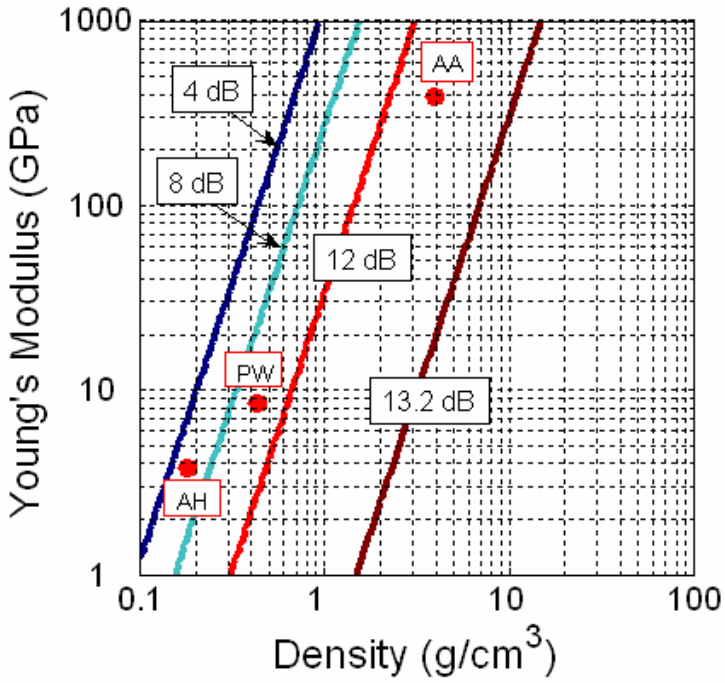

Fig. 3.8. Resulting relative stop band transmission loss for an optimum thickness plate versus Young's modulus and density. From left to right, red dots represent aluminum honeycomb, pine wood, and alumina.

3.8 Frequency Dependence of Coincidence Angle

The frequency dependence of the coincidence angle must also be examined to determine the range of available incidence angles and frequencies for sound transmission. As explained in Section 3.6, the coincidence angle is dispersive and is proportional to the arcsine of the inverse square root of frequency. The criterion of a 30° coincidence angle at 50 kHz is used to determine the frequency dependence of the coincidence angle for an array possessing a design frequency of 25 kHz. The bending wave speed at 50 kHz is

3000 m/s. Thus the ratio of bending stiffness to mass per unit area (units of m^4/s^2) may be solved for

$$c_B = 3000\frac{\text{m}}{\text{s}} = \sqrt{\omega}\sqrt{\sqrt{\frac{D}{m}}}, \tag{3.41}$$

$$\frac{D}{m} = \left(\frac{3000}{\sqrt{2\pi}\sqrt{50000}}\right)^4 = 820.7\frac{\text{m}^4}{\text{s}^2}. \tag{3.42}$$

Rearranging Eq. (3.36) yields the frequency dependence of the coincidence or filter angle

$$\theta_{CO} = \sin^{-1}\left[111.8\frac{1}{\sqrt{f}}\right]. \tag{3.43}$$

Figure 2.4 plotted the $m = -1$, 90° grating lobe angle curve and the location of the theoretical limit for an ideal brick wall passive filter. Figure 3.9 plots the angular dependence of the coincidence angle along with the 90° grating lobe location curve. It may be seen that region A (where the main lobe is passed and the grating lobe is attenuated) is gained at the expense of region B (where the main lobe is attenuated). Region C is an additional limit and is not usable since the grating lobe will still be passed even though the main lobe angle is shallower than the grating lobe angle. Again, it should be noted that these equations and design figures depend on criteria which will apply to the specific application chosen.

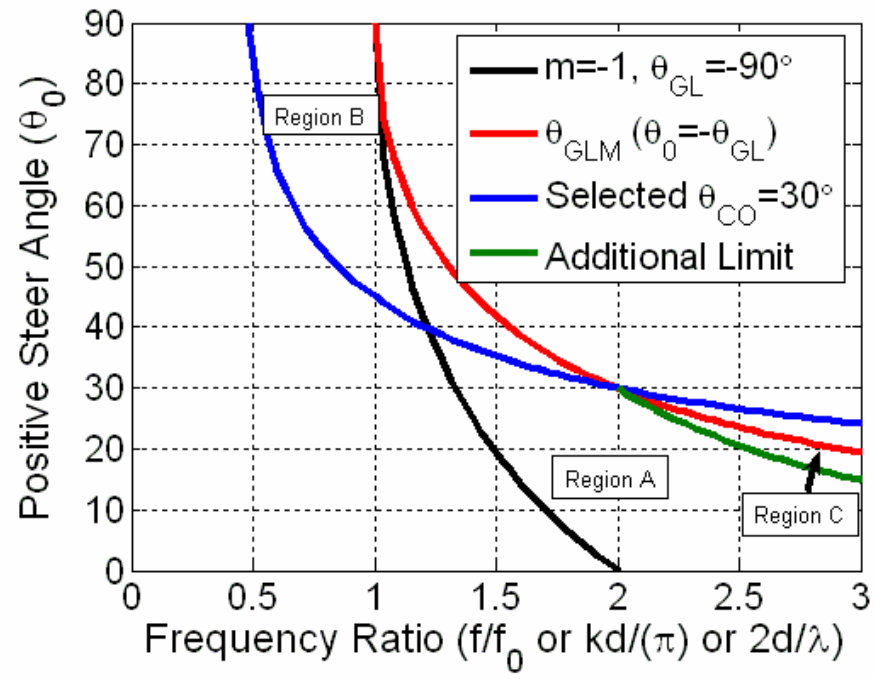

Fig. 3.9. Frequency and steer angle dependence of the angle of first encountered grating lobe ($m = -1$), the grating lobe mirror angle where $\theta_0 = \theta_{GL}$, the designed coincidence angle (which equals $\theta_{CO} = 30°$ at 50 kHz), and the additional limit of usable operation.

3.9 Design Discussion

Figure 3.10 shows the dependence of TL_{PB} and TL_{RSB} on plate density for a fixed Young's modulus and Poisson ratio. Unfortunately, the pass band transmission loss continues to increase, while the TL_{RSB} curve levels off with increasing density after passing a knee in the TL_{RSB} curve at a density of $1.0\, g/cm^3$. If a pass band transmission loss of 3 dB can be tolerated, then the resulting relative stop band transmission loss is approximately 10 dB. A plate with material properties which lie on these lines would provide a practical plate for grating lobe filtering. The additional variable is the thickness

required for the plate, which can be obtained from Fig. 3.6. This design criterion began with a selection of a 30° coincidence angle at 50 kHz. Table 3.1 indicates the potential design flexibility if the coincidence angle is varied. Decreasing the coincidence angle does increase the TL_{RSB}, at a faster rate than TL_{PB} increases. However, a narrower coincidence angle requires a higher stiffness to mass ratio. In addition, a lower limit exists for coincidence angles due to the breakdown of classical plate theory, where Timoshenko effects are required to model a plate at high frequencies (40, p. 172, Fig. 6.6). See Appendix A, Section A.6, for MATLAB code which generates the design plots Figs. 3.6-3.8.

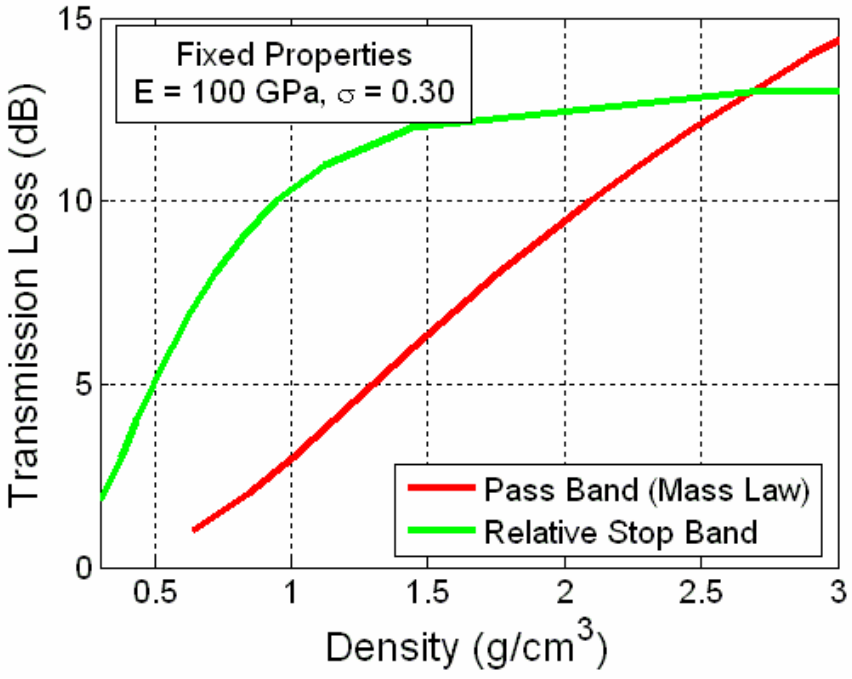

Fig. 3.10. Dependence of pass band transmission loss and relative stop band transmission loss on plate density for a Young's modulus of 100 GPa and a Poisson ratio of 0.30.

Table 3.1. Effect of varying the 50 kHz coincidence angle on required plate thickness, pass band transmission loss at 50 kHz, and relative stop band transmission loss at 50 kHz.

Coincidence Angle (degrees)	Thickness (inches)	Pass Band Transmission Loss (dB)	Relative Stop Band Transmission Loss (dB)
35°	0.30	2.0	5.0
32.5°	0.33	2.4	7.5
30°	0.38	3.0	10.2
27.5°	0.45	4.0	13.7
25°	0.50	4.5	17.5

3.10 Predicted Performance of Bars and Plates Used in Measurements

Table 3.2 lists the types of materials, along with their material and geometrical properties used in the measurements in Chapter 6. These bars and plates were selected according to the design criterion of a coincidence angle of 30° at a frequency of 50 kHz, as discussed in Section 3.7. Each plate or bar was assumed to be undamped ($\eta = 0$).

Table 3.2. Materials, and their properties, used in the measurements in Chapter 6. Measured values are denoted by an asterisk " * ". Other values were specified by the manufacturer or found in these reference numbers (34, p. 526) and (41, pp. 4-2, 4-3, and 4-7).

Material	Material Property Symmetry	Thickness (inches)	Other Dimensions (inches)	Young's Modulus (Gpa)	Density (kg/m³)	Poisson Ratio
Alumina	Isotropic	0.40*	*Rect. Bar* - Length 9.6*, Width 1.2*	391*	3956*	0.22
Aluminum Honeycomb	Orthotropic (Nearly Anisotrpic)	1.00*	*Circular Plate* - Diameter 10.5*	3.8	181*	0.33
Pine R-Direction	Orthotropic	0.98*	*Rect. Bar* - Length 10.38*, Width 1.23*	8.5	488*	0.33

Table 3.3 lists the calculated coincidence angles (at 50 kHz), pass band and relative stop band transmission losses (stop band value minus pass band value) and the maximum filter attenuation. Column 2 of Table 3.3 was calculated using Eq. (3.36), column 3 using Eq. (3.39), and column 4 using Eq. (3.40). All quantities are calculated at 50 kHz.

Table 3.3. Calculated structural filtering properties at 50 kHz of various bars and plates used in the measurements in Chapter 6.

Material	Coincidence Angle (degrees)	Pass Band Transmission Loss (dB)	Relative Stop Band Transmission Loss (dB)	Total Stop Band Transmission Loss (dB)
Alumina	29.3	13	13	26
Aluminum Honeycomb	27.3	1	10	11
Pine R-direction	25.6	4	12	17

Chapter 4

EQUIVALENT CIRCUIT MODELING

4.1 Introduction

The purpose of this chapter is to develop equations which model the measured frequency responses of an array with and without the insertion of a plate. The chapter begins with an introduction to Tonpilz transducers. An equivalent circuit for a Tonpilz transducer is then presented along with equations to model the no-plate frequency response. Next, an equivalent circuit is developed for a transducer receiving sound through a plate along with the corresponding equations to model the frequency response. The measured transducer parameters are then given. Finally, the chapter ends with a discussion of the effect of inserting a plate on the frequency response quality factor. Equivalent circuit analysis given in this chapter follows standard methods.

4.2 Tonpilz Transducers

The transducers used in this thesis work were of the Tonpilz configuration with piezoelectric motor elements. A typical Tonpilz transducer layout is given in Fig. 4.1. Tonpilz transducers consist of relatively lightweight rigid head masses which radiate the desired acoustic signal, a motor section which is often electrically insulated, and a relatively heavy tail mass. The motor section may consist of a single piezoelectric layer or, as used in this thesis, multiple layers in a stack as depicted in Fig. 4.1. The

piezoelectric layers are configured in the so called 3-3 orientation in which the mechanical motion is in the same plane as the piezoelectric polarization direction. The electrode plates are alternately wired positive and negative. The piezoelectric layers have their polarization directions alternated so that their electric fields line up with the electrode plate polarization directions. The tail mass is designed to be massive enough so that, at the fundamental resonance, a node is located near the tail mass. All of these parts are held together by a stress bolt.

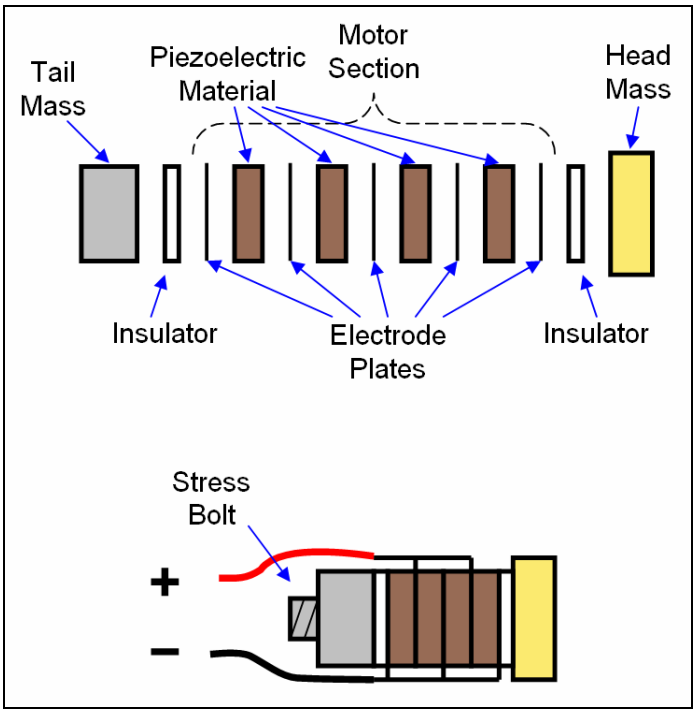

Fig. 4.1. Schematic drawing of a typical Tonpilz piezoelectric transducer in pieces (upper plot) and assembled (lower plot).

4.3 Transducer Equivalent Circuit

An acoustically unloaded and electrically unloaded Tonpilz transducer may be modeled at low frequencies (near resonance) using a lumped element equivalent circuit consisting of a mechanical mass M_{M1}, mechanical compliance C_{M1}, and mechanical resistance R_{M1} system in parallel with a mechanical equivalent electrical capacitance C_{M0} (the electro-mechanical coupling factor ϕ is used to convert circuit parameters between electrical and mechanical domains) as shown in Fig. 4.2. An acoustic plane wave normally incident upon the head mass of the transducer may be modeled as a pressure voltage source (pressure times surface area, S, in the mechanical impedance domain) in series with the radiation impedance loading, Z_{MA}, in the mechanical impedance domain as shown in Fig. 4.3. This equivalent circuit transducer model may be improved at high frequencies by adding so-called waveguide circuits for the ceramic motor section and for the head and tail masses.

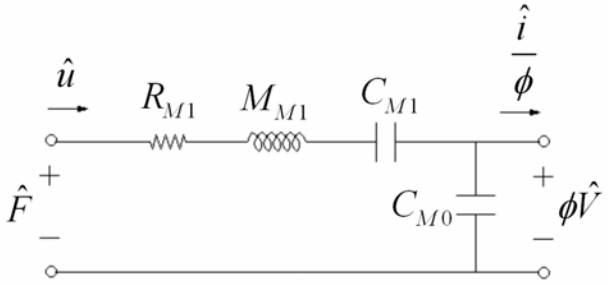

Fig. 4.2. Equivalent circuit model of a Tonpilz piezoelectric transducer in a receive condition with mechanical inputs on the left and electrical outputs on the right.

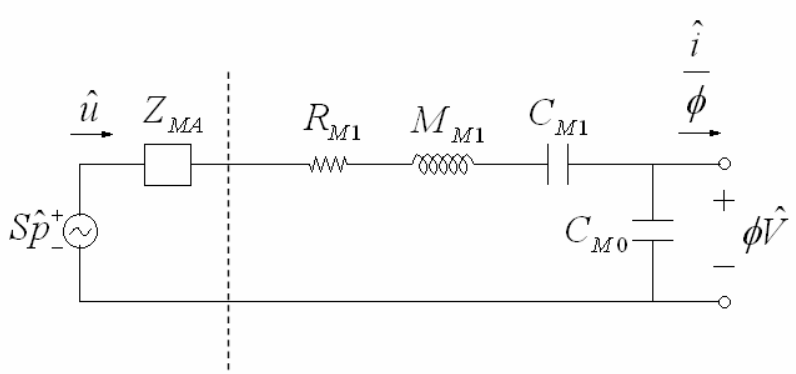

Fig. 4.3. Equivalent circuit model of an acoustically loaded Tonpilz piezoelectric transducer in a receive condition. The acoustical components are on the left of the dashed line with the transducer components on the right.

Circuit analysis of the circuit in Fig. 4.3 allows a transfer function between the incident pressure input, $\hat{p}$, and the voltage signal output, $\hat{V}$, to be solved for. The current quantity, which is the mechanical velocity, in the circuit in Fig. 4.3 is equal through all circuit elements, therefore the transfer function results in a ratio of the total loop impedance to the impedance due to C_{M0},

$$\frac{\hat{V}}{\hat{p}} = \frac{S}{\phi}\frac{Z_{MA} + Z_{M1} + Z_{M0}}{Z_{M0}}, \tag{4.1}$$

where

$$Z_{M1} = R_{M1} + j\omega M_{M1} + \frac{1}{j\omega C_{M1}}, \tag{4.2}$$

$$Z_{M0} = \frac{1}{j\omega C_{M0}}. \tag{4.3}$$

4.4 Equivalent Circuit of a Plate Loaded Transducer

The impedance of a layer of material may be modeled with a so-called waveguide equivalent circuit. A waveguide circuit consists of a T network of impedances as shown in Fig. 4.4. The mechanical impedances, Z_{ML1} and Z_{ML2}, in Fig. 4.4 are given by

$$Z_{ML1} = j\rho cS \tan\left(\frac{kL}{2}\right), \tag{4.4}$$

$$Z_{ML2} = -j\rho cS \csc(kL), \tag{4.5}$$

where ρ is the density of the layer, c is the speed of sound in the layer, k is the acoustic wavenumber in the layer and L is the thickness of the layer.

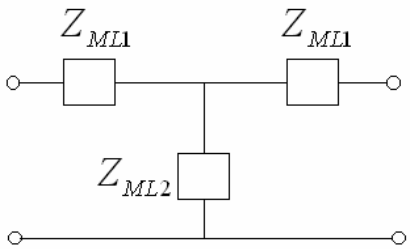

Fig. 4.4. Equivalent circuit model of a waveguide circuit. The impedances for the waveguide circuit may be found in Eq. (4.4) and Eq. (4.5).

For a transducer radiating through a lossy compliant layer and a plate, two waveguide circuits may be added to the circuit in Fig. 4.3 to model these two layers as shown in Fig. 4.5 where the waveguide impedances are determined from Eq. (4.4) and Eq. (4.5). To include the model the lossy behavior of the compliant layer, a resistance may be added to Z_{ML2}. The mechanical resistance in the lossy compliant layer was

adjusted to a value of $5000\,\mathrm{N\cdot s/m}$ to provide the best fit for modeled frequency responses to experimentally obtained frequency responses.

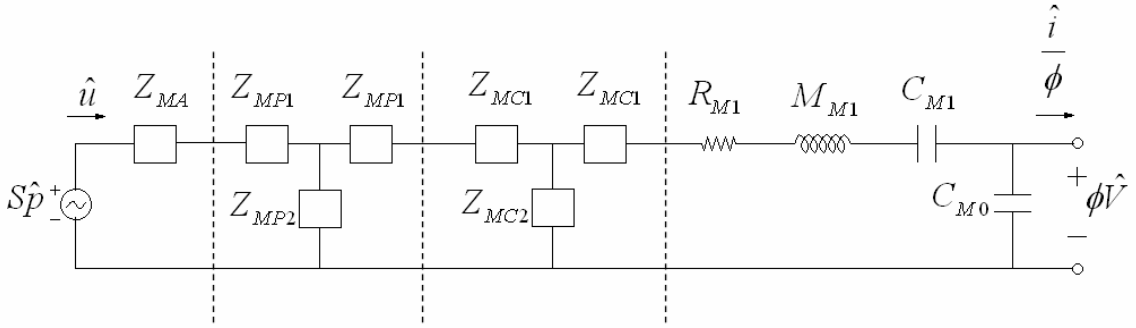

Fig. 4.5. Equivalent circuit model of an acoustically loaded and plate loaded Tonpilz piezoelectric transducer in a receive condition with waveguide circuits for the plate and compliant layer. The dashed lines separate, from left to right, the acoustical components, the waveguide model of the plate, the waveguide model of the compliant layer, and finally the transducer components on the right.

The transfer function between the input pressure and the output voltage from the circuit in Fig. 4.5 is a complicated expression to solve for. The expressions given in Eqs. (4.2)-(4.5) will be used in this Kirchhoff loop analysis. The first step is to define current loops as shown in Fig. 4.6.

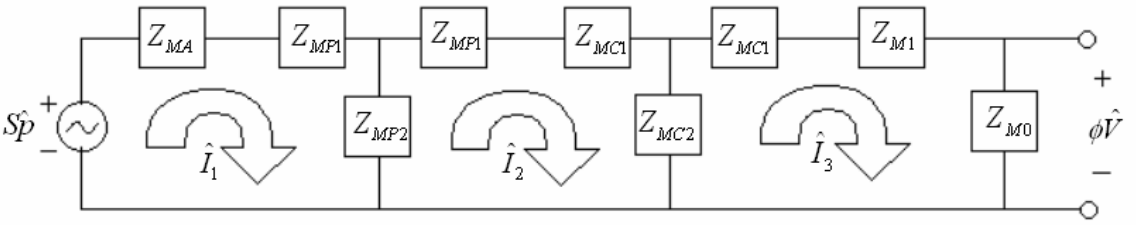

Fig. 4.6. Kirckhoff loop equivalent circuit for the circuit given in Fig. 4.5 .

The sum of the potential drops around a closed current loop is equal to zero. The loops are numbered according to the subscripts listed in Fig. 4.6. The sums of the potentials around each loop are

$$S\hat{p} - \hat{I}_1\left(Z_{MA} + Z_{MP1} + Z_{MP2}\right) + \hat{I}_2 Z_{MP2} = 0\,, \tag{4.6}$$

$$\hat{I}_1 Z_{MP2} - \hat{I}_2\left(Z_{MP2} + Z_{MP1} + Z_{MC1} + Z_{MC2}\right) + \hat{I}_3 Z_{MC2} = 0\,, \tag{4.7}$$

$$\hat{I}_2 Z_{MC2} - \hat{I}_3\left(Z_{MC2} + Z_{MC1} + Z_{M1} + Z_{M0}\right) = 0\,. \tag{4.8}$$

The output voltage may also be expressed in terms of $\hat{I}_3$,

$$\hat{V} = \frac{1}{\phi}\hat{I}_3 Z_{M0}\,. \tag{4.9}$$

The solution to this set of 4 equations (Eqs. (4.6)-(4.9)) results in the desired transfer function,

$$\frac{\hat{V}}{\hat{p}} = \frac{S}{\phi}\frac{Z_{MP2}Z_{MC2}Z_{M0}}{Z_\alpha Z_\beta Z_\gamma}\,, \tag{4.10}$$

where

$$Z_\alpha = Z_{MA} + Z_{MP1} + Z_{MP2}\,, \tag{4.11}$$

$$Z_\beta = Z_{MP2} + Z_{MP1} + Z_{MC1} + Z_{MC2}\,, \tag{4.12}$$

$$Z_\gamma = Z_{MC2} + Z_{MC1} + Z_{M1} + Z_{M0}\,. \tag{4.13}$$

4.5 Equivalent Circuit Parameter Values

The Tonpilz piezoelectric transducers used in this thesis were of three slightly different designs. Each of the three types of transducers had approximately the same equivalent circuit parameter values. These parameters are measured in the electrical impedance domain, thus an electro-mechanical coupling factor, ϕ, is also required to determine the mechanical impedance equivalent circuit parameters. The mechanical parameters depicted in Fig. 4.2 may be obtained from the measured electrical impedance parameter values as follows

$$R_{E1} = 55.9\Omega, \tag{4.14}$$

$$L_{E1} = 0.113\mathrm{H}, \tag{4.15}$$

$$C_{E1} = 391\mathrm{pF}, \tag{4.16}$$

$$C_{E0} = 1209\,\mathrm{pF}, \tag{4.17}$$

$$\phi = 0.700, \tag{4.18}$$

$$R_{M1} = \phi^2 R_{E1} = 27.4\frac{\mathrm{N\cdot s}}{\mathrm{m}}, \tag{4.19}$$

$$M_{M1} = \phi^2 L_{E1} = 0.0554\,\mathrm{kg}, \tag{4.20}$$

$$C_{M1} = \frac{C_{E1}}{\phi^2} = 798\,\mathrm{p}\frac{\mathrm{m}}{\mathrm{N}}, \tag{4.21}$$

$$C_{M0} = \frac{C_{E0}}{\phi^2} = 2467\,\mathrm{p}\frac{\mathrm{m}}{\mathrm{N}}, \tag{4.22}$$

where R_{E1} is the electrical resistance equivalent parameter related to the mechanical resistance, M_{E1} is the electrical inductance equivalent parameter related to the mechanical head mass, C_{E1} is the electrical capacitance equivalent parameter related to the mechanical compliance, and C_{E0} is the parallel electrical capacitance. Figure 4.7 (left plot) shows modeled frequency responses of the no plate model displayed in Fig. 4.3, and with plate frequency responses for an alumina plate and an aluminum honeycomb plate modeled using the circuit displayed in Fig. 4.5. The difference between the no-plate and the with-plate models for each plate material is expressed as a transmission loss due to the plate and is also shown in Fig. 4.7 (right plot). Note that the aluminum honeycomb plate insertion results in a high quality factor, Q, response since it is a low impedance ($\rho_P c$) plate, and that the alumina, which has a high $\rho_P c$, lowers both the resonance frequency and the Q. Also, note that the plate adds another resonance at a somewhat higher frequency.

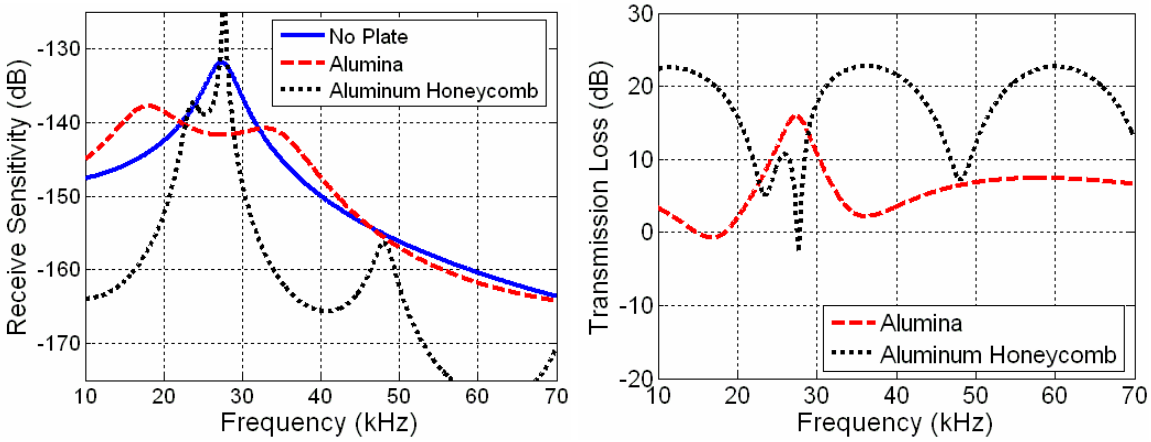

Fig. 4.7. Modeled frequency responses of the no-plate model displayed in Fig. 4.3, and modeled with-plate frequency responses for an alumina plate and an aluminum honeycomb plate modeled using the circuit displayed in Fig. 4.5 (right plot). The difference between the no-plate and the with-plate models for each plate material is expressed as a transmission loss due to the plate (left plot).

4.6 Frequency Response Quality Factor

The normal incidence frequency response is one of many common measures of the performance of a transducer array. This measurement may be performed with the transducers in a receive condition. A flat frequency response is desired for broadband frequency, receive sensitivity. The quality factor Q of a frequency response is a measure of how sharp the resonance peak is. For a frequency response transfer function, the quality factor is determined from the frequency of the peak value at resonance f_0, and the higher and lower frequencies, f_H, and f_L, respectively, corresponding to the half power points at which the transfer function decibel level is 3 dB down from the peak decibel level

$$Q = \frac{f_0}{f_H - f_L}. \tag{4.23}$$

The mechanical impedance equivalent circuit parameter values from Eqs. (4.19)-(4.22) were used to model the frequency response of a single transducer operating in a receive condition with and without a plate in front of the transducer. The plate's material properties were varied (according to the range outlined in Section 3.7) in an equivalent circuit analysis to determine the dependence of frequency response quality factor on the plate's material properties. The plate's thickness was determined using Fig. 3.6. Each with-plate frequency response was analyzed to determine the quality factor, Q_{WP}, and compared to the frequency response quality factor without a plate, Q_{WO}. The difference in these quality factors, Q_{Diff}, where

$$Q_{Diff} = Q_{WP} - Q_{WO}, \tag{4.24}$$

is plotted in Fig. 4.8 versus the plate's material properties. The colorbar to the right represents the Q_{Diff} value (yellow, orange and red lines represent increases in Q_{Diff}, while green and blue lines represent no change and/or decreases in Q_{Diff}). Contour lines are given at 1 dB intervals from -5 dB to 0 dB and at 2 dB intervals from 2 dB to 10 dB (a value of -6 dB is not found anywhere in the plot). From Fig. 4.8 it is apparent that plate material property combinations from the upper left hand region (defined by the black dashed lines) of the plot result in either no significant modification of the quality factor or a broadening improvement (low quality factors are desired in broadband applications) due to the presence of the plate. In Chapter 7 it will be shown that, of the three materials indicated, aluminum honeycomb detrimentally alters the frequency

response quality factor as expected. It must be noted here that Fig. 4.8 is specific to the transducers modeled, if one modeled transducers with different equivalent circuit parameters, then the quality factor analysis would change as well. See Appendix A, Section A.6, for MATLAB code which generates the design plot.

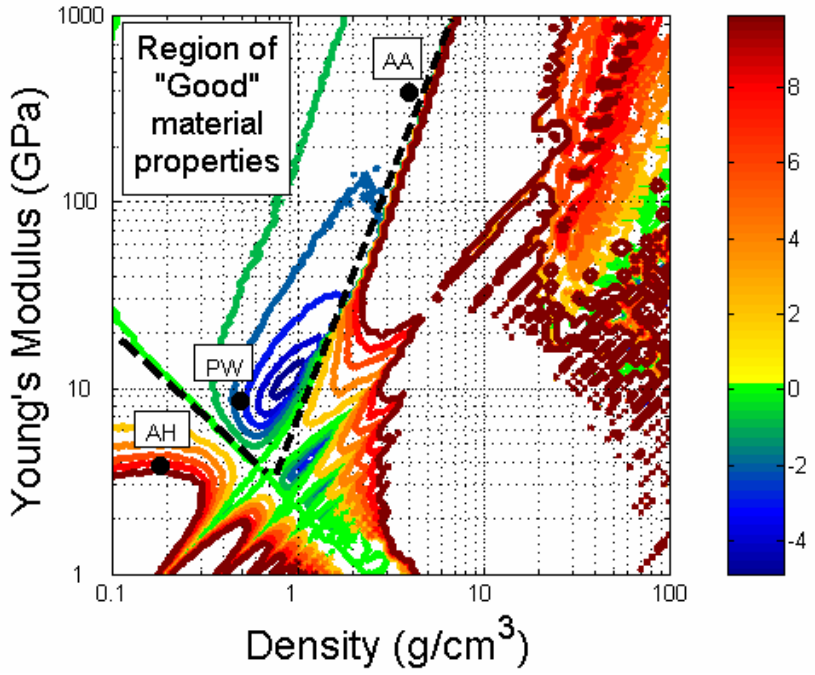

Fig. 4.8. Contour plot of the frequency response quality factor difference, Q_{Diff}, determined from equivalent circuit analysis. The numbered colorbar on the right indicates the Q_{Diff} value for the corresponding color. Materials used in experiments are denoted by red dots. The red boxes indicate the material (AA=Alumina, AH=Aluminum Honeycomb, PW=Pine Wood).

Chapter 5

NUMERICAL MODELING

5.1 Introduction

This chapter discusses the ANSYS numerical finite element model used in this thesis and the results obtained from its use. The chapter begins with a description of the ANSYS model used. Next is a discusson of two types of input conditions. This is followed by discussing a parameterization study to determine optimal material properties. Next, the issue of the plate and compliant layer thicknesses is discussed. An investigation of the ability to amplitude shade an array with a plate is discussed. Finally, the performance of a plate in reducing grating lobes is investigated versus drive frequency and steer angle.

5.2 ANSYS Model

A finite element numerical model was created in ANSYS to model the structural filtering of a plate inserted in front of an array of transducer elements with a compliant layer between the plate and the transducers as shown in Fig. 5.1. The model was two dimensional, meaning that the model depicted in Fig. 5.1 effectively extended infinitely into and out of the page. Each transducer's head motion was modeled with either constant displacement inputs or constant force inputs along a line. The compliant layer and plate layer were both modeled with isotropic plate finite structural elements. The

plate's properties were varied to study their effects on filtering performance. The compliant layer's properties were set to a Young's modulus of $2.59\,\text{GPa}$, a density of $980\,\text{kg}/\text{m}^3$, and a Poisson ratio of 0.47 representing the properties of a commonly used polyurethane. The left and right hand sides of the plate were free to vibrate, thus simulating a free-free bar condition. Between the plate layer and the water, a sound structure interaction interface was applied to the applicable finite elements. The water was modeled with fluid finite elements with a speed of sound of $1500\,\text{m}/\text{s}^2$ and a density of $1000\,\text{kg}/\text{m}^3$. An infinite baffle was applied to the lower border of the water, excluding the portion in contact with the plate. The finite elements on the hemisphere border of the water were no-reflection elements which simulate an infinitely extended water medium. The model was purely a lossless model (no damping).

Time-harmonic single-frequency sine waves were used as inputs. These inputs could be steered by applying an incrementally increasing phase shift as explained in Section 2.3. After the numerical analysis was performed, the velocity component in the vertical direction along the plate-water interface is used to generate the directivity pattern using the well known Rayleigh Integral. See Appendix A, Section A.7 for the MATLAB code used to process the ANSYS results.

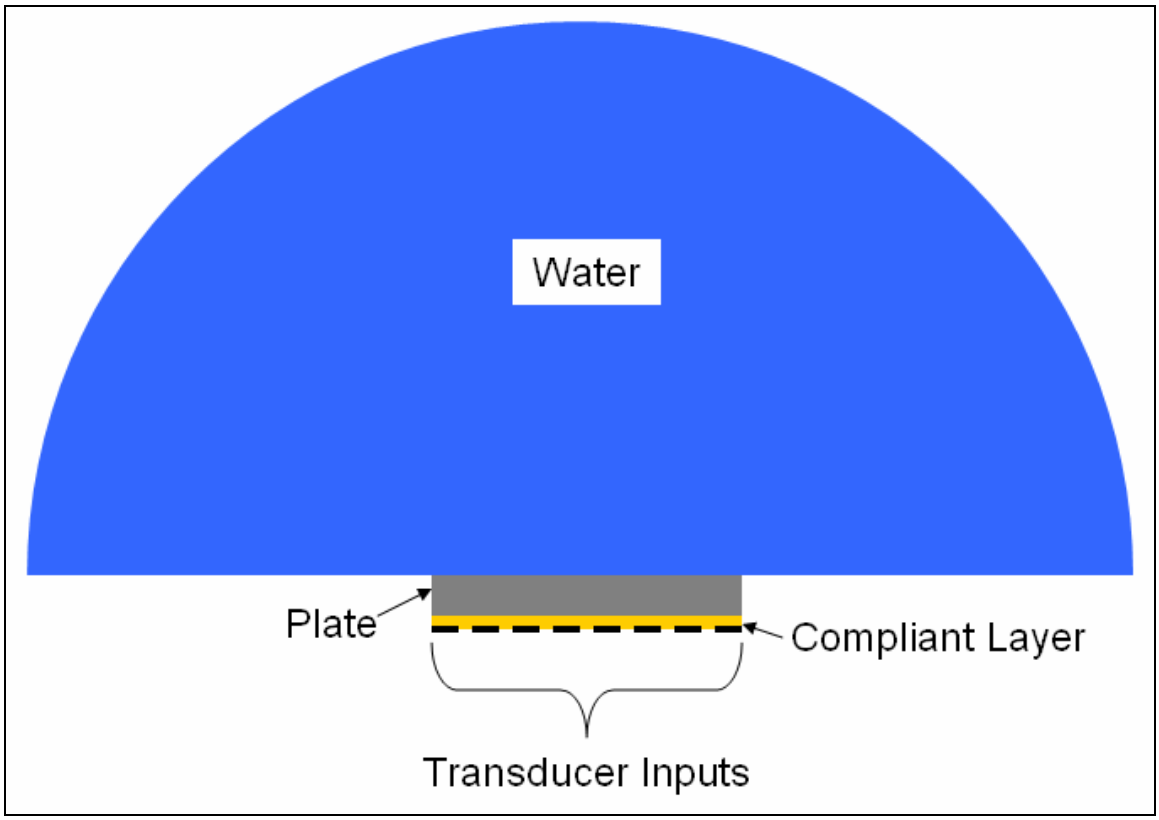

Fig. 5.1. Schematic drawing of ANSYS model (not to scale).

5.3 Constant Displacement versus Constant Force Inputs

Constant displacement drive inputs simulate transducers having much larger impedance than the load placed on it (the compliant layer, plate, and acoustic loading). When a plate is rigidly driven along its entire length, free-bending waves cannot propagate in the plate, thus the driven wave dominates. In the ANSYS model, as long as the compliant layer thickness was sufficiently thin, the plate could be considered as being rigidly driven along its entire length.

Constant force drive inputs simulate transducers having much lower impedance than the load placed on it. Constant force inputs allow free-bending waves to propagate and therefore they will affect the directivity pattern. Constant force inputs model the physical situation for this thesis work better than constant displacement inputs since the required material properties for the plate generally result in a higher impedance load than the transducer impedance.

Figure 5.2 shows a plot of directivity patterns at a frequency of 50 kHz and a steer angle of 15° for an optimized thickness alumina plate using constant displacement inputs along with the same plate being driven by constant force inputs. Implementation of either constant displacement or constant force inputs appears to generally yield a similar amount of filtering of the grating lobe. One should note the presence of extra energy in the side lobes in the with-plate directivity pattern with constant force inputs. These high side lobes are at ±32° and result from free-bending wave radiation.

5.4 Optimal Plate Material Properties

Thesis work began with optimization analysis using ANSYS modeling. There were at least four optimization degrees of freedom to begin with for the plate. These degrees of freedom were the plate's Young's modulus, density, Poisson ratio, and thickness. To simplify the optimization, the Poisson ratio for the plate was fixed to a common value 0.30. Materials, forming a grid with imaginary material properties, were each modeled to determine the dependence of grating lobe reduction on the plate's thickness, Young's modulus, and density. The Young's modulus varied from 15.6 GPa

to 1100 GPa. The density was varied from 1400 kg/m^3 to 9000 kg/m^3. The compliant layer thickness was fixed to a value of 0.0625 inches. The drive frequency was fixed at 50 kHz and the steer angle was fixed to 15°.

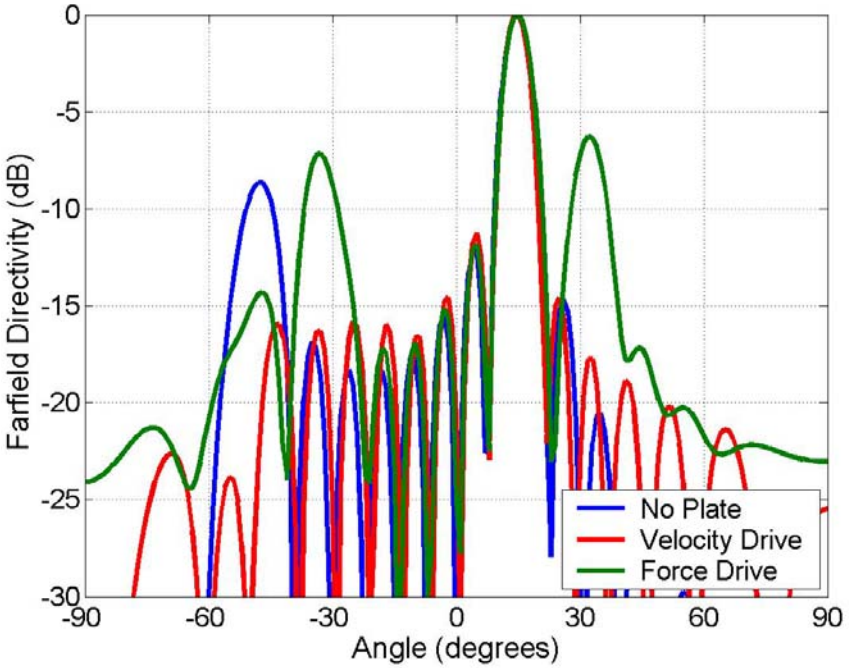

Fig. 5.2. Normalized directivity patterns from finite element analysis for an optimized thickness alumina plate with constant velocity (or constant displacement) inputs and constant force inputs as noted in the figure legend. The drive frequency is 50 kHz and steer angle is 15°.

With-plate directivity patterns were compared to theoretical no-plate directivity patterns to determine the optimal plate thickness. This comparison analysis included two comparison metrics, the grating lobe energy ratio (GLER), and the side lobe energy ratio (SLER). GLER is a ratio of the energy contained in the no-plate grating lobe (from null to null) to the energy contained at the same angles for a with-plate directivity pattern. SLER is a ratio of the energy contained in the no-plate side lobes (all angles excluding the main lobe from null to null) to the energy contained at the same angles for a with-plate directivity pattern. The optimized thickness dependence versus longitudinal

velocity, $c_L = \sqrt{E/\rho_P}$, and density ρ_P is displayed in Fig. 5.3. The black and white scale in Fig. 5.3 represents the plate thickness in inches. The plot in Fig. 5.3 shows that lower density materials require a thicker plate for grating lobe filtering than higher density materials do. This comparison is only valid for materials which possess the same longitudinal wave speed, in other words the same Young's modulus to density ratio.

The grating lobe energy ratio, GLER, dependence versus longitudinal velocity, $c_L = \sqrt{E/\rho_P}$, and density ρ_P is displayed in Fig. 5.4 . The black and white scale in Fig. 5.4 represents GLER in dB relative to zero reduction in the grating lobe total energy. The side lobe energy ratio, SLER, dependence versus longitudinal velocity, $c_L = \sqrt{E/\rho_P}$, and density ρ_P is displayed in Fig. 5.5. The black and white scale in Fig. 5.5 represents SLER in dB relative to zero reduction in the total energy of the side lobes. Figures 5.4-5.5 show that a plate material must possess a high stiffness to mass ratio, E/ρ_P . These plots also show there exists a point of diminishing returns ($c_L \geq 11050\, m/s$), where regardless of their E/ρ_P ratio, if 2 materials each possess materials properties which result in a longitudinal wave speed of 12 km/s or higher, both will achieve the same amount of grating lobe level reduction and reduction of average side lobe levels.

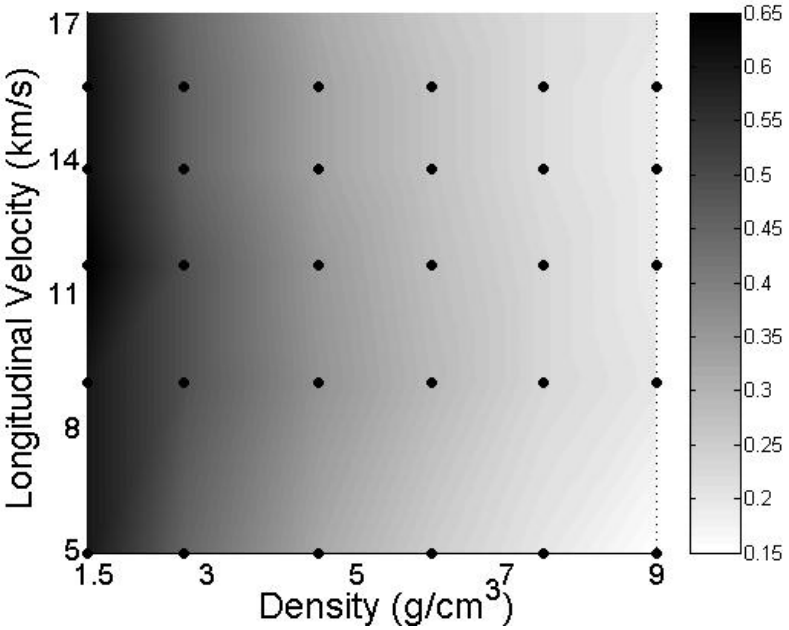

Fig. 5.3. Dependence of optimized thickness versus longitudinal velocity and density obtained from the ANSYS model. The drive frequency is 50 kHz and steer angle is 15°. The colorbar on the right indicates the plate thickness in inches.

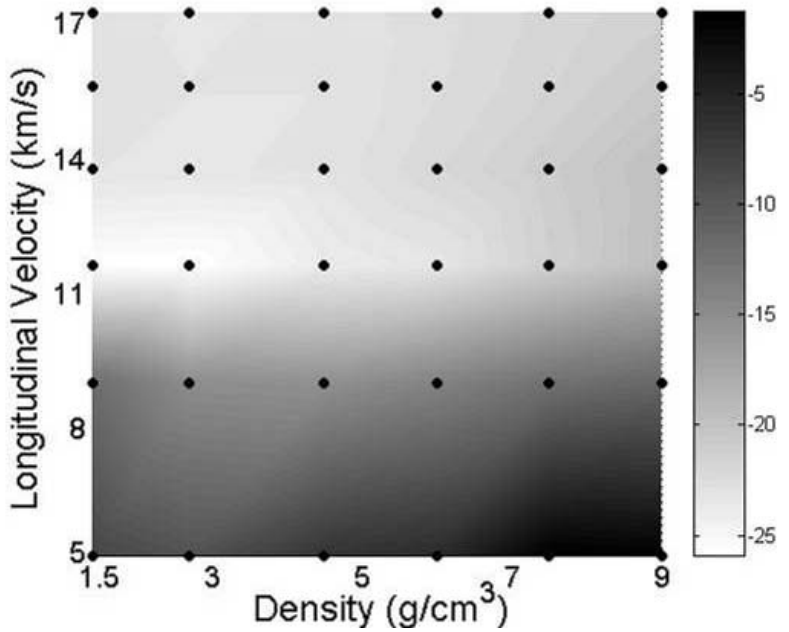

Fig. 5.4. Grating lobe energy ratio dependence versus longitudinal velocity ($c_L = \sqrt{E/\rho_P}$) and density obtained from the ANSYS model. The drive frequency is 50 kHz and steer angle is 15°. The colorbar on the right indicates the plate grating lobe energy ratio in dB (relative to no change).

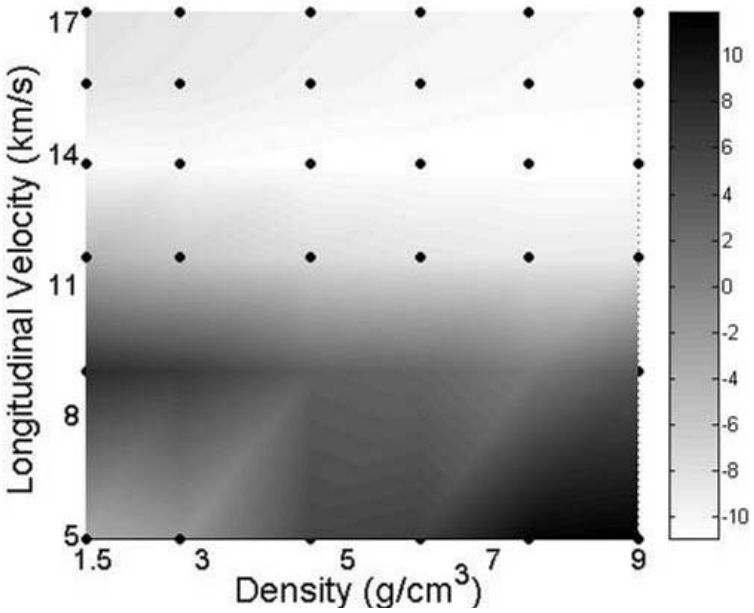

Fig. 5.5. Side lobe energy ratio dependence versus longitudinal velocity ($c_L = \sqrt{E/\rho_P}$) and density obtained from the ANSYS model. The drive frequency is 50 kHz and steer angle is 15°. The colorbar on the left indicates the side lobe energy ratio in dB (relative to no change).

5.5 Plate Thickness versus Compliant Layer Thickness

The purpose of using a compliant layer between the transducer heads and the plate is for practical retrofitting reasons and to reduce the effects of localized shear forces on the plate from adjacent transducer heads. One of the major aims for this project was to retrofit existing transducer arrays which have acoustic windows between the transducers and the water to protect transducers from corrosion and to protect electronics from being shorted. A simple method of retrofitting an existing array would be to machine down the acoustic window and mount the plate. However, the window should not be machined down too thin to avoid damaging the transducer heads. As mentioned earlier, another reason for a compliant layer is to reduce the effects of localized shear

forces. Typically transducer heads are placed very close together with small gaps between the heads in order to maximize the transducer's radiating/receiving surface area. When an array is steered from broadside, adjacent transducer heads move out of phase relative to each other, thus creating a localized area where two rigid surfaces are moving out of phase with each other. With the addition of a compliant layer, a buffer region would be provided between the localized opposing motion of adjacent transducer heads and the plate surface.

Throughout much of the preliminary thesis work of optimizing the material properties of the plate and optimizing the thickness of the plate, the compliant layer thickness was fixed to a value of 0.0625 inches to reduce the optimization degrees of freedom. Once an optimal thickness was found for an alumina plate, the compliant layer thickness was varied to determine if there was an optimal compliant layer thickness. The result was that increasing the compliant layer reduced the potential control of the grating lobe level. A compliant layer thinner than 0.0625 inches did not result in further reduction of the grating lobe level. A thinner compliant layer introduced more side lobe energy, likely due to localized shear forces (two closely spaced transducer heads moving out of phase). The compliant layer thickness was then varied, and a corresponding optimal plate thickness was determined. An inverse relationship was found between the optimal plate thickness and the optimal compliant layer thickness. Figure 5.6 shows the variation of the optimization parameters GLER and SLER as a function of optimized plate thickness and compliant layer thickness.

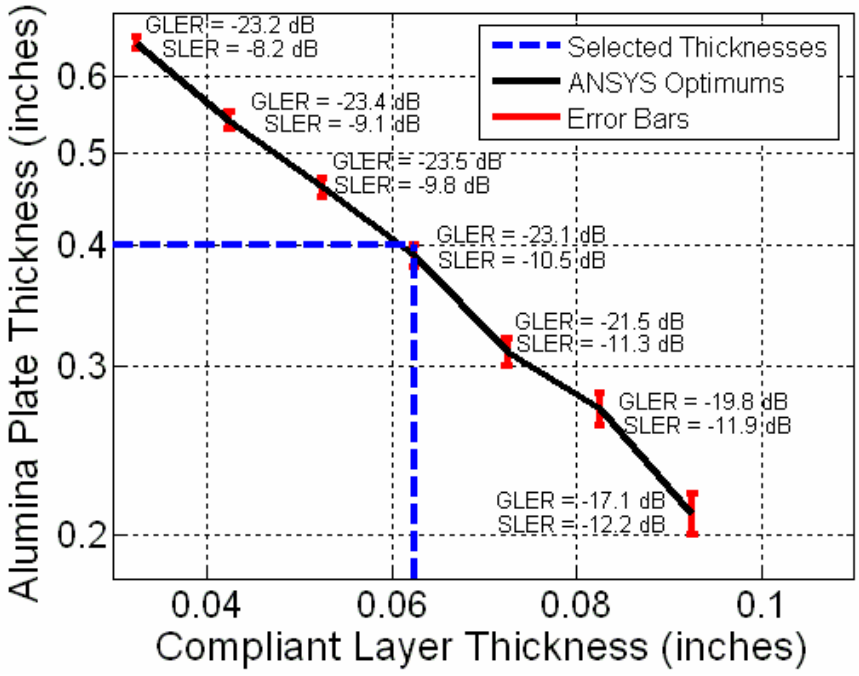

Fig. 5.6. Dependence of optimization parameters GLER and SLER versus optimized plate thickness and compliant layer thickness for an alumina plate, determined using the ANSYS model. Error bars represent the potential error due to the step size in plate thickness variation. The drive frequency is 50 kHz and steer angle is 15°.

5.6 Amplitude Shading

Amplitude shading was applied to the constant displacement drive inputs of the ANSYS model to determine its performance. Dolph-Tschebyscheff amplitude shading for -40 dB side lobes was used in this model (see Section 2.4). The result from the ANSYS model was that amplitude shading did reduce side lobe levels, but not down to the levels (-40 dB) expected when amplitude shading is applied to a transducer array without a plate. Also, as is found with amplitude shading in standard transducer arrays without a plate, amplitude shading proved to be ineffective at reducing the level of the grating lobe while increasing the width of both the main lobe and grating lobe. For

amplitude shading comparisons, the drive frequency was fixed at 50 kHz and the steer angle was fixed to 15°. Figure 5.7 shows the unshaded directivity patterns of a no-plate array and an alumina plate array. Figure 5.8 shows the 40 dB shaded directivity patterns of a no-plate array and an alumina plate array.

5.7 Steer Angle and Drive Frequency

The numerical modeling work focused on determining the required material and geometrical properties of the plate. An assumption was made, once the plate's material and geometrical properties were determined, that the grating lobe reduction would also be optimal in the sense that any frequency and steer angle could be selected for the plate optimization. A frequency of 50 kHz (or $f = 2F_0$) and 15° was selected so that a grating lobe was clearly in the directivity pattern, with the steer angle and frequency at reasonably low values. Once the plate's material and geometrical properties were optimized, an alumina plate of 0.4 inches was analyzed by varying the frequency and steer angle. The grating lobe level ratio, GLLR, (similar to GLER where the peak value of the grating lobe is compared) was computed and compared to a no plate theoretical line array. The GLLR, in dB relative to no reduction, is plotted versus the drive frequency and steer angle in Fig. 5.9. The dark red curved lines represent when a grating lobe is located at ±90°. The black dots in Fig. 5.9 denote the frequencies and steer angles that were analyzed. The lower left hand region contains no grating lobes, therefore GLLR was arbitrarily set to a value of zero. The lower right hand region contains two grating lobes but only the first grating lobe, where $m = -1$, was analyzed.

The plot of the grating lobe level ratio versus frequency and steer angle in Fig. 5.9 demonstrates that grating lobes can be reduced within a certain frequency and steer angle combination region (according to finite element analysis). At large steer angles and/or at large frequencies, grating lobe reduction is not achievable. In Section 3.8, it was explained that filtering of the grating lobe level, relative to the main lobe level, is achievable as long as the main lobe is restricted to angles less than the coincidence angle (the pass band region) and the grating lobe is at angles greater than the coincidence angle (the stop band region). The coincidence angle, or filter angle, decreases with frequency. Therefore, grating lobe levels are no longer reduced in level when the grating lobe angle decreases to the point at which the grating lobe angle has moved from the stop band region to the pass band region. The plot in Fig. 3.9 confirms this conclusion, as it shows that grating lobe levels are reduced only when the frequency/steer angle combination is below the blue and green lines.

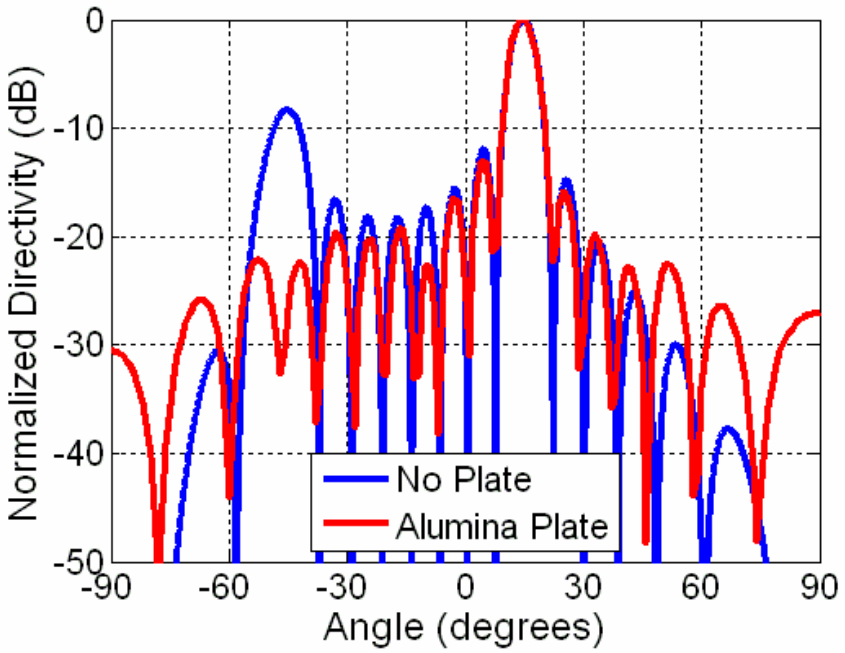

Fig. 5.7. Normalized unshaded directivity patterns computed from the constant displacement input ANSYS model for a no-plate array and an alumina plate array at 50 kHz and steer angle of 15°.

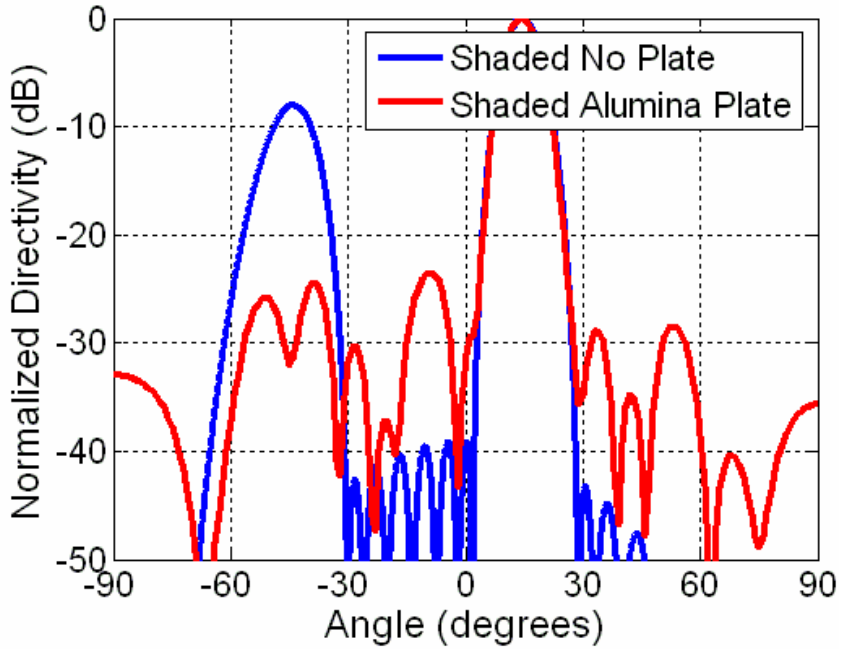

Fig. 5.8. Normalized unshaded directivity patterns computed from the constant displacement input ANSYS model for a no-plate array and an alumina plate array at 50 kHz and steer angle of 15°.

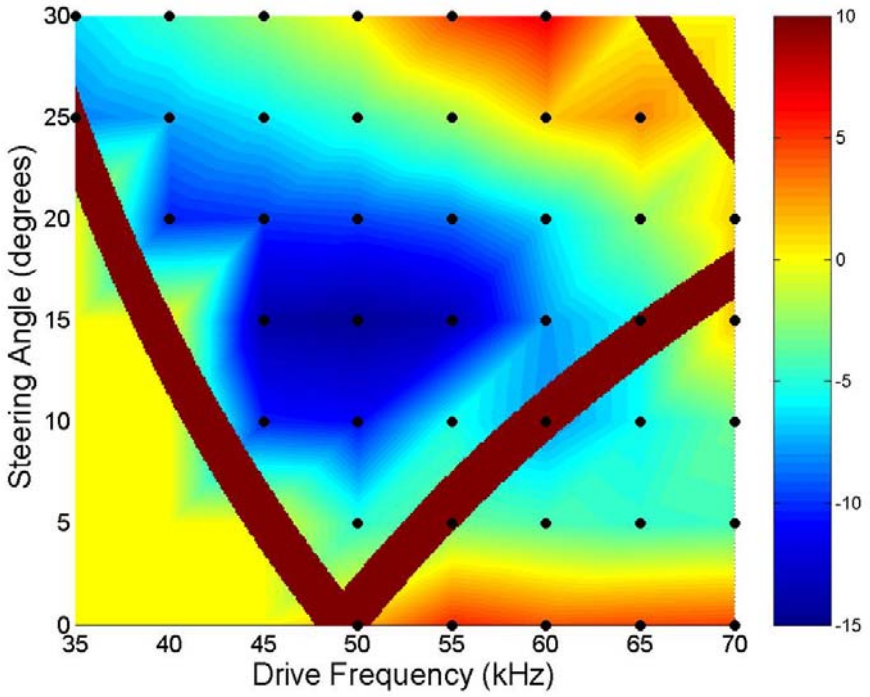

Fig. 5.9. Grating lobe level ratio, GLLR, values for a 0.4 inch thick alumina plate array from ANSYS modeling.

5.8 Discussion

Numerical finite element analysis has shown that grating lobe levels can be reduced with the appropriate selection of a plate possessing a high stiffness to mass ratio. The effect of free-bending wave radiation causing increases in side lobe levels was also modeled. It is important to note the absense of an increase in side lobes at the coincidence angles when constant displacement drive inputs are modeled. The plate's impedance is frequency dependent and generally increases with frequency, therefore a high degree of grating lobe reduction is expected to be limited to a certain operation region. The results from numerical modeling show that, when using constant

displacement (or constant velocity) inputs, the grating lobe may be reduced significantly as frequency and steer angle are varied, out to 60 kHz and 20° (see Fig. 5.9). Constant displacement drive inputs model the situation when the transducer's impedance is much higher than the plate's impedance, while constant force inputs model the situation when the transducer's impedance is much lower than the plate's impedance. Constant force inputs were more representative of the impedance ratio specific to the experimental situations in this thesis. The finite element model can be improved to include transducer impedance for highly accurate comparisons. The numerical modeling results also show that amplitude shading should work with constant displacement drive inputs, but measurements (not presented in this thesis in order to limit the scope of the thesis) did not confirm this conclusion.

Chapter 6

EXPERIMENT RESULTS

6.1 Introduction

This chapter presents results from the measurements conducted for this thesis. The chapter begins with a description of the water tank facility used, followed by a description of the measurement system used. A discussion of the 1-D array module setup is followed by presentation of the results from the measurements made with the 1-D array module. Then a discussion of the 2-D array module is followed by presentation of the results from the measurements made using the 2-D array module. Finally conclusions are presented to summarize the information gained from the directivity pattern surface plots.

6.2 Water Tank Measurement Facility

The Applied Research Laboratory (ARL) at Penn State houses a large anechoic water tank for transducer and array measurements. The water tank is 17.5 feet wide by 26 feet in length by 18 feet high as shown in Fig. 6.1. The water tank is lined with an acoustic absorbent lining and is structurally isolated from the building in which it is housed. The water in the tank is maintained at a temperature of 22°C (or 72°F) with thermoclines minimized by constant circulation and filtering of the water with a quiet pump. The PC-controlled console measurement system is based around the Hewlett-Packard 89410A vector signal analyzer, which utilizes precision time gated signal

processing for accurate calibration. The water tank is equipped with a PC-controlled turntable rotator which allows transducers and array systems to be rotated 360° for far-field directivity pattern measurements for transmit or receive conditions as shown in the photo in Fig. 6.2. Figure 6.3 shows the coordinate axes of a SONAR module along with rotation plane being in the x-z plane.

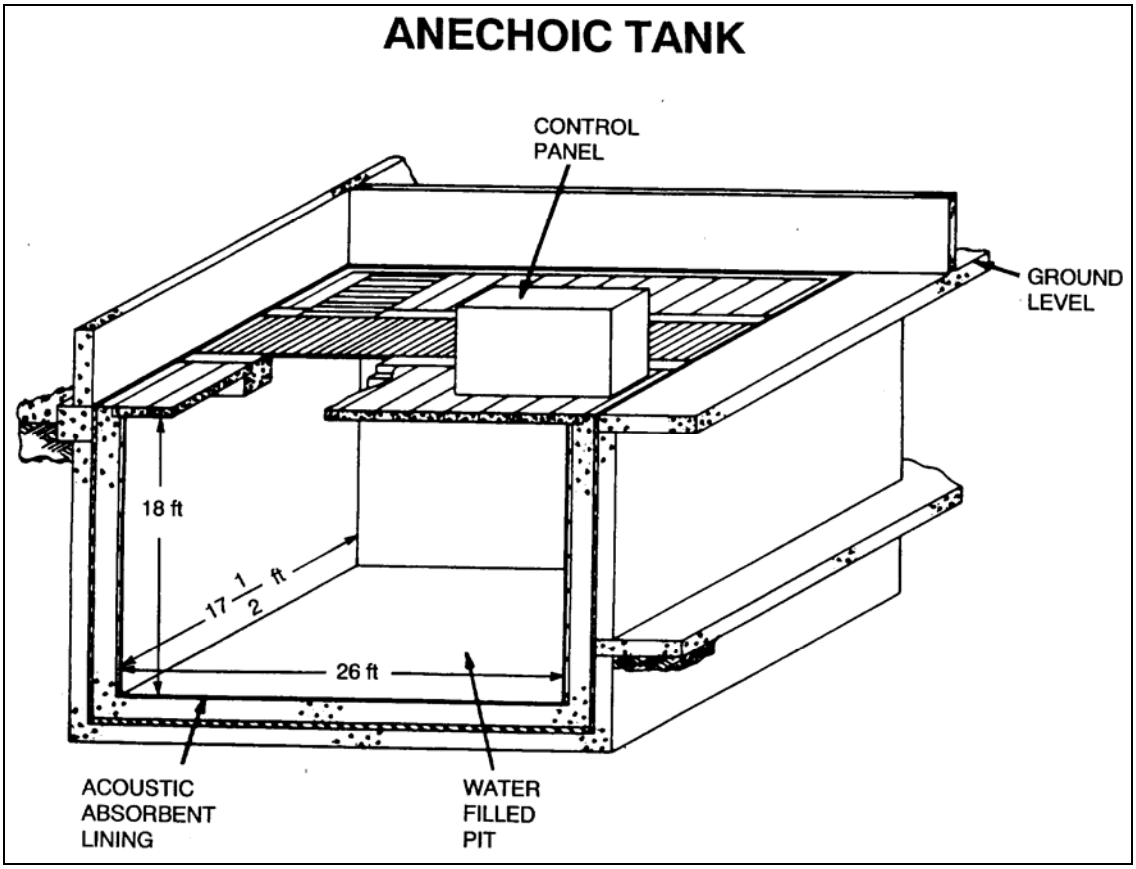

Fig. 6.1. Schematic drawing of the large anechoic water tank housed in the Applied Research Laboratory at Penn State.

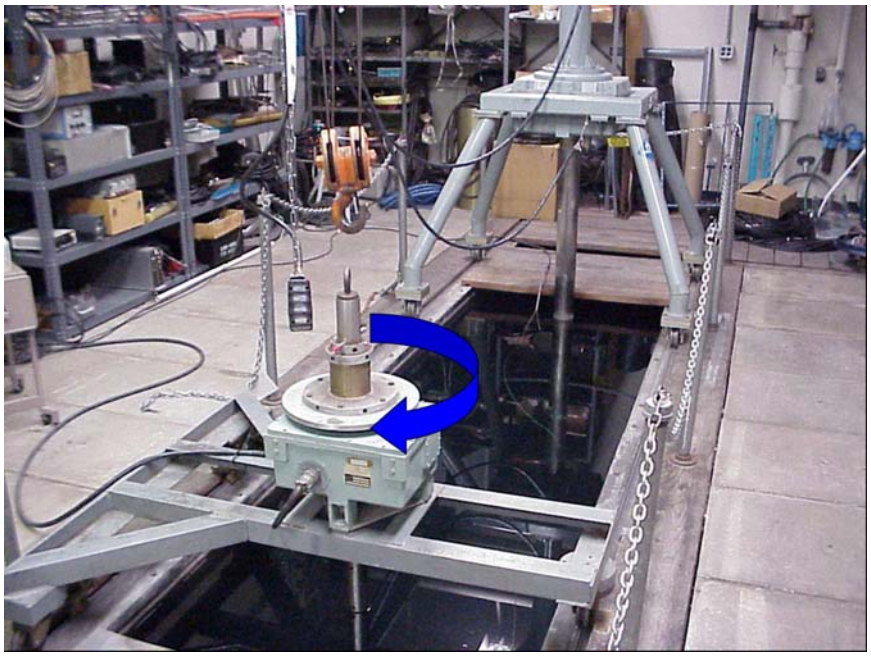

Fig. 6.2. Photo of the topside of the anechoic water tank housed in the Penn State Applied Research Laboratory. The rotator is denoted by the curved arrow.

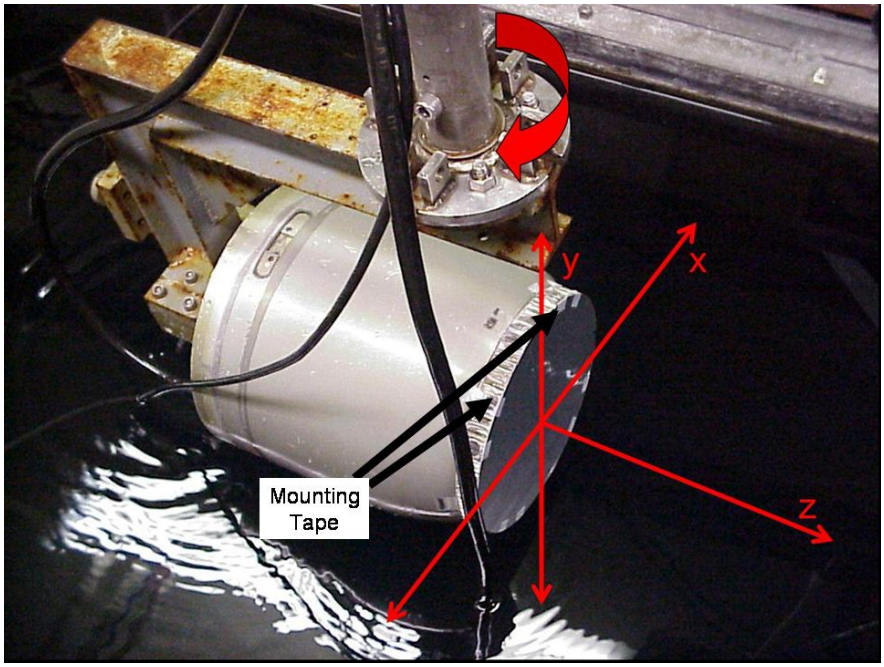

Fig. 6.3. Coordinate axes for directivity pattern measurements for a SONAR module with the axis of rotation in the x-z plane as noted by the curved arrow.

6.3 Element Based Measurements

The water tank facility at the ARL also possesses an element based data acquisition system, which allows up to 64 channels of complex data to be simultaneously acquired for arrays operated in a receive condition. For directivity pattern measurements of arrays it is common for the negative leads of all channels to share a common ground and acquire the data from each of the positive leads. The patch panel (an ATAR System panel) for this system is composed of banana plug inputs and is shown in the photo in Fig. 6.4.

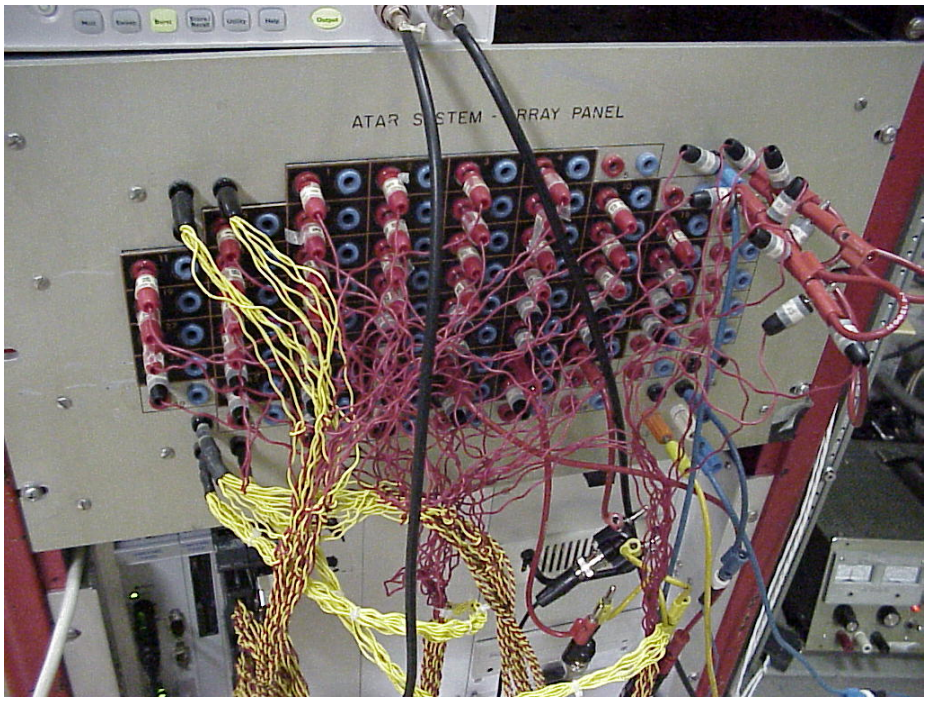

Fig. 6.4. Photo of the ATAR panel of the 64 channel element based data acquisition system at the ARL. The yellow wires are the common negative leads from each channel, while the red wires are the positive leads.

Element based measurements in a receive condition allow one to digitally steer, or amplitude shade, an array to any desired angle in the post-processing phase. For the n th

element, complex pressure data, $p_n(\theta)$, is taken for each angle measured. The steered pressure directivity pattern for an array, $p_{array}(\theta)$ (evaluated at a far field distance $r = r_{FF}$), is achieved by multiplying each element's magnitude, A_n, and phase, ϕ_n, by the appropriate phase, $i_n \omega \tau_0$, (see Section 2.3) corresponding to the appropriate i_n th column and then summing up each of the pressures from all N elements,

$$p_{array}(\theta)\Big|_{r=r_{FF}} = \sum_{n=1}^{N} A_n e^{j(\phi_n)} e^{j(i_n \omega \tau_0)}. \qquad (6.1)$$

In the case of the 2-D 52 element array used, the element numbering layout for n is found in Fig. 6.5a, while the corresponding phasing layout for i_n is found in Fig. 6.5b.

a.

		1	2	3	4		
	5	6	7	8	9	10	
11	12	13	14	15	16	17	18
19	20	21	22	23	24	25	26
27	28	29	30	31	32	33	34
35	36	37	38	39	40	41	42
	43	44	45	46	47	48	
		49	50	51	52		

b.

		3	4	5	6		
	2	3	4	5	6	7	
1	2	3	4	5	6	7	8
1	2	3	4	5	6	7	8
1	2	3	4	5	6	7	8
1	2	3	4	5	6	7	8
	2	3	4	5	6	7	
		3	4	5	6		

Fig. 6.5. (a) The element numbering, n, layout for the 52 element array used. **(b)** The element phasing layout by column for the 52 element array used.

6.4 One-Dimensional Array Tests Setup

Two eight element line arrays were used for the initial round of testing. One array was bonded to an alumina bar with the bar bonded to the acoustic window while the other

array was directly bonded to the acoustic window as shown in Fig. 6.6. The acoustic window was ½ inch thick and was made of EN-9 polyurethane. The transducers in each array configuration were similar Tonpilz transducers possessing a nominal 25 kHz resonance frequency and similar frequency responses, but were built with different materials and were slightly different sizes.

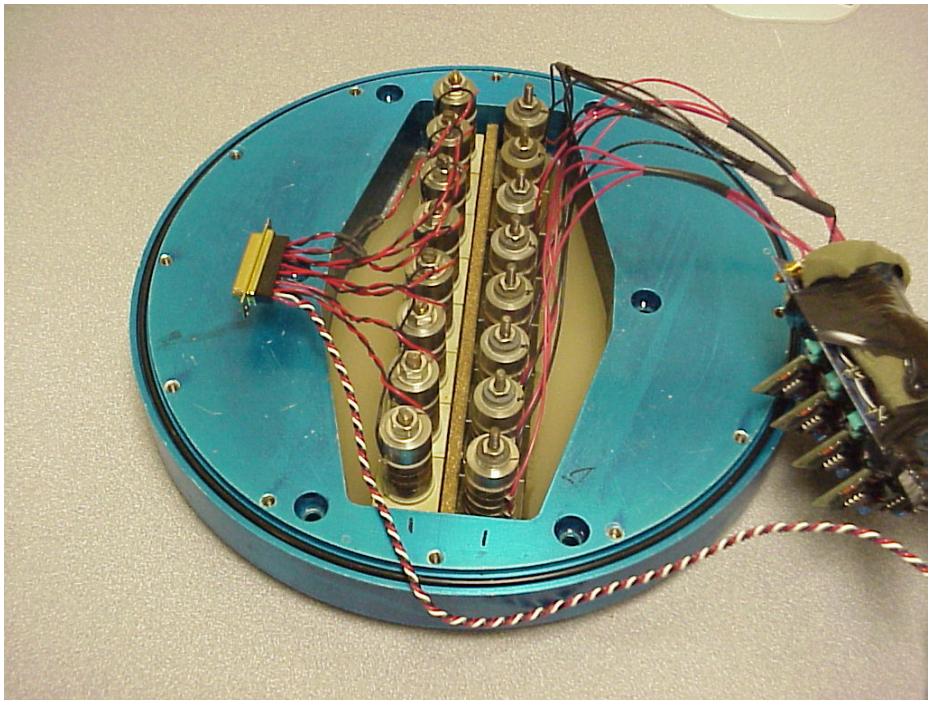

Fig. 6.6. Photo of the two 1-D arrays bonded on the acoustic window. The array on the left has an alumina bar bonded between the array and the window, while the array on the right is bonded directly to the window.

The transducers in the array bonded to the alumina bar have 1.148 inch square radiating surfaces, or heads. The transducers are spaced with a center-to-center distance of 1.164 inches apart. Plastic shims of thickness 0.016 inches were placed between the sides of the transducer heads to ensure consistent center-to-center spacing as shown in Fig. 6.7. A thin layer of polyurethane was first poured onto the alumina bar, then placed in a vacuum chamber to remove bubbles, and finally machined down to a thickness of

0.060 inches as suggested by the numerical modeling (see Section 5.5). A 0.002 inch valley was also machined down from the 0.060 inch surface with outer ridges. Liquid polyurethane was then applied to the heads of the transducers and the transducers were placed upon the thin layer of polyurethane, with the heads resting upon the ridges of the valley. This procedure minimized the presence of bubbles in the polyurethane. Liquid polyurethane was also applied to the other surface of the alumina bar to mount it onto the acoustic window. The alumina bar is a high purity 99.8% aluminum oxide ceramic (AmAlOx 68 alumina) and is 0.40 inches thick, 1.20 inches wide and 9.60 inches in length.

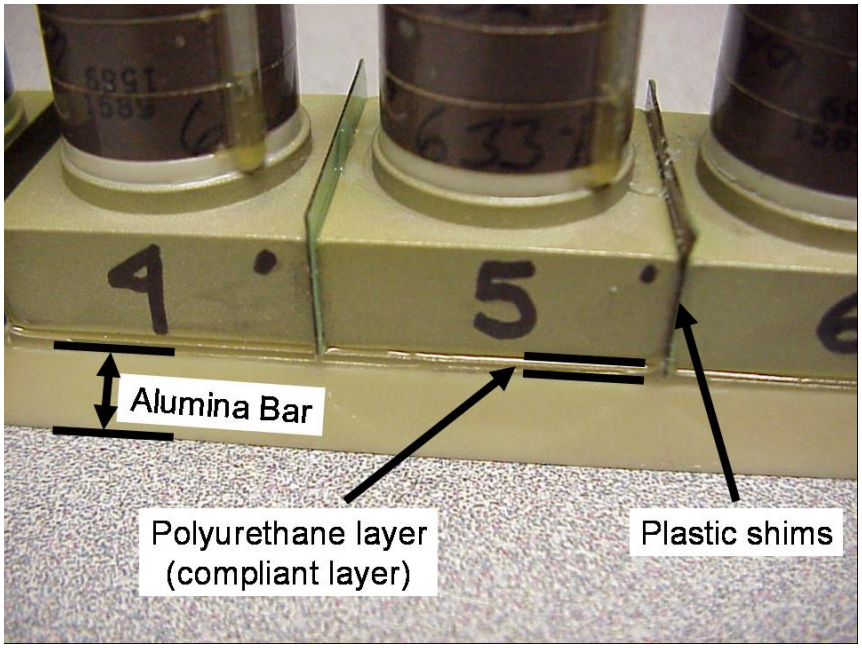

Fig. 6.7. Photo of the 1-D array bonded on the alumina bar. Plastic shims of a 0.016 inch total thickness were placed between transducer heads to ensure the proper center-to-center spacing.

The transducers in the array bonded directly to the acoustic window have 1.164 inch square radiating surfaces, or heads. The transducers are spaced a center-to-center distance of 1.189 inches apart. Plastic shims of thickness 0.025 inches were placed

between the sides of the transducer heads to ensure consistent center-to-center spacing as shown in Fig. 6.8 (the white material between the transducers on the lower array in the photo). This array was then bonded onto the acoustic window with a cork board separator placed between the two different line arrays, to ensure that the arrays were parallel with respect to each other, as shown in Fig. 6.8.

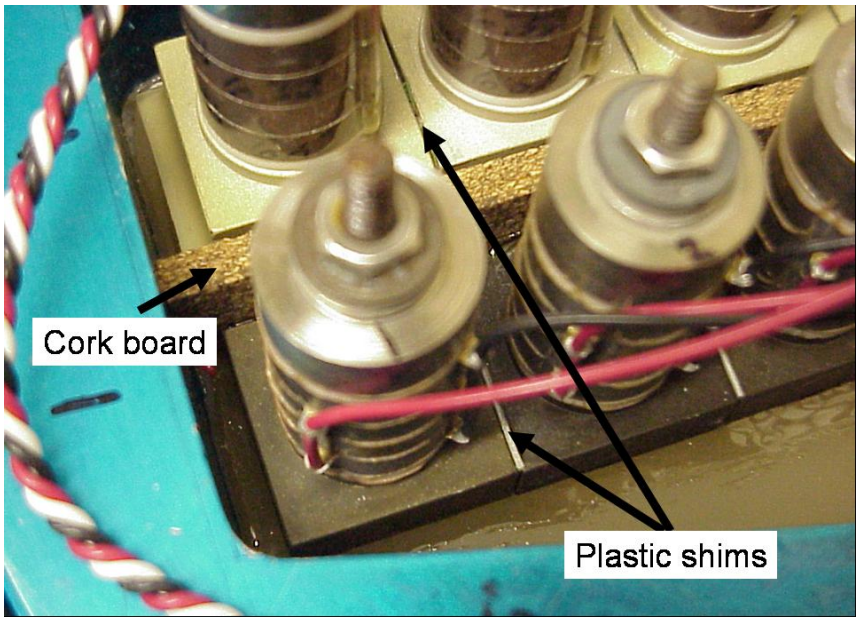

Fig. 6.8. Photo of the two 1-D arrays bonded on the acoustic window. Plastic shims were placed between transducer heads to ensure the proper center-to-center spacing, and a cork board separator was placed between the arrays.

The two 1-D transducer arrays were housed in a nominal 12 inch diameter cylindrical shell. In this round of measurements reciprocity was verified in transmit and receive directivity patterns for the array bonded to the alumina bar (see Appendix C for results). The transmitter was too large to fit inside the shell and was kept topside with the high voltage transmit signals traveling down twisted shielded wires directly to the transducers for the array on the bar. In a receive condition the transmitter was bypassed and connected directly into the multi-channel element based data acquisition system (no

pre-amplification used). This imposed a cable capacitance issue that had to be accounted for. Each transducer's total capacitance was effectively in parallel with its corresponding cable's capacitance. The average transducer capacitance was 1.722 nF and the average cable capacitance was 2.600 nF, resulting in a loss of

$$20\log_{10}\left(\frac{I_{Cable+Transducers}}{I_{Transducers}}\right) = 20\log 10\left(\frac{C_{Transducers}}{C_{Transducers}+C_{Cable}}\right) = 20\log 10\left(\frac{1.722x10^{-9}}{1.722x10^{-9}+2.600x10^{-9}}\right) = -8.0\,dB \quad (6.2)$$

The array bonded directly to the window was not used in transmit and therefore could allow pre-amplification chips to be placed inside the shell. 6 dB gain preamps were used; therefore cable capacitance was negligible.

6.5 Directivity pattern Plots from Experimental Data

Visualization of the directivity pattern of an array versus steer angle and receive angle, or angle of incidence, allows one to determine grating lobe locations and therefore steer angle limits. The unshaded directivity patterns plotted in the surface plots contained in this chapter were each generated at a specific frequency, noted in the figure title, by steering the array from -90° to +90°. The angular directivity pattern for a particular steer angle may be found as a vertical line cross section in each of the plots. The pattern is normalized with respect to its main lobe value at each steer angle. Color in these plots represents directivity pattern amplitude and the colorbar on the right of each subplot denotes the dB amplitude values corresponding to the various colors displayed. White colored portions indicate that the actual value is below -40 dB. These plots represent data

from measurements and may be compared to the theoretical angular directivity pattern plots found in Chapter 2. Table 6.1 tabulates information for each of the experimentally obtained angular directivity pattern plots and frequency responses contained in Chapter 6.

Table 6.1. Tabulated information for each of the experimentally obtained angular directivity pattern plots and frequency responses contained in Chapter 6.

Figure #	Frequency (kHz)	Plate Material	Line Array (1-D) or Planar Array (2-D)	8 Element Module or 52 Element Module
6.9	25	No Bar	Line	8
6.10	50	No Bar	Line	8
6.12	25	Alumina Bar	Line	8
6.13	50	Alumina Bar	Line	8
6.15	10-70	No Plate, No Bar	Planar & Line	52
6.16	25	No Plate	Planar	52
6.17	50	No Plate	Planar	52
6.18	10-70	Aluminum Honeycomb	Planar	52
6.19	25	Aluminum Honeycomb	Planar	52
6.20	50	Aluminum Honeycomb	Planar	52
6.22	10-70	Alumina Bar	Line	52
6.23	25	Alumina Bar	Line	52
6.24	50	Alumina Bar	Line	52
6.27	10-70	Pine Bar	Line	52
6.28	25	Pine Bar	Line	52
6.29	50	Pine Bar	Line	52

In directivity pattern surface plots, the main lobe, normalized for each steer angle to a value of 0 dB, is denoted by the dashed black line which runs diagonally across the plots. Grating lobe ridges for measured no-plate/bar plots are located at the same locations as the theory plots and are sometimes not as prominent in the with-plate/bar plots. One may count the six side lobe ridges expected between the main lobe ridge and the grating lobe ridge. An N element array will have $N-2$ side lobes. One may note the expected widening of the main lobe at large steer angles in the plots. To simplify the analysis, only directivity pattern surface plots at 25 and 50 kHz will be presented. For practical reasons, patterns are often steered only to ±30°; therefore the steer angle axis of

the directivity pattern surface plots (other than the one found in Fig. 6.12) have been limited to ±30°. Theoretical no-plate/bar directivity pattern surface plots are equivalent to the corresponding figures in Chapter 2. Theoretical with plate/bar directivity pattern surface plots are obtained by passing the no-plate/bar figures through the appropriate filter shape (pattern multiplied by a filter shape). To simplify the presentation of data, selected plots are given in this chapter and additional plots, for each material, are given in Appendix E.

6.6 One-Dimensional Array Measurements

6.6.1 Eight Element Line Array – No Bar

Figures 6.9-6.10 contain the theory and measured directivity pattern surface plots for the no-bar eight element line array at frequencies of 25 and 50 kHz, respectively. Visual inspection of these plots yields the conclusion that the measured no-bar line array data matches analytical line array theory very well. Differences between no-bar theory and measured surface plots result from baffle effects not being included in the theory plots and mismatching of transducer elements. The baffle effects generally lower the large incidence angle responses in the measured plots. Baffle effects increase the directivity in measured plots at 25 kHz, but baffle effects do not increase the directivity in measured plots at 50 kHz (see Appendix B). So called “soft” baffles tend to have a frequency dependent form of $1+\cos\theta$ angular dependence. Baffle effects were not included in the line array theory plots since they are highly frequency dependent.

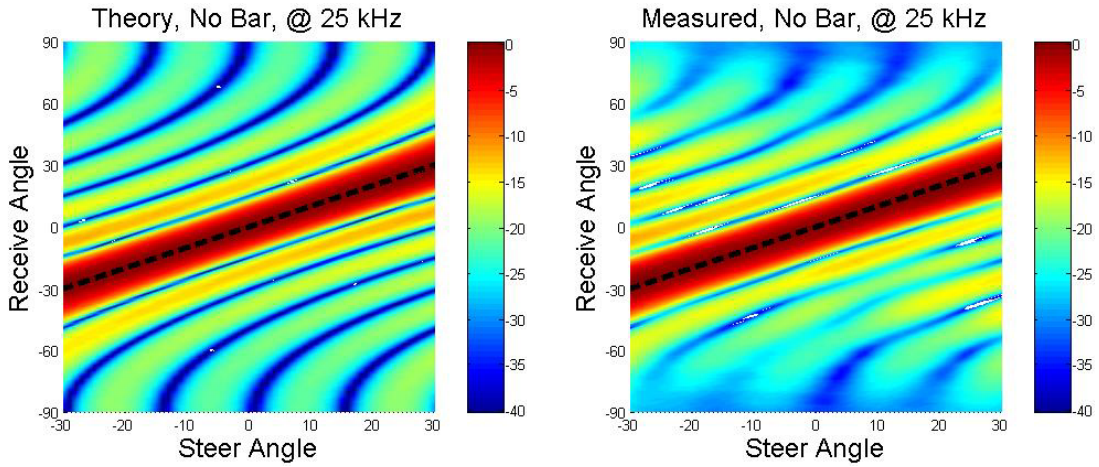

Fig. 6.9. Theoretical and measured receive angle versus steer angle directivity pattern surface plots for the 8-element no-bar line array driven at 25 kHz. Steer angle axis has been limited ±30° to represent the region of practical interest.

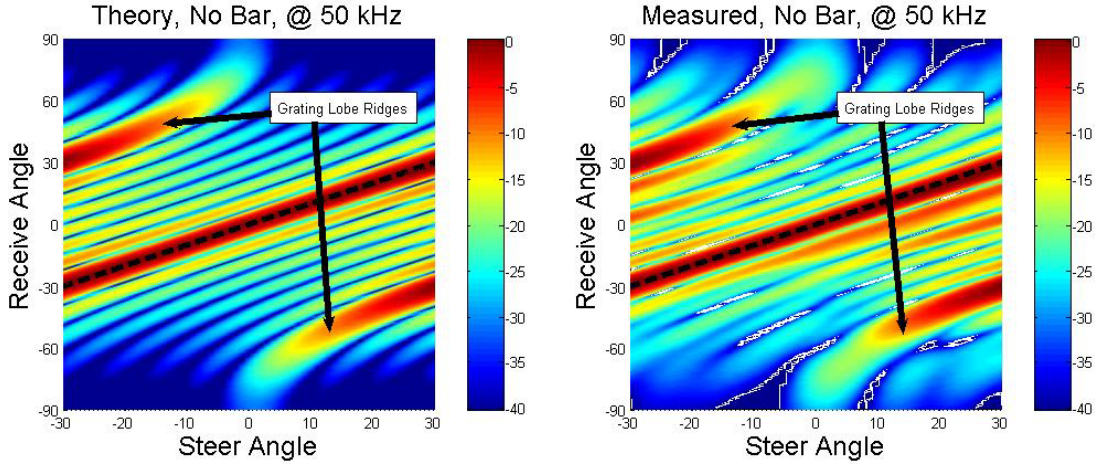

Fig. 6.10. Theory and measured receive angle versus steer angle directivity pattern surface plots for the 8-element no-bar line array driven at 50 kHz. Steer angle axis has been limited to ±30° to represent the region of practical interest.

6.6.2 Eight Element Line Array – Alumina Bar

Alumina was selected for the initial round of testing based upon the numerical modeling. Figure 6.11 contains a photograph of the shell module with the alumina bar array above the no-bar array.

Figure 6.12 contains a plot of steer angle versus receive angle versus amplitude for the alumina (AA) bar eight element line array at 50 kHz. Figure 6.12 will be reviewed as an example to point out features commonly seen in with-plate/bar plots. The red-colored, curved ridge, which runs from a steer angle of 10° and a receive angle of -90° to a steer angle of 90° and a receive angle of 0° is the $m = -1$ grating lobe. The $m = 1$ grating lobe ridge is a mirror ridge of the $m = -1$ grating lobe (mirrored and reversed about the main lobe). Note the missing grating lobe ridge in the alumina bar plots in the region above and below the main lobe ridge at receive angles larger than ±60° horizontal lines. The horizontal lines at receive angles of about ±30° are due to free-bending waves in the alumina bar at the expected coincidence angles. The horizontal line at 0° represents normal incidence for every vertical line pattern. See Appendix A, Section A.8 for the MATLAB code used to generate these plots.

Theoretical and measured receive angle versus steer angle directivity pattern surface plots for the no-bar 8-element line array and the alumina bar 8-element line array are shown in Figs. 6.13-6.14 for 25 and 50 kHz respectively. The steer angle axis has been limited to ±30° to represent the region of practical interest.

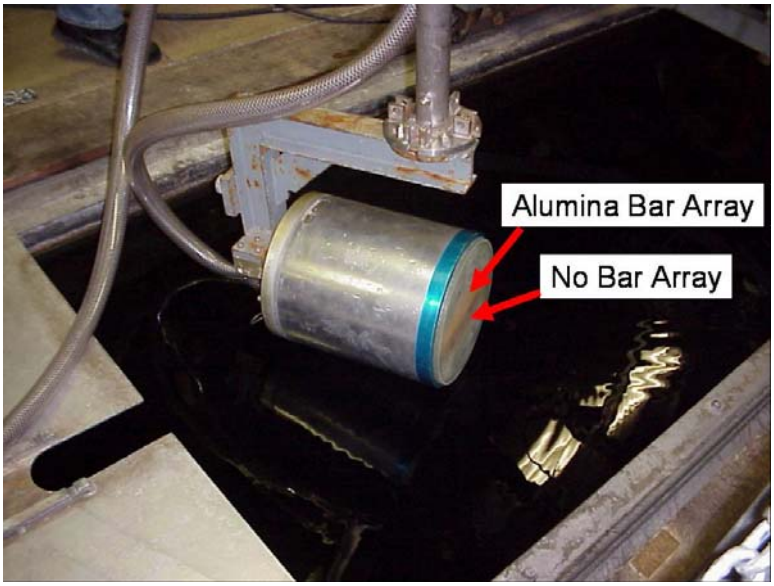

Fig. 6.11. Photograph of the shell module with the alumina bar array (light colored strip) above the no-bar array (dark colored strip).

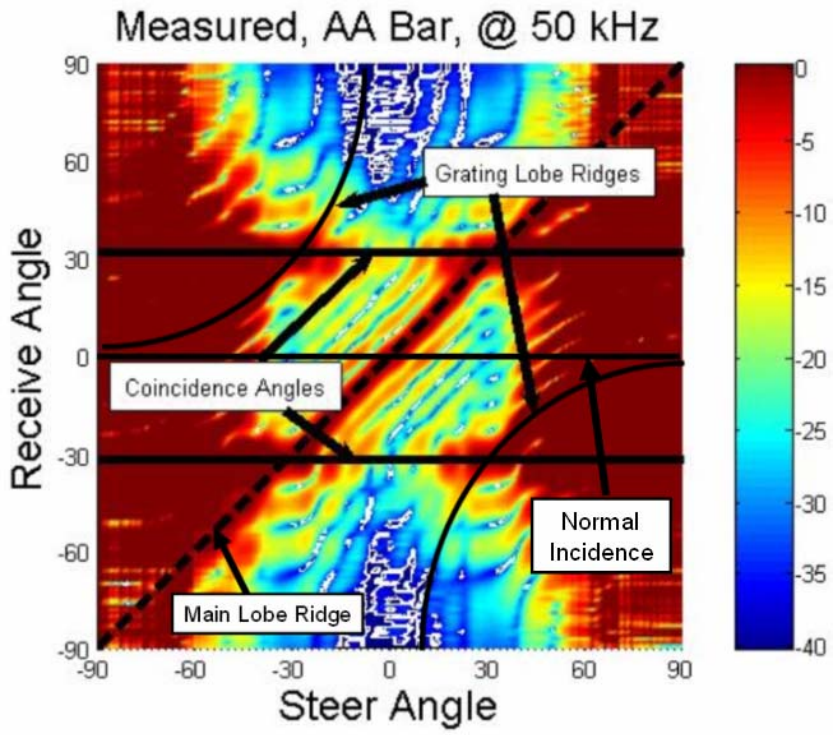

Fig. 6.12. Measured receive angle versus steer angle directivity pattern surface plot for the 8-element alumina bar line array driven at 50 kHz.

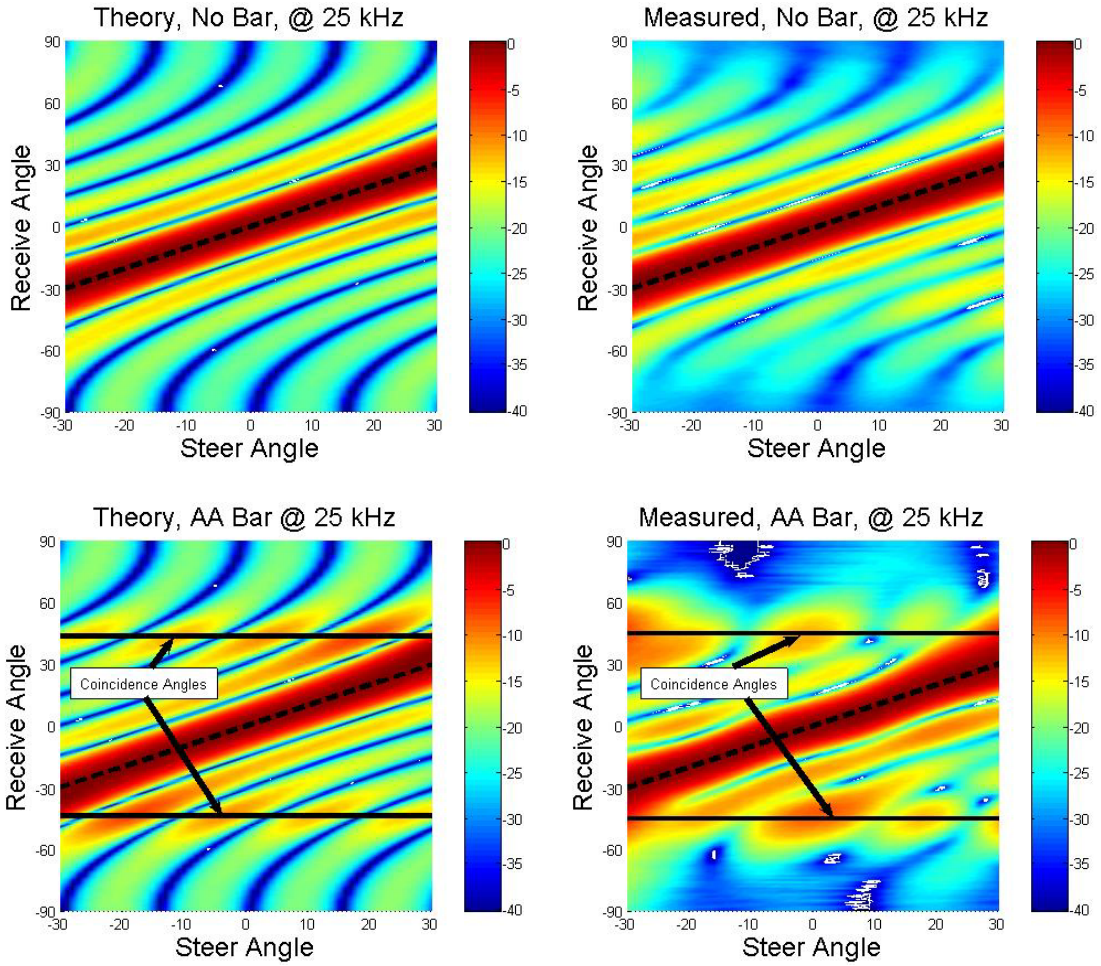

Fig. 6.13. Theory and measured receive angle versus steer angle directivity pattern surface plots for the no-bar 8-element line array and the alumina bar 8-element line array driven at 25 kHz. Steer angle axis has been limited to ±30° to represent the region of practical interest.

Inspection of the alumina bar theory directivity pattern surface plots in Fig. 6.13 (which do not have grating lobes) demonstrates the increase in side lobe level at the coincidence angles as seen experimentally. The level at large receive angles (>±70°) is more attenuated in the experimental patterns due to baffle effects. The conclusion drawn from comparison of the theoretical no-bar to the theoretical alumina bar surface plots is that the alumina bar increases the sensitivity at the coincidence angles while providing

minimal sensitivity reduction at receive angles greater than the coincidence angles. In contrast to the conclusion drawn from the theoretical plot comparison, the conclusion drawn from comparison of the measured no-bar plot to the measured alumina bar plot is that while the alumina bar increases sensitivity at the coincidence angles, the alumina bar also reduces sensitivity at receive angles greater than the coincidence angles. Therefore, the measured relative stop band attenuation for the measured alumina bar is greater than the theoretical prediction for the relative stop band attenuation for an alumina bar.

The directivity pattern surface plots in Fig. 6.14 show that the alumina bar does indeed reduce the grating lobe ridges as evidenced by the missing portions of the grating lobe ridges in the measured AA bar plot. At steer angles less than ±20°, it is clear that the grating lobe is reduced. Within receive angles of ±10°, the grating lobe ridge has been reduced to the -40 dB floor of the plots (the white color represents data below -40 dB). Comparison of theoretical plots to measured plots shows good agreement in reduction of the grating lobes and an increase in the side lobes at the coincidence angles. The increased side lobes, due to coincidence angle ridge, appear to be higher and more spread out than the theory predicted, but notice that the side lobes in the measured no-bar plot are higher than theory as well due to mismatching of elements.

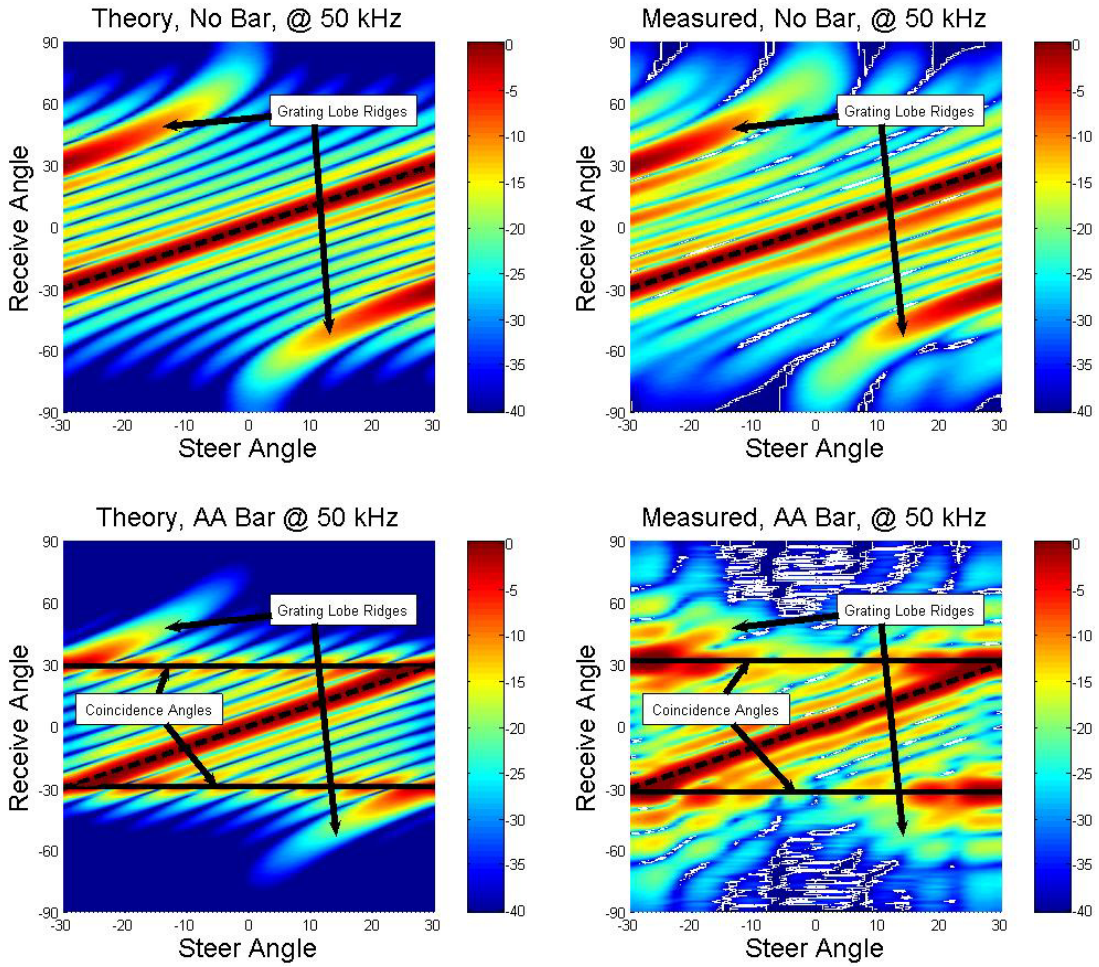

Fig. 6.14. Theoretical and measured receive angle versus steer angle directivity pattern surface plots for the no-bar 8-element line array and the alumina bar 8-element line array driven at 50 kHz. Steer angle axis has been limited to ±30° to represent the region of practical interest.

6.7 Two-Dimensional Array Test Setup

An existing 52 element 2-D Tonpilz transducer array housed in a 12 inch diameter shell was used to measure unidirectional directivity patterns. The transducers in this array also possessed a nominal resonance frequency of 25 kHz. The transducer

numbering layout has been previously shown in Fig. 6.5a. This array was used only in a receive condition and had preamplifiers inside the shell.

The plate and bars used in these measurements were not bonded to the compliant layer as with the eight element line array. Coupling gel (used in ultrasound applications) was applied to both the plate and to the compliant layer. Placement of a bar/plate on the compliant layer created a large amount of surface tension between the two surfaces with or without ultrasound gel; therefore tape was used to hold the bar/plate in place vertically (see Fig. 6.3), but the tape was not tight enough to apply any extra static pressure. Tests indicated that the same results are obtained both with and without the gel (see Fig. 6.24). The bar/plate was then placed on the compliant layer and smoothed around in an attempt to minimize bubbles. Figure 6.15 shows a cross section schematic drawing of the aluminum honeycomb plate placed on the compliant layer.

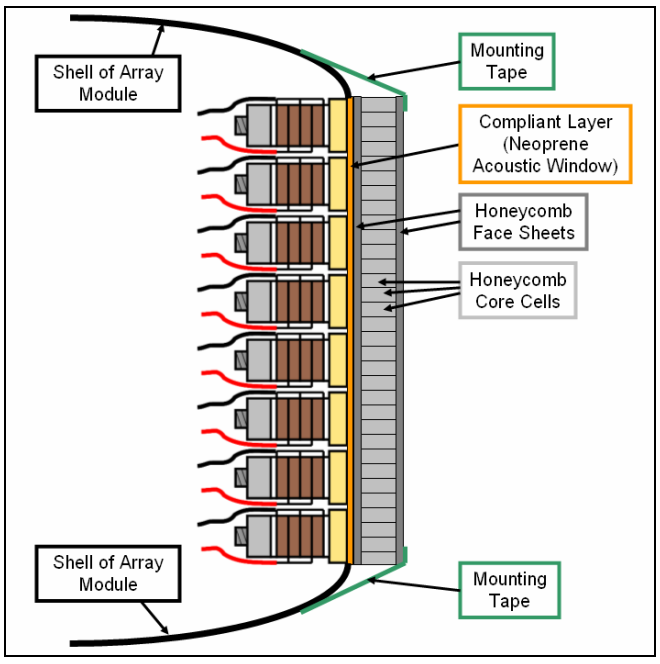

Fig. 6.15. Schematic drawing of a cross section view of the aluminum honeycomb plate placed on the compliant layer with tape holding it vertically in place.

6.8 Two-Dimensional Array Measurements

In addition to the directivity pattern measurements, the frequency response of the array was also measured. The frequency response of the 52 element array, in a receive condition, was measured under each bar/plate configuration using a calibrated projector. The array was oriented so that the incident sound energy was normal to the front of the array. The total frequency response for the array was determined by taking the magnitude of the sum of all the complex voltage signals. The resulting frequency response is the receive sensitivity of the array.

6.8.1 Fifty-Two Element Planar Array – No Plate

Figure 6.16 shows a photograph of the 52 element planar array without a plate or bar attached to the front. The neoprene acoustic window on the front of the array was machined down to 0.0625 inches to provide a compliant layer buffer between the transducers and the plate or bar under test (this is the same compliant layer thickness used in the 8-element line array tests). Figure 6.17 shows the measured frequency response, or receive sensitivity, of the 52-element no-plate array and of the 8 elements used as a line array for bar tests. Theoretical and measured receive angle versus steer angle directivity pattern surface plots for the no-plate 52-element planar array are given in Figs. 6.18-6.19 for 25 and 50 kHz respectively. Theoretical plots were generated using an 8-element line array model. The steer angle axis has been limited to ±30° to represent the region of practical interest.

The two frequency responses shown in Fig. 6.17 represent the 52-element planar array and an 8-element line array (8 of the 52 elements), and reveal a constant offset difference between the frequency responses. One may verify that this difference equals the logarithmic ratio of the different numbers of elements in the two arrays $20\log_{10}(52/8) = 16\,\text{dB}$.

Visual inspection of Figs. 6.18-6.19 yields the conclusion that the measured no-plate planar array data matches the shape of the analytical line array theory well but not the amplitude. The difference in amplitude between theory and measured is due to the decreased side lobe levels of a 52 element array consisting of 8 adjacent line arrays versus a single 8 element line array. Additional differences between theory and measured surface plots result from baffle effects not being included in the theory plots and mismatching of transducer elements. See Appendix B for baffle directivity measurements.

A 52-element planar array should yield lower side lobe levels than an 8-element line array, as suggested by the more bluish color found in the measured no-plate plot of Fig. 6.18 relative to the no-bar plot of Fig. 6.9. However, comparison of theory and measured plots in Fig. 6.19 show that the side lobe level differences may have detrimentally decreased at the higher 50 kHz frequency relative to the side lobe level differences seen at 25 kHz. In some cases the side lobes are 5 dB higher in level in the measured plot versus the theory plot despite the differing number of elements, and the grating lobe ridge is 5-10 dB higher in level, at large receive angles, in the measured plot versus the theory plot.

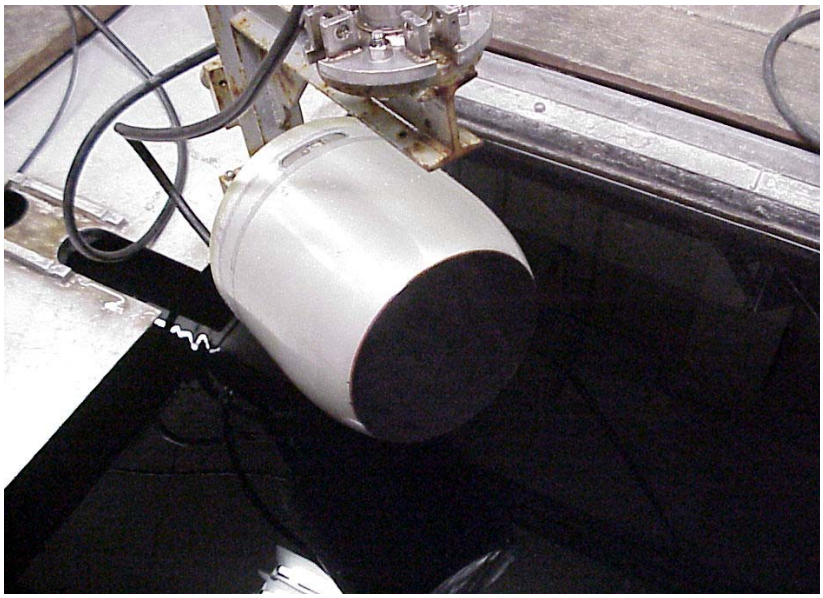

Fig. 6.16. Photograph of the 52 element no-plate array module.

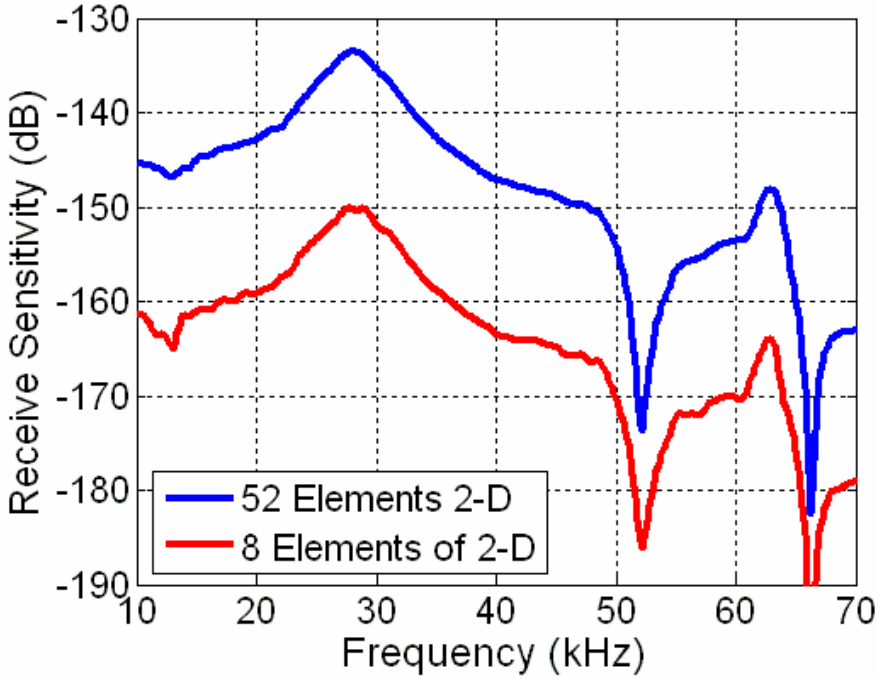

Fig. 6.17. Measured frequency response, or receive sensitivity, for the no-plate 52 element array and the 8 element of the 52 used for the reference line array for bar tests. Level difference is equal to $20\log_{10}(52/8)$.

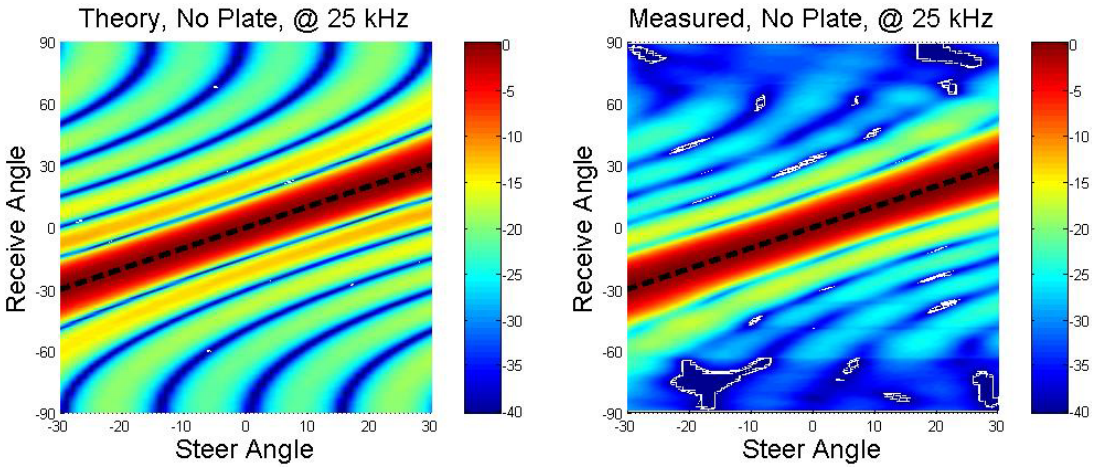

Fig. 6.18. Theoretical (using an 8-element line array model) and measured receive angle versus steer angle directivity pattern surface plots for the 52-element no-plate 52-element line array driven at 25 kHz. Steer angle axis has been limited to ±30° to represent the region of practical interest.

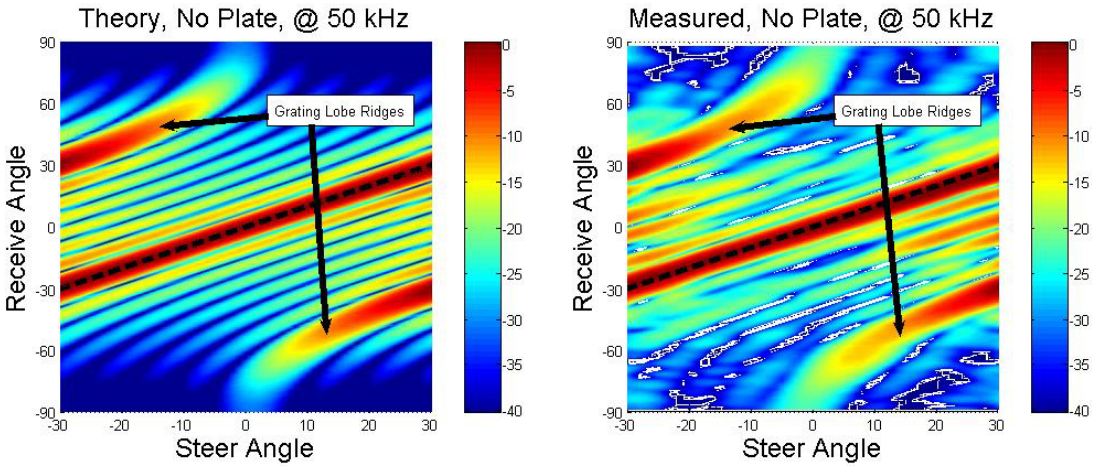

Fig. 6.19. Theoretical (using an 8-element line array model) and measured receive angle versus steer angle directivity pattern surface plots for the 52-element no-plate 52-element line array driven at 25 kHz. Steer angle axis has been limited to ±30° to represent the region of practical interest.

6.8.2 Fifty-Two Element Planar Array – Aluminum Honeycomb Plate

Aluminum honeycomb was selected for measurements as a result of its low mass and large stiffness to mass ratio. Figure 6.20 shows the measured frequency response, or receive sensitivity, of the aluminum honeycomb (AH) plate array along with the no-plate array. The large change in the quality factor, Q, at resonance is modeled by the equivalent circuit analysis in Chapter 4 as due to the radiation unloading of the elements by the low impedance plate. Figure 6.3 shows the aluminum honeycomb plate mounted to the 52 element array. Theory and measured receive angle versus steer angle directivity pattern surface plots for the no-plate 52-element planar array and the aluminum honeycomb plate 52-element planar array are given in Figs. 6.21-6.22 for 25 and 50 kHz respectively. Theoretical plots were generated using an 8-element line array model.

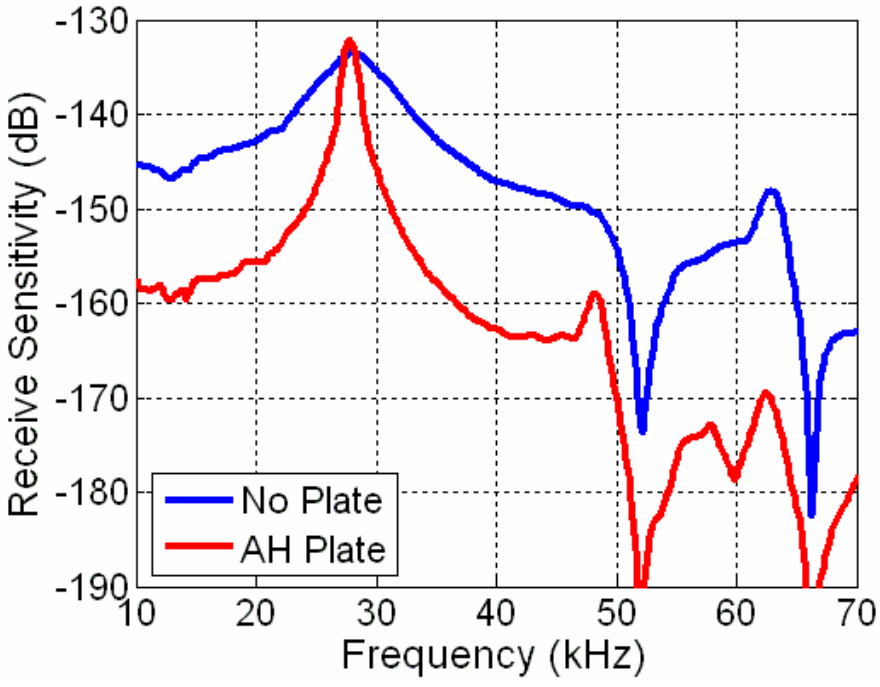

Fig. 6.20. Measured frequency response, or receive sensitivity, for the aluminum honeycomb plate array and the no-plate 52 element array.

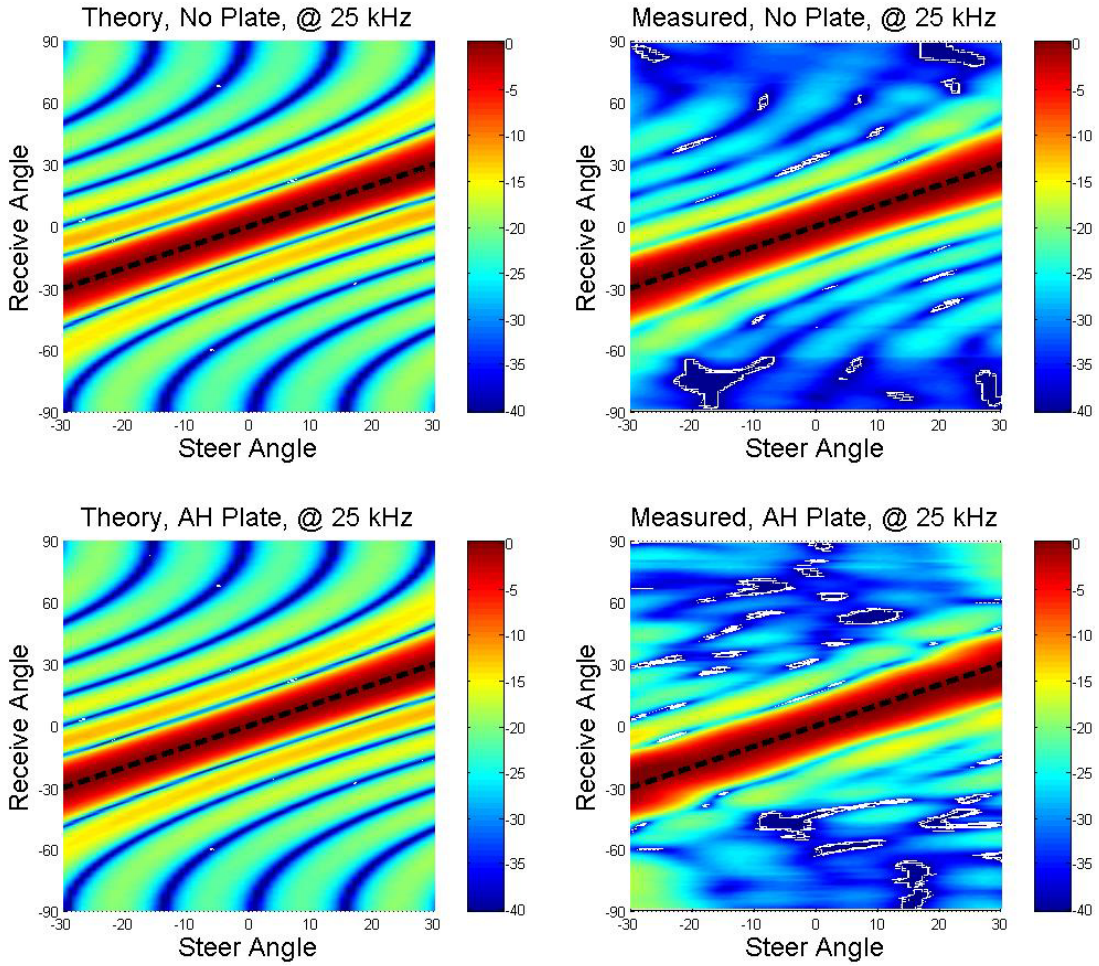

Fig. 6.21. Theoretical and measured receive angle versus steer angle directivity pattern surface plots for the no-plate 52-element planar array and the aluminum honeycomb plate 52-element line array driven at 25 kHz. Theoretical plots were generated using an 8-element line array model. Steer angle axis has been limited to ±30° to represent the region of practical interest.

The frequency response comparison seen in Fig. 6.20 shows the dramatic increase in the quality factor, Q, near the transducer resonance frequency of 28 kHz. This increase in the quality factor was predicted by the equivalent circuit modeling (see Fig. 4.8) and is the result of providing a lower impedance load to the transducers than the no-plate radiation impedance. The frequency response with the aluminum honeycomb

plate does show a relatively constant offset difference relative to the no-plate frequency response aside from the high Q peak at resonance, the peak introduced around 48 kHz, and the dip seen at 60 kHz. A detailed analysis of the equivalent circuit's ability to predict the change in frequency response will be discussed later (see Section 7.4).

Comparison of the measured no-plate plot to the measured aluminum honeycomb plate plot found in Fig. 6.21 shows that the insertion of the plate generally reduces the side lobe levels. Analytical line array theory and measured aluminum honeycomb array with-plate plots in Fig. 6.21 do not show an increase in the side lobes at the coincidence angles, as expected due to the relatively low mass of the aluminum honeycomb plate, therefore the coincidence angles are not identified in the plots.

The theoretical and measured aluminum honeycomb plate plots (50 kHz) in Fig. 6.22 do not reveal a great deal of agreement in the side lobe structure. However, comparison of the grating lobe ridges in the measured no-plate and aluminum honeycomb plate plots shows that the grating lobe structure is broken up and reduced in level due to the insertion of the honeycomb plate, particularly at small steer angles (<10°). The side lobe structure in the 50 kHz measured honeycomb plate plot has many random peaks.

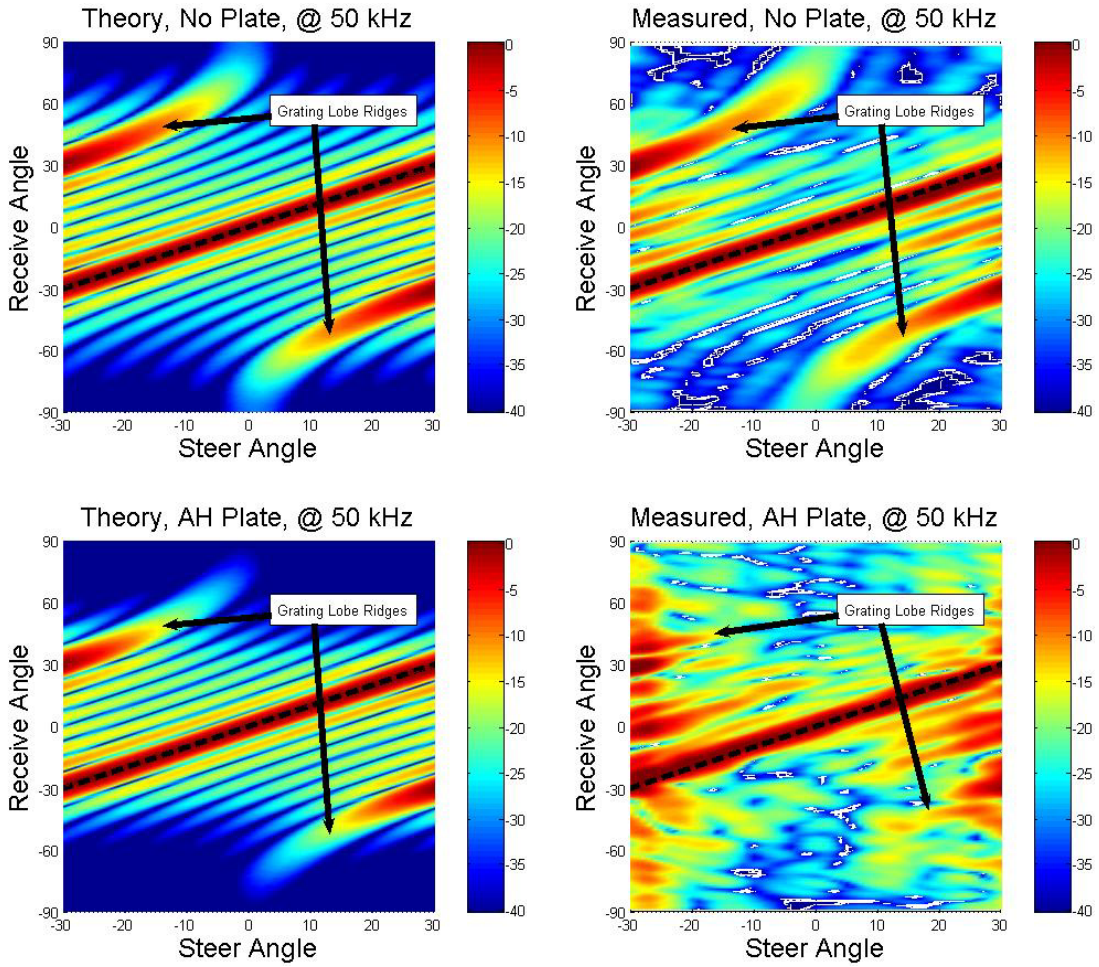

Fig. 6.22. Theory and measured receive angle versus steer angle directivity pattern surface plots for the no-plate 52-element planar array and the aluminum honeycomb plate 52-element line array driven at 50 kHz. Theoretical plots were generated using an 8-element line array model. Steer angle axis has been limited to ±30° to represent the region of practical interest.

6.8.3 Eight Element Line Array on 52-Element Planar Array – Alumina Bar Revisited

In an effort to verify continuity between the first round of testing on 8-element line arrays and the second round of testing on the 52-element planar array, another alumina bar (identical to the bar measured in Section 6.6.2) configuration was measured

by placing the bar across 8 elements of the 52-element planar array. Also, the frequency response was measured, since it was not measured in the initial round of measurements with the 1-D line arrays. Figure 6.23 shows the alumina bar mounted to the 52-element array. Figure 6.24 shows the measured receive frequency response, of the alumina (AA) bar array, with and without ultrasound gel between the acoustic window and the bar (bar was held in place vertically with tape), along with the corresponding 8 elements from the no-plate 52 element array. Theoretical and measured receive angle versus steer angle directivity pattern surface plots for the no-bar 8-element line array (52-element planar array) and the revisited alumina bar 8-element line array (52-element planar array) are given in Figs. 6.25-6.26 for 25 and 50 kHz respectively.

In Fig. 6.24, the shift in the resonance frequency, and the decrease in peak amplitude in the alumina bar frequency response relative to the no-bar array is due to the mass loading effect of placing the bar in front of the array. The alumina bar had to be reapplied to the array module during the change in application of the ultrasound gel. Thus, the agreement seen between the two measured frequency responses demonstrates that ultrasound gel is not required. The agreement also demonstrates the repeatability of the mounting procedure used to apply the bar to the front of the array module and suggests that the mounting procedure is not sensitive to slight changes in the way the bar is mounted.

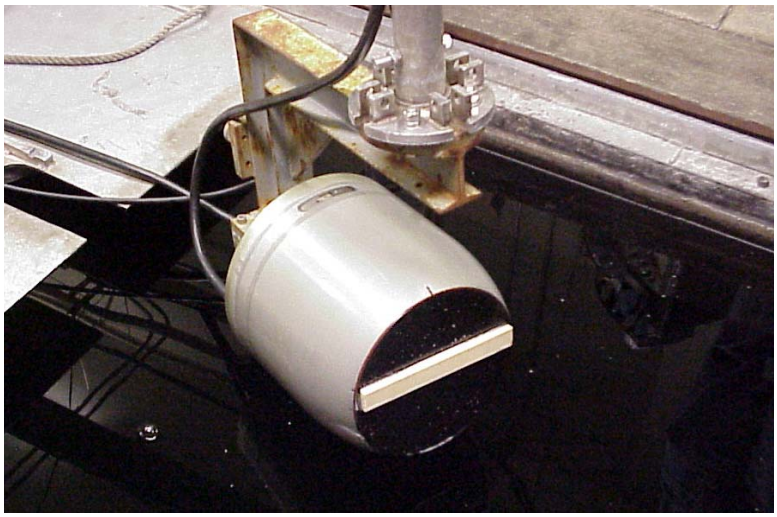

Fig. 6.23. Photograph of the revisited alumina bar array.

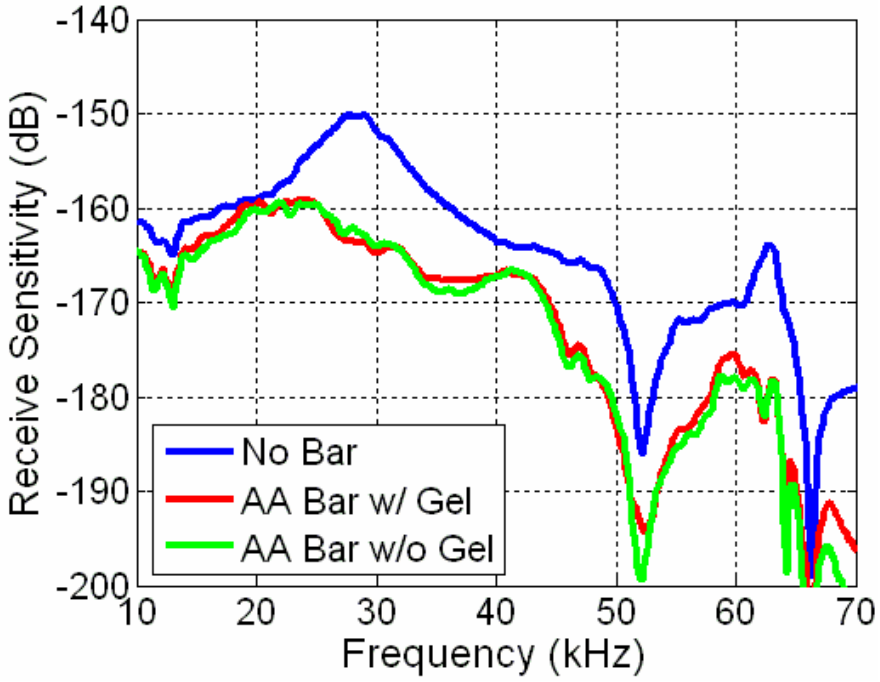

Fig. 6.24. Measured frequency response, or receive sensitivity, for the revisited alumina bar array and the no-bar 8 element line array (the 8 elements are 8 of the 52 element array).

The measured directivity pattern surface plot for the revisited alumina bar in Fig. 6.25 shows a similar, but not as strong, increase in side lobe levels at the coincidence angles as seen in the corresponding pattern plot from Fig. 6.13. The side lobe levels in both measured no-bar and revisited alumina bar plots at receive angles larger than ±60° are higher than the side lobe levels in the corresponding plots for the original alumina bar data as evidenced by the abundance of lighter blue colors relative to the darker blue colors in the original alumina bar plots. Another observation of the plots for the revisited alumina bar is that the side lobe structure tends to be more smeared out than in the original alumina bar plots.

Similar observations may be made for the 50 kHz plots in Fig. 6.26 relative to the 50 kHz plots from Fig. 6.14. The side lobe levels in the revisited alumina bar are higher than the corresponding levels for the original alumina bar. The positive-angle grating lobe ridge for the revisited alumina bar plot appears to be reduced fairly significantly relative to the corresponding no-bar positive-angle grating lobe ridge in the measured original alumina bar plot, while the negative-angle grating lobe ridge does not appear to have been reduced by much, if at all. As noted for the 25 kHz plots, the side lobe structure in the 50 kHz revisited alumina bar plot tends to be more smeared out than the original alumina bar plots, and includes random peaks in the side lobe structure.

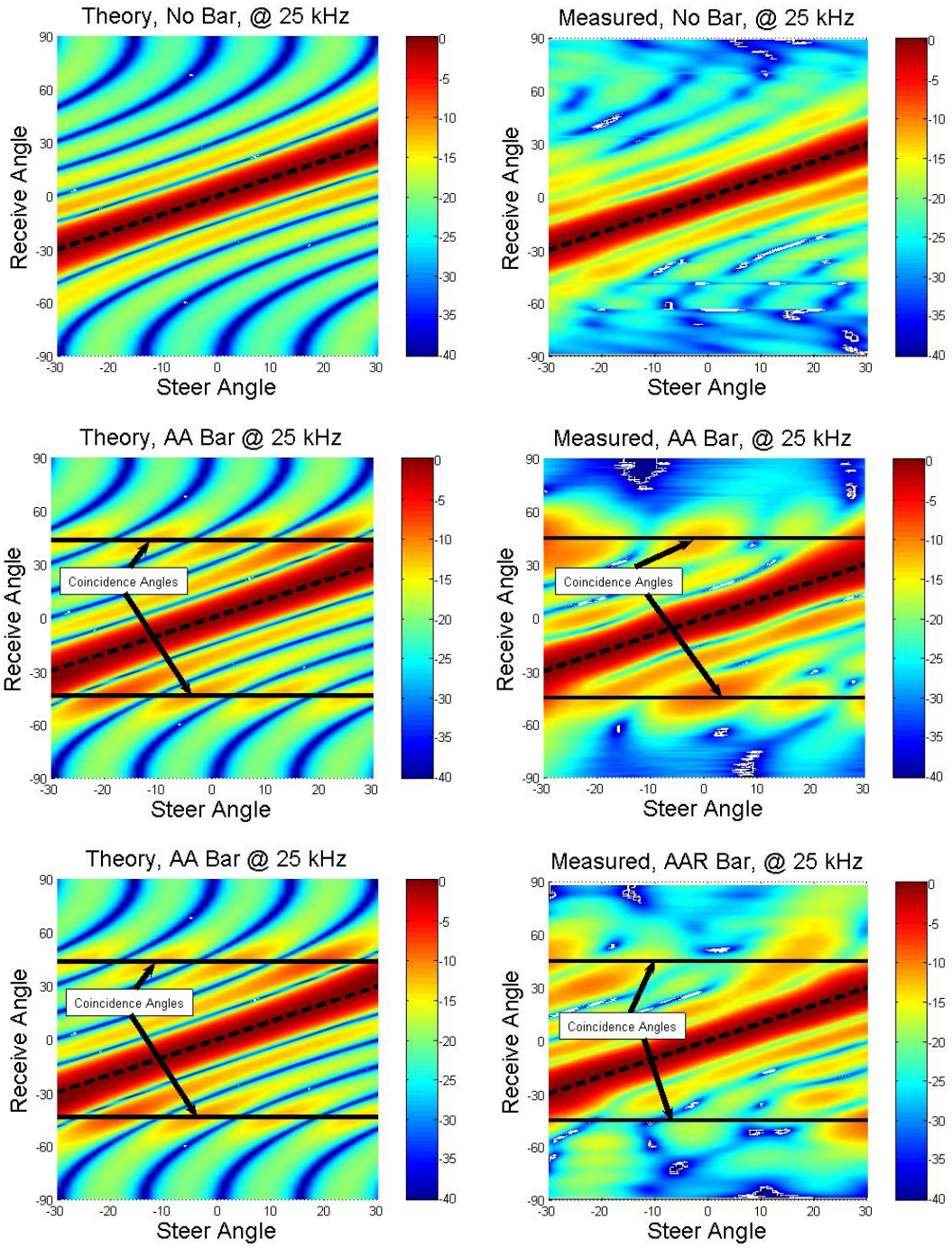

Fig. 6.25. Theoretical and measured receive angle versus steer angle directivity pattern surface plots for the no-bar 8-element line array, original alumina bar 8-element line array, and the revisited alumina bar 8-element line array (52 element planar array) driven at 25 kHz. Steer angle axis has been limited to ±30° to represent the region of practical interest. The original alumina bar data is denoted AA, while the revisited alumina bar data is denoted AAR.

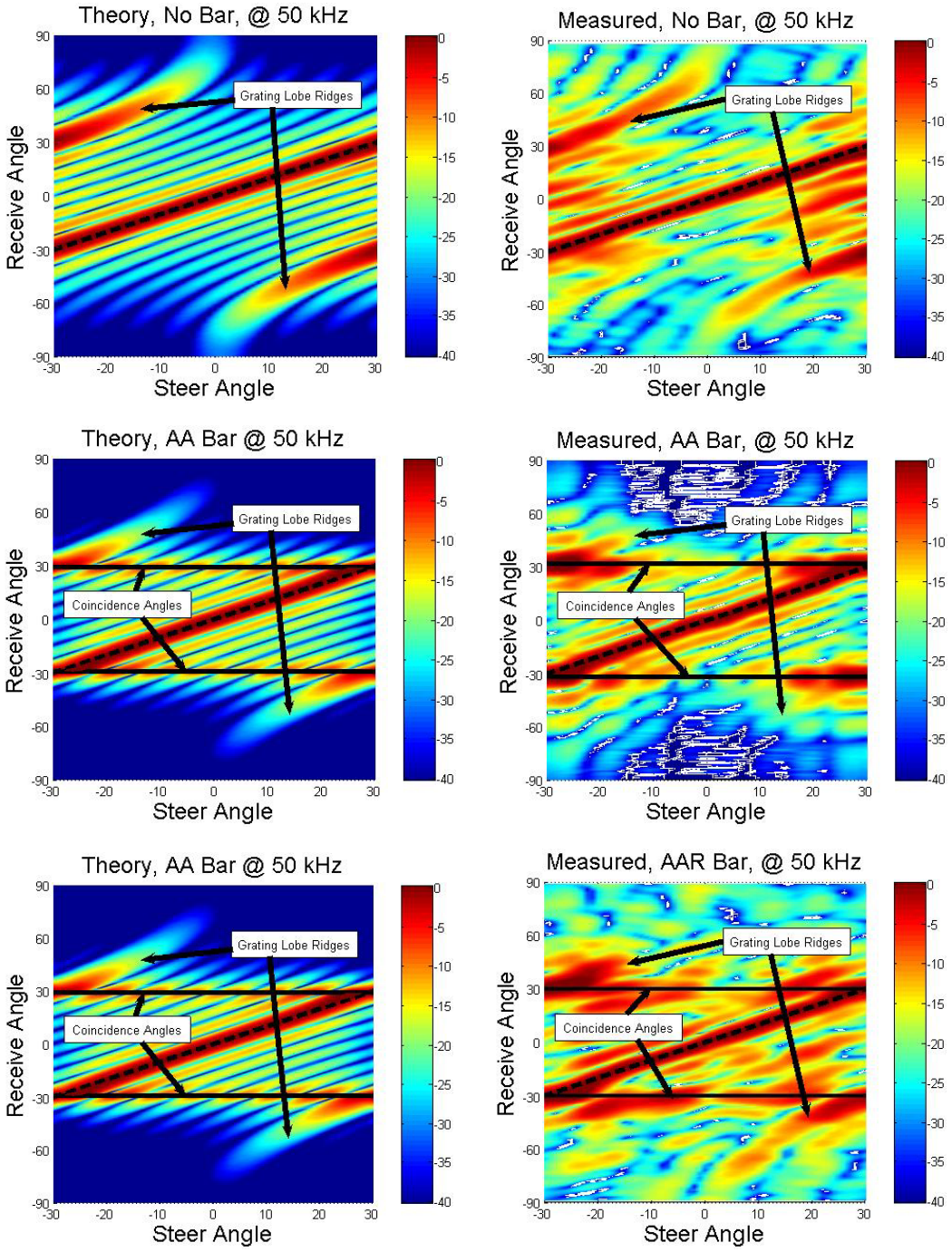

Fig. 6.26. Theoretical and measured receive angle versus steer angle directivity pattern surface plots for the no-bar 8-element line array, original alumina bar 8-element line array, and the revisited alumina bar 8-element line array (52 element planar array) driven at 50 kHz. Steer angle axis has been limited to ±30° to represent the region of practical interest. The original alumina bar data is denoted AA, while the revisited alumina bar data is denoted AAR.

6.8.4 Eight Element Line Array on 52-Element Planar Array – Pine Bar

Wood is one of few natural materials to possess a very high stiffness to mass ratio. Pine has one of the higher stiffness to mass ratios among wood and is easily obtainable. The difficulty with obtaining a good wood sample is in finding a section of wood with grain that is parallel to one of its surfaces. Figure 6.27 shows a diagram depicting the names of the orthogonal directions in a wooden board. The Young's modulus is largest, by a factor of at least 10, in the longitudinal direction. A radial (R-direction) direction wooden bar, was cut such that the length of the bar is in the longitudinal direction, the width of the bar is in the tangential direction and the thickness of the bar is in the radial direction. The pine was coated with polyurethane to reduce water absorption. Figure 6.28 shows a wooden bar mounted to the 52-element array. Figure 6.29 shows the measured frequency response, or receive sensitivity, of the R-direction pine (PR) bar array along with the corresponding 8 elements from the no-plate 52-element array. Theoretical and measured receive angle versus steer angle directivity pattern surface plots for the no-bar 8-element line array (52-element planar array) and the R-direction pine bar 8-element line array (52-element planar array) are given in Figs. 6.30-6.31 for 25 and 50 kHz respectively.

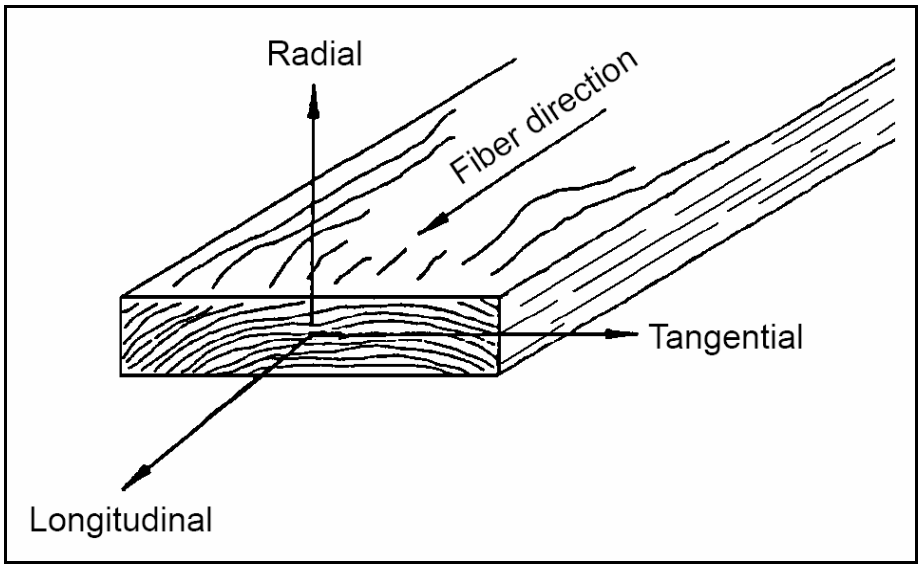

Fig. 6.27. Three principal axes of wood with respect to grain direction and growth rings. Reproduced from Figure 4-1 of Wood Handbook–Wood as an Engineering Material (41, p. 4-2).

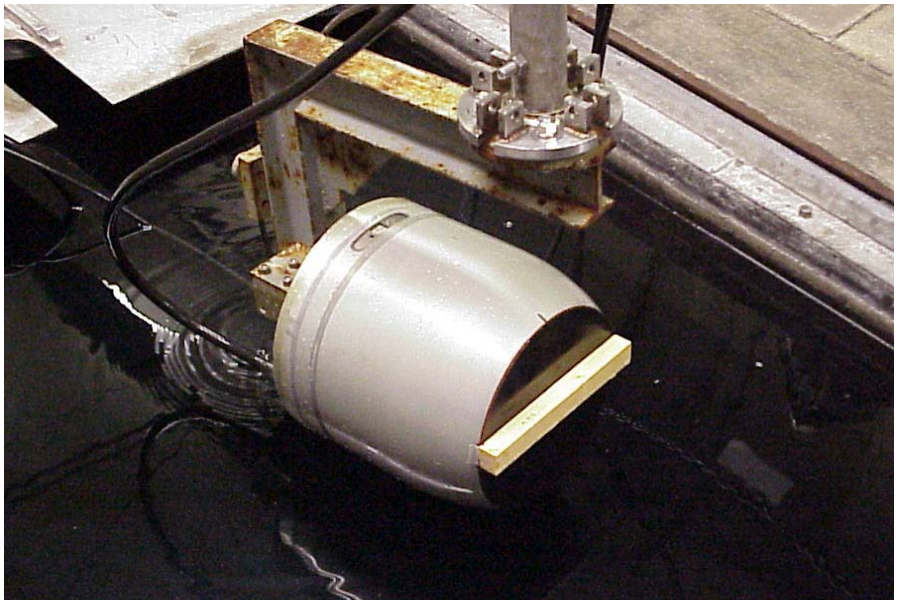

Fig. 6.28. Photograph of a pine bar array.

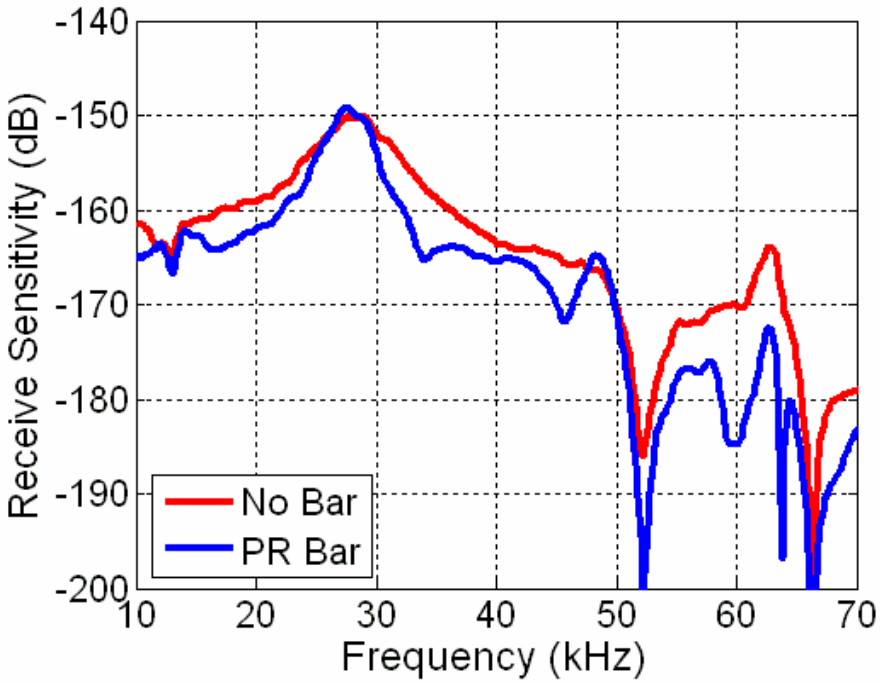

Fig. 6.29. Measured frequency response, or receive sensitivity, for the R-direction pine bar array and the no-bar 8 element line array (the 8 elements are 8 of the 52 element array).

The increase in the frequency response quality factor at the transducer resonance due to the insertion of the pine bar may be seen in Fig. 6.29. However, equivalent circuit analysis presented in Fig. 4.8 predicted a decrease in the quality factor. The R-direction of pine was chosen for the high Young's modulus in the longitudinal direction, which provides a high bending stiffness. However, pine wood is an orthotropic material and possesses lower mechanical impedance through the thickness of the bar relative to that found in the longitudinal direction. Thus the equivalent circuit analysis for the pine bar should be based upon the material properties of pine in the thickness direction. This topic will be further addressed in Section 7.4 and will show that, in fact, an increase in the frequency response quality factor is modeled by the equivalent circuit when the thickness direction material properties are used for the plate model. It is apparent that the R-

direction pine bar reduces the overall level of the frequency response by the least amount relative to the revisited alumina bar and the aluminum honeycomb plate. This is likely due to a better impedance match of the plate impedance to the transducer impedance of the pine bar than the alumina bar and the aluminum honeycomb plate.

As seen with the insertion of the aluminum honeycomb plate, the R-direction pine bar does not exhibit an obvious coincidence angle in the measured pine bar 25 kHz plot and is therefore not denoted in Fig. 6.30. Comparison of the measured no-bar plot with the measured pine bar plot shows that, in general, the side lobes levels have remained the same or decreased due to the insertion of the pine bar.

Figure 6.31 shows that the grating lobe ridges have been reduced in the 50 kHz measured pine bar plot relative to the measured no-bar plot. It is clear than within a steer angle limitation of ±10° that the pine bar patterns should not suffer from high grating lobe levels, and that the side lobe levels have been decreased due to the insertion of the pine bar. The reason for the apparent increase in side lobes at steer angles of about ±15° is unclear. The side lobe structure in the 50 kHz measured pine bar plot tends to possess a few random peaks in the side lobe structure.

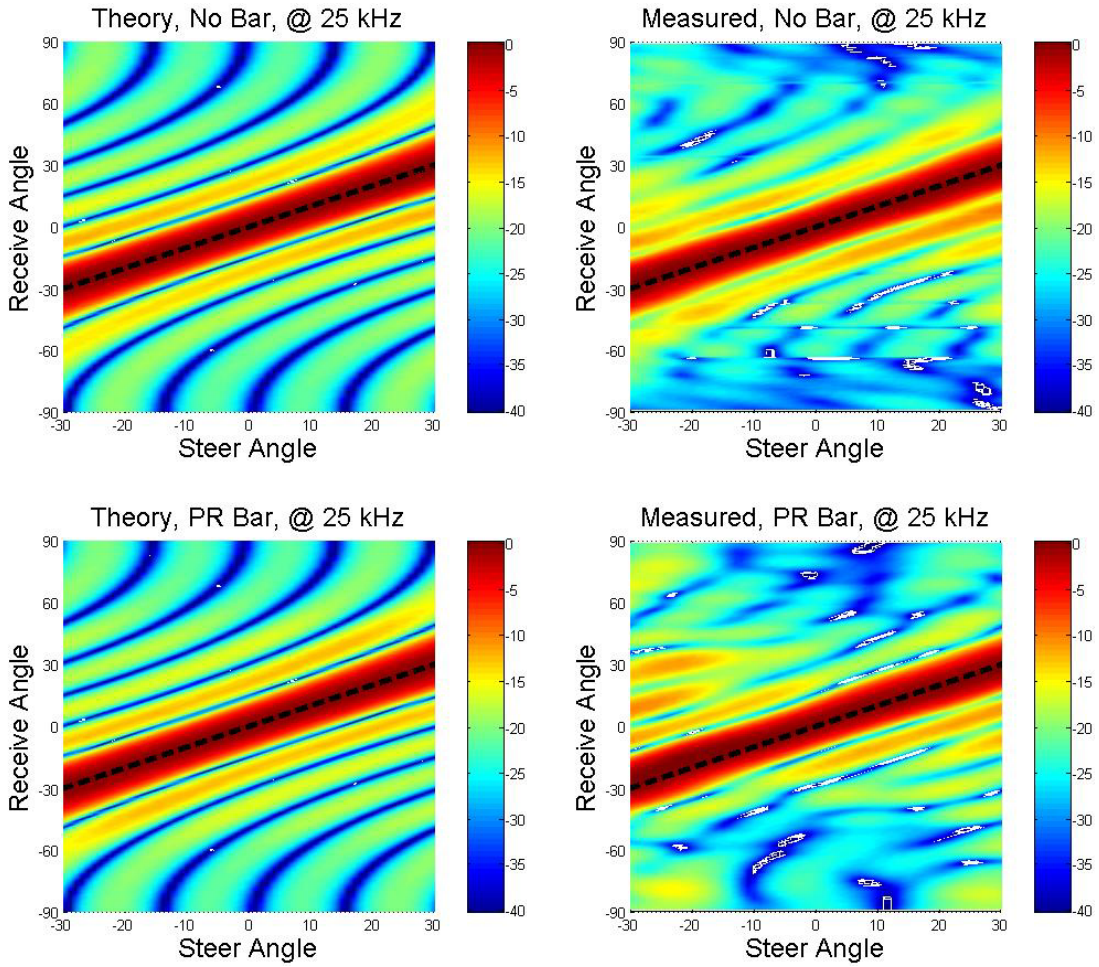

Fig. 6.30. Theoretical and measured receive angle versus steer angle directivity pattern surface plots for the no-bar 8-element line array (8 elements of the 52-element array) and the R-direction pine bar 8-element line array (placed on 8 elements of the 52-element array) driven at 25 kHz. Steer angle axis has been limited to ±30° to represent the region of practical interest.

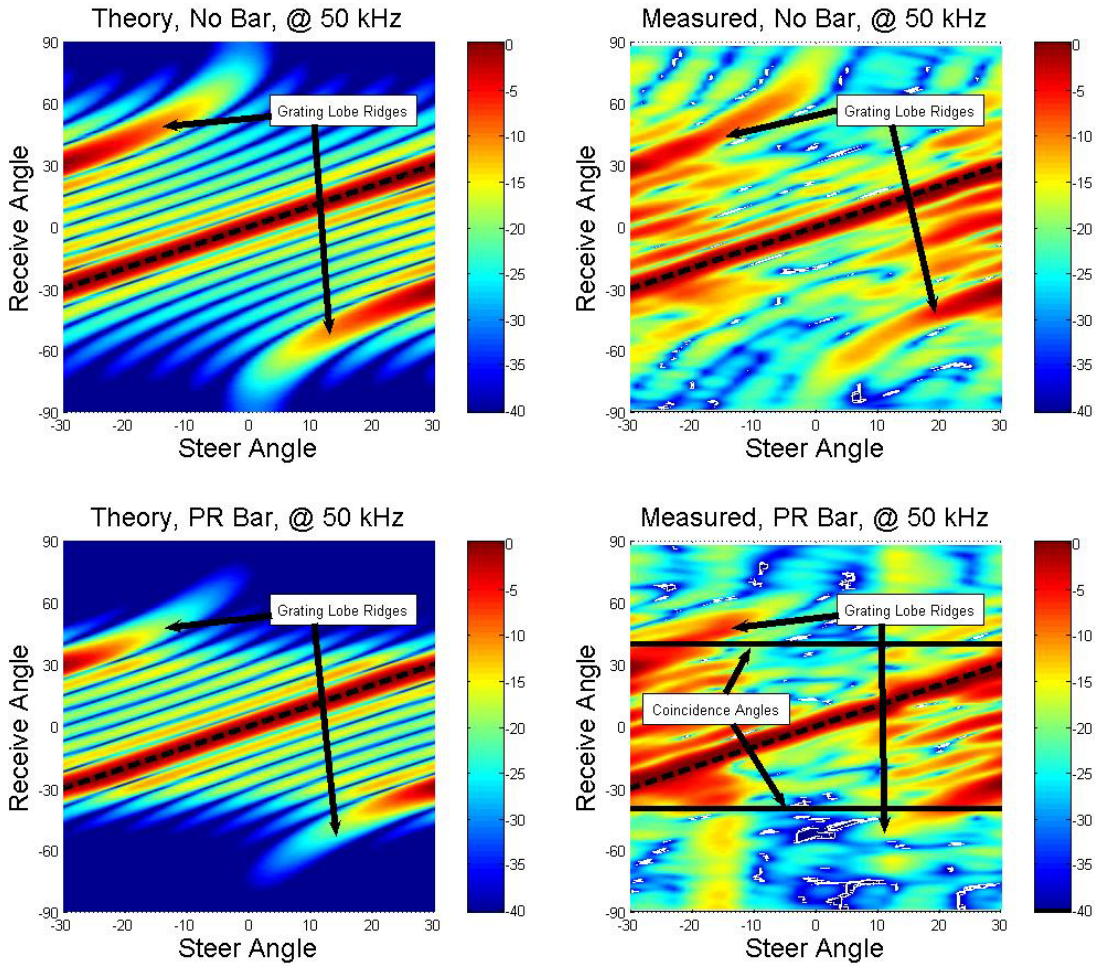

Fig. 6.31. Theoretical and measured receive angle versus steer angle directivity pattern surface plots for the no-bar 8-element line array (8 elements of the 52-element array) and the R-direction pine bar 8-element line array (placed on 8 elements of the 52-element array) driven at 50 kHz. Steer angle axis has been limited to ±30° to represent the region of practical interest.

6.9 Conclusions from Directivity Pattern Surface Plots

The directivity pattern surface plots show that grating lobe levels can be reduced by inserting a bar or plate over the array. The plots also show that a plate possessing low mass does not introduce a significant increase in side lobe levels at the coincidence angles. The plate impedance can have a large impact on the frequency response. Large

impedance plates shift the resonance frequency downward, while low impedance plates increase the Q of resonance. The original alumina bar plots from measured data agree well with theory in side lobe structure and grating lobe level reduction. The data taken with and without the plate and bars placed on the 52-element planar array shows that the side lobe structure is not as well defined as in the data for the 8-element linear array in the corresponding alumina bar and no-bar conditions (see Section 7.6 for additional discussion on this topic). Unsteered patterns, or patterns with a small steer angles ($<\pm 10°$), do appear to benefit from reduced grating lobe and side lobe levels due to the insertion of the original alumina bar and the R-direction pine bar, particularly at 50 kHz.

Although not pointed out for each bar and plate tested, one may notice that the main lobe ridge does not appear to be modified in main lobe beamwidth or suffer from diffraction in the receive angle (the receive angle for the main lobe equals the steer angle despite the presence of the plate). The absence of these effects suggests that the plate insertion doesn't alter the speed of the driven wave induced by the transducers in the plane of the transducer array. The absense of refraction due to plate insertion means that experimental results confirm the validity of the assumption made that refraction may be ignored in Fahy's derivation for the angular dependence of sound transmission through a plate (see Section 3.5).

Chapter 7

COMPARISON AND ANALYSIS OF RESULTS

7.1 Introduction

Chapter 6 presented plots from experimentally obtained data which are difficult to analyze without simple direct comparisons. Chapter 7 presents three different types of comparisons to determine the effects of inserting a plate in front of an array. These three types of comparison include directivity patterns, filter shapes, and frequency responses. Chapter 7 then presents similar comparison plots for a theoretical "ideal" plate. Chapter 7 also presents single element pattern and array pattern comparisons between the 8-element line array and the 52-element planar array.

7.2 Directivity Pattern Comparison

The most basic method of quantifying the impact of inserting a plate to reduce grating lobe levels is to plot the measured directivity patterns for data taken before and after insertion of a plate. Figures 7.1-7.2 display unnormalized, unsteered and 15° steered, 25 kHz and 50 kHz patterns for the no-bar 8-element line array and the alumina bar 8-element line array. The offset differences between no-bar and with-bar patterns in Figs. 7.1-7.2 should each equal the respective differences at each of those frequencies found in the measured frequency responses. The main lobe reductions in Figs. 7.1-7.2 are denoted by black lines and a vertical double arrow.

Figures 7.3-7.11 display normalized directivity patterns for each of the plates/bars tested. Each figure contains 4 subfigures of theoretical and measured, unsteered and 15° steered patterns as noted in each subfigure. In Figs. 7.3-7.4, the alumina (AA) bar data is plotted against the other eight element line array housed in the same shell. The aluminum honeycomb (AH) plate data is plotted against corresponding directivity patterns from the no-plate 52-element planar array data in Figs. 7.5-7.6. The alumina bar revisited, and R-direction pine (PR) bar pattern data are plotted against directivity patterns generated from the same eight elements used under each bar from the no-plate 52-element planar array data in Figs. 7.7-7.8, and Figs. 7.9-7.10 respectively. Grating lobes in Figs. 7.1-7.11 are identified by θ_{GL} and free-bending wave lobes at the coincidence angles are identified by θ_{CO} (θ_{CO} is identified only when the increase in side lobe level is significant). Vertical green arrows in Figs. 7.1-7.10 denote reductions in the grating lobe levels. Theoretical no-bar/plate patterns in Figs. 7.1-7.10 were generated from 8-element line array theory plus appropriate single element directivity corresponding to actual transducer head size. Theoretical with-bar/plate patterns in Figs. 7.1-7.10 were generated from 8-element line array theory plus appropriate single element directivity plus the corresponding theoretical angular filter shape.

In the unnormalized, theoretical with-bar patterns of Figs. 7.1-7.2, the with-bar pattern is adjusted such that the difference in no-bar and with-bar main lobes equals the difference predicted by the equivalent circuit modeling at the appropriate frequency. The unnormalized pattern plots show that while grating lobes can be reduced by significant amounts, the main lobe also is reduced by a substantial amount. The main lobe

reductions in Fig. 7.1 show good agreement between theory and measured data, while the main lobe reductions in Fig. 7.2 do not show good agreement between theory and measured data. This difference will be explained in Section 7.4, but is the result of a broader null in the frequency response around 50 kHz due to the insertion of the alumina bar (see Fig. 7.21).

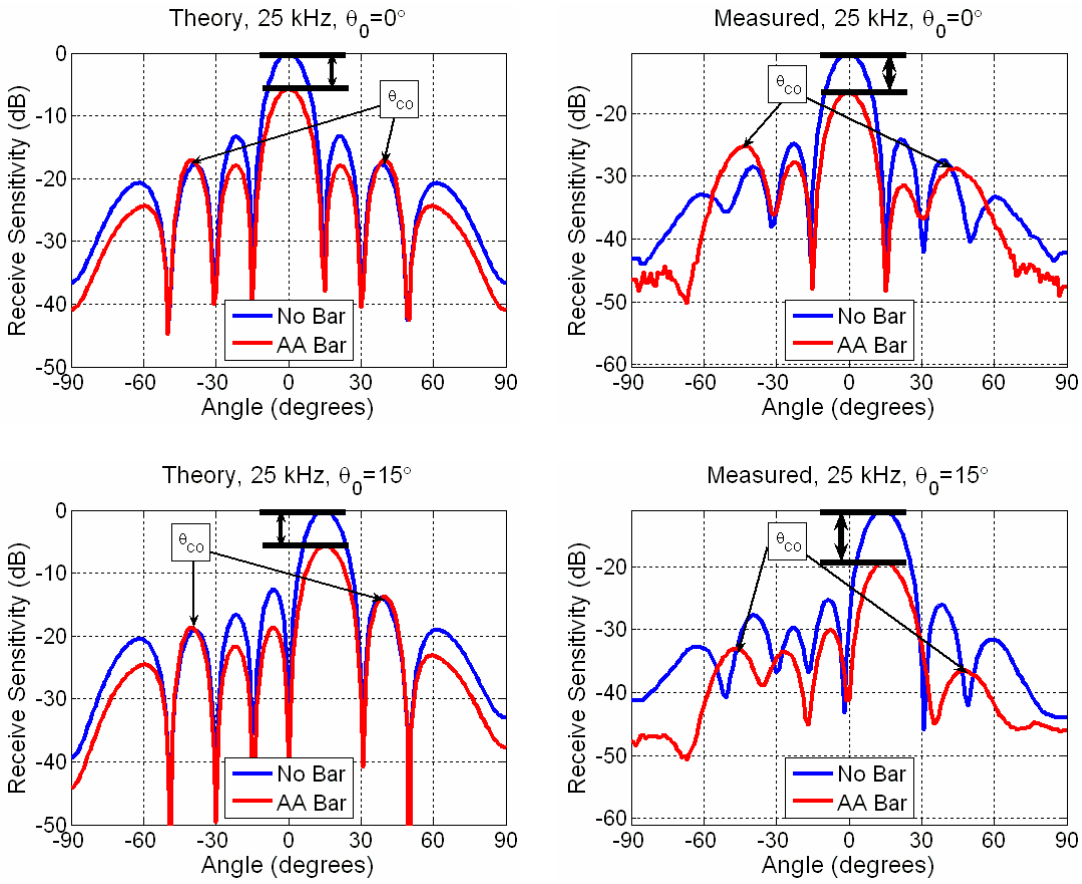

Fig. 7.1. Unnormalized patterns from theory and measured data, in no-bar and with an alumina bar conditions at 25 kHz. The measured data is from the 8-element no-bar and alumina bar line array data. Top plots are unsteered, bottom plots are steered to 15°.

A common practice in the plotting of directivity patterns is to provide comparison of pattern angular dependence by normalizing the patterns such that their main lobes are at 0 dB. The remaining directivity pattern plots in Figs. 7.3-7.11 contain only normalized

patterns. The offset difference in amplitude dependence in unnormalized pattern plots is assumed to be found by a comparison of the frequency responses at the frequency of interest.

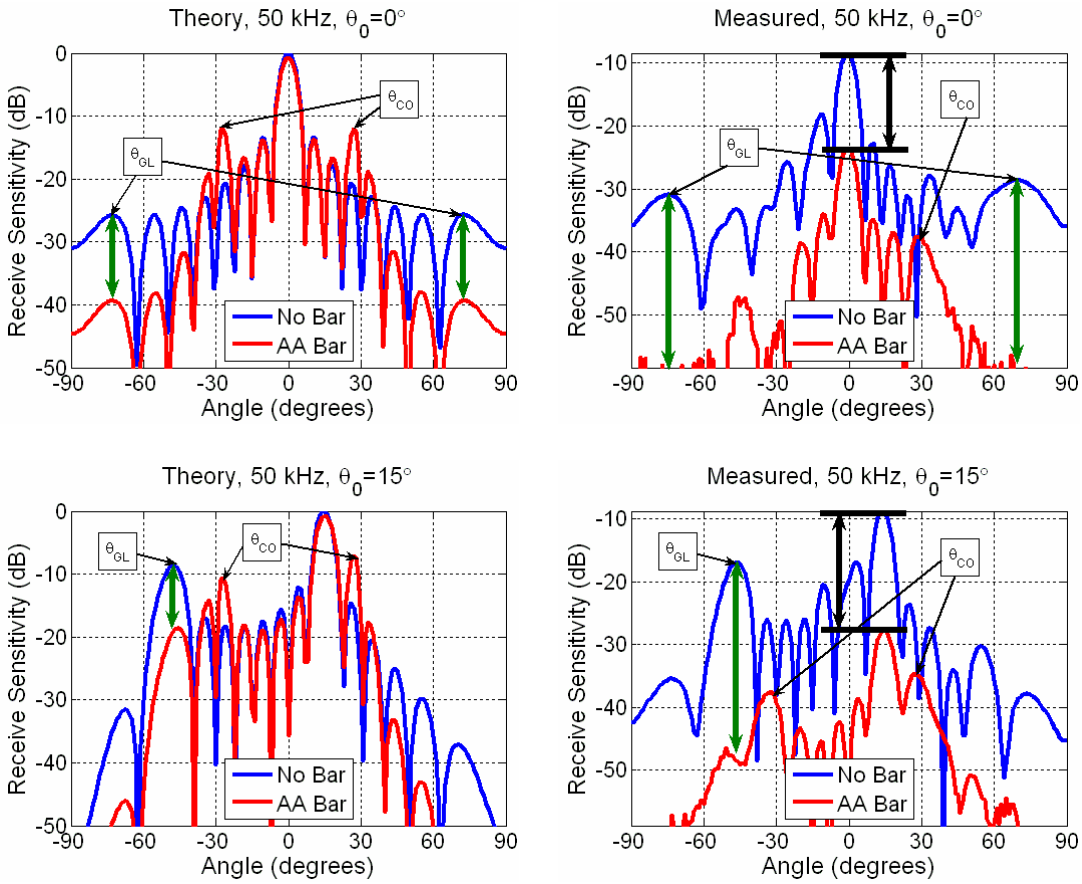

Fig. 7.2. Unnormalized patterns from theory and measured data, in no-bar and with an alumina bar conditions at 50 kHz. The measured data is from the 8-element no-bar and alumina bar line array data. Main lobe transmission loss from equivalent circuit modeling is very small, therefore no black arrow were placed on the theory plots. Top plots are unsteered, bottom plots are steered to 15°.

The alumina bar directivity patterns in Fig. 7.3 show that, as predicted from theory, the side lobe levels increase at or near the coincidence angles. The measured side lobe level increases at the coincidence angles are as high as 6 dB for theory and as high as 9 dB for measured patterns.

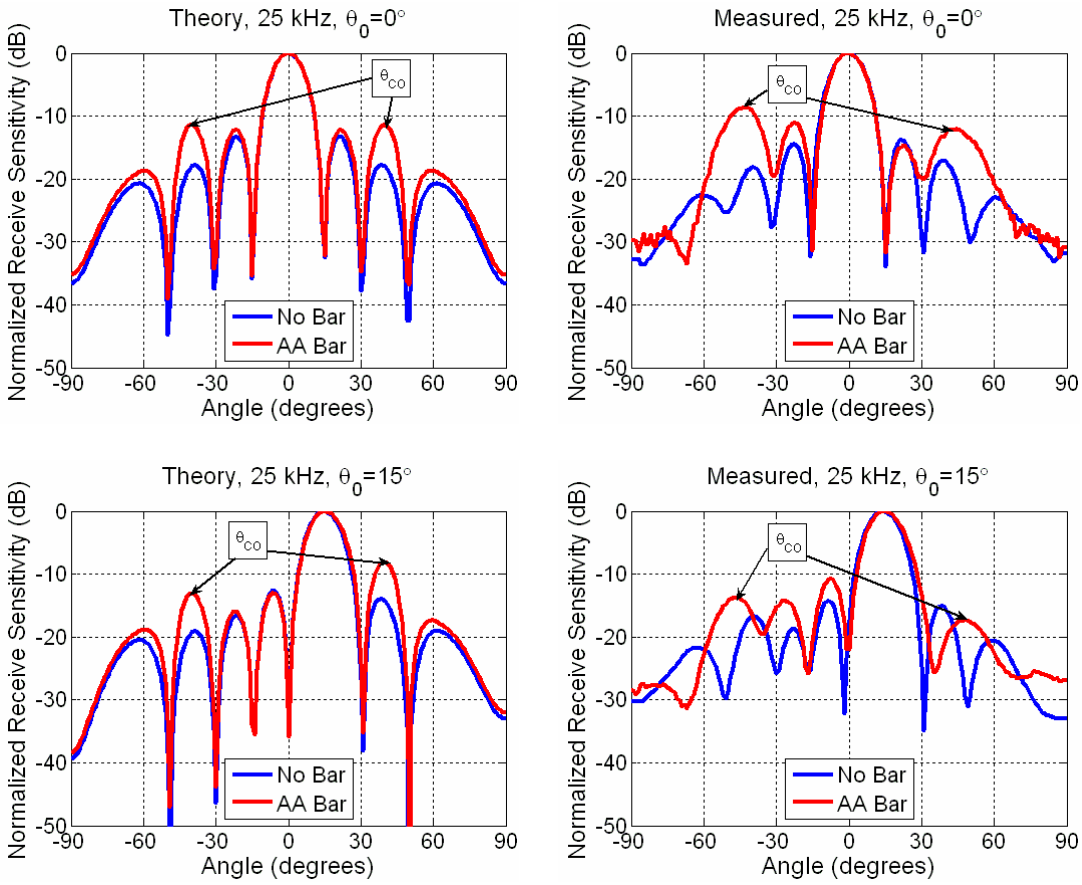

Fig. 7.3: Normalized patterns from theory and measured data, in no-bar and with an alumina bar conditions at 25 kHz. The measured data is from the 8-element no-bar and alumina bar line array data. Top plots are unsteered, bottom plots are steered to 15°.

The alumina bar directivity patterns in Fig. 7.4 do show that grating lobes at (50 kHz, $\theta_0 = 0°$ and $\theta_{GL} = \pm 75°$) and at (50 kHz, $\theta_0 = 15°$ and $\theta_{GL} = -45°$) can be significantly reduced. The grating lobe level reductions are 12 dB for unsteered and 9 dB for 15° steered, theoretical patterns, and are 13 dB for unsteered and 11 dB for 15° steered, measured patterns. The 50 kHz measured directivity patterns show fairly significant increases (5-7 dB) in side lobe levels, modeled well by theory, the highest concentration of which is located at or near the coincidence angle at ±30°. The reason for

the asymmetry in the side lobes for the unsteered 50 kHz pattern is unknown, but is likely due to mismatching of transducer elements due to array conditions (different element positioning in an array is affected differently by radiation impedance, baffle loading, and edge conditions).

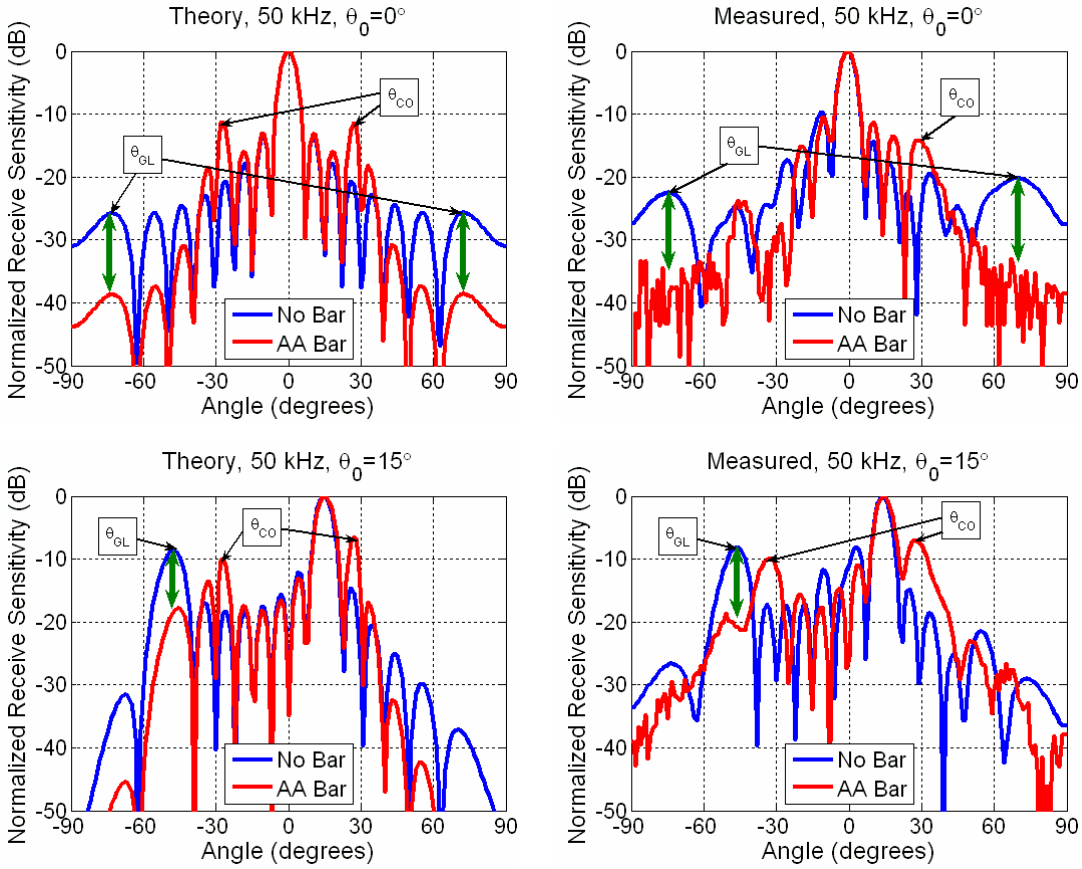

Fig. 7.4: Normalized patterns from theory and measured data, in no-bar and with an alumina bar conditions at 50 kHz. The measured data is from the 8-element no-bar and alumina bar line array data. Top plots are unsteered, bottom plots are steered to 15°.

Figures 7.5-7.6 show directivity patterns from the aluminum honeycomb plate data and from corresponding no-plate data. Increased side lobe levels at the coincidence angles are not found in the 25 kHz patterns, as predicted by theory, but increased side lobe levels are found in the measured 50 kHz patterns, higher than predicted by theory.

The measured aluminum honeycomb plate directivity patterns show minimal grating lobe level reductions of 2-5 dB compared to 6-10 dB theoretical reductions. Both the no-plate and the aluminum honeycomb plate patterns contain what appear to be extra artificial ripples due to mismatching of elements, particularly at 50 kHz. No visible difference is apparent between theoretical no-plate patterns and theoretical aluminum honeycomb plate patterns at 25 kHz, as is expected from the theoretical filter shape at 25 kHz.

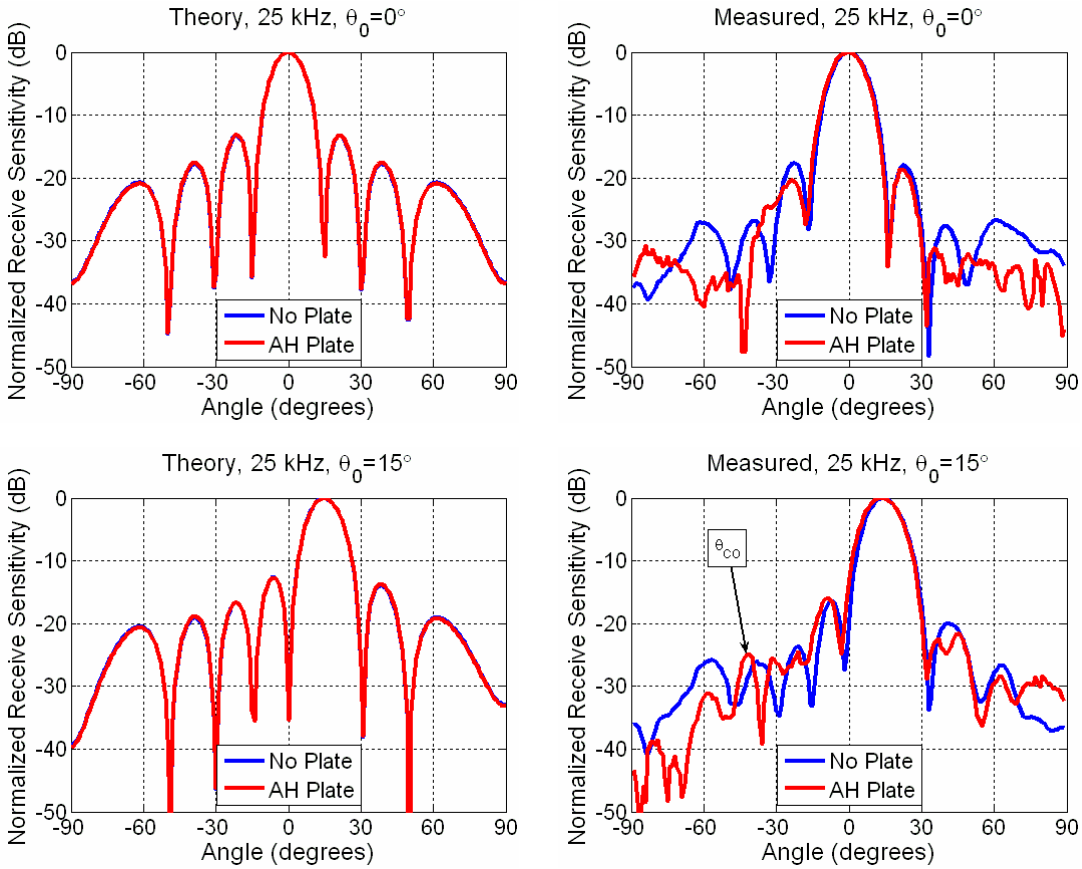

Fig. 7.5: Normalized patterns from theory and measured data, in no-plate and with an aluminum honeycomb plate conditions at 25 kHz. Theoretical patterns represent an 8-element line array model. The measured data is from the 52-element no-plate and aluminum honeycomb plate planar array data. Top plots are unsteered, bottom plots are steered to 15°.

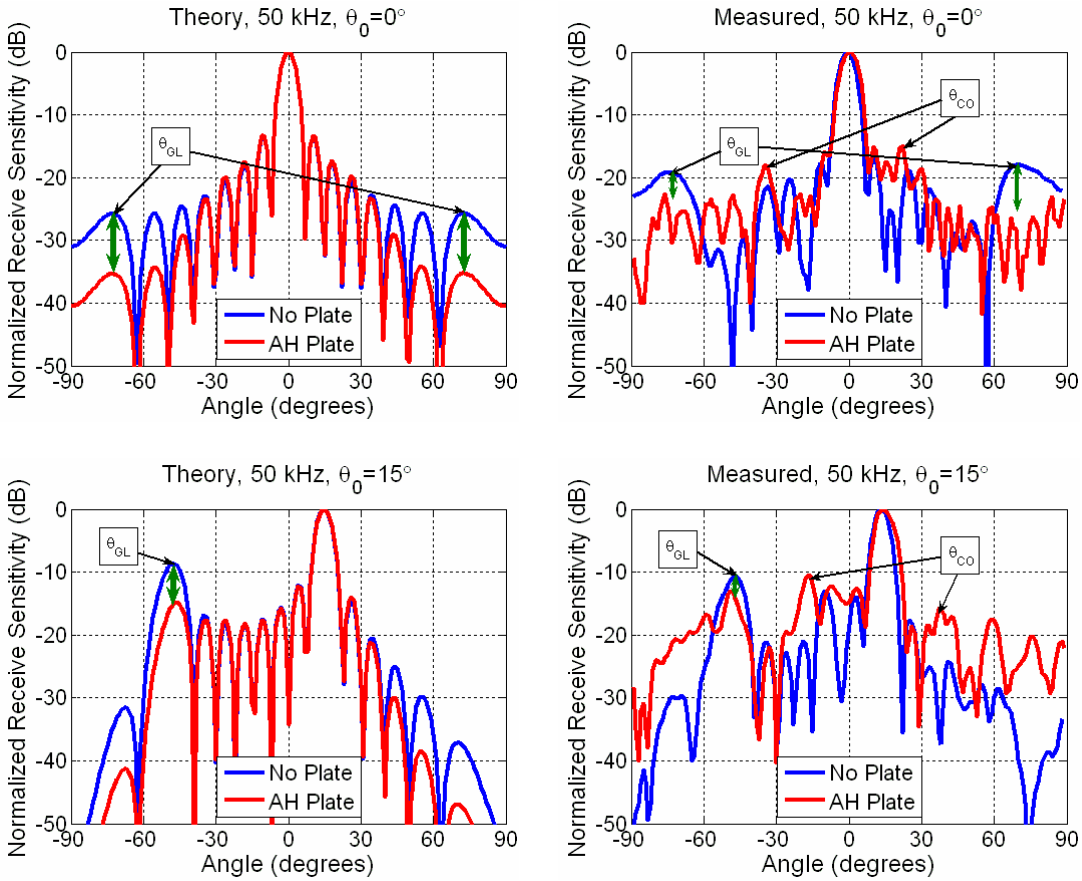

Fig. 7.6: Normalized patterns from theory and measured data, in no-plate and with an aluminum honeycomb plate conditions at 50 kHz. Theoretical patterns represent an 8-element line array model. The measured data is from the 52-element no-plate and aluminum honeycomb plate planar array data. Top plots are unsteered, bottom plots are steered to 15°.

The directivity patterns of the alumina bar on the 52-element array (Figs. 7.7-7.8) do not compare well to the corresponding directivity patterns on the 8-element array Figs. 7.3-7.4. For example, the measured directivity patterns in Fig. 7.8, for 50 kHz, show extra ripples (not seen in Fig. 7.4 patterns) and do not show a reduction in the grating lobes. The measured 25 kHz patterns show little to no increases in side lobe levels at the coincidence angles. The reason for this discrepancy may be due to the different mounting techniques used, the different transducers used, or a combination of

the two. Section 7.6 discusses the differences inherent in the two different no-plate/bar transducers used.

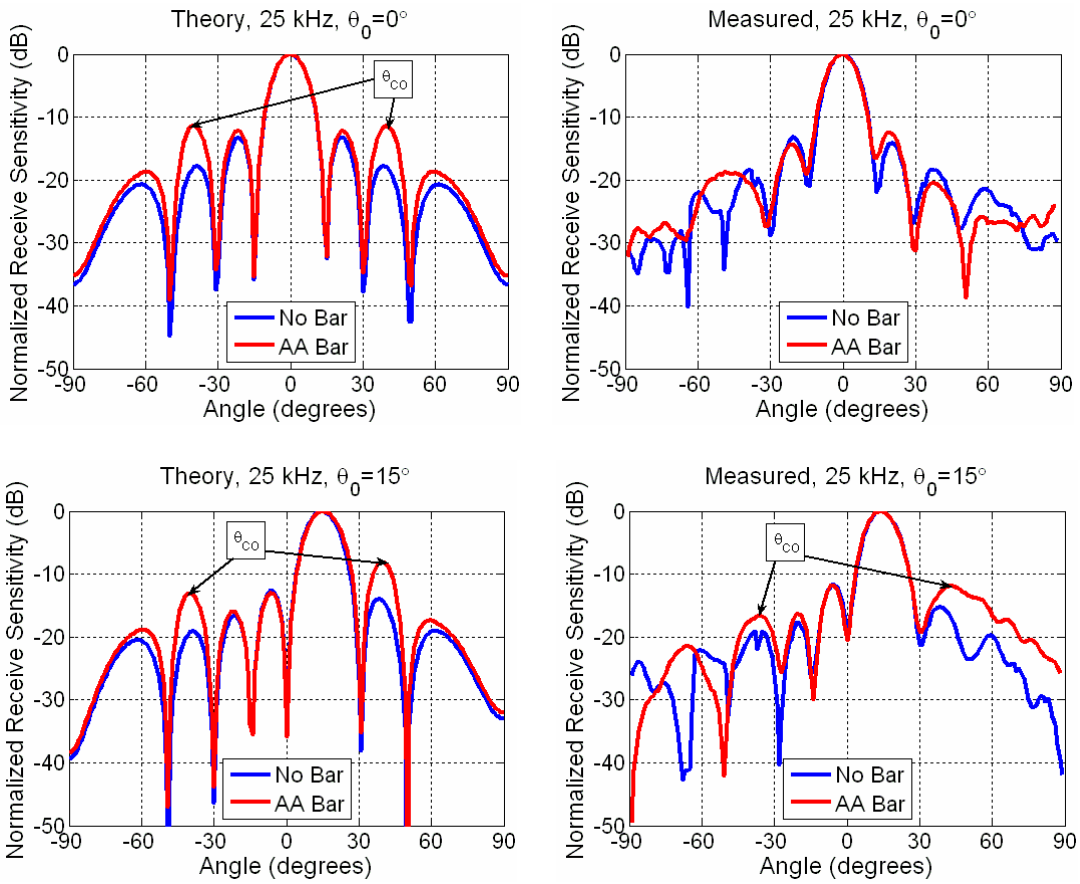

Fig. 7.7. Normalized patterns from theory and measured data, in no-bar and with an alumina bar conditions at 25 kHz. The measured data is from the corresponding 8 elements of the 52-element planar array data in no-bar and the revisited alumina bar conditions. Top plots are unsteered, bottom plots are steered to 15°.

Figures 7.9-7.11 show directivity patterns obtained from the R-direction (R-direction defined in Section 6.8.4) pine bar data with the corresponding no-bar data. Ripples are again found in the directivity patterns for the pine bar as found previously in Figs. 7.5-7.8. The measured pine bar patterns show some reduction of the grating lobes particularly for the unsteered pattern. At 50 kHz, the measured pine bar pattern steered to 15° shows an increase in many side lobes, not just at the coincidence angles as seen in the

measured pine bar directivity surface plot in Fig. 6.31. Increased side lobes at the coincidence angles are either nonexistent or minimal as expected (see Figs. 7.18-7.19). No visible difference is apparent between theoretical no-plate patterns and theoretical pine bar patterns at 25 kHz, as is expected when one views the theoretical filter shape for the pine bar at 25 kHz.

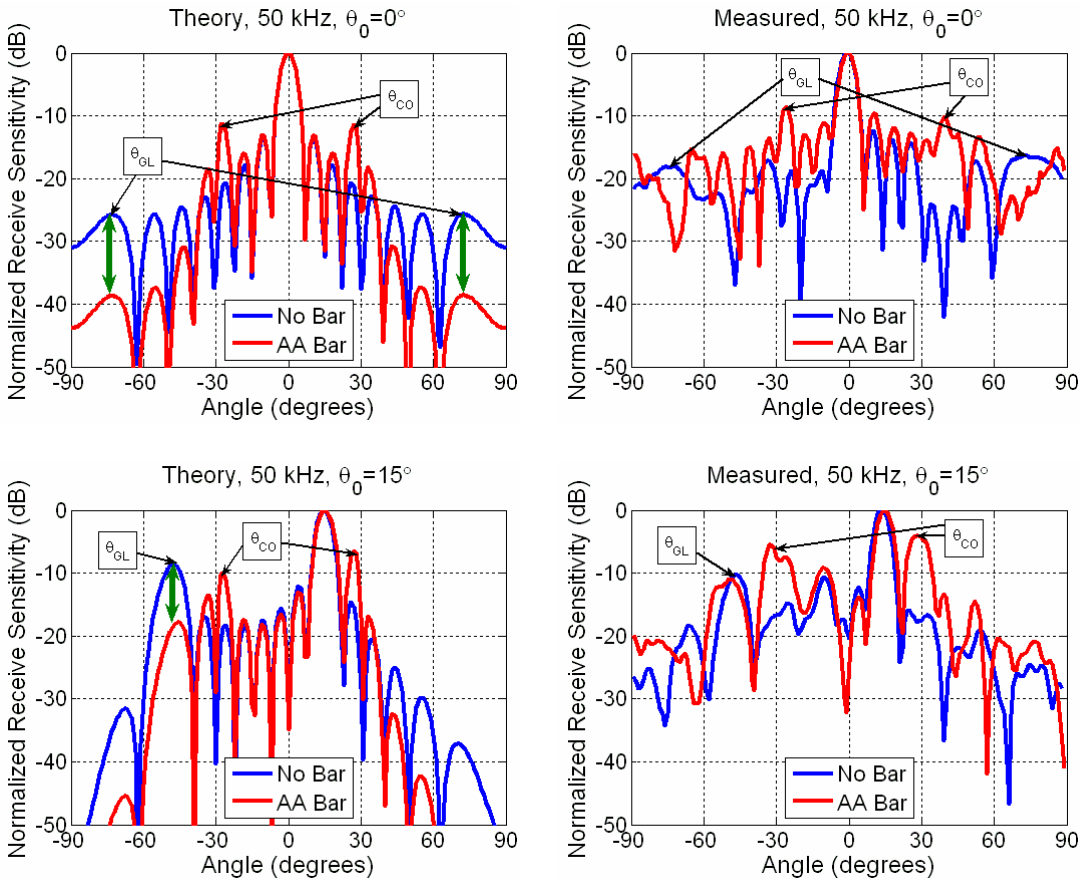

Fig. 7.8. Normalized patterns from theory and measured data, in no-bar and with an alumina bar conditions at 50 kHz. The measured data is from the corresponding 8 elements of the 52-element planar array data in no-bar and the revisited alumina bar conditions. Top plots are unsteered, bottom plots are steered to 15°.

Inspection of these sample directivity patterns has shown that, there is promise that pattern control may be possible if baffle conditions and element variability can be controlled better. It has been shown that grating lobes levels may be reduced, particularly

from the original alumina bar measurements. Side lobe levels, at coincidence angles, are an issue and suggest that a plate/bar should possess a low mass. The various frequency and steer angle combinations presented in Figs. 7.1-7.10 are representative of what is generally found at other frequency and steer angle combinations. It is also apparent that the 52-element planar array patterns contain many ripples with or without the presence of a bar or plate due to apparent increased mismatching of transducer elements relative to the 8-element line arrays for the original alumina bar data.

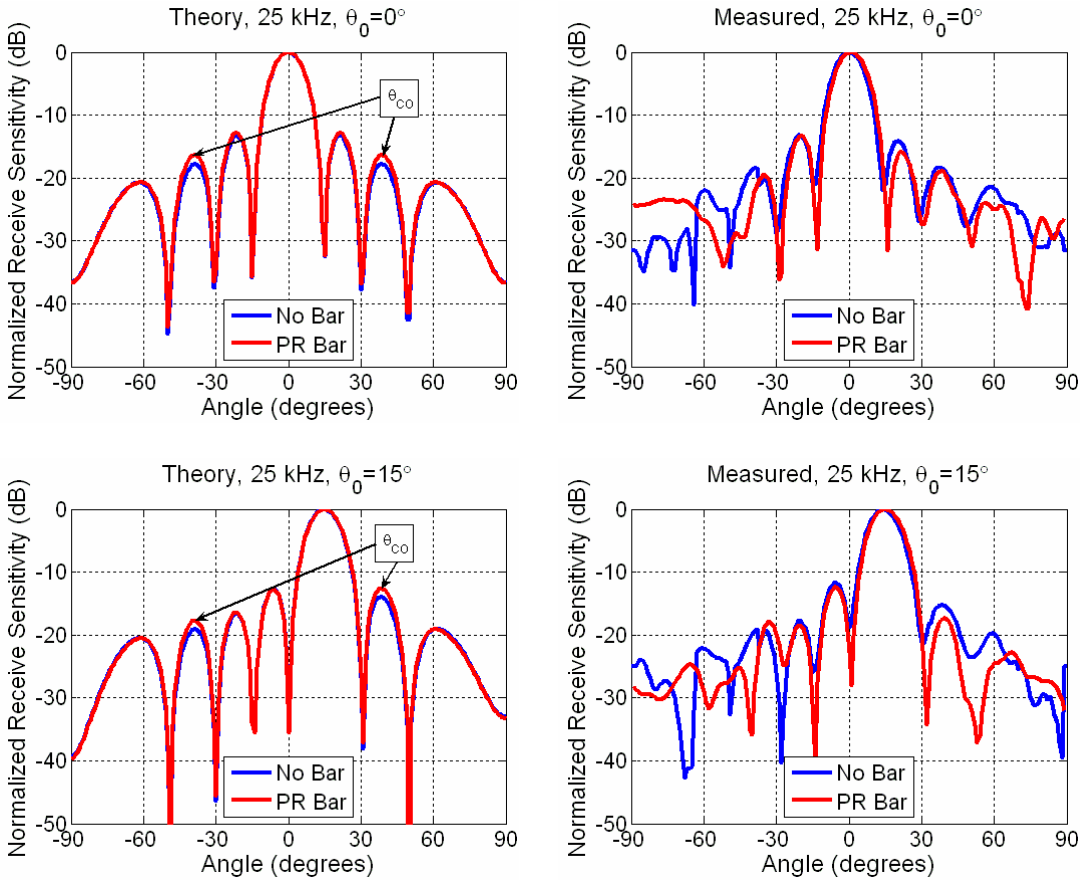

Fig. 7.9. Normalized patterns from theory and measured data, in no-bar and with a pine bar conditions at 25 kHz. The measured data is from the corresponding 8 elements of the 52-element planar array data in no-bar and R-direction pine bar conditions. Top plots are unsteered, bottom plots are steered to 15°.

As discussed in Section 6.9, each of the directivity pattern comparisons in Figs. 7.1-7.10 show that all of the main lobes from the with-plate directivity patterns line up with the main lobes in all of the corresponding no-plate directivity patterns. The fact that the main lobes line up demonstrates that no refraction of the direction of the steered energy may be expected when steering through a plate. It is also worth noting that the beamwidth of the main lobes does not change due to the insertion of a plate. The absence of these effects suggests that the plate insertion does not alter the speed of the driven wave induced by the transducers in the plane of the transducer array.

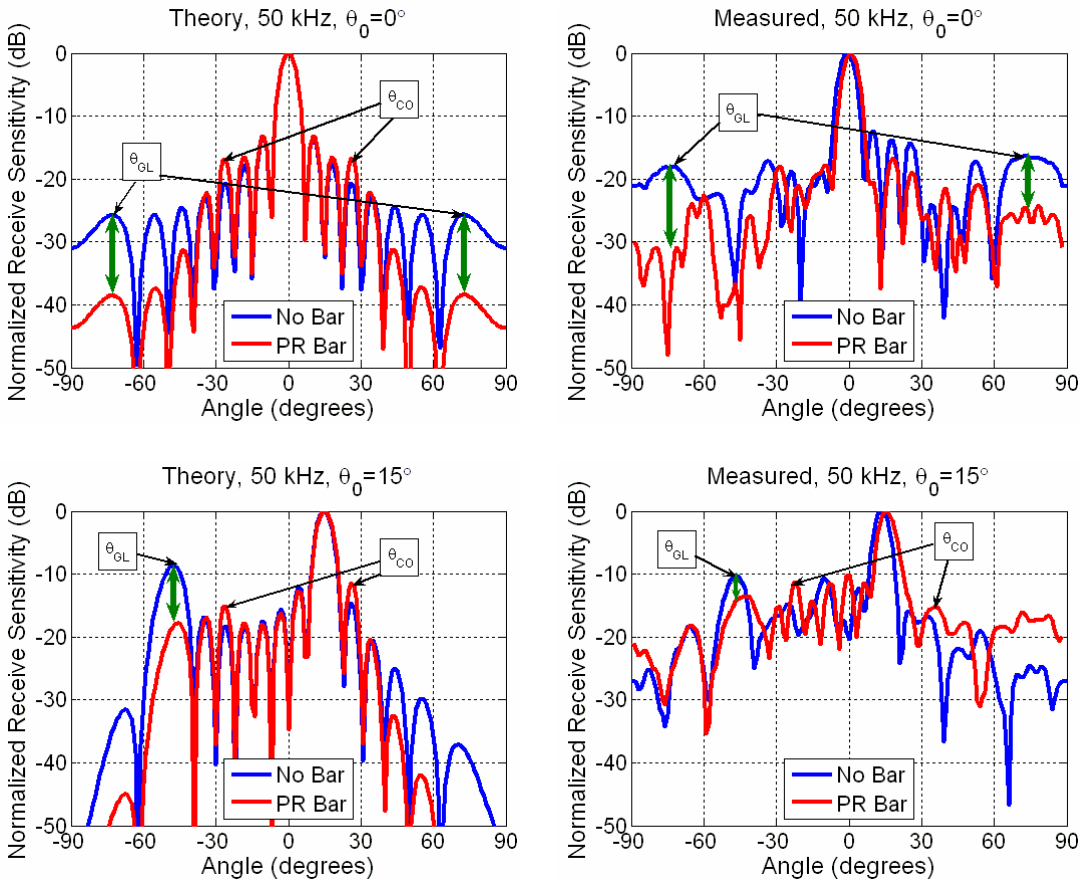

Fig. 7.10. Normalized patterns from theory and measured data, in no-bar and with a pine bar conditions at 50 kHz. The measured data is from the corresponding 8 elements of the 52-element planar array data in no-bar and R-direction pine bar conditions. Top plots are unsteered, bottom plots are steered to 15°.

A comparison may also be made of the 50 kHz and $\theta_0 = 15°$ pattern from the alumina bar line array data to the corresponding pattern obtained from numerical finite element modeling. As discussed in Chapter 5, the ANSYS model with constant force inputs show the increases seen in experimental results at the coincidence angles due to free bending waves better than the constant displacement inputs which suppresses the increases at the coincidence angles. Figure 7.11 displays the pattern comparison of the numerical finite element constant force inputs model to measured results for the alumina bar line array and the measured no-bar line array at 50 kHz and $\theta_0 = 15°$. The numerical model suggests an expected 10 dB increase in side lobe levels at the coincidence angles while measured data results in an increase of 7-8 dB in side lobe levels at the coincidence angles. The numerical model suggests an expected 6.5 dB decrease in the grating lobe level while measured data results in a decrease of 12 dB in the grating lobe level. The numerical finite element model overestimates the increase in the side lobe levels at the coincidence angle and underestimates the decrease in the grating lobe level. Baffle directivity was not included in the ANSYS model and could account for some of the difference. In addition, some of the difference may be attributed to the actual impedance of the transducer being finite, whereas the constant force inputs model the transducer as having zero impedance.

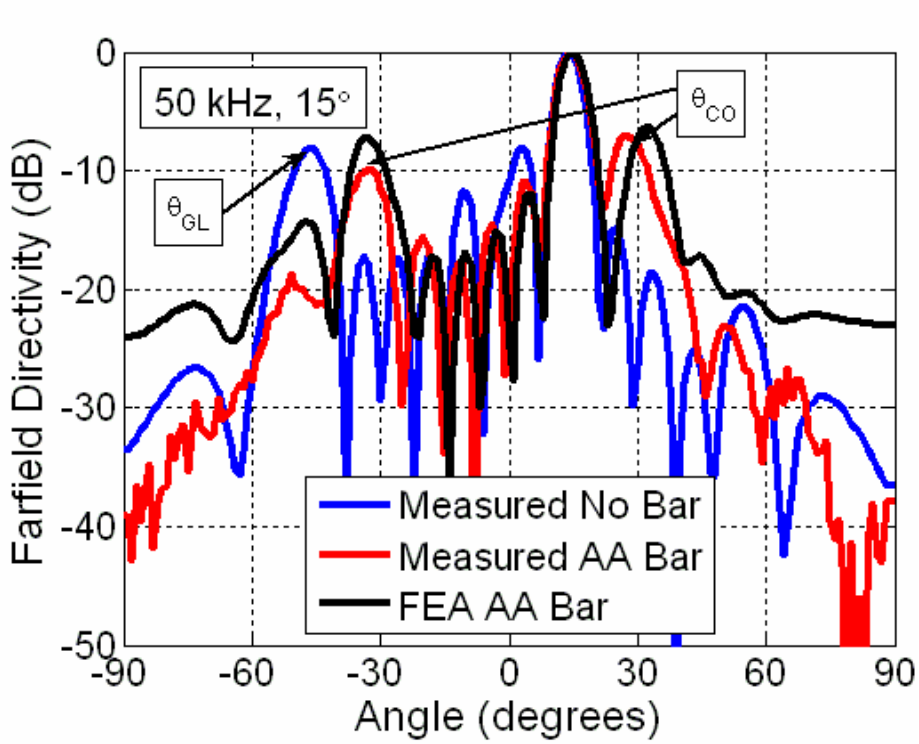

Fig. 7.11. Normalized pattern comparison of the numerical finite element constant force inputs model to measured results for the alumina bar line array and the no-bar line array at 50 kHz and $\theta_0 = 15°$. FEA refers to the finite element analysis ANSYS model.

7.3 Filter Shape Comparison

Chapter 3 presented theory which governs the transmission coefficient of sound transmission through an unbounded plate. In particular, a theoretical expression was developed for the angular dependence of sound transmission through an unbounded plate, referred to as filter shapes (see Eq. (3.32)). Figures 7.12-7.19 contain plots of filter shapes (transmission loss of main lobe as a function of steer angle) obtained from experimental data and filter shapes obtained from the theoretical expression contained in Eq. (3.32).

The measured filter shapes were obtained from experimental element based receive data and generated by taking the difference between filter shape directivity patterns of the arrays with and without the bar or plate. These filter shape directivity patterns were generated by steering to every degree from -90° to +90° and recording the value at the main lobe only, for each steer angle. The experimentally obtained filter shapes are normalized to provide the best angular dependence comparison, in general this means that their respective pass band levels were adjusted so that measured and theoretical filter shapes were equal. The theoretical filter shapes were obtained by using the material and geometrical properties found in Table 3.2 in Eq. (3.32). Figures 7.12-7.19 show the filter shapes obtained from measured array data for the alumina bar, the revisited alumina bar, the aluminum honeycomb plate, and the R-direction pine bar.

The alumina bar filter shapes appear to closely follow the filter roll off portions at angles higher than the coincidence angles. The peaks at the coincidence angles generally do not appear to be quite as high as predicted, except for the experimentally obtained filter shape at 50 kHz (see Appendix F). The 50 kHz filter shape for the alumina bar array on the 8-element 1-D array appears to match the theoretical filter shape quite well, aside from the large level offset difference due to the frequency being near the transducer response null around 50 kHz with the alumina bar insertion (see Fig. 7.21). Assuming that this experimentally determined filter shape were normalized with respect to its pass band transmission loss (as shown in the right plot of Fig. 7.13), the pass band transmission loss, TL_{PB}, is 12 dB, while the relative stop band transmission loss, TL_{RSB}, is 11.3 dB. When noise dominates at large angles an increase in apparent level is present due to comparing to a standard projector. This appears to be the case in Fig. 7.13. The

coincidence angles are located at ±31° in this filter shape. Subtraction of these numbers from the theoretical values calculated in Table 3.3 results in a TL_{PB} difference of 0.7 dB, a TL_{RSB} difference of 1.6 dB and -1.7°. These similar results provide confidence in using the theoretical filter shape equation (see Eq. (3.32)) for modeling mounted bars.

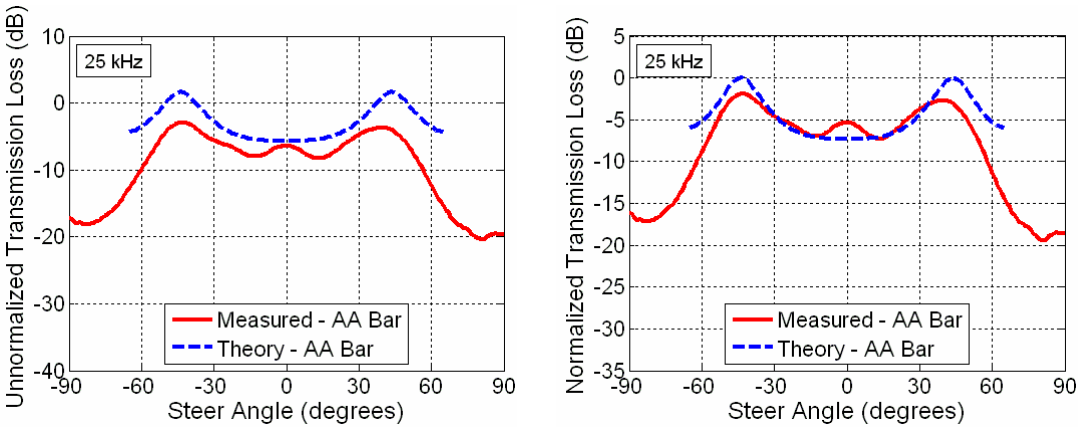

Fig. 7.12. Filter shapes (main lobe transmission loss versus steer angle) obtained from experimental data and from theory for the 8-element alumina bar line array and its corresponding no-bar data at 25 kHz. The plot on the left is unnormalized while the plot on the right is normalized.

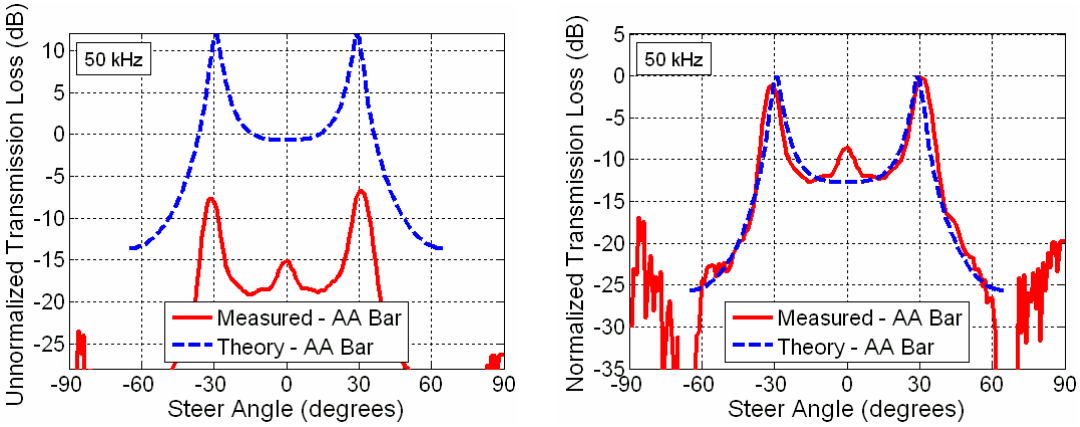

Fig. 7.13. Filter shapes (main lobe transmission loss versus steer angle) obtained from experimental data and from theory for the 8-element alumina bar line array and its corresponding no-bar data at 50 kHz. The plot on the left is unnormalized while the plot on the right is normalized.

The bars and plate (including the revisited alumina bar) tested on the 52-element planar array do not appear to possess a consistent amount of stop band attenuation (the regions greater than the coincidence angles). The measured filter shapes in Fig. 7.15 and Fig. 7.19 demonstrate good agreement with their respective theoretical filter shapes. The level offsets in the unnormalized plots of Figs. 7.14 and 7.15 are due to the low impedance of the plate, which unloads the transducers relative to the no-plate radiation impedance. Some measured filter shapes possess higher stop band attenuations than the theoretical filter shapes (see Figs. 7.12, 7.14, 7.16, and 7.18). The higher stop band loss beneficially increases the pattern directivity and suppresses sensitivity at large angles where flow noise can be problematic. A few measured filter shapes, from the 52-element array data, resemble theoretical filter shapes near the coincidence angles and at shallower angles, including normal incidence but not at larger angles (see Fig. 7.17). See Table 8.1 for filter shape performance metrics to compare theoretical and experimentally obtained coincidence angles, pass band transmission losses, and stop band transmission losses.

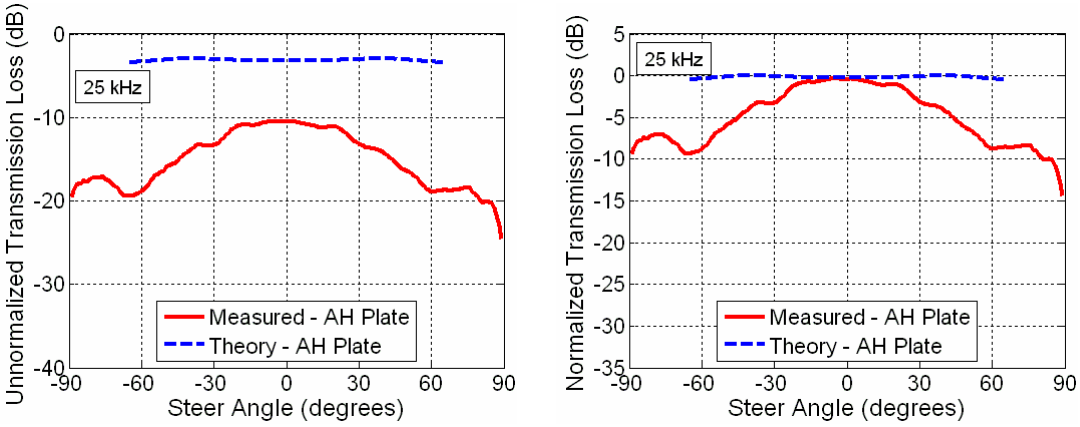

Fig. 7.14. Filter shapes (main lobe transmission loss versus steer angle) obtained from experimental data and from theory for the 8-element aluminum honeycomb plate planar array and its corresponding no-plate data at 25 kHz. The plot on the left is unnormalized while the plot on the right is normalized.

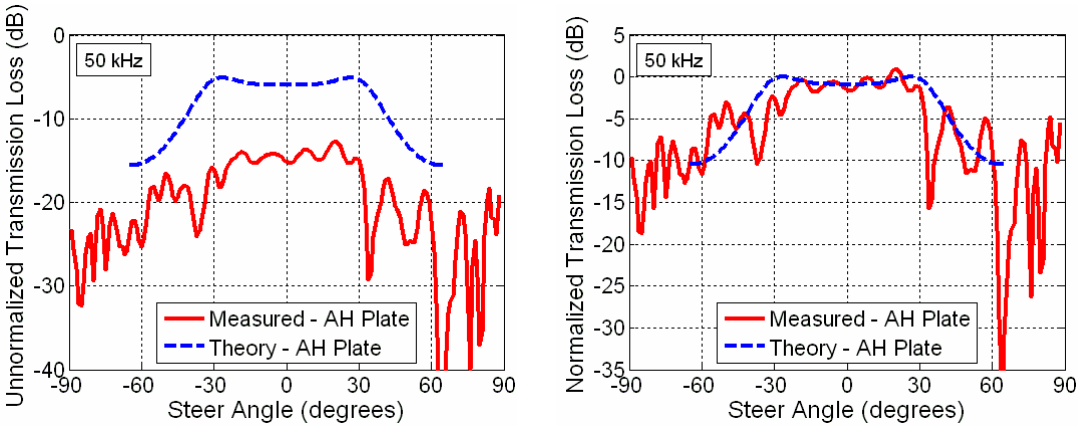

Fig. 7.15. Filter shapes (main lobe transmission loss versus steer angle) obtained from experimental data and from theory for the 8-element aluminum honeycomb plate planar array and its corresponding no-plate data at 25 kHz. The plot on the left is unnormalized while the plot on the right is normalized.

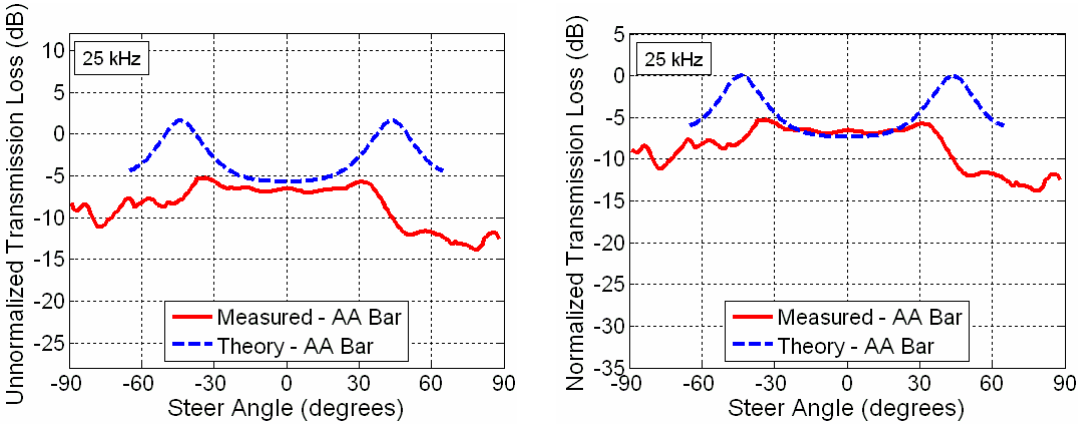

Fig. 7.16. Filter shapes (main lobe transmission loss versus steer angle) obtained from experimental data and from theory for the 8-element revisited alumina bar line array and its corresponding no-bar data at 25 kHz. The plot on the left is unnormalized while the plot on the right is normalized.

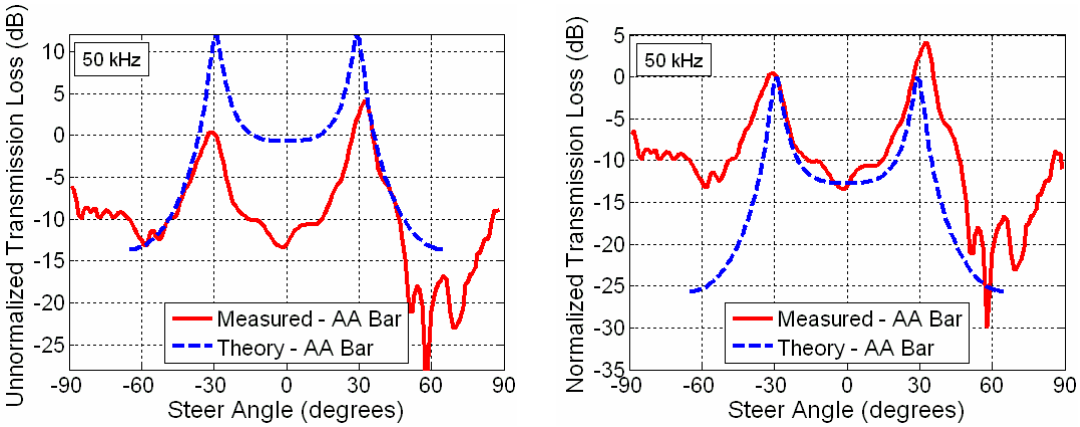

Fig. 7.17. Filter shapes (main lobe transmission loss versus steer angle) obtained from experimental data and from theory for the 8-element revisited alumina bar line array and its corresponding no-bar data at 50 kHz. The plot on the left is unnormalized while the plot on the right is normalized.

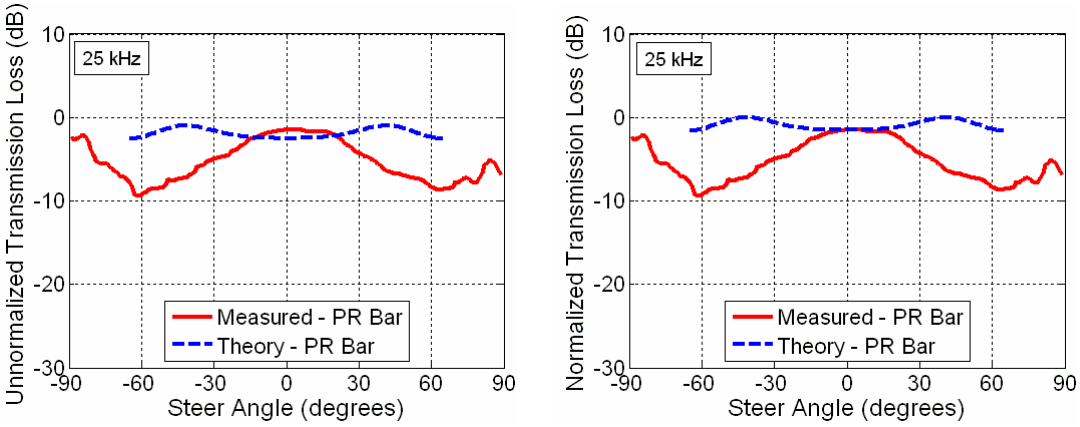

Fig. 7.18. Filter shapes (main lobe transmission loss versus steer angle) obtained from experimental data and from theory for the 8-element R-direction pine bar line array and its corresponding no-bar data at 25 kHz. The plot on the left is unnormalized while the plot on the right is normalized.

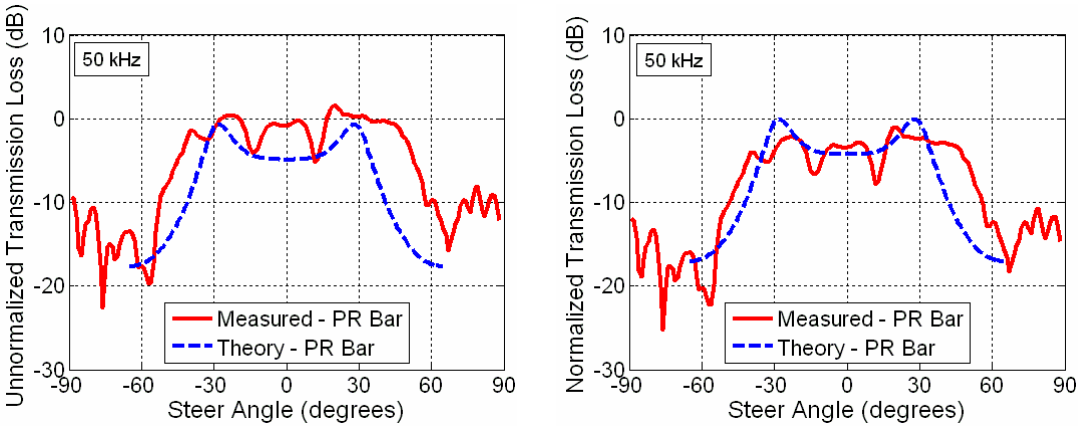

Fig. 7.19. Filter shapes (main lobe transmission loss versus steer angle) obtained from experimental data and from theory for the 8-element R-direction pine bar line array and its corresponding no-bar data at 50 kHz. The plot on the left is unnormalized while the plot on the right is normalized.

7.4 Frequency Response Comparison

Chapter 6 presented measured normal incidence frequency responses from no-plate and with-plate data. Chapter 4 presented a layered media equivalent circuit model

for the frequency response of a transducer receiving sound at normal incidence through a plate layer and a lossy compliant layer. The low-frequency equivalent circuit model does not match measured data at all frequencies but does show trends in frequency response deviations due to plate insertion.

Figures 7.20-7.22 contain no-plate and with-plate measured frequency responses along with the modeled frequency responses obtained from Eqs. (4.1) and (4.10) found in the left subplots. Figures 7.20-7.22 also show the normal incidence transmission losses (right subplots) obtained from theoretical expressions (see discussion below), from the difference between the no-plate and with-plate equivalent circuit frequency response models (E.C. Model), and measured array data for the aluminum honeycomb plate (Fig. 7.20), the revisited alumina bar (Fig. 7.21), and the R-direction pine bar (Fig. 7.22).

The normal incidence mass law transmission loss (see Eq. (3.35)) is valid when the wavelength of sound through the thickness of the plate structure is large compared to the plate thickness. When this structural wavelength, $\lambda_{P\perp}$, is twice the plate thickness, a half wavelength resonance in the plate thickness dimension occurs. The normal incidence mass law transmission loss is obviously no longer valid at this frequency. Instead the problem may be considered using a normal incidence, three layer transmission loss (3 Layer TL) problem (34, pp. 152-155), (42, pp. 218-227). If the fluid media on either side of the middle layer have equivalent properties, the expression for the transmission loss through the middle layer, $TL_{3LayerModel}$, is

$$TL_{3LayerModel} = 10\log_{10}\left[\frac{\left(1-R^2\right)^2}{4R^2}\sin^2\left(kh\right)+1\right], \qquad (7.1)$$

$$R = \frac{\rho_P c_{P\perp}}{\rho c}, \tag{7.2}$$

where ρ_P is the plate density, $c_{P\perp}$ is the speed of sound through the thickness of the plate, ρ is the density of the fluid media on both sides of the plate, and c is the acoustic speed of sound in the fluid media on both sides of the plate. The reason for the plate speed of sound distinction $\perp$ is that some of the plates used in this thesis are orthotropic and therefore have a different speed of sound through their thicknesses than in the plane of the plate. The theoretical, normal incidence transmission loss plots found in Figs. 7.20-7.22 are obtained using appropriate expressions in Eq. (7.1).

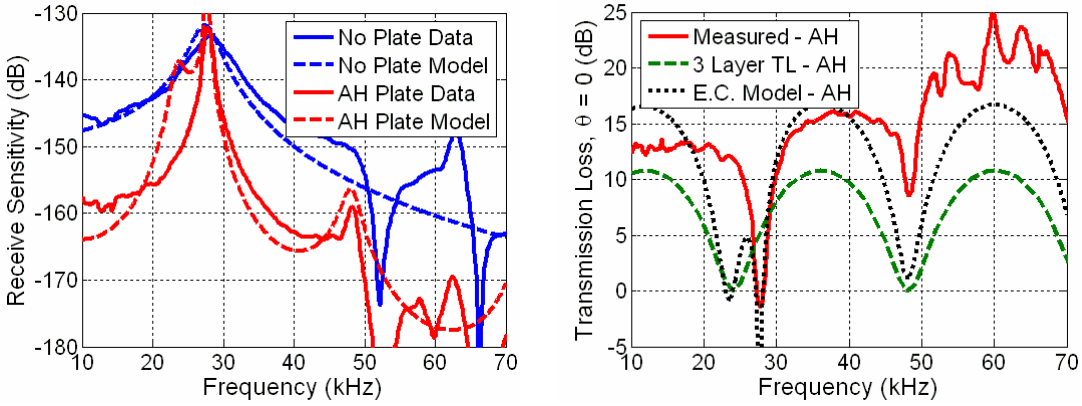

Fig. 7.20. Aluminum honeycomb plate measured and modeled frequency responses for no-plate and with-plate conditions, from the no-plate data and aluminum honeycomb plate data (left subplot). Measured, theoretical, and modeled normal incidence transmission loss plots from the aluminum honeycomb plate data (right subplot). Theory refers to the 3 layer transmission loss model and E. C. Model refers to the equivalent circuit model.

In the case of the aluminum honeycomb, the half wavelength resonances are clearly seen at 27.8 kHz, 48.3 kHz, and 72.0 kHz (though 72 kHz is not shown in Fig. 7.20). One would expect these frequencies to be integer multiples of the first resonance ($f_1 = 27.8kHz$, $f_2 = 2*27.8kHz = 55.6kHz$, and $f_3 = 3*27.8kHz = 83.4kHz$)

but they are in fact inharmonic on the low side. The reason for the inharmonicity (or upward shift in the fundamental frequency) is due to a coupling effect of the plate and the transducer, as the fundamental frequency is in close proximity to the transducer's receive resonance. Instead of using the value for the first null in frequency, the average assumed fundamental frequency from the other two null frequencies may be used as a corrected f_1^*,

$$f_1^* = \frac{\frac{f_2}{2} + \frac{f_3}{3}}{2} = \frac{24.2kHz + 24kHz}{2} = 24.1kHz\,. \tag{7.3}$$

The corrected fundamental half wavelength resonance frequency, f_1^*, suggests a speed of sound, $c_{AH\perp}$, through the thickness, h_{AH}, of the aluminum honeycomb plate to be

$$c_{AH\perp} = \left(2 f_1^*\right)\left(\frac{\lambda_{P\perp}}{2}\right) = 2 f_1 h_{AH} = (48.2kHz)(0.0254m) = 1223\frac{m}{s}. \tag{7.4}$$

The theoretical transmission loss in Fig. 7.20 was obtained using $c_{AH\perp}$ and ρ_{AH} in Eq. (7.1) and Eq. (7.2). The Young's modulus used in the modeled transmission loss in Fig. 7.20 was adjusted to fit the peaks in the measured frequency response ($E = 1.1GPa$). The modeled transmission loss appears to model the measured transmission loss better than the theoretical expression, but does create a null at f_1 not seen in measured data, too wide of a null for the full wavelength null at f_2, and tends to under estimate the loss at higher frequencies. Finally, as Fig. 4.8 points out, the aluminum honeycomb plate does significantly change the quality factor of the frequency response resonance.

The normal incidence transmission loss through the alumina bar should not possess any half wavelength resonances in the displayed frequency range in Fig. 7.21

since alumina is an isotropic material and $f_1 > 100kHz$. The reason for the offset deviation from the theory at all frequencies is unknown, but it appears that the equivalent circuit model does match the shape of the lower frequency transmission loss. Theoretical and modeled transmission loss plots in Fig. 7.21 were obtained using material properties found in Table 3.2.

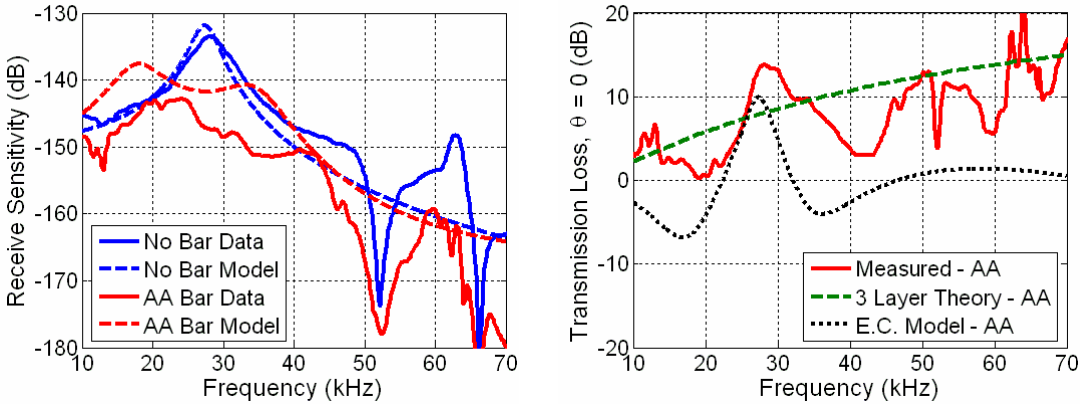

Fig. 7.21. Alumina bar measured and modeled frequency responses for no-bar and with-bar conditions, from the no-bar data and the revisited alumina bar data (left subplot). Measured, theoretical, and modeled normal incidence transmission loss plots from the revisited alumina bar data (right subplot). Theory refers to the 3 layer transmission loss model and E. C. Model refers to the equivalent circuit model.

As noted in Section 6.8.3, the downward shift of 6 kHz in the frequency response resonance frequency is due to the mass loading of the alumina bar on the transducers. Additionally, notice how the roll off down to the frequency response null at 52 kHz has a decreased slope and the null is broader in frequency. There is a second resonance at 42 kHz due to the insertion of the alumina bar which has been shifted down in frequency from the no-bar frequency response "bump" at 48 kHz (another downward 6 kHz shift). This decreased slope led to the large offset difference at 50 kHz between no-bar and

alumina bar patterns and filter shapes. The equivalent circuit model overestimated the downward shift in the first and second resonances.

The pine bar is an orthotropic material. The value for the Young's modulus through the thickness of the R-direction bar is given in the Wood Handbook (41, p. 4-2, Table 4-1, and p. 4-7, Table 4-3a) as $0.663 GPa$. This value yields a lower sound speed through the thickness of the pine bar, than its corresponding longitudinal speed. The resulting sound speed for the R-direction bar is $1166 m/s$. Theoretical and modeled transmission loss plots in Fig. 7.22 are obtained using the Young's modulus and sound speed specified above. The theoretical and modeled transmission loss plots follow the trends found in the measured transmission loss fairly well for the R-direction bar, but additional deviations found in measured data are not modeled by the equivalent circuit.

In general it has been found that the equivalent circuit model does a good job of modeling the normal incidence measured transmission loss for a plate. A further revision of the model could include waveguide circuits for the transducer ceramic stack, a better radiation impedance model, incorporation of impedance loading due to neighboring transducer elements, and better loss models for the compliant layer and in the plate layer.

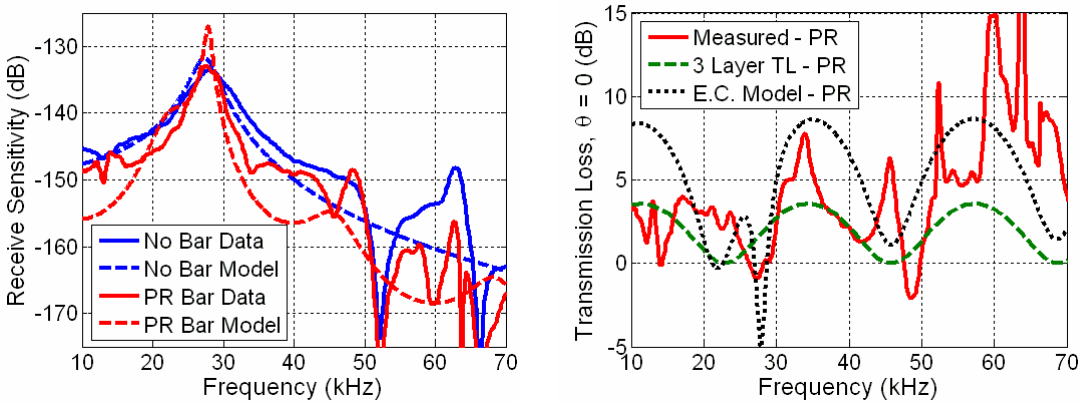

Fig. 7.22. Pine bar measured and modeled frequency responses for no-bar and with-bar conditions, from the no-bar data and R-direction pine bar data (left subplot). Measured, theoretical, and modeled normal incidence transmission loss plots from the R-direction pine bar data (right subplot). Theory refers to the 3 layer transmission loss model and E. C. Model refers to the equivalent circuit model.

7.5 Ideal Plate Material

In Section 3.9 a design discussion was presented which specified material properties which lie simultaneously on the -3 dB pass band transmission loss curve and the -10 dB relative stop band transmission loss curve. One combination of "ideal" material (IM) properties which falls on these lines is a Young's modulus of $E = 100\,\text{GPa}$, and a density of $\rho = 1000\,\text{kg}/\text{m}^3$, with a plate thickness of $h = 0.375\,\text{in}$. To the author's knowledge there is no such isotropic solid material which possesses this combination of material properties. The performance of such a plate material may be predicted using the theory from Chapters 3 and 4. Figures 7.23-7.24 presents normalized theoretical patterns, at the same frequencies and steering conditions as in Section 7.2 , for a no-plate array (from Eq. (2.20) plus Eq. (2.21)) and for a with-plate array (from Eq. (2.20) plus Eq. (2.21) plus Eq. (3.32)) for the ideal plate with properties specified above.

Figures 7.25-7.26 presents theoretical filter shapes for the same frequencies used in Section 7.3 for the ideal plate. Figure 7.27 presents modeled no-plate and with-plate frequency responses and transmission loss plots in the same manner as shown in Section 7.4 for the ideal plate, without measured data.

From the pattern comparisons displayed in Figs. 7.23-7.24, it is apparent that the ideal plate would attenuate grating lobes to near the average side lobe levels. The ideal plate insertion would not impose unreasonably large increases in side lobe levels at the coincidence angles. As desired, the low frequency pattern at 25 kHz is minimally affected by the plate insertion, while grating lobes at higher frequencies are attenuated. The 50 kHz filter shape in Fig. 7.26 shows that for only a 1.8 dB loss in the main lobe, one may obtain up to a 12 dB reduction in side lobes and grating lobes outside of the coincidence angles. A potential design improvement would be to increase the thickness of the plate, thereby decreasing the coincidence angle. A lower coincidence angle would increase the relative stop band transmission loss more than the pass band transmission loss.

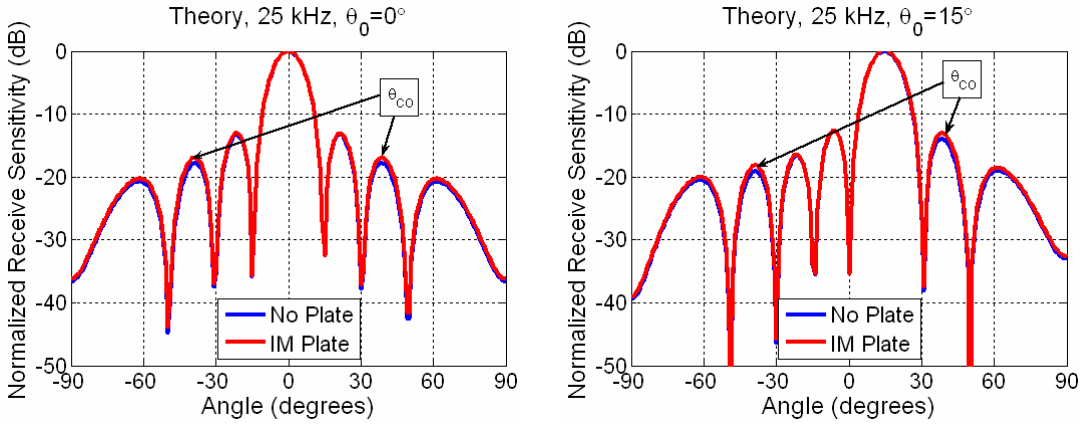

Fig. 7.23. Theoretical, normalized directivity pattern comparison plots comparing no-plate array patterns to with-plate array patterns for the "ideal" plate discussed in Section 7.5 at 25 kHz.

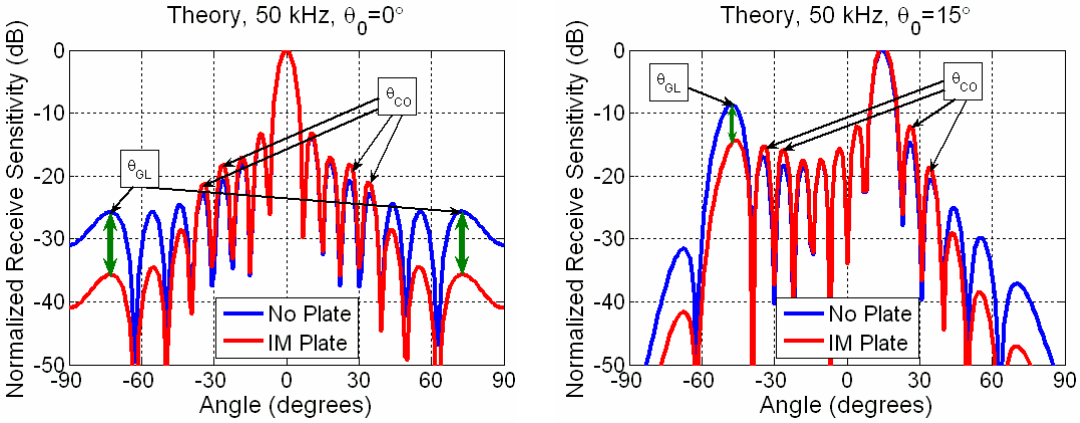

Fig. 7.24. Theoretical, normalized directivity pattern comparison plots comparing no-plate array patterns to with-plate array patterns for the "ideal" plate discussed in Section 7.5 at 50 kHz.

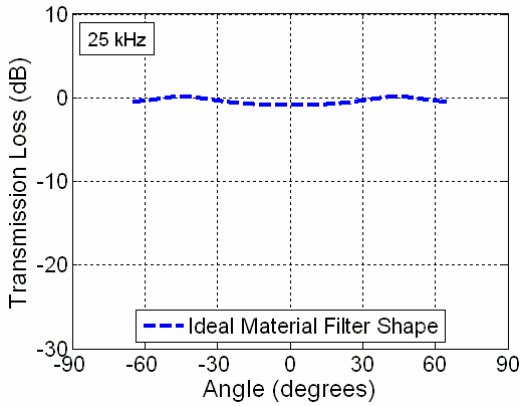

Fig. 7.25. Filter shape at 25 kHz obtained from theory for the "ideal" plate discussed in Section 7.5. The plot is unnormalized to show the normal incidence transmission loss obtained from the equivalent circuit model.

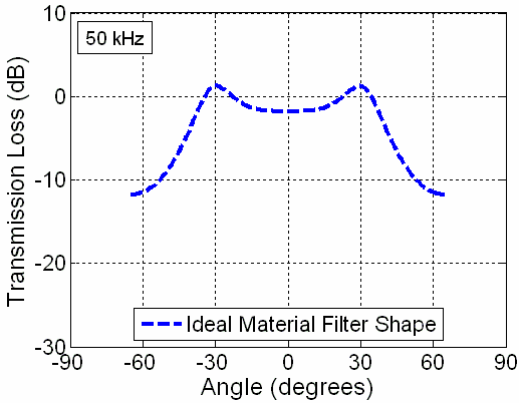

Fig. 7.26. Filter shape at 50 kHz obtained from theory for the "ideal" plate discussed in Section 7.5. The plot is unnormalized to show the normal incidence transmission loss obtained from the equivalent circuit model.

The equivalent circuit frequency response modeling for the ideal material shows that the main lobe would be attenuated by a maximum of 2.6 dB over the entire frequency band displayed in Fig. 7.27. The resonance frequency of the frequency response would not shift in frequency due to the plate insertion, but the quality factor of its resonance would increase somewhat. An increased amount of damping in the compliant layer would tend to decrease the quality factor to the no-plate value.

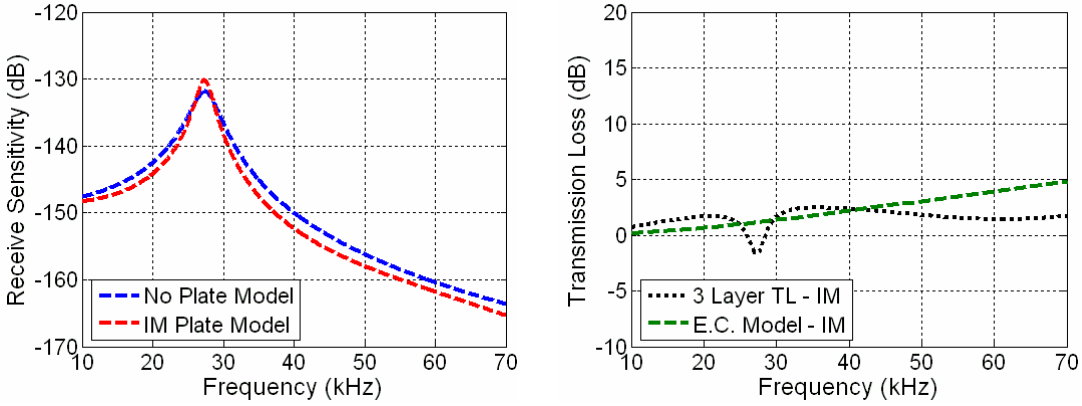

Fig. 7.27. Theoretical frequency responses for no-plate and with-plate arrays, calculated from theory, and equivalent circuit modeling of normal incidence transmission loss for the "ideal" plate discussed in Section 7.5.

7.6 Patterns from No-Bar and No-Plate Data

The presence of ripples in the directivity patterns and filter shapes obtained from the 52-element planar array prompted an investigation in to the stability of the single element directivity patterns obtained without the insertion of a plate or bar. The eight single element directivity patterns obtained from the array elements used in the original round of no-bar measurements using 1-D arrays are displayed in Fig. 7.28, with 25 kHz in the left subplot and 50 kHz in the right subplot. The eight single element directivity patterns from the line array of elements used in the bar measurements, which were obtained from the no-plate 52-element planar array data, are displayed in Fig. 7.29, with 25 kHz in the left subplot and 50 kHz in the right subplot. Visual comparison of Fig. 7.28 and Fig. 7.29 reveals extra ripples in the no-plate directivity patterns when compared to the no-bar directivity patterns. These extra ripples are due to baffle edge conditions as shown by Hughes (43, p. 142, Fig. 6.22) and the presence of other elements which have slightly different resonance frequencies. Inspection of Fig. 7.28 reveals that the single element directivity patterns of elements on opposite ends of the line array mirror each other as expected (particularly note how element 1 mirrors element 8, and element 2 mirrors element 7 in the 25 kHz subplot). This is not the case for the element in the 52-element planar array, however. See Appendix A, Section A.9 for the MATLAB code used to plot single element directivity patterns from experimental data.

To further investigate the quality of the no-bar and no-plate array data, unsteered patterns were generated with various amplitude shading conditions. Figures 7.30-7.31 contain array patterns for the no-bar 8-element line array and the 8-element no-plate line

array (8 of the 52 elements) respectively. Figures 7.30-7.31 each contain an unshaded pattern, a 30 dB amplitude shaded pattern, and a 40 dB amplitude shaded pattern. Inspection of 25 kHz patterns in Figs. 7.30-7.31 yields the conclusion that, for both arrays, the maximum reduction in side lobe levels is nearly 30 dB. When a point-source array is amplitude shaded, the side lobe level is at a flat value, but here it tapers off at large angles due to baffle directivity. One may observe that, in the shaded 25 kHz no-bar 8-element array patterns, the side lobe levels trail off at large angles, while the side lobe levels remain fairly constant for the shaded 25 kHz no-plate 52-element array patterns. The fact that the shaded 25 kHz no-plate array side lobe levels do not trail off at large angles suggest that the elements are mismatched due to array conditions (different element positioning in an array is affected differently by radiation impedance, baffle loading, and edge conditions). Additionally, one may notice the difference in the depth of the nulls on either side of the main lobe in the unshaded 25 kHz patterns in Figs. 7.30-7.31. Deep nulls on each side of the main lobe suggest that elements in an array are matched well. An accurate observation of how deep the nulls are does require that the angular resolution be sufficient to portray the actual level of the nulls. The angular resolution in both the no-plate and no-bar pattern measurements is approximately the same, therefore the shallower nulls in the no-plate 52-element planar array again suggest that the elements are mismatched due to array conditions. The 50 kHz patterns in Figs. 7.30-7.31 both show that amplitude shading is basically ineffective in reducing side lobe levels at high frequencies. If the full 52 elements were used, then better side lobe control would likely be evident.

The extra ripples in the single element patterns from the no-plate 52-element planar array, the constant side lobe levels from shaded no-plate array patterns, and the shallow main lobe nulls in the no-plate array patterns all suggest that the no-plate array does not provide an accurate system to test the filtering characteristics of a plate or bar. Future testing of bars or plates should be done on a different array and the bar or plate should be bonded to elements as outlined in Section 6.4 which discussed the setup for the no-bar 8-element line array.

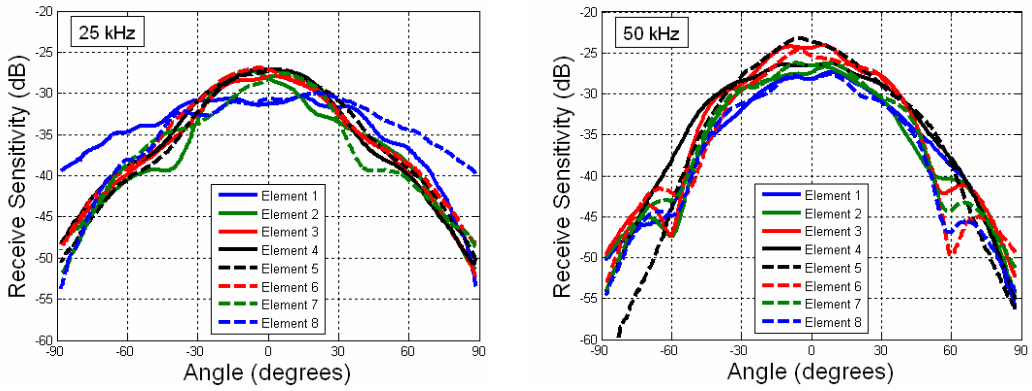

Fig. 7.28. Single element directivity patterns obtained from the 8-element no-bar line array data. The element numbering represents the elements positioning from one side of the array to the other.

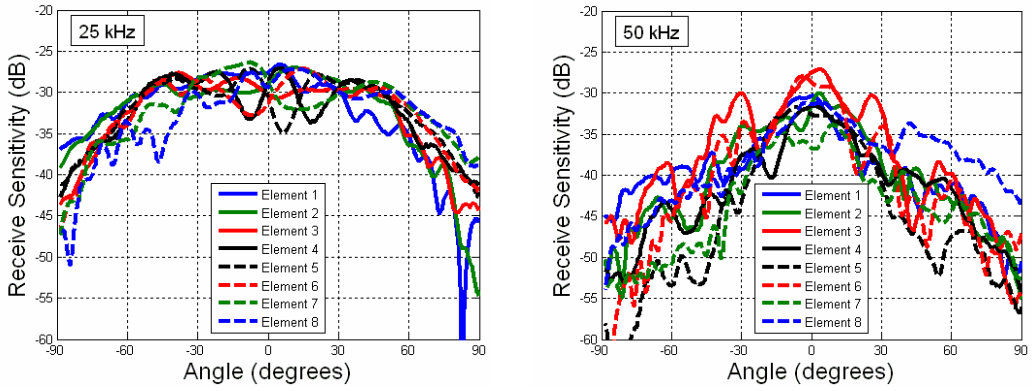

Fig. 7.29. Single element directivity functions obtained from the 8 channels of data used for testing bars on the 52-element no-plate planar array. The element numbering represents the elements positioning from one side of the array to the other.

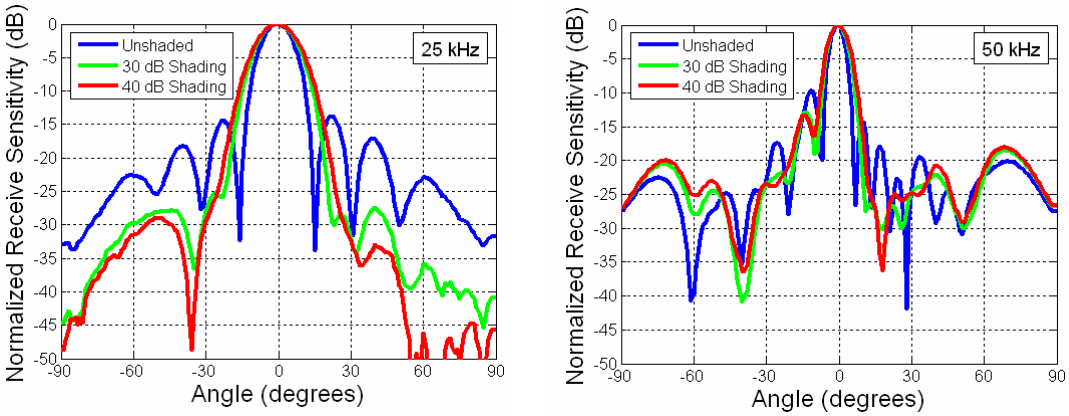

Fig. 7.30. Unsteered array patterns for the no-bar 8-element array in unshaded, 30 dB amplitude shaded, and 40 dB amplitude shaded conditions.

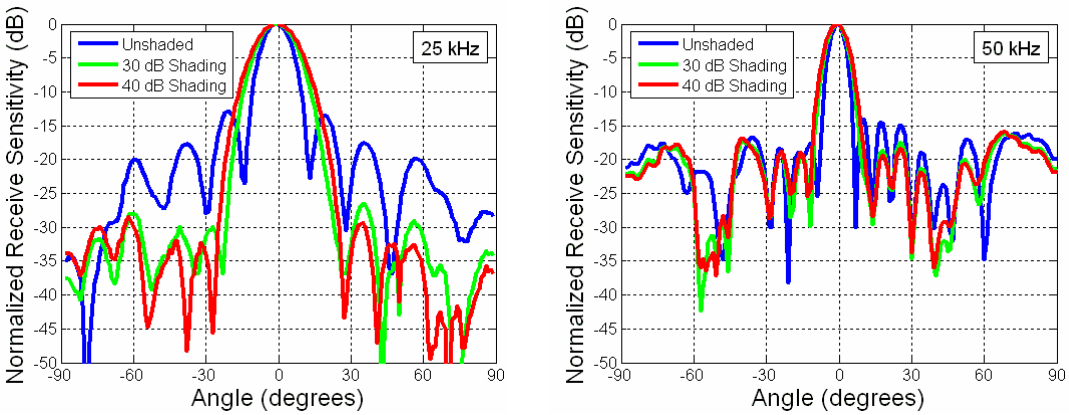

Fig. 7.31. Unsteered array patterns for the 8-element (52-element array) no-plate array in unshaded, 30 dB amplitude shaded, and 40 dB amplitude shaded conditions.

Chapter 8

CONCLUSION AND RECOMMENDATIONS

8.1 Conclusion

To the author's knowledge, this thesis represents the first attempt to advantageously utilize a plate to provide angular dependent sound transmission filtering of array patterns above the plate's critical frequency (the supercritical frequency region). This thesis reviews line array theory and structural acoustics theory. Plate design is discussed in great detail. Results are given to show the angular dependence of supercritical plate filtering (filter shape comparisons in Section 7.3), and the amplitude dependence of supercritical plate filtering (frequency response transmission loss comparisons in Section 7.4). The theoretical angular dependence of supercritical plate filtering does match experimental data well especially when an isotropic plate is used and is bonded to transducer elements correctly (the original alumina bar setup). In addition to reducing grating lobes, the relative stop band transmission loss serves to increase the pattern directivity and suppress levels at large angles where flow noise can be problematic. The frequency response modeling of supercritical plate filtering does show general trends and does a fairly good job of matching experimental data. The modeling also confirms the "good" material property region found in Fig. 4.8 where the aluminum honeycomb would significantly increase the frequency response quality factor, while other materials noted in the figure do not.

Table 8.1 tabulates values for coincidence angles, relative and absolute (or total) pass band transmission losses, and relative and absolute (or total) stop band transmission losses, from theoretically obtained filter shapes and experimentally obtained filter shapes from Figs. 7.12-7.19. Coincidence angles were obtained from the theoretical filter shape peak and from the average of the two angles from measured filter shapes, when a coincidence angle was apparent. Relative (Rel) pass band transmission losses were determined from normalized filter shapes (the right hand normal incidence transmission loss plots). Absolute (Abs) pass band transmission losses were determined from unnormalized filter shapes (the left hand normal incidence transmission loss plots). Relative stop band transmission losses were determined from the normalized filter shapes (the average transmission loss at large angles, relative to the pass band level, in the right hand plots). Absolute stop band transmission losses were determined from the unnormalized filter shapes (the average transmission loss at large angles in the left hand plots). The relative pass band transmission loss values for theory and experiment should be about the same since they were normalized to be nearly equal. The important theory and experiment values to compare are the absolute pass band transmission loss values and the relative stop band transmission loss values. The absolute pass band transmission losses indicate the agreement of the equivalent circuit modeling. The relative stop band transmission losses give an indication of how well the experiment filter shape roll off compared to the roll-off for theoretical filter shapes.

This thesis has shown that while grating lobe levels can be significantly reduced, a practical material has yet to be found for the specific array configuration used. None of the physical materials tested in this thesis provided optimal results from a practical

standpoint, but the physics behind this technique has provided compelling evidence that this technique will succeed in reducing grating lobe levels when a plate is developed which possesses material properties similar to those discussed in Section 7.5.

Table 8.1. Filter performance metrics for theoretical/modeled structural angular filters and the corresponding experimentally measured structural angular filters at 25 and 50 kHz. Question marks indicate that no coincidence angle could be easily determined. Rel and Abs refer to relative and absolute (or total) values. All values were obtained from the filter shape plots contained in Section 7.3.

Material	Frequency (kHz)	Coincidence Angle (degrees)		Pass Band Transmission Loss (dB)				Stop Band Transmission Loss (dB)			
		Theory	Experiment	Theory		Experiment		Theory		Experiment	
				Rel	Abs	Rel	Abs	Rel	Abs	Rel	Abs
Alumina Bar (Bonded Bar)	25	43.8	45	7	6	5	6	-1	4	11	17
Aluminum Honeycomb Plate	25	39.4	?	0	3	0	11	0	3	7	17
Pine Bar (R-direction)	25	41.7	?	2	3	2	2	2	3	2	2
Alumina Bar (Bonded Bar)	50	29.3	32	13	1	13	19	13	14	11	30
Aluminum Honeycomb Plate	50	27.3	30	1	6	1	15	11	16	10	23
Pine Bar (R-direction)	50	25.6	40	4	5	4	2	17	18	13	10

It has been shown that sound energy can pass through a plate (or that sound radiation can be steered through a plate) without refraction of the direction of the steered energy. The absense of refraction due to plate insertion means that experimental results confirm the validity of the assumption made that refraction may be ignored in Fahy's derivation for the angular dependence of sound transmission through a plate (see Section 3.5).

Use of a plate as an angular filter does restrict steering between the positive and negative coincidence angles. The presence of the plate causes an insertion loss of the main lobe level, which is highly dependent on the mass per unit area of the plate.

Selection of a plate for directivity pattern filtering involves a number of considerations including mass-law insertion loss, a high Young's modulus requirement and low density, practical considerations of plate thickness, and plate mounting considerations. Although not conclusively proven, results suggest that the plate must be made of an isotropic material.

The experiments conducted in this thesis for the bonded alumina bar provided better agreement with theory than the results from the alumina bar which was held onto the 2-D array by surface tension and tape was used to hold it vertically in place. Therefore the plate should be bonded to the transducer elements, with a thin compliant layer between the plate and transducers, for consistent performance at large angles (relative to normal incidence).

8.2 Recommendations for Future Work

Research conducted for this thesis brought many ideas to the author's mind and his advisor's mind for future work. These ideas are listed below in bullet form.

- Further refine the equivalent circuit modeling to include waveguide circuits for the transducer ceramic stack, a better radiation impedance model, incorporation of impedance loading due to neighboring transducer elements, incorporation of damping in the plate, and physically justified loss models for the compliant layer and the plate layer.
- It may be worth mounting anisotropic or orthotropic plates and bars to determine whether an isotropic material is required for agreement with theory or whether the

2-D 52-element array used in measurements is to blame for the lack of agreement with theory (see Section 7.6).

- One very expensive, isotropic material that has material properties which are closer to optimal than alumina is an aluminum beryllium composite called AlBeMet. AlBeMet's material properties are approximately $E = 193$ GPa, $\rho_P = 2071$ kg/m³, and $\sigma = 0.17$. An AlBeMet plate would require an approximate thickness of about 0.375 inches, which would impose a pass band transmission loss, TL_{PB}, of about 7 dB and a relative stop band transmission loss, TL_{RSB}, of about 12 dB. It may be possible to create an even better composite material with materials such as magnesium and beryllium since magnesium ($\rho_P = 1740$ kg/m³) is much less dense than aluminum ($\rho_P = 2700$ kg/m³). It may be possible to form a honeycomb by drilling holes in the plate and putting face sheet plates on it.
- The plates used in this thesis were designed to impose a significant amount of relative stop band transmission loss due to each plate's high bending stiffness (which depends on Young's modulus and plate thickness). It is possible that there exists a limit in the slope of the bending controlled portion of Fahy's filtering equation, Eq. (3.32), see (30, p. 151, Eq. (4.38a)). One could attempt to find a possible mechanism which would impose a theoretical limit.
- Although not investigated in this thesis work, it is possible that use of the technique presented in this thesis may prove to be a practical method of reducing grating lobes in ultrasound arrays. At one point ANSYS models were computed

at ultrasound frequencies with the thickness of the plate reduced by the same multiplication factor as the increase in frequency multiplication factor and the resulting directivity pattern was equivalent to the original low frequency results.

- An additional research area this technique may be useful is that of audio arrays in air. An attempt was made to determine what type of "plate" would be required for this application. It was determined that there may not be a material which would be practical, the closest "plate" material being plastics. However, an idea was given by an associate, Dave Van Tol, to put plates under tension and thus create a higher bending stiffness.
- The theory discussed in Chapter 3 may be useful in predicting the feasibility of using a transducer array to "listen" through a wall, or "see" into a structure through its walls.
- Investigate the reason for the variation in the level increase seen at the coincidence angles relative to what theory predicts. Appendix F shows that only a couple measured filter shapes (50, 65, and 70 kHz) match the theoretical filter shapes in coincidence angle height. The reason for this agreement at some frequencies and not at others is unknown, but suggests that the plate damping, or compliant layer losses, vary with frequency. This would imply that there is virtually no damping ($\eta \approx 0$) at 50, 60 and 70 kHz, but a significant amount of damping at the other frequencies ($\eta \approx 0.5$).
- Investigate the possibility of creating higher impedance source transducers to simulate the constant displacement drive inputs required to eliminate the increases

in side lobe levels at the coincidence angles, as discussed in Chapter 5. One potential higher impedance transducer could be achieved with exponential, quarter-wavelength head masses so that the mechanical impedance is increased due to the same force applied over a decreased area, as is commonly done in ultrasonic drill designs.

Bibliography

1 V. M. Albers, *Underwater Acoustics Handbook* – II, The Pennsylvania State University Press, 1965.

2 D. Stansfield, *Underwater Electroacoustic Transducers*, Peninsula Publishing, 1991.

3 D. T. Blackstock, *Fundamentals of Physical Acoustics*, John Wiley & Sons, Inc., 2000.

4 O. T. von Ramm, S. W. Smith, and F. L. Thurstone, "Grey scale imaging with complex TGC and transducer arrays," Proc. Soc. Photo-opt Inst. Engineers, Medicine IV, vol. 70, pp. 266-270, 1975.

5. S. W. Smith, H. G. Pavey, and O.T. von Ramm, "High speed ultrasound volumetric imaging system – Part 1: Transducer design and beam steering," IEEE Trans. Ultrasonics, Ferroelec., Freq. Contr., vol. 38, pp. 100-108, 1991.

6. G. R. Lockwood, and F. S. Foster, "Optimizing sparse two-dimensional transducer arrays using an effective aperture approach," Proc. IEEE Ultrasonics Symp., vol. 3, pp. 1497-1501, 1994.

7. E. B. Hutchinson, M. T. Buchanan, and K. Hynynen, "Evaluation of an aperiodic phased array for prostate thermal therapies," Proc. IEEE Ultrasonics Symp., vol. 2, pp. 1601-1604, 1995.

8. W. J. Zehner, "SONAR Array with Reduced Grating Lobes," U. S. Patent 5,414,676, (1995).

9. G. R. Lockwood, P. Li, M. O'Donnell, and F. S. Foster, "Optimizing the radiation pattern of sparse periodic linear arrays," IEEE Trans. Ultrasonics, Ferroelec., and Freq. Contr., vol. 43, pp. 7-14, 1996.

10. E. B. Hutchinson, and K. Hynyen, "Intracavitary ultrasound phased arrays for noninvasive prostate surgery," IEEE Trans. Ultrasonics, Ferroelec., and Freq. Contr, vol.43, pp. 1032-1042, 1996.

11. S. A. Goss, L. A. Frizzell, J. T. Kouzmanoff, J. M. Barich, and J. M. Yang, "Sparse random ultrasound phased array for focal surgery," IEEE Trans. Ultrasonics, Ferroelec., and Freq. Contr, vol. 43, pp. 1111-1121, 1996.

12. L. R. Gavrilov, J. W. Hand, P. Abel, and C. A. Cain, “A Method of Reducing Grating Lobes Associated with an Ultrasound Linear Phased Array Intended for Transrectal Thermotherapy,” IEEE Transactions on Ultrasonics, Ferroelec., and Freq. Contr., vol. 44, pp. 1010-1017, (1997, no. 5).

13. S. D. Sokka, R. L. King, N. J. McDonald, and K. H. Hynynen, “Design and evaluation of linear intracavitary ultrasound phased array for MRI-guided prostate ablative therapies,” Proc. IEEE Ultrasonics Symp., vol. 2, pp. 1435-1438, 1999.

14. A. Trucco, “Aperture and element minimization in linear sparse arrays with desired beam patterns,” Ultrasonics, vol. 38, pp. 161-165, Mar. 2000.

15. G. T. Silva, and M. Fatemi, “Linear array transducers for vibro-acoustography,” Proc. IEEE Ultrasonics, Symp., vol. 1, pp. 629-632, 2002.

16. Y. Liu, and Z. Lin, “Active array beamforming using the frequency-response masking technique,” Proc. IEEE Internat. Symp. Cir. Syst., vol. 3, pp. 197-200, 2004.

17. O. Martinez, G. Godoy, M. A. G. Izquierdo, and L. G. Ullate, “Application of vernier thinning techniques to segmented annular arrays,” J. Ultrasonics, vol. 42, pp. 977-982, 2004.

18. S. Umemura, and C. A. Cain, “Acoustical evaluation of a prototype sector-vortex phased-array applicator,” IEEE Trans. Ultrasonics, Ferroelec., and Freq. Contr., vol. 39, pp. 32-38, 1992.

19. O. Martinez, L. G. Ullate, M. A. G. Izquierdo, and T. Sanchez, “Incidence of element distribution on the ultrasonic field of segmented annular arrays,” Ultrasonics, vol. 38, pp. 176-178, 2000.

20. O. Martinez, L. G. Ullate, and A. Ibanez, “Comparison of CW patterns from segmented annular arrays and squared arrays,” Sensors and Actuat., A: Physical, vol. 85, pp. 33-37, 2000.

21. K. A. Snook, T. A. Ritter, T. R. Shrout, K. K. Shung, “Design of a high frequency annular array for medical ultrasound,” Proc. IEEE Ultrasonics Symp., vol. 2, pp. 1161-1164, 2001.

22. O. Martinez, M. Akhnak, L. G. Ullate, and F. Montero de Espinosa, “A small 2D ultrasonic array for NDT applications,” NDT and E. Internat., vol. 36, pp. 57-63, 2003.

23. B. P. Hildebrand and G. J. Posakony, “Method and Apparatus for Energizing an Array of Acoustic Transducers to Eliminate Grating Lobes,” U. S. Patent 4,179,683, (1979).

24. J. R. Talman, and G. R. Lockwood, “Theoretical evaluation of a 50 MHz split aperture linear phased array,” Proc. IEEE Ultrasonics Symp., vol. 2, pp. 1675-1678, 1997.

25. F. J. Pompei, and S. C. Wooh, “Phased array element shapes for suppressing grating lobes,” J. Acoust. Soc. Am., vol. 111, pp. 2040-2048, (2002 no. 5).

26. F. Dupenloup, J. Y. Chapelon, D. Cathignol, and O. Sapozhnikov, “The Use of Broadband Signals to Reduce Grating Lobe Effects in HIFU Tissue Ablation,” IEEE Ultrasonics Symposium, pp. 1865-1868, 1994.

27. J. Y. Chapelon, F. Dupenloup, H. Cohen, and P. Lenz, “Reduction of Cavitation Using Pseudorandom Signals,” IEEE Transactions on Ultrasonics, Ferroelectrics, and Frequency Control, vol. 43, pp. 623-625, (1996, no. 4).

28. F. Dupenloup, J. Y. Chapelon, D. J. Cathignol, and O. A. Sapozhnikov, “Reduction of the Grating Lobes of Annular Arrays Used in Focused Ultrasound Surgery,” IEEE Transactions on Ultrasonics, Ferroelectrics, and Frequency Control, vol. 43, pp. 991-998, (1996, no. 6).

29. A. Bouakaz, C. T. Lancee, P. J. A. Frinking, and N. de Jong, “Simulations and measurements of nonlinear pressure field generated by linear array transducers,” Proc. IEEE Ultrasonics Symp., vol. 2, pp. 1511-1514, 1999.

30. F. Fahy, *Sound and Structural Vibration, Radiation, Transmission and Response 5th Edition*, (Academic Press Limited, Great Britain, 1985).

31. F. Hutto, “Wave Number-Frequency Response of Free-Free Timoshenko Beams with Multiple Sources,” Penn State University Master’s Thesis in Acoustics, May 1986.

32. K. Grosh, “An Experimental System for Measuring the Wave Number-Frequency Response of Timoshenko Beams,” Penn State University Master’s Thesis in Engineering Science, December 1988.

33. J. Phillips, “The Wave Number-Frequency Filtering Characteristics of Compliant Layers,” Penn State University Master’s Thesis in Acoustics, December 1989.

34. L. E. Kinsler, A. R. Frey, A. B. Coppens, J. V. Sanders, *Fundamentals of Acoustics, Fourth Edition*, (John Wiley & Sons, Inc., 2000).

35. C. L. Dolph, “A Current Distribution of Broadside Arrays Which Optimizes the Relationship Between Beam Width and Side-Lobe Level,” Proceedings of the Institute of Radio Engineers, June 1946, pp. 335-348.

36. W. Thompson Jr., *Acoustics 514 "Transducers" Course Notes*, Graduate Program in Acoustics.

37. L. L. Beranek, *Acoustics*, McGraw-Hill, 1954, and Acoustical Society of America, 1986.

38. F. Fahy, *Foundations of Engineering Acoustics*, Academic Press, 2001.

39. M. Ashby, *Materials Selection in Mechanical Design, 3rd Edition*, Butterworth-Heinemann, 2005.

40. D. Ross, *Mechanics of Underwater Noise*, Peninsula Publishing, 1987.

41. Forest Products Laboratory, USDA Forest Service, *Wood Handbook, Wood As An Engineering Material*, Forest Products Laboratory, 1999.

42. C. B. Officer, *Introduction to the Theory of Sound Transmission*, McGraw Hill, Inc., New York, 1958.

43. W. J. Hughes, "Diffraction Effects of Baffles on Acoustic Directivity Patterns," Penn State University Doctoral Thesis in Acoustics, April 1978.

44. C. H. Walter, *Traveling Wave Antennas*, McGraw-Hill, 1965.

Appendix A

MATLAB CODE

This appendix contains various MATLAB m-files which were used in this thesis. The m-file lines of code are given in the format in which they were used.

A.1 Array Directivity Pattern

```
function [b,theta]=array(N,f,a,d,theta0,c,Ashade)

theta=-90:90;
phi=pi/180*theta+.001;
phi0=pi/180*theta0;

k=2*pi*f/c;

[SED]=sed(f,a,c,theta);

if Ashade==0
    H=abs(1/N*(sin(N/2*k*d*(sin(phi)-
        sin(phi0)))./(sin(.5*k*d*(sin(phi)-sin(phi0)))));
    b=20*log10(abs(H))+SED;b=b-b(91+theta0);
end

if Ashade~=0
    A=shadingcoeffs(N,Ashade);
    n=1:N;
    ps=zeros(length(phi),N);
    L=(7*d+a)*.0254;
    for i=1:length(phi)
        ps(i,:)=A.*exp(j*(k*d*n*sin(phi(i))-k*d*n*sin(phi0)));
        p(i)=abs(sum(ps(i,:)));
    end
    b=20*log10(p)-max(20*log10(p))+SED;
end
```

A.2 Single Element Directivity Pattern

```
function [SED]=sed(f,a,c,theta)

k=2*pi*f/c;
v=1/2*k*a*sin(theta*pi/180);
H=abs((sin(v))./(v));
SED=20*log10(H);
i=1;
while theta(i)~=0
    i=i+1;
end
if theta(i)==0
    SED(i)=0;
end
```

A.3 Amplitude Shading

```
%[A]=shadingcoeffs(N,Latten)
%
%This function calculates the normalized shading coefficients for an
%array with an even number of total elements.  The user must supply
%N and Latten, which are the total number of elements (EVEN NUMBER
%ONLY) and the desired minor lobe attenuation level respectively.
%
%Please note that a higher Latten results in a wider main beam
bandwidth.
%
%The coefficients are based off of the Dolph-Tschebyscheff method of
%shading arrays.  An explanation of this method, along with an example
%of it, may be found in Vernon M. Albers book the Underwater Acoustics
%Handbook II, The Pennsylvania State University Press, 1965, pp. 188-
199.
%This function was written by Brian E. Anderson.

function [A]=shadingcoeffs(N,Latten)

%20*log10(r)=Latten
r=10^(Latten/20);
n=N-1;
xo=.5*((r+sqrt(r^2-1))^(1/n)+(1/(r+sqrt(r^2-1)))^(1/n));
A=ones(1,N/2);
v=ones(1,N/2);
v(N/2)=n;
for i=N/2-1:-1:1
    v(i)=v(i+1)-2;
end
T=zeros(length(v),length(v));
for i=1:length(v)
    for ii=1:i
```

```
        T(i,ii)=v(i)/2*(-1)^(ii-1)*factorial(v(i)-(ii-1)-
1)/factorial(ii-1)/factorial(v(i)-2*(ii-1))*2^(v(i)-2*(ii-1));
    end
end
temp=T;
T=zeros(length(v),length(v));
for i=1:length(v)
    indexarray=find(temp(i,:));
    nn=1;
    for ii=length(v)-indexarray(max(size(indexarray)))+1:length(v)
        T(i,ii)=temp(i,indexarray(nn));nn=nn+1;
    end
end
Tn=T(length(v),:);
A(N/2)=xo^v(length(v));
for i=length(v)-1:-1:1
    temp2=0;
    for ii=1:length(v)-i
        temp=-T(length(v)-ii+1,length(v)-i+1)*A(length(v)-
ii+1)/T(i,length(v)-i+1);
        temp2=temp2+temp;
    end
    A(i)=temp2+Tn(length(v)-i+1)*xo^v(i)/T(i,length(v)-i+1);
end
temp=A./A(1);
clear A
for i=1:length(temp)
    A(i)=temp(length(temp)-i+1);
end
A(length(temp)+1:2*length(temp))=temp;
```

A.4 Directivity pattern Surface Plots

```
c=1500;
a=1.148*.0254;
d=1.164*.0254;
N=8;
iscomplex=0;
Ashade=0;

f=10000:5000:70000;
theta0=-90:90;
for ii=1:length(f)
    for i=1:length(theta0)
        [b,theta]=array(N,f(ii),a,d,theta0(i),c,Ashade,iscomplex);
        M(i,:)=b;
        i
    end

    for io=1:length(M)
        for iio=1:length(M)
```

```
            if M(io,iio)<-40
                M(io,iio)=-40;
            end
            if M(io,iio)>0
                M(io,iio)=0;
            end
        end
    end

    figure(2*ii-1)
    surf(theta0,theta0,M')
    axis([-90 90 -90 90 -40 0]);axis square
    shading interp
    xlabel('Steer Angle','fontsize',18)
    ylabel('Receive Angle','fontsize',18)
    hold on;plot3([-f(ii)*1000*2*pi/1500 f(ii)*1000*2*pi/1500],[-
f(ii)*1000*2*pi/1500 f(ii)*1000*2*pi/1500],[0 0],'k--','linewidth',3)
    view(0,90)
    set(gca,'xtick',[-90 -60 -30 0 30 60 90])
    set(gca,'ytick',[-90 -60 -30 0 30 60 90])
    titlestring=['Angle Plot @ ',num2str(f(ii)/1000),' kHz'];
    title(titlestring,'fontsize',18)
    caxis([-40.5 0.5])
    colorbar


    figure(2*ii)

surf(2*pi*f(ii)/1500*sin(pi/180*theta0),2*pi*f(ii)/1500*sin(pi/180*thet
a0),M')
    axis([-f(ii)*2*pi/1500 f(ii)*2*pi/1500 -f(ii)*2*pi/1500
f(ii)*2*pi/1500 -40 0]);axis square
    shading interp
    xlabel('Driven Wavenumber','fontsize',18)
    ylabel('Receive Wavenumber','fontsize',18)
    hold on;plot3([-f(ii)*1000*2*pi/1500 f(ii)*1000*2*pi/1500],[-
f(ii)*1000*2*pi/1500 f(ii)*1000*2*pi/1500],[0 0],'k--','linewidth',3)
    view(0,90)
    titlestring=['Wavenumber Plot @ ',num2str(f(ii)/1000),' kHz'];
    title(titlestring,'fontsize',18)
    caxis([-40.5 0.5])
    colorbar
end
```

A.5 Unbounded Plate Filter Shape

```
sigma=.3;
rho=3956;
E=391e9;
h=.4*.0254;
eta=0;
```

```
D=E*h^3/(12*(1-sigma^2));
m=rho*h;
w=2*pi*25000;
k=w/1500;
phi=-90:90;
tau=(2*1000*1500*sec(phi*pi/180)).^2./...
    ((2*1000*1500*sec(phi*pi/180)...
    +D./w*eta.*k.^4*(sin(phi*pi/180)).^4).^2+...
    (w*m-D./w.*k.^4*(sin(phi*pi/180)).^4).^2);
T=10*log10(tau);
figure
plot(phi,T)
```

A.6 Plate Design Plots

```
clear
rho=logspace(-1,2,100); %g/cm^3
E=logspace(0,3,100); %GPa
sigma=0.30; %assumed Poisson Ratio
FilterAngle=30;
cb=1500/sin(FilterAngle*pi/180); %chosen bending wave speed so that
thetaCO=30deg
f=25000;w=2*pi*f;k=w/1500; %freq. at which cb was chosen
constant=12*(1-sigma^2)*(cb/sqrt(w))^4;

rhom=980;
cm=1619;
Lm=0.06*.0254;
r=3.16;
for i=1:length(E)
    h(i,:)=sqrt(rho*1000./E(i)/1e9)*sqrt(constant);
    TL(i,:)=10*log10(1+(w*rho*1000.*h(i,:)/(2*1000*1500)).^2);

TF(i,:)=10*log10(h(i,:).*sqrt(1e9*E(i)./rho/1000)*w/(sqrt(3)*1500^2));
%     h=.0254;
    D=E(i)*1e9*h(i,:).^3/(12*(1-sigma^2));
    m=rho.*h(i,:);
    phi=-90:90;
    for ii=1:length(rho)
        tau=(2*1000*1500*sec(phi*pi/180)).^2./...
            ((2*1000*1500*sec(phi*pi/180)).^2+...
            (w*m(ii)-D(ii)./w.*k.^4*(sin(phi*pi/180)).^4).^2);
        T=10*log10(tau);
        TFilter(i,ii)=-min(T)-TL(i,ii);
    end

    for iii=1:length(rho)
    Lp=h(i,iii);
    Ep=E(i)*1e9;
    rhop=rho(iii)*1000;
    S=1.168^2*.0254^2;
```

```
C0=1209e-12;
C1=391e-12;
L1=.113;
R1=55.9;
phi=.7;
fa=100:100:100000;
wa=2*pi*fa;
km=wa/cm;
cp=sqrt(Ep/rhop);
kp=wa/cp;
Z0=phi^2./(j*wa*C0);
Z1=phi^2*(1./(j*wa*C1)+j*wa*L1+R1);
Z2=j*rhom*cm*S*tan(km*Lm/2);
Z3=-j*rhom*cm*S*csc(km*Lm)+5000;
Z4=j*rhop*cp.*S*tan(kp*Lp/2);
Z5=-j*rhop*cp.*S*csc(kp*Lp);
Za=1000*1500*S;
Zz=Z4+Z5+Za;
Zy=Z2+Z3+Z4+Z5;
Zx=Z0+Z1+Z2+Z3;
Zm=Zx-Z0;
Zn=Zy-Z3.^2./(Zx-Z0);
Zk=Zy-Z5.^2./Zz;
Zl=Zx-Z3.^2./Zk;
Z6=Z0+Z1+Z2;
Z7=Z3.*Z6./(Z3+Z6);
Z8=Z4+Z2+Z7;
Z9=Z5.*Z8./(Z5+Z8);
Ztwp=Za+Z4+Z9;
Ztwo=Za+Z0+Z1;
Vwor=Z0./(Z0+Z1+Za);
Vwpr=Z0.*Z3.*Z5./(Zz.*Zk.*Zl);
pwor=sqrt(1000*1500*real(Za))/(sqrt(4*pi)*r).*abs(Vwor);
pwpr=sqrt(1000*1500*real(Za))/(sqrt(4*pi)*r).*abs(Vwpr);
Pwor=20*log10(abs(pwor));
Pwpr=20*log10(abs(pwpr));
APD(i,iii)=mean(Pwor-Pwpr);
[a,b]=max(Pwor);
fwor=fa(b);
ii=b;
while a-6<=Pwor(ii)
    ii=ii+1;
end
fwopr=fa(ii);
ii=b;
while a-6<=Pwor(ii)
    ii=ii-1;
end
fwomr=fa(ii);
Qwor=fwor/(fwopr-fwomr);
[a,b]=max(Pwpr);
fwpr=fa(b);
ii=b;
while a-6<=Pwpr(ii)
    ii=ii+1;
```

```
    end
    fwppr=fa(ii);
    ii=b;
    while ii~=1 & a-6<=Pwpr(ii)
        ii=ii-1;
    end
    fwpmr=fa(ii);
    Qwpr=fwpr/(fwppr-fwpmr);
    Qdiff(i,iii)=Qwpr-Qwor;
    %figure;plot(fa/1000,Pwor-135.6,fa/1000,Pwpr-135.6-TF(i,iii));pause
    end
end

figure
contour(rho,E,log10(h/.0254),[-1.204 -.903 -.602 -.301 0 .301
.602],'LineWidth',3);
set(gca,'XScale','log','YScale','log')
xlabel('Density (g/cm^3)','fontsize',18)
ylabel('Young''s Modulus (GPa)','fontsize',18)
title('Required Thickness for Optimum Plate Design','fontsize',18)
axis square
grid on
set(gca,'xticklabel',[0.1 1.0 10 100])
set(gca,'yticklabel',[1 10 100 1000])

figure
contour(rho,E,TL,[1 3 5 10 15 20 25 30],'LineWidth',3);
xlabel('Density (g/cm^3)','fontsize',18)
ylabel('Young''s Modulus (GPa)','fontsize',18)
title('Resulting Mass-Law TL for Optimum Plate Design','fontsize',18)
set(gca,'XScale','log','YScale','log')
axis square
grid on
set(gca,'xticklabel',[0.1 1.0 10 100])
set(gca,'yticklabel',[1 10 100 1000])

figure
contour(rho,E,TFilter,[10 15 18]);view(0,90);colorbar
xlabel('Density (g/cm^3)','fontsize',18)
ylabel('Young''s Modulus (GPa)','fontsize',18)
title('Resulting Relative Filter Reduction','fontsize',18)
set(gca,'XScale','log','YScale','log')
axis square
grid on
set(gca,'xticklabel',[0.1 1.0 10 100])
set(gca,'yticklabel',[1 10 100 1000])

figure
contour(rho,E,Qdiff,[1 2 3 4 5 10 15
20],'linewidth',3);%view(0,90);caxis([0,50]);colorbar;
xlabel('Density (g/cm^3)','fontsize',18)
ylabel('Young''s Modulus (GPa)','fontsize',18)
title('Difference in Q,  (Qwp-Qwo)','fontsize',18)
set(gca,'XScale','log','YScale','log')
axis square
```

```
grid on
set(gca,'xticklabel',[0.1 1.0 10 100])
set(gca,'yticklabel',[1 10 100 1000])
```

A.7 ANSYS Results Processing Code

```
%This file processes data from the ANSYS runs.  The following files
must be
%in the run folder - postout.csv and Run200-Imag_disp.txt

%This file is called from the MATLAB command window with a sequence of
%commands such as these:
%runs=[run#'s seperated by spaces or commas];
%for iii=1:length(runs)
%    FEAprocessing
%end

%Current run number output
run=runs(iii)

%Opens appropriate folder for data
foldername=['Run',num2str(run)];
pathname=['Z:\PhDResearch\Numerical\',foldername];
cd(pathname)

%Reads in data file
%node#    x-position    real(uy)    imag(uy)
M=csvread('postout.csv');
node=M(:,1);
xtemp=M(:,2);
uy=M(:,3)+j*M(:,4);

%Reads in the frequency
[junk,f,junk2,junk3,junk4]=textread('Run200-
Imagi_disp.txt','%s%n%s%s%n',1,'headerlines',14);

%Sorts the x-position values of xtemp in order to determine the correct
%node numbering order
x=sort(xtemp);
for i=1:length(node)
    for ii=1:length(node)
        if x(i)==xtemp(ii)
            correctorder(i)=ii;
        end
    end
end
correctorder=correctorder;

%Reordering uy according to the correct order
for i=1:length(node)
    uyr(i)=real(uy(correctorder(i)));
```

```
    uyx(i)=imag(uy(correctorder(i)));
end
uy=uyr'+j*uyx';
uy=uy*j*2*pi*f;  %uy is now a velocity

c=1500; %speed of sound in water
k=2*pi*f/c;  %wavenumber

theta=0:180;
Ttheta=theta-90;

rff=5;  %farfield distance

%Computation of the farfield pressure
for n=1:length(theta)
    p(n)=sum((uy.*exp(-j*k*sqrt(rff^2+x.^2-
2*rff*x*cos(theta(n)*pi/180)))).*(2*pi*sqrt(rff^2+x.^2-
2*rff*x*cos(theta(n)*pi/180))));
end

%Computes the beam pattern
b=20*log10(abs(p)/max(abs(p(91:181))));

figure;
plot(Ttheta,b,'r-','linewidth',3);
ylabel('Farfield Directivity (dB)','fontsize',18)
xlabel('Angle (degrees)','fontsize',18)
axis([-90 90 -50 0])
set(gca,'fontsize',16)
set(gca,'xtick',[-90 -60 -30 0 30 60 90])
grid on

%Plots the beam pattern
figure
plot(Ttheta,b,'r-','linewidth',3);
ylabel('Farfield Directivity (dB)','fontsize',18)
xlabel('Angle (degrees)','fontsize',18)
axis([-90 90 -50 0])
set(gca,'fontsize',16)
set(gca,'xtick',[-90 -60 -30 0 30 60 90])
grid on

%Plots the velocity profile along the beam
figure
plot(x/.0254,real(uy),x/.0254,imag(uy),'linewidth',3)
ylabel('Velocity (m/s)','fontsize',18)
xlabel('Position Along Bar (inches)','fontsize',18)
set(gca,'fontsize',16)
grid on

cd Z:\PhDResearch\Numerical
```

A.8 Experimentally Obtained Directivity Pattern and Filter Shape

```
woreceive50kHz
wodata=data;
wpreceive50kHz
wpdata=data;
freq=50;


Msteerangle=-90:90;
for ss=1:length(Msteerangle)
    steerangle=Msteerangle(ss);
    data=wodata;
    angle=data(:,1);
    for i=1:length(angle)
        angle(i)=angle(i)-360;
    end

    A=-90:1:90;

    arraypos=[3:6 10:15 17:48 50:55 59:62];

    for i=1:52
        temp=interp1(data(:,1),data(:,2*i+3),A);
        ii=1;
        DATA(:,i)=10.^(temp/20).*exp(j*tempP);
    end

    phaseshift=2*pi*freq*1000*(1.164*.0254)/1500*sin(-
steerangle*pi/180);

    SDATA=DATA;
    SDATA(:,11)=DATA(:,11);
    SDATA(:,19)=DATA(:,19);
    SDATA(:,27)=DATA(:,27);
    SDATA(:,35)=DATA(:,35);
    SDATA(:,5)=DATA(:,5)*exp(j*phaseshift);
    SDATA(:,12)=DATA(:,12)*exp(j*phaseshift);
    SDATA(:,20)=DATA(:,20)*exp(j*phaseshift);
    SDATA(:,28)=DATA(:,28)*exp(j*phaseshift);
    SDATA(:,36)=DATA(:,36)*exp(j*phaseshift);
    SDATA(:,43)=DATA(:,43)*exp(j*phaseshift);
    SDATA(:,1)=DATA(:,1)*exp(2*j*phaseshift);
    SDATA(:,6)=DATA(:,6)*exp(2*j*phaseshift);
    SDATA(:,13)=DATA(:,13)*exp(2*j*phaseshift);
    SDATA(:,21)=DATA(:,21)*exp(2*j*phaseshift);
    SDATA(:,29)=DATA(:,29)*exp(2*j*phaseshift);
    SDATA(:,37)=DATA(:,37)*exp(2*j*phaseshift);
    SDATA(:,44)=DATA(:,44)*exp(2*j*phaseshift);
    SDATA(:,49)=DATA(:,49)*exp(2*j*phaseshift);
    SDATA(:,2)=DATA(:,2)*exp(3*j*phaseshift);
    SDATA(:,7)=DATA(:,7)*exp(3*j*phaseshift);
    SDATA(:,14)=DATA(:,14)*exp(3*j*phaseshift);
```

```
    SDATA(:,22)=DATA(:,22)*exp(3*j*phaseshift);
    SDATA(:,30)=DATA(:,30)*exp(3*j*phaseshift);
    SDATA(:,38)=DATA(:,38)*exp(3*j*phaseshift);
    SDATA(:,45)=DATA(:,45)*exp(3*j*phaseshift);
    SDATA(:,50)=DATA(:,50)*exp(3*j*phaseshift);
    SDATA(:,3)=DATA(:,3)*exp(4*j*phaseshift);
    SDATA(:,8)=DATA(:,8)*exp(4*j*phaseshift);
    SDATA(:,15)=DATA(:,15)*exp(4*j*phaseshift);
    SDATA(:,23)=DATA(:,23)*exp(4*j*phaseshift);
    SDATA(:,31)=DATA(:,31)*exp(4*j*phaseshift);
    SDATA(:,39)=DATA(:,39)*exp(4*j*phaseshift);
    SDATA(:,46)=DATA(:,46)*exp(4*j*phaseshift);
    SDATA(:,51)=DATA(:,51)*exp(4*j*phaseshift);
    SDATA(:,4)=DATA(:,4)*exp(5*j*phaseshift);
    SDATA(:,9)=DATA(:,9)*exp(5*j*phaseshift);
    SDATA(:,16)=DATA(:,16)*exp(5*j*phaseshift);
    SDATA(:,24)=DATA(:,24)*exp(5*j*phaseshift);
    SDATA(:,32)=DATA(:,32)*exp(5*j*phaseshift);
    SDATA(:,40)=DATA(:,40)*exp(5*j*phaseshift);
    SDATA(:,47)=DATA(:,47)*exp(5*j*phaseshift);
    SDATA(:,52)=DATA(:,52)*exp(5*j*phaseshift);
    SDATA(:,10)=DATA(:,10)*exp(6*j*phaseshift);
    SDATA(:,17)=DATA(:,17)*exp(6*j*phaseshift);
    SDATA(:,25)=DATA(:,25)*exp(6*j*phaseshift);
    SDATA(:,33)=DATA(:,33)*exp(6*j*phaseshift);
    SDATA(:,41)=DATA(:,41)*exp(6*j*phaseshift);
    SDATA(:,48)=DATA(:,48)*exp(6*j*phaseshift);
    SDATA(:,18)=DATA(:,18)*exp(7*j*phaseshift);
    SDATA(:,26)=DATA(:,26)*exp(7*j*phaseshift);
    SDATA(:,34)=DATA(:,34)*exp(7*j*phaseshift);
    SDATA(:,42)=DATA(:,42)*exp(7*j*phaseshift);

    SixDATA=sum(SDATA(:,20:25),2);
    SPLSix=20*log10(abs(SixDATA));

    VDATA=SDATA(:,11)+SDATA(:,19)+SDATA(:,27)+SDATA(:,35);
    SPLV1=20*log10(abs(VDATA));

VDATA=SDATA(:,5)+SDATA(:,12)+SDATA(:,20)+SDATA(:,28)+SDATA(:,36)+SDATA(
:,43);
    SPLV2=20*log10(abs(VDATA));

VDATA=SDATA(:,2)+SDATA(:,7)+SDATA(:,14)+SDATA(:,22)+SDATA(:,30)+SDATA(:
,38)+SDATA(:,45)+SDATA(:,50);
    SPLV3=20*log10(abs(VDATA));

VDATA=SDATA(:,3)+SDATA(:,8)+SDATA(:,15)+SDATA(:,23)+SDATA(:,31)+SDATA(:
,39)+SDATA(:,46)+SDATA(:,51);
    SPLV4=20*log10(abs(VDATA));

VDATA=SDATA(:,4)+SDATA(:,9)+SDATA(:,16)+SDATA(:,24)+SDATA(:,32)+SDATA(:
,40)+SDATA(:,47)+SDATA(:,52);
    SPLV5=20*log10(abs(VDATA));
```

```
VDATA=SDATA(:,10)+SDATA(:,17)+SDATA(:,25)+SDATA(:,33)+SDATA(:,41)+SDATA
(:,48);
    SPLV6=20*log10(abs(VDATA));
    VDATA=SDATA(:,18)+SDATA(:,26)+SDATA(:,34)+SDATA(:,42);
    SPLV7=20*log10(abs(VDATA));

VDATA=SDATA(:,2)+SDATA(:,7)+SDATA(:,14)+SDATA(:,22)+SDATA(:,30)+SDATA(:
,38)+SDATA(:,45)+SDATA(:,50);
    SPLV8=20*log10(abs(VDATA));

    PDATA=sum(SDATA,2);
    SPLDATAwo=20*log10(abs(PDATA));
    WOFS(ss)=SPLDATAwo(ss);


    steerangle=Msteerangle(ss);
    data=wpdata;
    angle=data(:,1);
    for i=1:length(angle)
        angle(i)=angle(i)-360;
    end

    A=-90:1:90;

    arraypos=[3:6 10:15 17:48 50:55 59:62];

    for i=1:52
        temp=interp1(data(:,1),data(:,2*i+3),A);
        ii=1;
        DATA(:,i)=10.^(temp/20).*exp(j*tempP);
    end

    phaseshift=2*pi*freq*1000*(1.164*.0254)/1500*sin(-
steerangle*pi/180);

    SDATA=DATA;
    SDATA(:,11)=DATA(:,11);
    SDATA(:,19)=DATA(:,19);
    SDATA(:,27)=DATA(:,27);
    SDATA(:,35)=DATA(:,35);
    SDATA(:,5)=DATA(:,5)*exp(j*phaseshift);
    SDATA(:,12)=DATA(:,12)*exp(j*phaseshift);
    SDATA(:,20)=DATA(:,20)*exp(j*phaseshift);
    SDATA(:,28)=DATA(:,28)*exp(j*phaseshift);
    SDATA(:,36)=DATA(:,36)*exp(j*phaseshift);
    SDATA(:,43)=DATA(:,43)*exp(j*phaseshift);
    SDATA(:,1)=DATA(:,1)*exp(2*j*phaseshift);
    SDATA(:,6)=DATA(:,6)*exp(2*j*phaseshift);
    SDATA(:,13)=DATA(:,13)*exp(2*j*phaseshift);
    SDATA(:,21)=DATA(:,21)*exp(2*j*phaseshift);
    SDATA(:,29)=DATA(:,29)*exp(2*j*phaseshift);
    SDATA(:,37)=DATA(:,37)*exp(2*j*phaseshift);
    SDATA(:,44)=DATA(:,44)*exp(2*j*phaseshift);
    SDATA(:,49)=DATA(:,49)*exp(2*j*phaseshift);
```

```
    SDATA(:,2)=DATA(:,2)*exp(3*j*phaseshift);
    SDATA(:,7)=DATA(:,7)*exp(3*j*phaseshift);
    SDATA(:,14)=DATA(:,14)*exp(3*j*phaseshift);
    SDATA(:,22)=DATA(:,22)*exp(3*j*phaseshift);
    SDATA(:,30)=DATA(:,30)*exp(3*j*phaseshift);
    SDATA(:,38)=DATA(:,38)*exp(3*j*phaseshift);
    SDATA(:,45)=DATA(:,45)*exp(3*j*phaseshift);
    SDATA(:,50)=DATA(:,50)*exp(3*j*phaseshift);
    SDATA(:,3)=DATA(:,3)*exp(4*j*phaseshift);
    SDATA(:,8)=DATA(:,8)*exp(4*j*phaseshift);
    SDATA(:,15)=DATA(:,15)*exp(4*j*phaseshift);
    SDATA(:,23)=DATA(:,23)*exp(4*j*phaseshift);
    SDATA(:,31)=DATA(:,31)*exp(4*j*phaseshift);
    SDATA(:,39)=DATA(:,39)*exp(4*j*phaseshift);
    SDATA(:,46)=DATA(:,46)*exp(4*j*phaseshift);
    SDATA(:,51)=DATA(:,51)*exp(4*j*phaseshift);
    SDATA(:,4)=DATA(:,4)*exp(5*j*phaseshift);
    SDATA(:,9)=DATA(:,9)*exp(5*j*phaseshift);
    SDATA(:,16)=DATA(:,16)*exp(5*j*phaseshift);
    SDATA(:,24)=DATA(:,24)*exp(5*j*phaseshift);
    SDATA(:,32)=DATA(:,32)*exp(5*j*phaseshift);
    SDATA(:,40)=DATA(:,40)*exp(5*j*phaseshift);
    SDATA(:,47)=DATA(:,47)*exp(5*j*phaseshift);
    SDATA(:,52)=DATA(:,52)*exp(5*j*phaseshift);
    SDATA(:,10)=DATA(:,10)*exp(6*j*phaseshift);
    SDATA(:,17)=DATA(:,17)*exp(6*j*phaseshift);
    SDATA(:,25)=DATA(:,25)*exp(6*j*phaseshift);
    SDATA(:,33)=DATA(:,33)*exp(6*j*phaseshift);
    SDATA(:,41)=DATA(:,41)*exp(6*j*phaseshift);
    SDATA(:,48)=DATA(:,48)*exp(6*j*phaseshift);
    SDATA(:,18)=DATA(:,18)*exp(7*j*phaseshift);
    SDATA(:,26)=DATA(:,26)*exp(7*j*phaseshift);
    SDATA(:,34)=DATA(:,34)*exp(7*j*phaseshift);
    SDATA(:,42)=DATA(:,42)*exp(7*j*phaseshift);

    SixDATA=sum(SDATA(:,20:25),2);
    SPLSixp=20*log10(abs(SixDATA));

    VDATA=SDATA(:,11)+SDATA(:,19)+SDATA(:,27)+SDATA(:,35);
    SPLVP1=20*log10(abs(VDATA));

VDATA=SDATA(:,5)+SDATA(:,12)+SDATA(:,20)+SDATA(:,28)+SDATA(:,36)+SDATA(
:,43);
    SPLVP2=20*log10(abs(VDATA));

VDATA=SDATA(:,2)+SDATA(:,7)+SDATA(:,14)+SDATA(:,22)+SDATA(:,30)+SDATA(:
,38)+SDATA(:,45)+SDATA(:,50);
    SPLVP3=20*log10(abs(VDATA));

VDATA=SDATA(:,3)+SDATA(:,8)+SDATA(:,15)+SDATA(:,23)+SDATA(:,31)+SDATA(:
,39)+SDATA(:,46)+SDATA(:,51);
    SPLVP4=20*log10(abs(VDATA));

VDATA=SDATA(:,4)+SDATA(:,9)+SDATA(:,16)+SDATA(:,24)+SDATA(:,32)+SDATA(:
,40)+SDATA(:,47)+SDATA(:,52);
```

```
    SPLVP5=20*log10(abs(VDATA));

VDATA=SDATA(:,10)+SDATA(:,17)+SDATA(:,25)+SDATA(:,33)+SDATA(:,41)+SDATA
(:,48);
    SPLVP6=20*log10(abs(VDATA));
    VDATA=SDATA(:,18)+SDATA(:,26)+SDATA(:,34)+SDATA(:,42);
    SPLVP7=20*log10(abs(VDATA));

VDATA=SDATA(:,2)+SDATA(:,7)+SDATA(:,14)+SDATA(:,22)+SDATA(:,30)+SDATA(:
,38)+SDATA(:,45)+SDATA(:,50);
    SPLVP8=20*log10(abs(VDATA));

    PDATA=sum(SDATA,2);
    SPLDATAwp=20*log10(abs(PDATA));
    WPFS(ss)=SPLDATAwp(ss);
    WPM(ss,:)=SPLDATAwp-SPLDATAwp(ss);
    WOM(ss,:)=SPLDATAwo-SPLDATAwo(ss);
    PatternDifference(:,ss)=SPLDATAwp-SPLDATAwo;
    ss
end

% figure
% plot(A,SPLDATAwo-max(SPLDATAwo),A,SPLDATAwp-
max(SPLDATAwp),'linewidth',3)
% grid on
% axis([-90 90 -50 0])
% xlabel('Angle (degrees)','fontsize',18)
% ylabel('Normalized Amplitude (dB)','fontsize',18)
% set(gca,'fontsize',16,'xtick',[-90 -60 -30 0 30 60 90])

% figure;plot(A,WPFS-WOFS,'color',[0 .5 0],'linewidth',3)
% xlabel('Angle (degrees)','fontsize',18)
% ylabel('Directivity (dB)','fontsize',18)
% axis([-90 90 -50 0])
% grid on
% set(gca,'fontsize',16,'xtick',[-90 -60 -30 0 30 60 90])
%
% figure;plot(A,mean(PatternDifference,2))

% for i=1:length(WPM)
%     for ii=1:length(WPM)
%         if WPM(i,ii)-max(max(WPM))<-40
%             WPM(i,ii)=max(max(WPM))-40;
%         end
%         if WOM(i,ii)-max(max(WOM))<-40
%             WOM(i,ii)=max(max(WOM))-40;
%         end
%     end
% end
%
%
figure;surf(2*pi*freq*1000/1500*sin(pi/180*A),2*pi*freq*1000/1500*sin(p
i/180*A),WOM-max(max(WOM)))
% axis([-freq*1000*2*pi/1500 freq*1000*2*pi/1500 -freq*1000*2*pi/1500
freq*1000*2*pi/1500 -40 0]);axis square
```

```
% shading interp
% xlabel('Driven Wavenumber','fontsize',12)
% ylabel('Receive Wavenumber','fontsize',12)
% hold on;plot3([-freq*1000*2*pi/1500 freq*1000*2*pi/1500],[-
freq*1000*2*pi/1500 freq*1000*2*pi/1500],[0 0],'k--','linewidth',3)
% view(0,90)
% titlestring=['No Plate @ ',num2str(freq),' kHz'];
% title(titlestring,'fontsize',12)
% colorbar
% figurestring=['kkplot No Plate ',num2str(freq),'kHz'];
% saveas(gcf,figurestring)
%
%
figure;surf(2*pi*freq*1000/1500*sin(pi/180*A),2*pi*freq*1000/1500*sin(p
i/180*A),WPM-max(max(WPM)))
% axis([-freq*1000*2*pi/1500 freq*1000*2*pi/1500 -freq*1000*2*pi/1500
freq*1000*2*pi/1500 -40 0]);axis square
% shading interp
% xlabel('Driven Wavenumber','fontsize',12)
% ylabel('Receive Wavenumber','fontsize',12)
% hold on;plot3([-freq*1000*2*pi/1500 freq*1000*2*pi/1500],[-
freq*1000*2*pi/1500 freq*1000*2*pi/1500],[0 0],'k--','linewidth',3)
% view(0,90)
% titlestring=['Aluminum Honeycomb Plate @ ',num2str(freq),' kHz'];
% title(titlestring,'fontsize',12)
% colorbar
% figurestring=['kkplot AH Plate ',num2str(freq),'kHz'];
% saveas(gcf,figurestring)



for i=1:length(WPM)
    for ii=1:length(WPM)
        if WPM(i,ii)<-40
            WPM(i,ii)=-40;
        end
        if WPM(i,ii)>0
            WPM(i,ii)=0;
        end
        if WOM(i,ii)<-40
            WOM(i,ii)=-40;
        end
        if WOM(i,ii)>0
            WOM(i,ii)=0;
        end
    end
end

figure;surf(2*pi*freq*1000/1500*sin(pi/180*A),2*pi*freq*1000/1500*sin(p
i/180*A),WPM')
axis([-freq*1000*2*pi/1500 freq*1000*2*pi/1500 -freq*1000*2*pi/1500
freq*1000*2*pi/1500 -40 0]);axis square
shading interp
xlabel('Driven Wavenumber','fontsize',18)
ylabel('Receive Wavenumber','fontsize',18)
```

```
hold on;plot3([-freq*1000*2*pi/1500 freq*1000*2*pi/1500],[-
freq*1000*2*pi/1500 freq*1000*2*pi/1500],[0 0],'k--','linewidth',3)
view(0,90)
titlestring=['Wavenumber Plot @ ',num2str(freq),' kHz'];
title(titlestring,'fontsize',18)
caxis([-40.5 0.5])
colorbar
figurestring=['kkplot AA Bar ',num2str(freq),'kHz'];
%saveas(gcf,figurestring)
%print(gcf)

figure;surf(A,A,WPM')
axis([-90 90 -90 90 -40 0]);axis square
shading interp
xlabel('Steer Angle','fontsize',18)
ylabel('Receive Angle','fontsize',18)
hold on;plot3([-freq*1000*2*pi/1500 freq*1000*2*pi/1500],[-
freq*1000*2*pi/1500 freq*1000*2*pi/1500],[0 0],'k--','linewidth',3)
view(0,90)
set(gca,'xtick',[-90 -60 -30 0 30 60 90])
set(gca,'ytick',[-90 -60 -30 0 30 60 90])
titlestring=['Angle Plot @ ',num2str(freq),' kHz'];
title(titlestring,'fontsize',18)
caxis([-40.5 0.5])
colorbar
figurestring=['aaplot AA Bar ',num2str(freq),'kHz'];
%saveas(gcf,figurestring)
%print(gcf)

figure;surf(2*pi*freq*1000/1500*sin(pi/180*A),2*pi*freq*1000/1500*sin(p
i/180*A),WOM')
axis([-freq*1000*2*pi/1500 freq*1000*2*pi/1500 -freq*1000*2*pi/1500
freq*1000*2*pi/1500 -40 0]);axis square
shading interp
xlabel('Driven Wavenumber','fontsize',18)
ylabel('Receive Wavenumber','fontsize',18)
hold on;plot3([-freq*1000*2*pi/1500 freq*1000*2*pi/1500],[-
freq*1000*2*pi/1500 freq*1000*2*pi/1500],[0 0],'k--','linewidth',3)
view(0,90)
titlestring=['Wavenumber Plot @ ',num2str(freq),' kHz'];
title(titlestring,'fontsize',18)
caxis([-40.5 0.5])
colorbar
figurestring=['kkplot wo Bar ',num2str(freq),'kHz'];
%saveas(gcf,figurestring)
%print(gcf)

figure;surf(A,A,WOM')
axis([-90 90 -90 90 -40 0]);axis square
shading interp
xlabel('Steer Angle','fontsize',18)
ylabel('Receive Angle','fontsize',18)
hold on;plot3([-freq*1000*2*pi/1500 freq*1000*2*pi/1500],[-
freq*1000*2*pi/1500 freq*1000*2*pi/1500],[0 0],'k--','linewidth',3)
view(0,90)
```

```
set(gca,'xtick',[-90 -60 -30 0 30 60 90])
set(gca,'ytick',[-90 -60 -30 0 30 60 90])
titlestring=['Angle Plot @ ',num2str(freq),' kHz'];
title(titlestring,'fontsize',18)
caxis([-40.5 0.5])
colorbar
figurestring=['aaplot wo Bar ',num2str(freq),'kHz'];
%saveas(gcf,figurestring)
%print(gcf)
```

A.9 Experimentally Obtained Single Element Directivity Pattern

```
clear
woreceive50kHz
angle=data(:,1);
for i=1:length(angle)
    angle(i)=angle(i)-360;
end

A=-90:1:90;

arraypos=[3:6 10:15 17:48 50:55 59:62];

figure
for i=1:52
    temp=interp1(data(:,1),data(:,2*i+3),A);
    ii=1;
    while isnan(temp(ii))
        ii=ii+1;
    end
    iii=length(A);
    while isnan(temp(iii))
        iii=iii-1;
    end
    temp(1:ii)=temp(ii+1);
    temp(iii:length(temp))=temp(ii-1);
    tempP=interp1(data(:,1),unwrap(data(:,2*i+4)*pi/180),A);
    tempP(1:ii)=tempP(ii+1);
    tempP(iii:length(tempP))=tempP(ii-1);
    DATA(:,i)=10.^(temp/20).*exp(j*tempP);
    subplot(8,8,arraypos(i))
    plot(A,20*log10(abs(DATA(:,i))))
    axis([-90 90 -70 -30])
end
```

Appendix B

BAFFLE DIRECTIVITY MEASUREMENTS

Inherent differences exist between the theoretical single element directivity patterns obtained from Eq. (2.21) and experimentally obtained single element directivity patterns found in Figs. 7.28-7.29. The differences arise from the baffle conditions assumed in the theoretical expression compared to that found experimentally. Assumptions made in the theoretical single element directivity function include, infinitely rigid baffles, spatially infinitely-extended baffles, and no mutual impedance effects. In both of the array modules used, the baffle obviously does not extend infinitely, and varies in length depending on element placement (some elements are near the edge, while some are in the center of the acoustic window, see Fig. 6.6). The baffle impedance, seen by each array element in the actual array modules possesses a finite value. Mutual impedance effects also exist in physical array systems which affect single element directivity patterns.

A straight forward method to obtain baffle directivity patterns is to steer the no-plate array data from -90° to +90° record the value at the main lobe and then subtract the theoretical single element directivity pattern value at its main lobe (effectively this is the main lobe insertion loss as a function of steer angle, which traces out the single element directivity pattern). The problem with this method is that, at high frequencies, the nulls in the theoretical single element directivity patterns do not show up in experimentally obtained steering envelopes (compare the theoretical patterns [red solid line] which

contain nulls and the experimentally obtained patterns [blue solid line] which do not contain nulls in Fig. B.3), likely due to non-pistonic motion of the element heads at high frequencies (in other words head "flexing" modes). One method of removing the nulls is to fit a function to the peaks of the theoretical single element directivity patterns (44, p. 391). This fitted function is similar to setting the numerator of Eq. (2.21) equal to one, H_{Peaks},

$$H_{Peaks}(\theta) = \frac{1}{\frac{1}{2}ka\sin\theta}. \tag{B.1}$$

The problem with strictly using H_{Peaks} is that at normal incidence the expression approaches an infinite value. To correct this the fitted function is set equal the theoretical single element directivity pattern at angles less than the final crossing point on the primary lobe as shown in Fig. B.1.

The baffle directivity pattern may be defined as the difference between the experimentally obtained steering envelope and the corresponding fitted function. Figures B.2 and B.3 show the theoretical single element directivity patterns, the corresponding fitted patterns as described above, the experimentally obtained steering envelopes, and the estimated baffle directivity patterns at various frequencies. Experimentally obtained steering envelopes were obtained from the no-bar 8-element line array data. If the theoretical single element directivity patterns were used instead of the fitted patterns, then the baffle directivity patterns would possess steep peaks at locations corresponding to the nulls of the theoretical single element directivity patterns. A further improvement to the baffle directivity patterns would be to smooth out the peaks which sometimes exceed

0 dB. One should note that these baffle directivity patterns were obtained from a line array adjacent to another line array and may not be representative of a 2-D planar array since the baffle impedance would be different.

One may argue that it does not make sense to use the fitted functions in obtaining baffle directivity patterns from the lower frequency patterns (Fig. B.2). The author chose consistency and utilized the same procedure for low and high frequencies. It may also be argued that the baffle directivity patterns should be obtained directly from subtraction of the experimentally obtained patterns from the theoretical patterns. The 50 kHz patterns in particular show that theory and experimental patterns nearly overlay. However, if the theoretical patterns were used instead of the fitted function for the higher frequency baffle directivity patterns (Fig. B.3), large peaks would be found in the baffle directivity functions (as a result of the missing nulls in the experimentally obtained patterns).

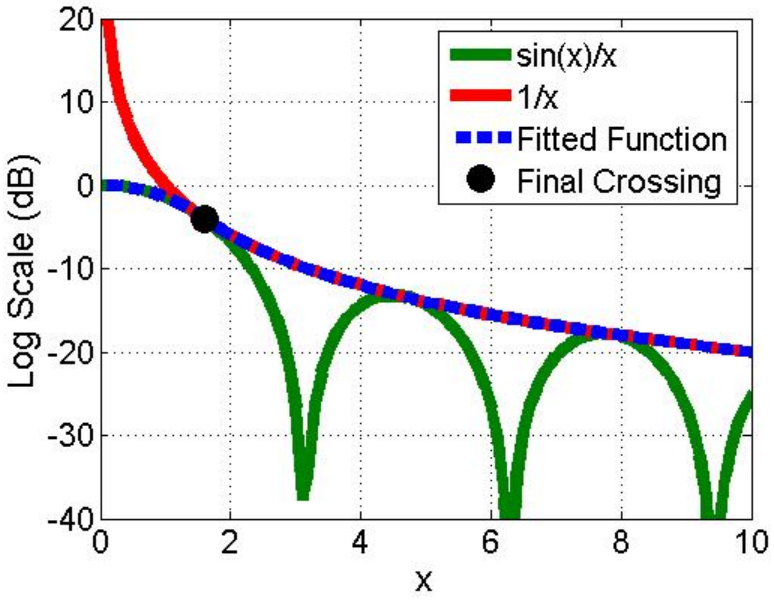

Fig. B.1. Depiction of the fitted function used to obtain the baffle directivity patterns. Equation (2.21) has the form of $\sin(x)/x$, and H_{Peaks} has the form of $1/x$, where $x = 1/2(ka\sin\theta)$.

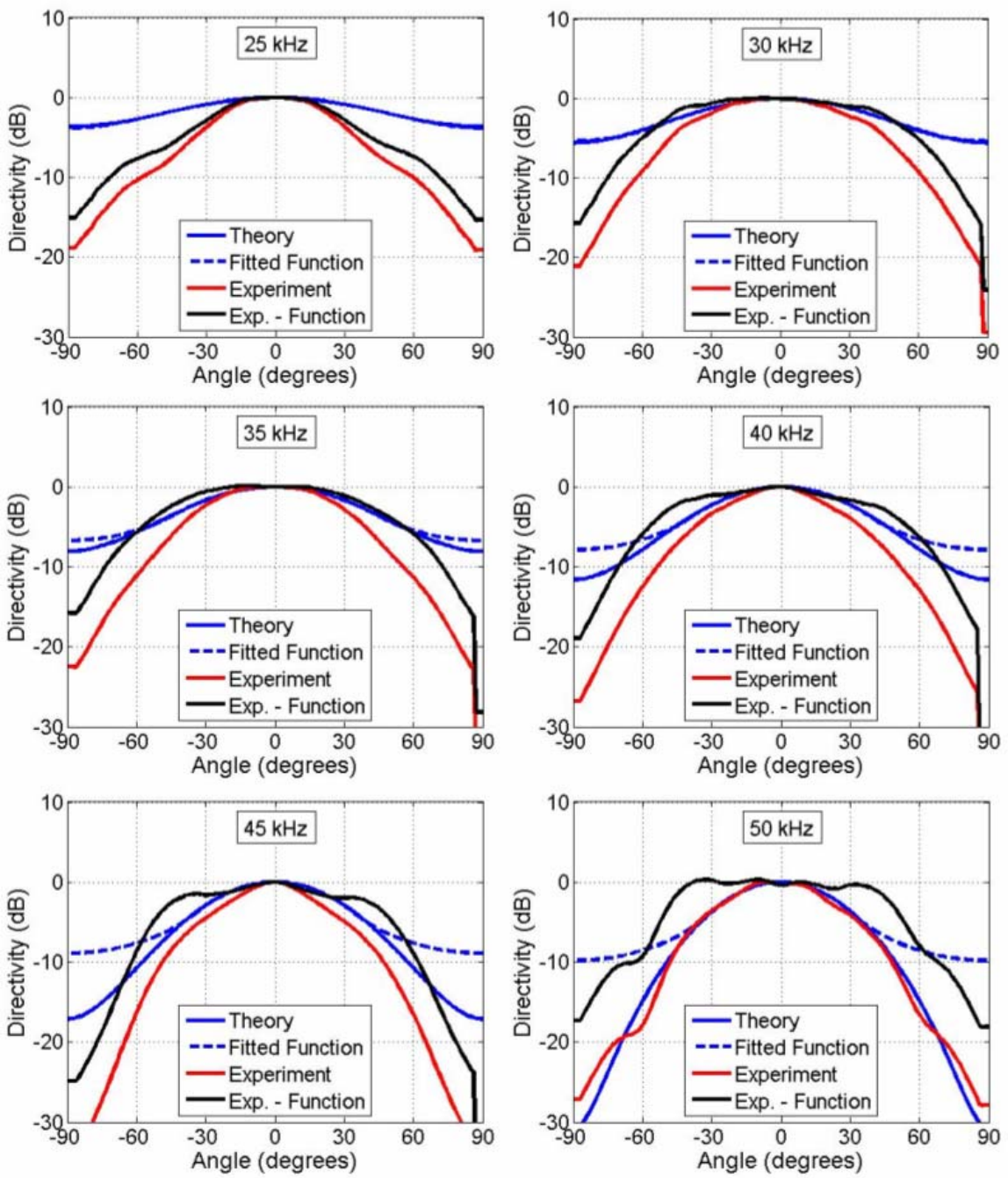

Fig. B.2. Single element directivity patterns from theory (blue solid line), fitted function (blue dashed line), measurement from 8 element no-bar line array (red), and estimated baffle directivity (black) for the six frequencies noted at the tops of each subfigure.

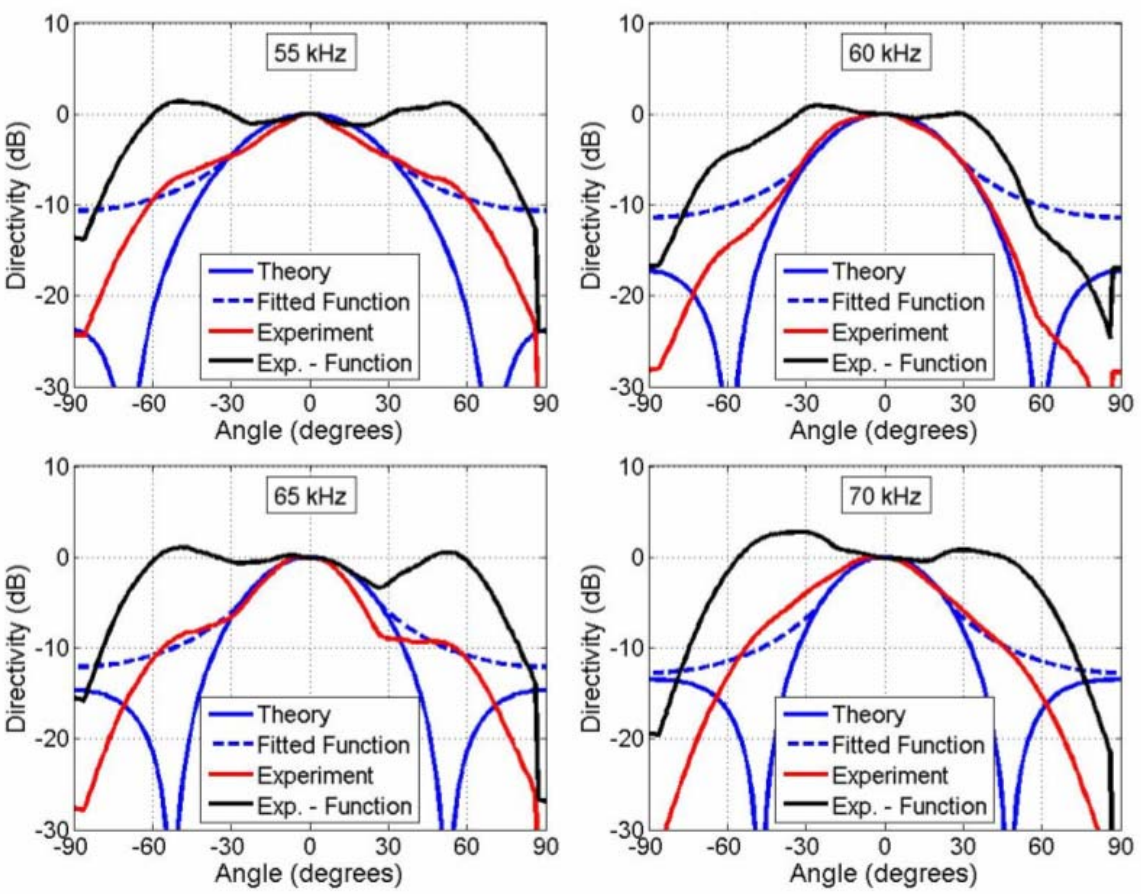

Fig. B.3. Single element directivity patterns from theory (blue solid line), fitted function (blue dashed line), measurement from 8 element no-bar line array (red), and estimated baffle directivity (black) for the four frequencies noted at the tops of each subfigure.

Appendix C

RECIPROCITY MEASUREMENTS

One aspect of the principle of reciprocity states that the directivity patterns of a given transducer at the same distance r are the same whether it is used as a receiver or as a transmitter (37, p. 378). The same principle applies to the directivity patterns for arrays of transducers.

Early in the research efforts, the question arose of whether a plate bonded to an array was a reciprocal system or not. As part of the first round of in-water measurements with the 8-element line array bonded to the alumina bar, a transmit system was configured in addition to the receive element based system outlined in Section 6.3. The transmit system was built to provide the freedom of having independent magnitudes and phases for each of the eight channels. For these measurements, the amplitudes were kept constant, while varying the phase according to the required phase shift increment, ϕ_0, as discussed in Section 2.3

$$\phi_0 = \omega\tau_0 = kd\sin\theta_0. \qquad \text{(C.1)}$$

Figures C.1-C.4 contain the directivity patterns for transmit (red) and receive (green) for the 19 combinations of various frequencies and steer angles tested as indicated above each subfigure. Visual inspection of Figs. C.1-C.4 yields the conclusion that a plate bonded to an array is a reciprocal system, despite the occasional minor deviations.

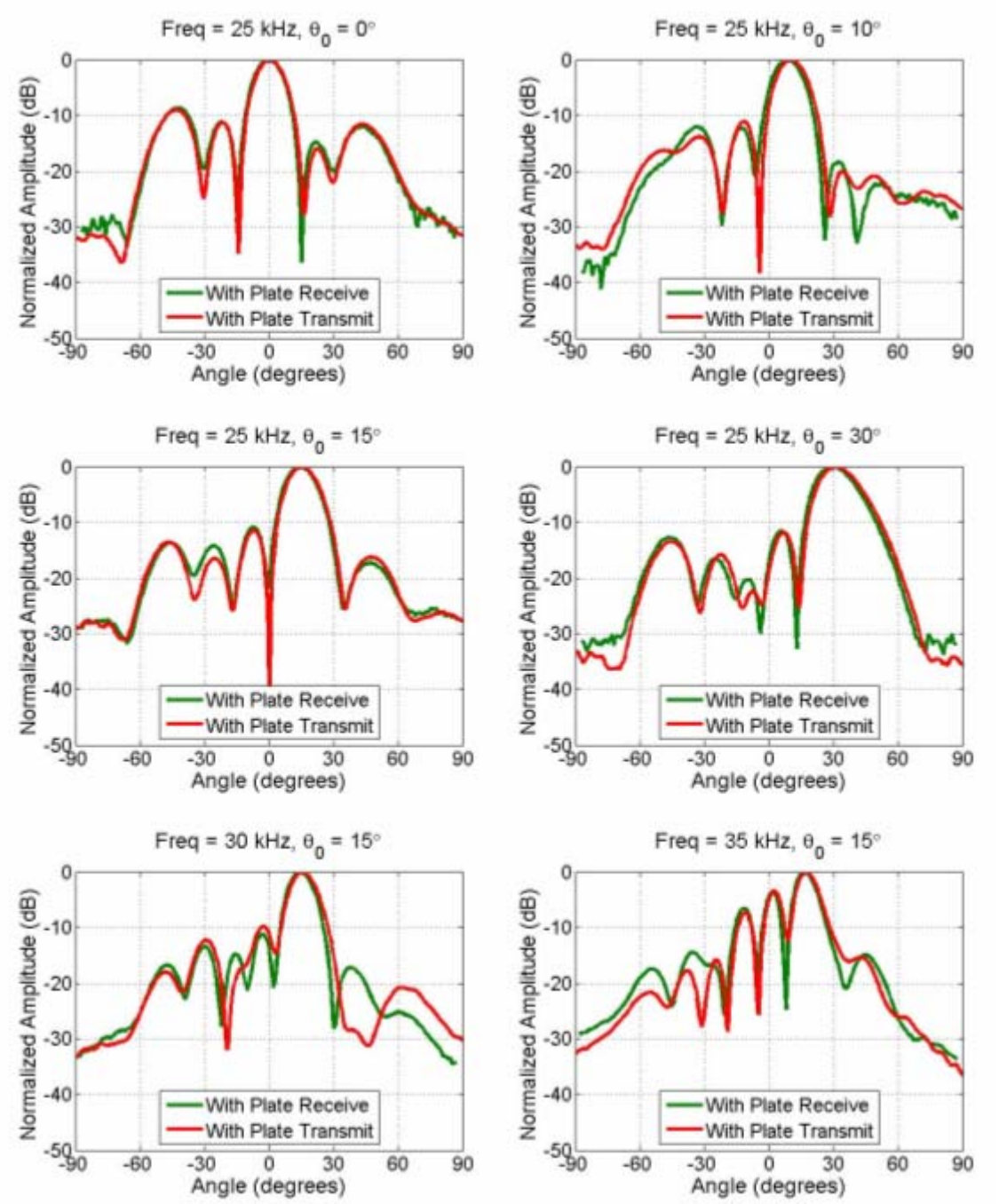

Fig. C.1. Reciprocity verification patterns for transmit (red) and receive (green) for the six combinations of various frequencies and steer angles tested as indicated above each subfigure.

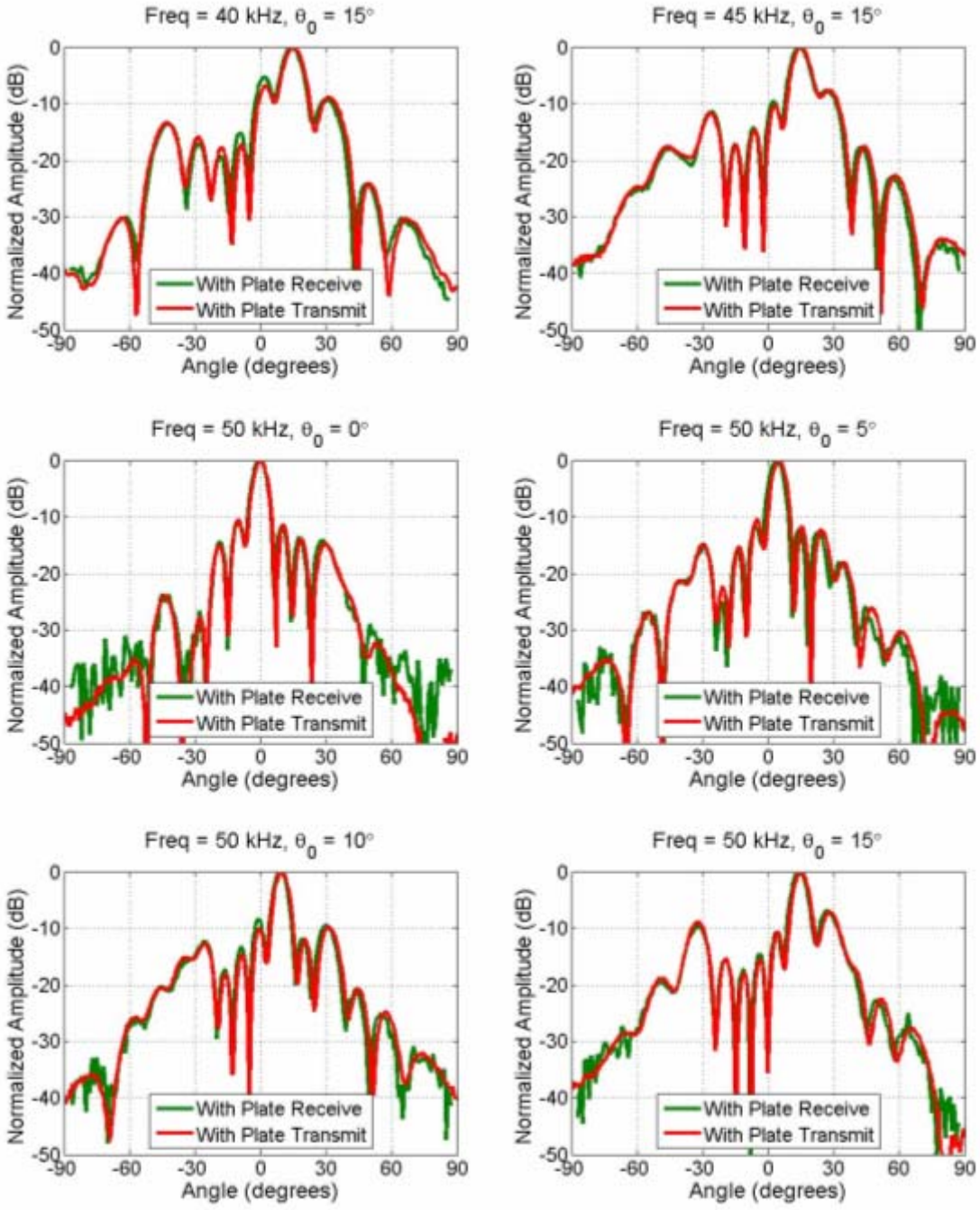

Fig. C.2. Reciprocity verification patterns for transmit (red) and receive (green) for the six combinations of various frequencies and steer angles tested as indicated above each subfigure.

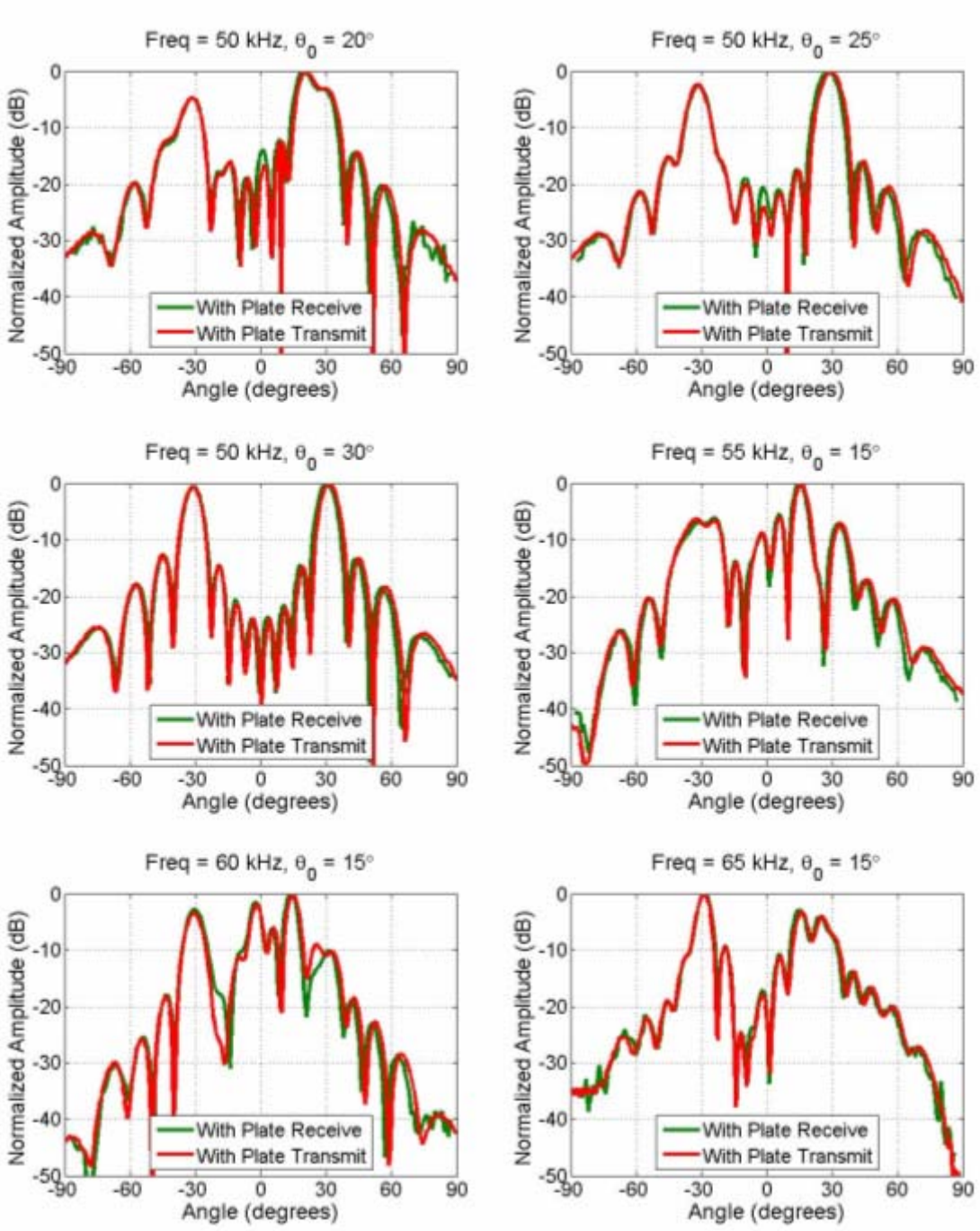

Fig. C.3. Reciprocity verification patterns for transmit (red) and receive (green) for the six combinations of various frequencies and steer angles tested as indicated above each subfigure.

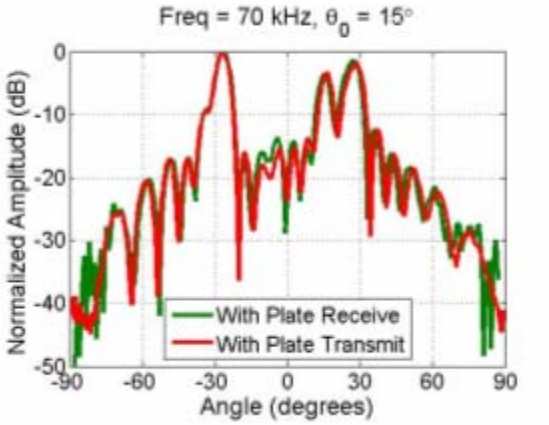

Fig. C.4. Reciprocity verification pattern for transmit (red) and receive (green) for the frequency and steer angle tested as indicated above the figure.

Appendix D

ADDITIONAL PHOTOS

Figures D.1 through D.22 contains additional photos which were not required in the thesis text.

Fig. D.1. Photo of the computer and impedance analyzer used to measure mechanical and electrical parameters of Tonpilz transducers.

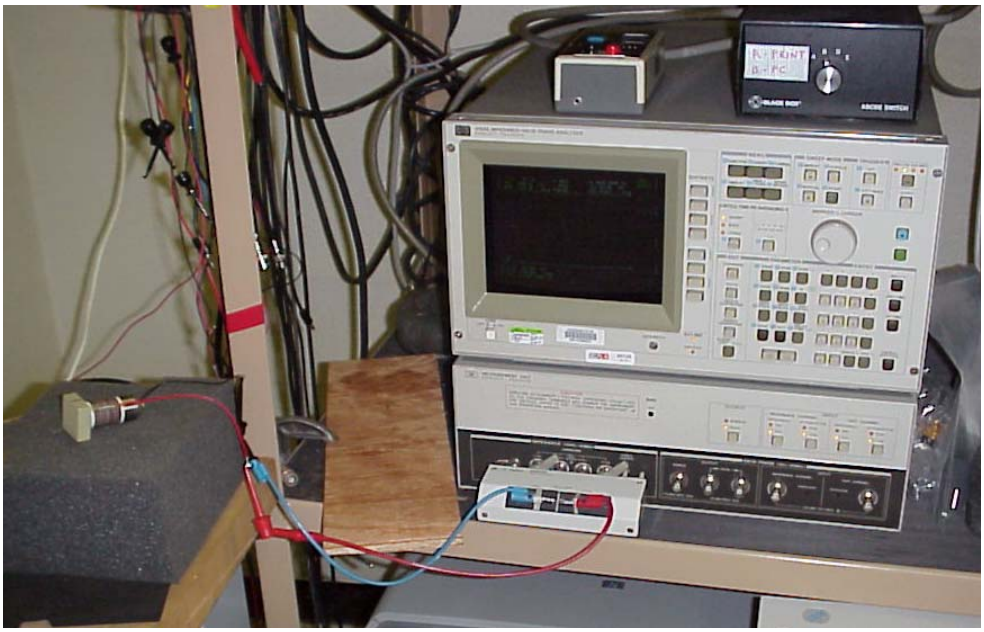

Fig. D.2. Photo of the HP 4194A Impedance/Gain-Phase Analyzer used in this thesis to generate impedance curves.

Fig. D.3. Photo of the oven used to cure polyurethane for the eight element line array mounted to a bar.

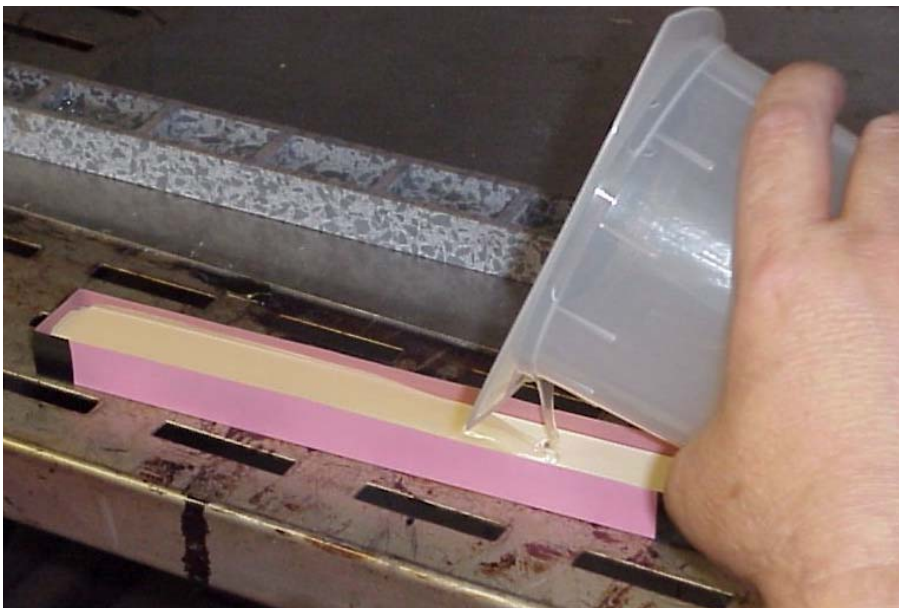

Fig. D.4. Photo of liquid polyurethane being poured onto alumina bar to make the compliant layer in the eight element line array mounted to a bar.

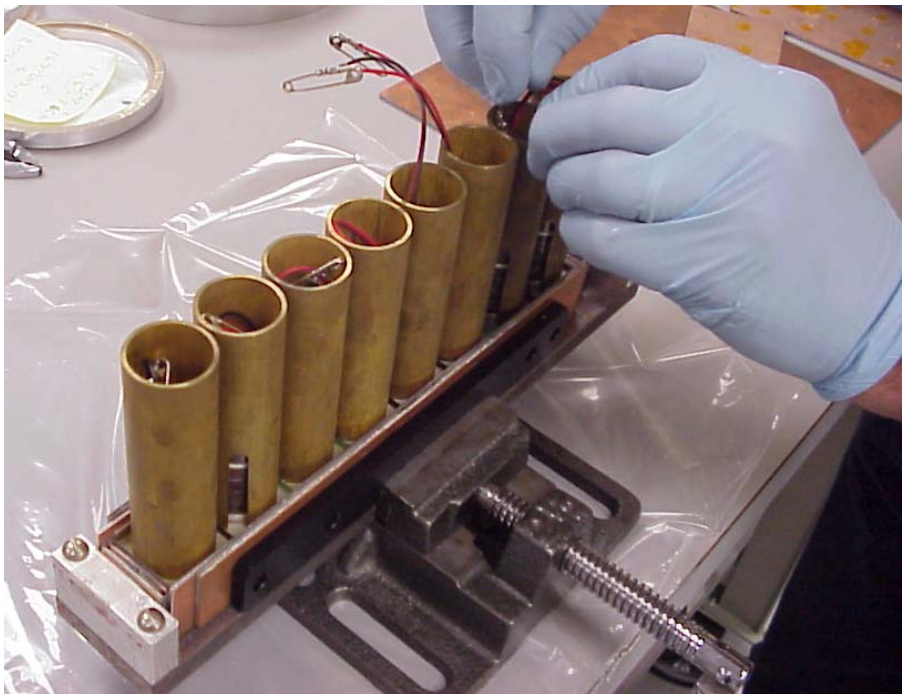

Fig. D.5. Photo of the construction of the eight element line array mounted on a bar. The cylinders were used to ensure a tight bond between the transducers and the compliant layer.

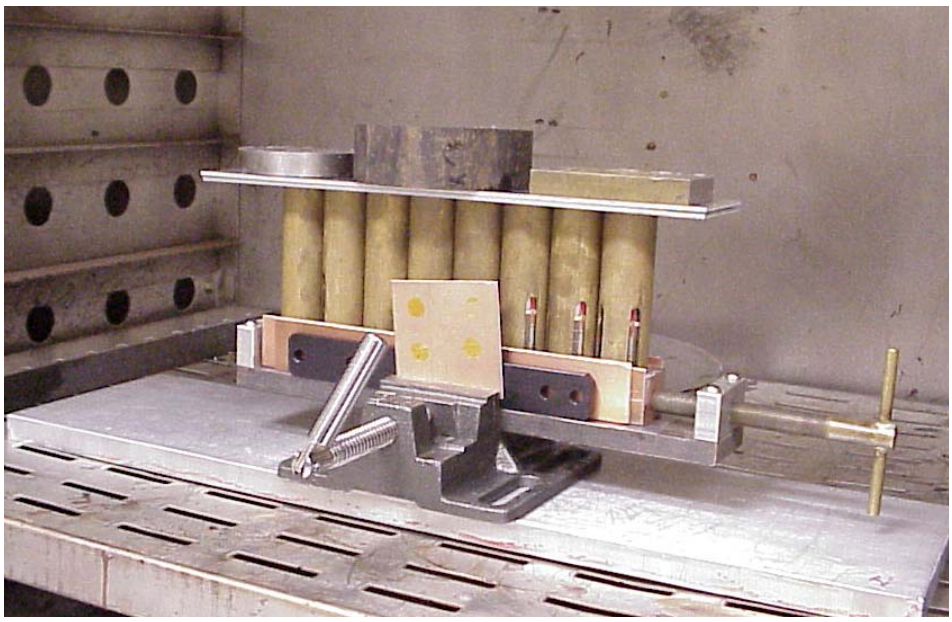

Fig. D.6. Photo of eight element line array mounted on a bar being held in a jig with the jig placed inside the oven shown in Fig. D.3.

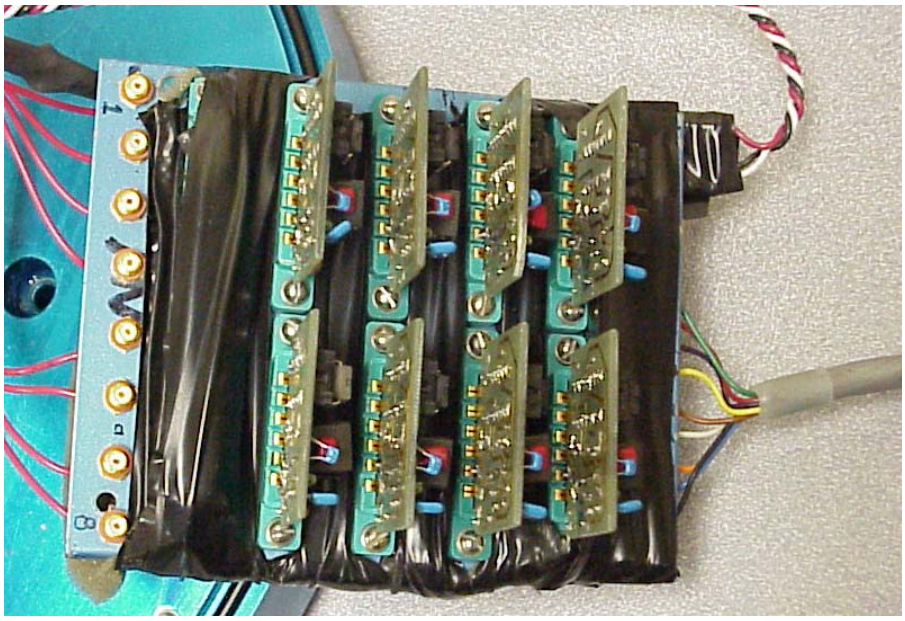

Fig. D.7. Photo of the eight 6 dB preamps used in a receive condition for the eight element line array not mounted to a bar.

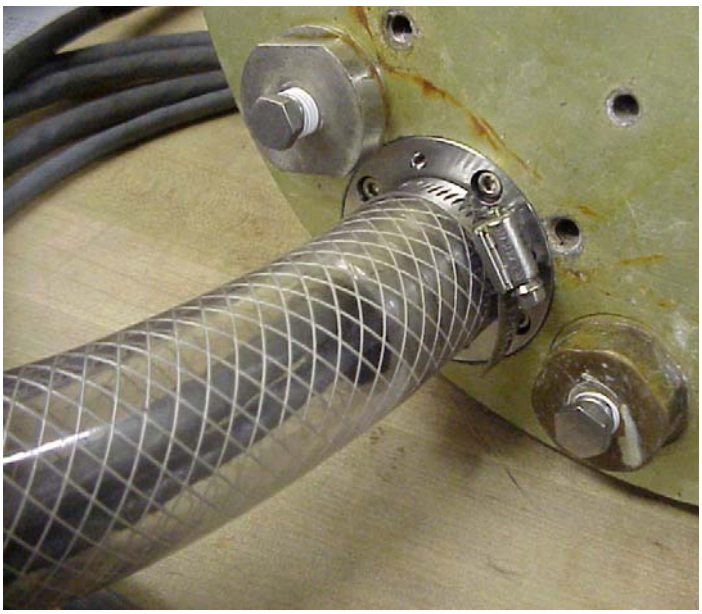

Fig. D.8. Photo of the cable housing and connection to the back of the shell. The cable housing ensured that the cables were protected from water.

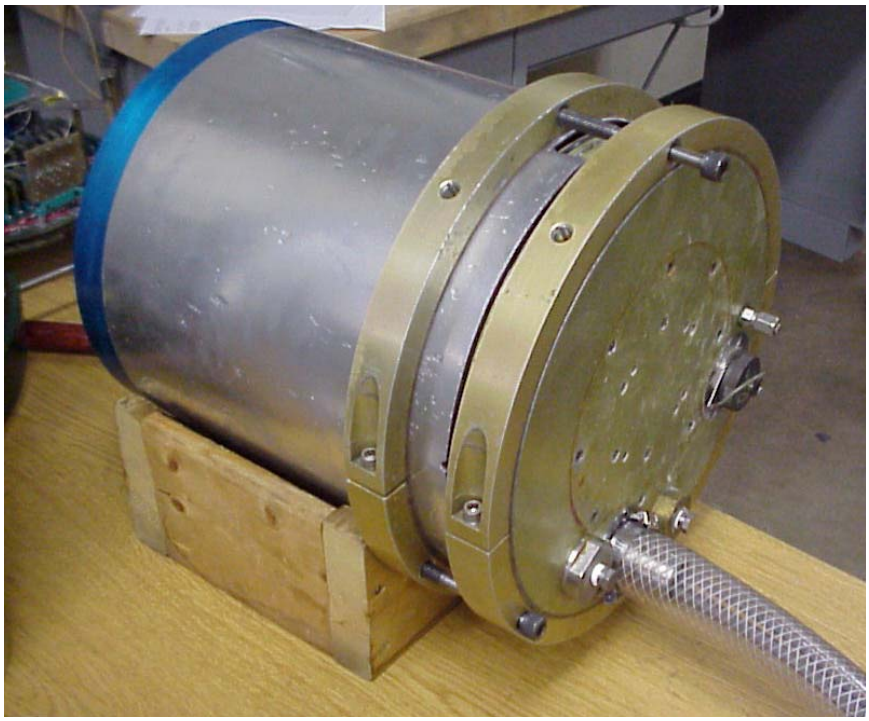

Fig. D.9. Photo of the mounting brackets on the shell housing the line arrays.

Fig. D.10. Photo of the transmitter hardware used in the reciprocity measurements found in Appendix C.

Fig. D.11. Photo of the computer hardware used to control the Polytec Scanning Laser.

Fig. D.12. Photo of the Polytec Scanning Laser during a scan of the velocity distribution on the alumina bar line array.

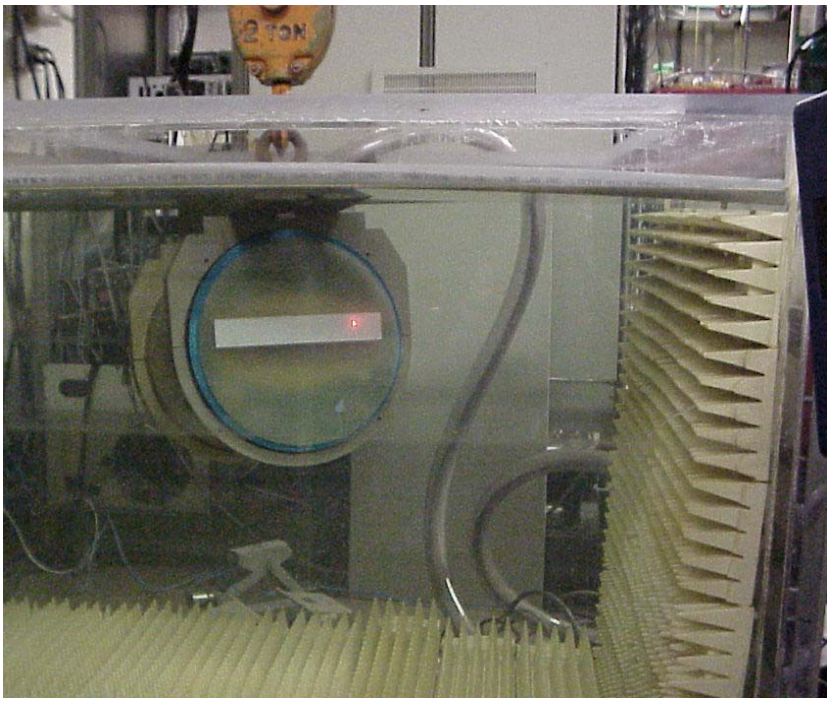

Fig. D.13. Photo of a scan in progress of the line array shell in a small semi-anechoic water tank.

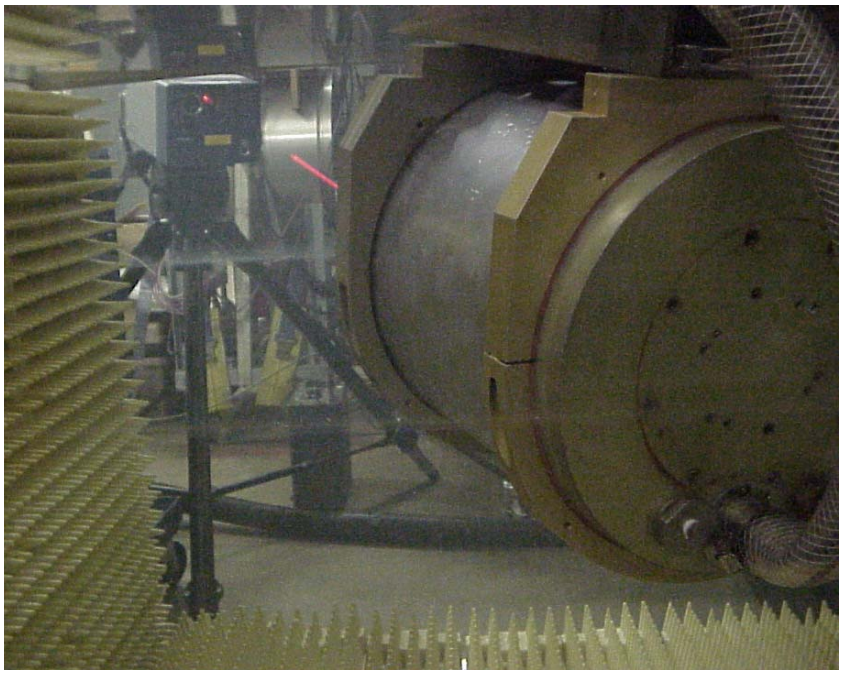

Fig. D.14. Photo of the back side a scan in progress of the line array shell in a small semi-anechoic water tank.

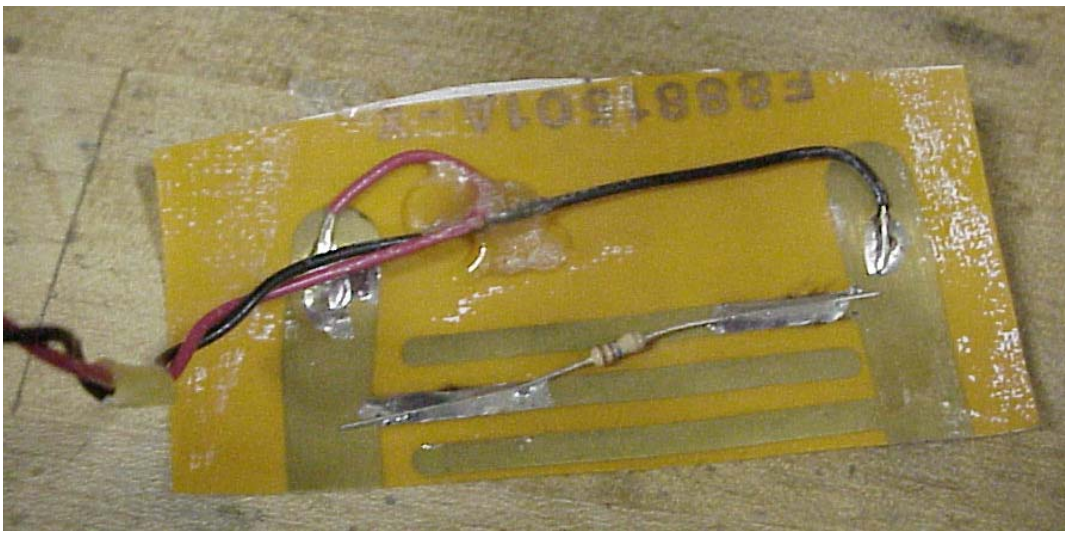

Fig. D.15. Photo of the leak detector placed inside the shell used in water tank tests. A buzzer sounds when water enters the shell seen in Fig. D.16.

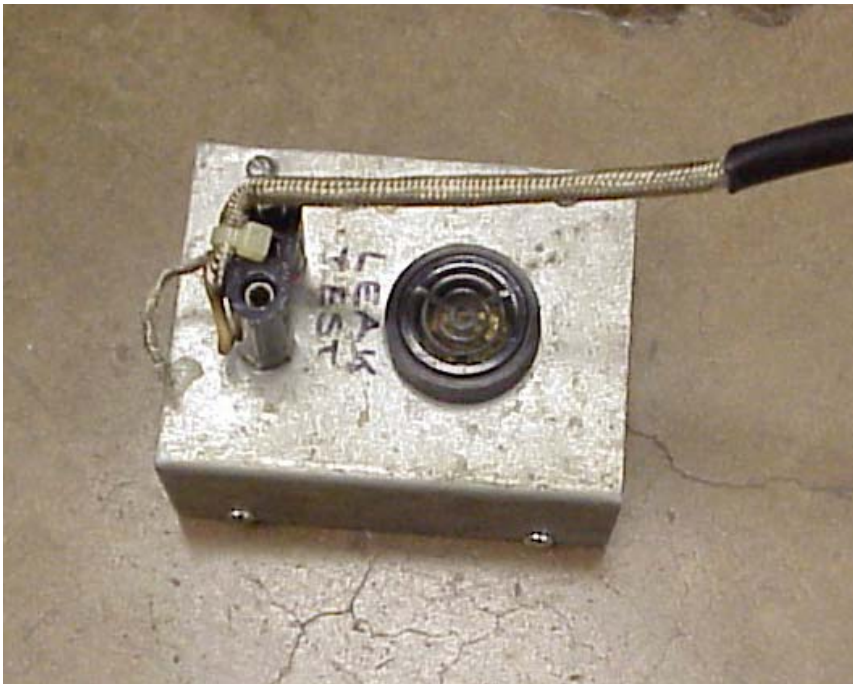

Fig. D.16. Photo of the topside portion of the leak detector used in water tank tests. The buzzer sounds when water enters the shell and shorts the connection seen in Fig. D.15.

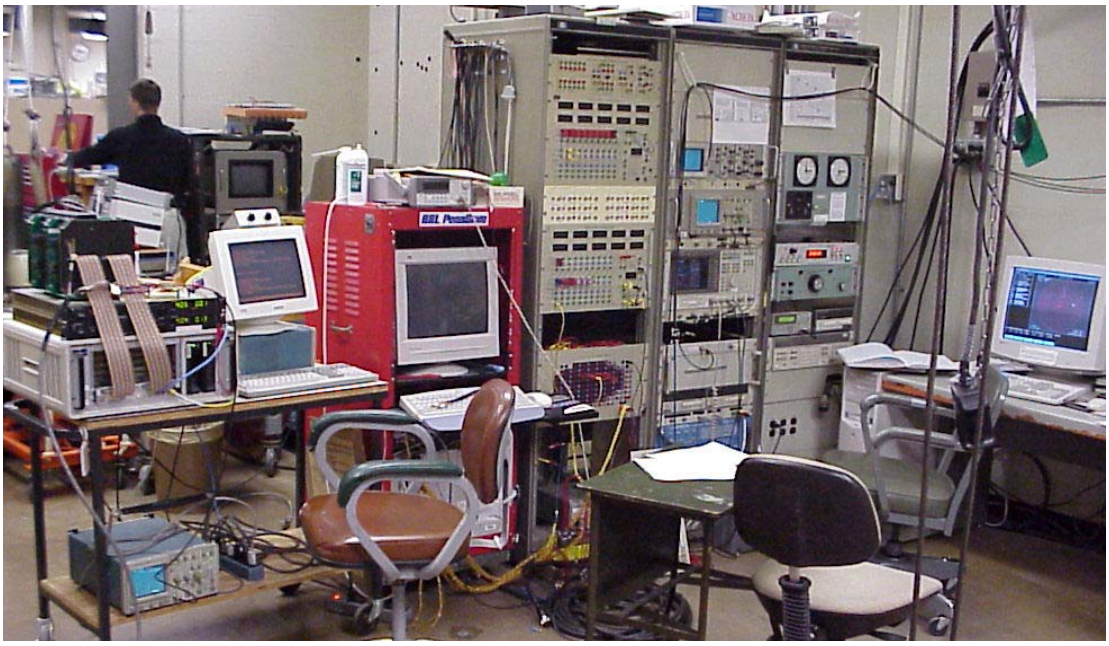

Fig. D.17. Photo of the hardware and analyzers used in water tank tests.

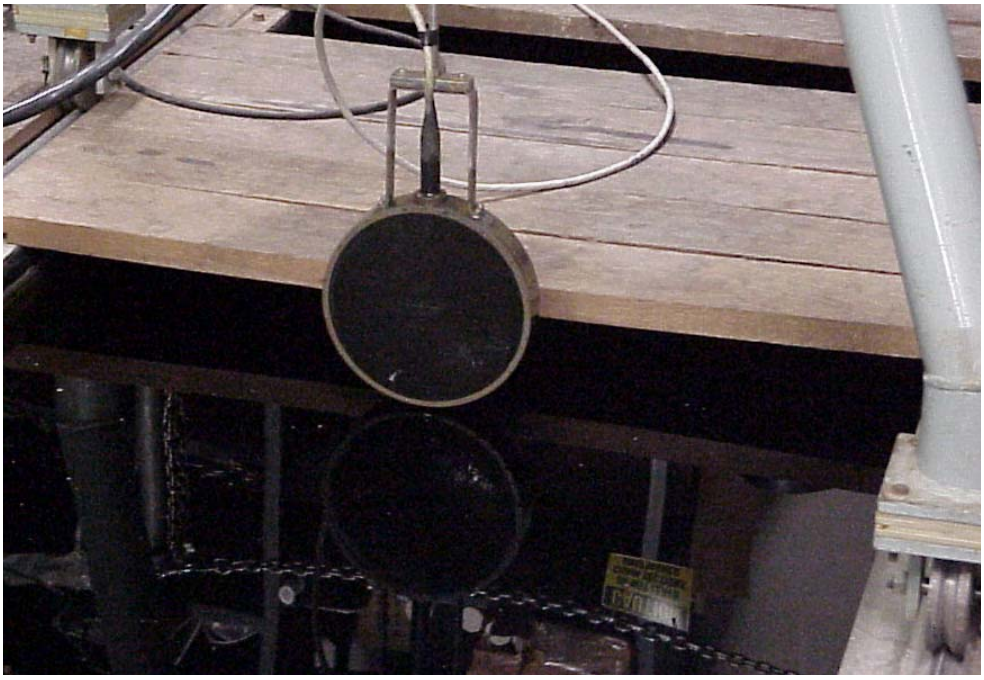

Fig. D.18. Photo of the calibrated transmitter/receiver used in water tank measurements.

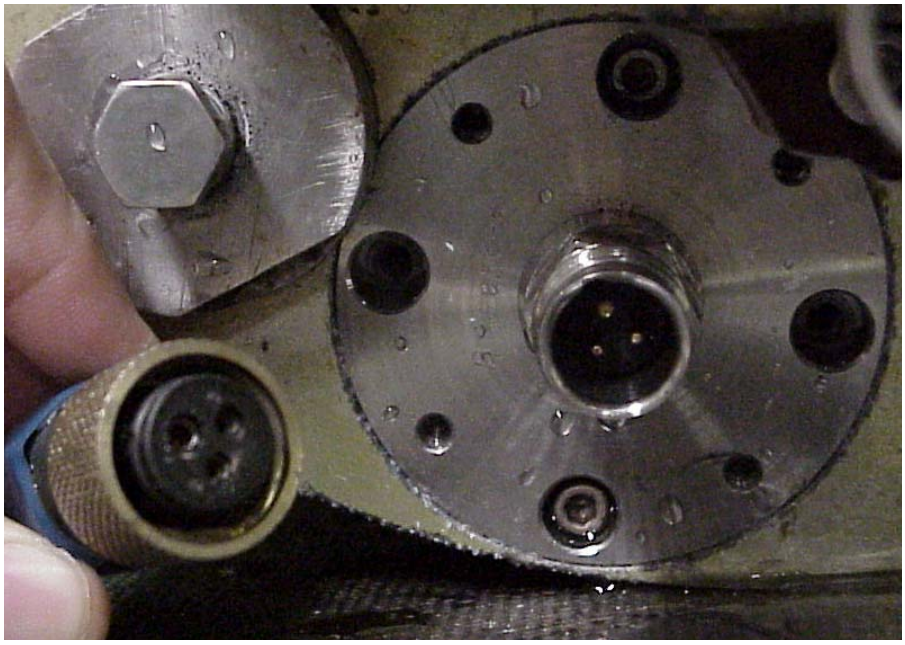

Fig. D.19. Photo of the 3-pin leak detector connection on the fifty-two element shell.

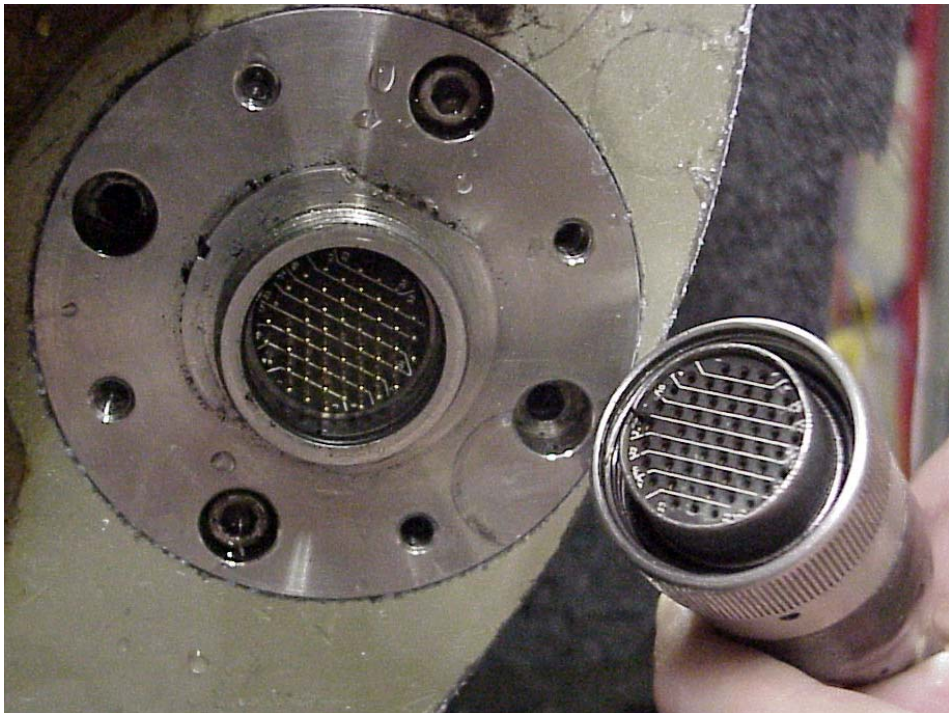

Fig. D.20. Photo of the 54-pin cable connection used to carry receive signals from the fifty-two element array.

Fig. D.21. Photo of the fifty-two element array shell with the window machined down to a 0.0625 inch thickness.

Fig. D.22. Photo of the author with the line array shell at the ARL water tank.

Appendix E

Directivity Pattern Surface Plots

E.1 Introduction

This appendix contains theoretical and experimental directivity pattern surface plots of steer angle versus receive angle versus amplitude for no-bar/plate and with-bar/plate conditions. Each figure contains plots corresponding to a different bar or plate. The frequency of each figure is different. Grating lobe ridges and extra side lobe sensitivity at the coincidence angles are not denoted in each figure. In this appendix, results from the no-bar 1-D line array module, the alumina bar on the 1-D line array module, the no-plate 2-D planar array module, the aluminum honeycomb plate on the 2-D planar array module, the alumina bar on the 2-D planar array module, and the R-direction pine bar on the 2-D planar array module are given with each figure representing one of the various frequencies measured. See Chapters 2 and 6 for discussions of these plots.

E.2 Theoretical Directivity Pattern Surface Plots

Figures E.1-E.13 are theoretical directivity pattern surface plots, similar to those found in Section 2.14 at every 5 kHz multiple from 10 kHz to 70 kHz.

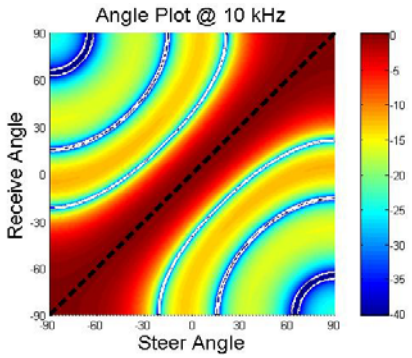

Fig. E.1. Theoretical receive angle versus steer angle directivity pattern surface plot at 10 kHz from 8 element line array theory plus appropriate single element directivity.

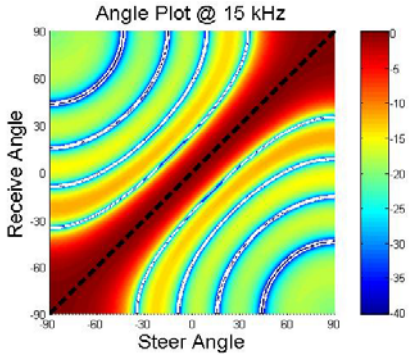

Fig. E.2. Theoretical receive angle versus steer angle directivity pattern surface plot at 15 kHz from 8 element line array theory plus appropriate single element directivity.

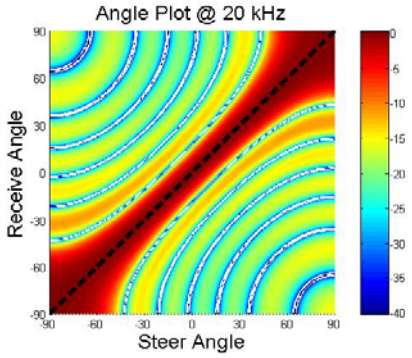

Fig. E.3. Theoretical receive angle versus steer angle directivity pattern surface plot at 20 kHz from 8 element line array theory plus appropriate single element directivity.

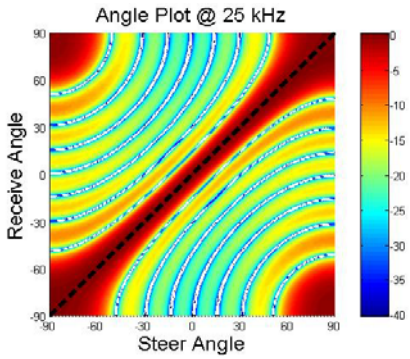

Fig. E.4. Theoretical receive angle versus steer angle directivity pattern surface plot at 25 kHz from 8 element line array theory plus appropriate single element directivity.

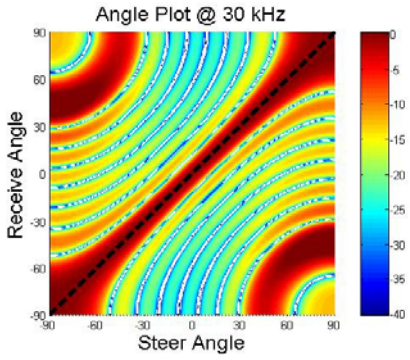

Fig. E.5. Theoretical receive angle versus steer angle directivity pattern surface plot at 30 kHz from 8 element line array theory plus appropriate single element directivity.

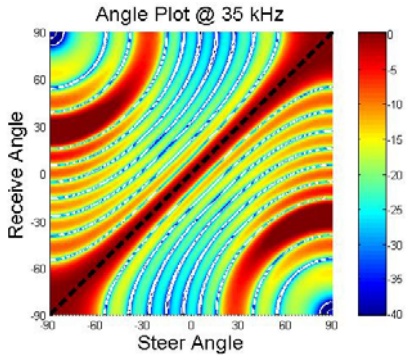

Fig. E.6. Theoretical receive angle versus steer angle directivity pattern surface plot at 35 kHz from 8 element line array theory plus appropriate single element directivity.

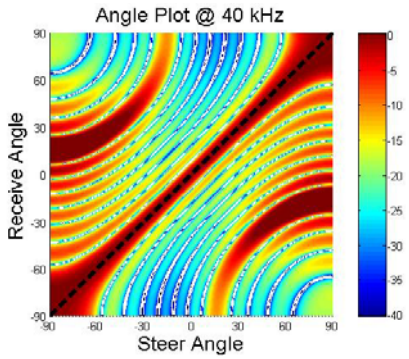

Fig. E.7. Theoretical receive angle versus steer angle directivity pattern surface plot at 40 kHz from 8 element line array theory plus appropriate single element directivity.

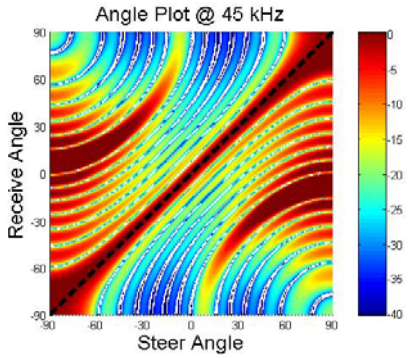

Fig. E.8. Theoretical receive angle versus steer angle directivity pattern surface plot at 45 kHz from 8 element line array theory plus appropriate single element directivity.

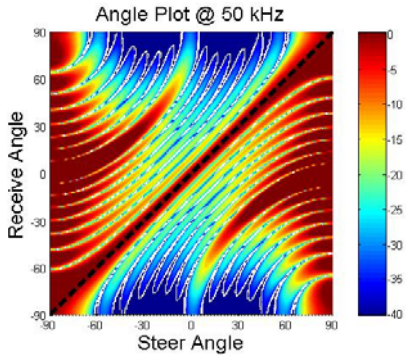

Fig. E.9. Theoretical receive angle versus steer angle directivity pattern surface plot at 50 kHz from 8 element line array theory plus appropriate single element directivity.

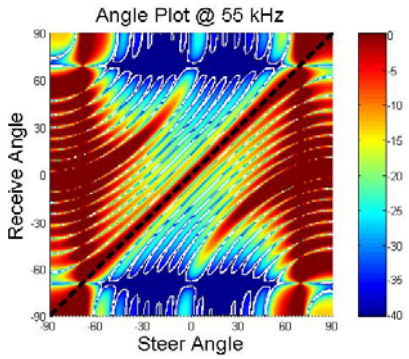

Fig. E.10. Theoretical receive angle versus steer angle directivity pattern surface plot at 55 kHz from 8 element line array theory plus appropriate single element directivity.

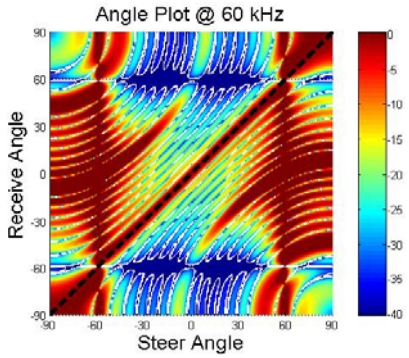

Fig. E.11. Theoretical receive angle versus steer angle directivity pattern surface plot at 60 kHz from 8 element line array theory plus appropriate single element directivity.

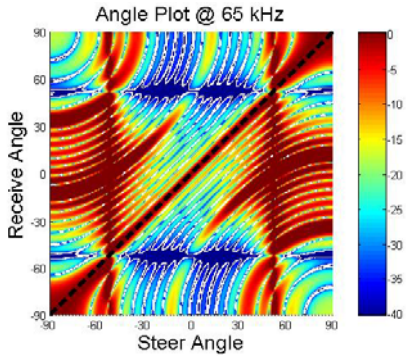

Fig. E.12. Theoretical receive angle versus steer angle directivity pattern surface plot at 65 kHz from 8 element line array theory plus appropriate single element directivity.

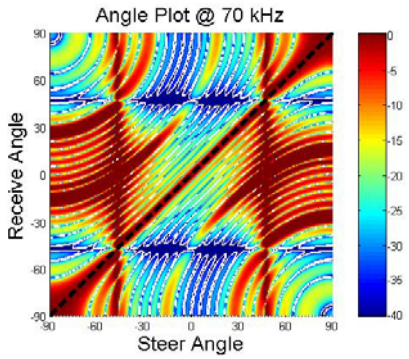

Fig. E.13. Theoretical receive angle versus steer angle directivity pattern surface plot at 70 kHz from 8 element line array theory plus appropriate single element directivity.

E.3 Eight Element Line Array – No Bar Measurements

Figures E.14-E.23 are measured directivity pattern surface plots, similar to those found in Section 6.6.1 at every 5 kHz multiple from 25 kHz to 70 kHz.

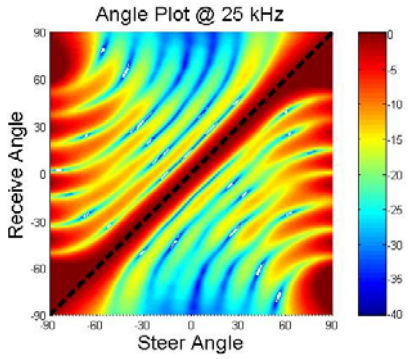

Fig. E.14. Measured receive angle versus steer angle directivity pattern surface plot at 25 kHz from no-bar 8-element line array data.

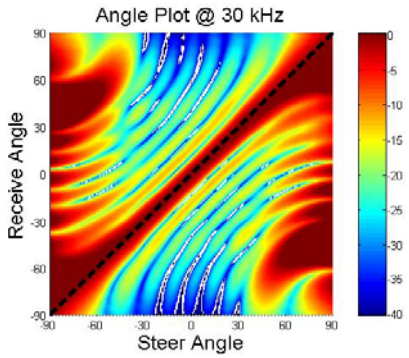

Fig. E.15. Measured receive angle versus steer angle directivity pattern surface plot at 30 kHz from no-bar 8-element line array data.

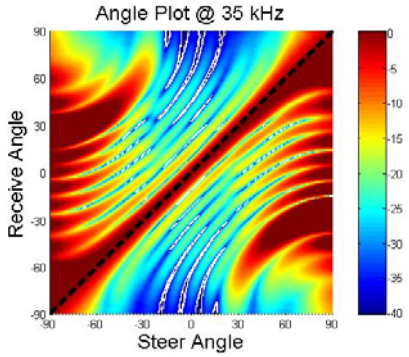

Fig. E.16. Measured receive angle versus steer angle directivity pattern surface plot at 35 kHz from no-bar 8-element line array data.

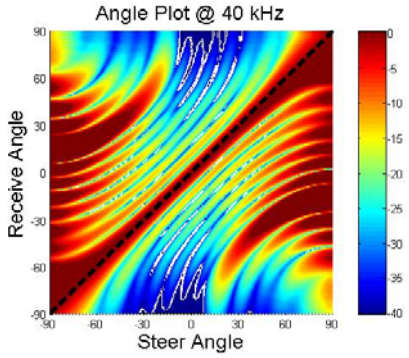

Fig. E.17. Measured receive angle versus steer angle directivity pattern surface plot at 40 kHz from no-bar 8-element line array data.

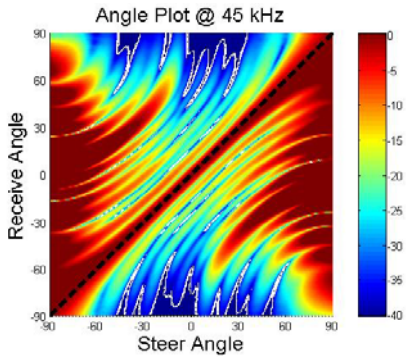

Fig. E.18. Measured receive angle versus steer angle directivity pattern surface plot at 45 kHz from no-bar 8-element line array data.

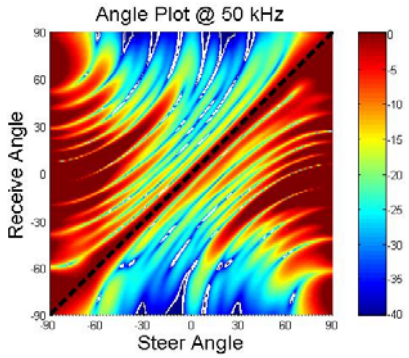

Fig. E.19. Measured receive angle versus steer angle directivity pattern surface plot at 50 kHz from no-bar 8-element line array data.

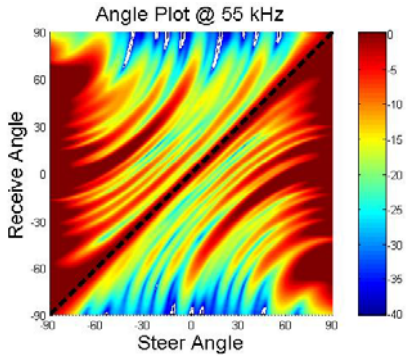

Fig. E.20. Measured receive angle versus steer angle directivity pattern surface plot at 55 kHz from no-bar 8-element line array data.

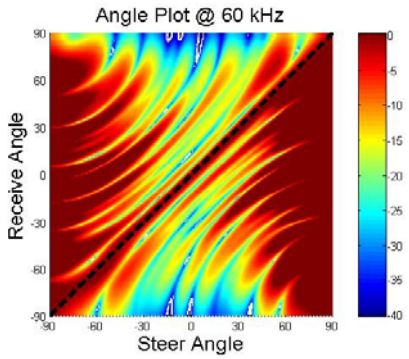

Fig. E.21. Measured receive angle versus steer angle directivity pattern surface plot at 60 kHz from no-bar 8-element line array data.

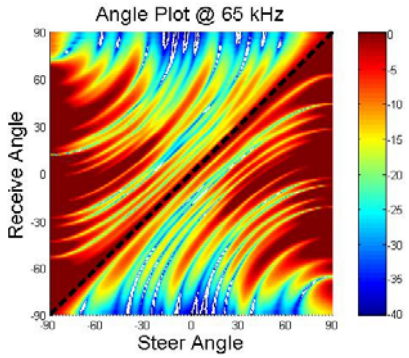

Fig. E.22. Measured receive angle versus steer angle directivity pattern surface plot at 65 kHz from no-bar 8-element line array data.

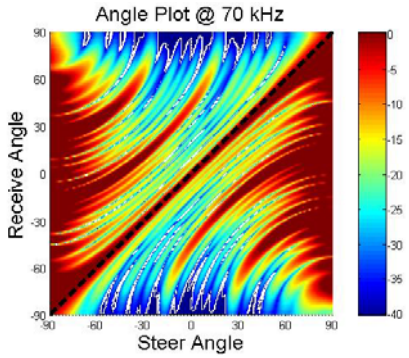

Fig. E.23. Measured receive angle versus steer angle directivity pattern surface plot at 70 kHz from no-bar 8-element line array data.

E.4 Eight Element Line Array – Alumina Bar Measurements

Figures E.24-E.33 are measured directivity pattern surface plots, similar to those found in Section 6.6.2 at every 5 kHz multiple from 25 kHz to 70 kHz.

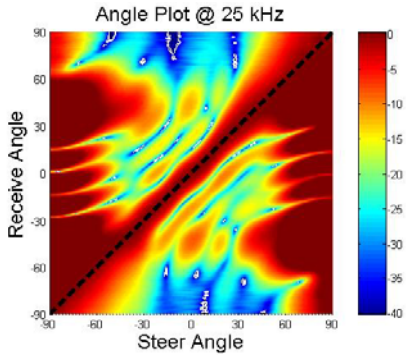

Fig. E.24. Measured receive angle versus steer angle directivity pattern surface plot at 25 kHz from alumina bar 8-element line array data.

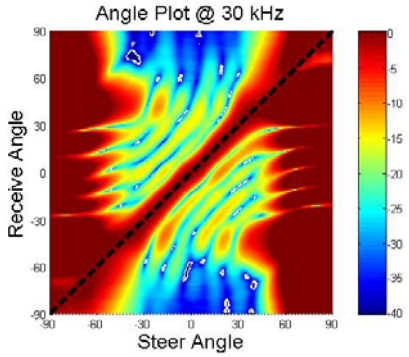

Fig. E.25. Measured receive angle versus steer angle directivity pattern surface plot at 30 kHz from alumina bar 8-element line array data.

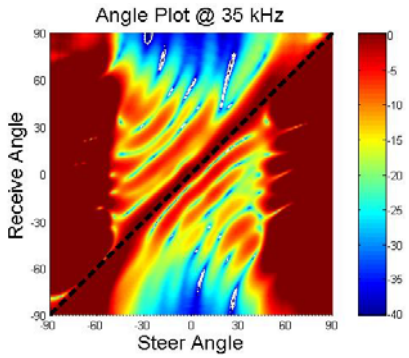

Fig. E.26. Measured receive angle versus steer angle directivity pattern surface plot at 35 kHz from alumina bar 8-element line array data.

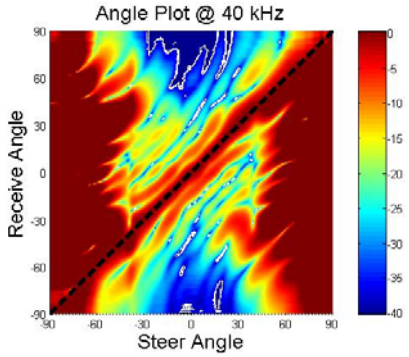

Fig. E.27. Measured receive angle versus steer angle directivity pattern surface plot at 40 kHz from alumina bar 8-element line array data.

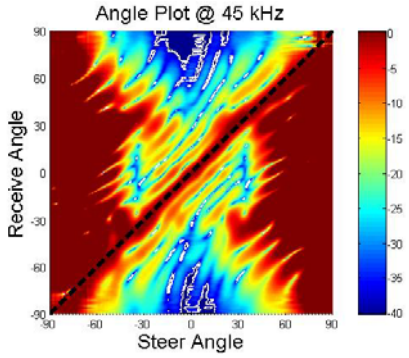

Fig. E.28. Measured receive angle versus steer angle directivity pattern surface plot at 45 kHz from alumina bar 8-element line array data.

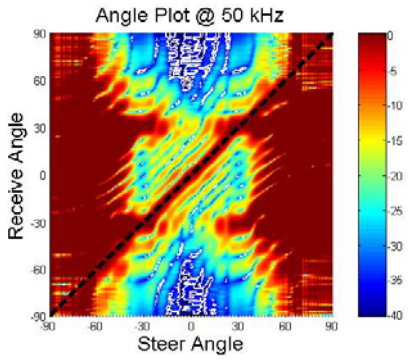

Fig. E.29. Measured receive angle versus steer angle directivity pattern surface plot at 50 kHz from alumina bar 8-element line array data.

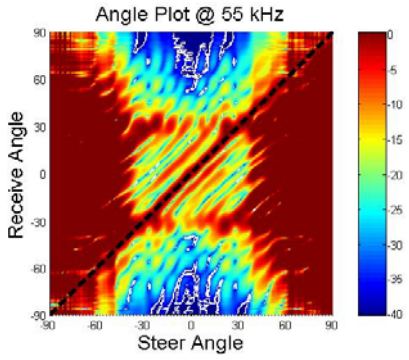

Fig. E.30. Measured receive angle versus steer angle directivity pattern surface plot at 55 kHz from alumina bar 8-element line array data.

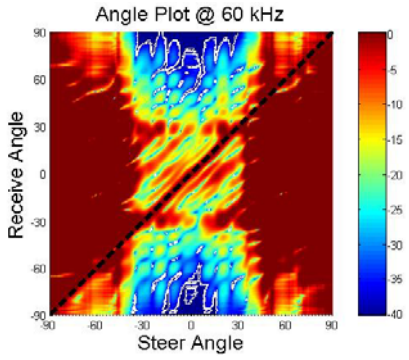

Fig. E.31. Measured receive angle versus steer angle directivity pattern surface plot at 60 kHz from alumina bar 8-element line array data.

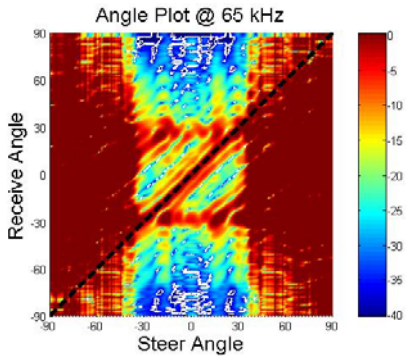

Fig. E.32. Measured receive angle versus steer angle directivity pattern surface plot at 65 kHz from alumina bar 8-element line array data.

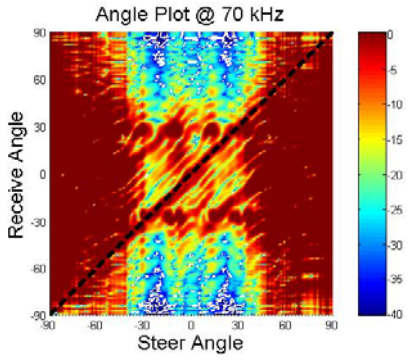

Fig. E.33. Measured receive angle versus steer angle directivity pattern surface plot at 70 kHz from alumina bar 8-element line array data.

E.5 Fifty-Two Element Planar Array – No Plate Measurements

Figures E.34-E.46 are measured directivity pattern surface plots, similar to those found in Section 6.8.1 at every 5 kHz multiple from 10 kHz to 70 kHz.

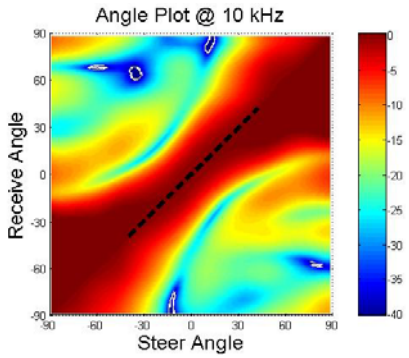

Fig. E.34. Measured receive angle versus steer angle directivity pattern surface plot at 10 kHz from no-plate 52-element planar array data.

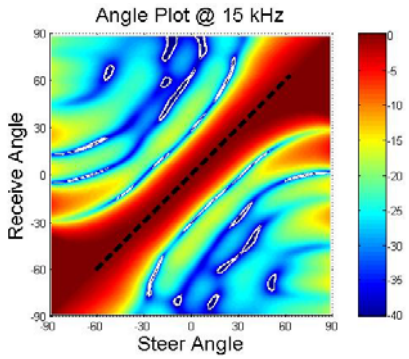

Fig. E.35. Measured receive angle versus steer angle directivity pattern surface plot at 15 kHz from no-plate 52-element planar array data.

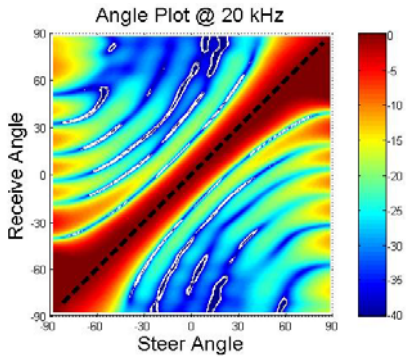

Fig. E.36. Measured receive angle versus steer angle directivity pattern surface plot at 20 kHz from no-plate 52-element planar array data.

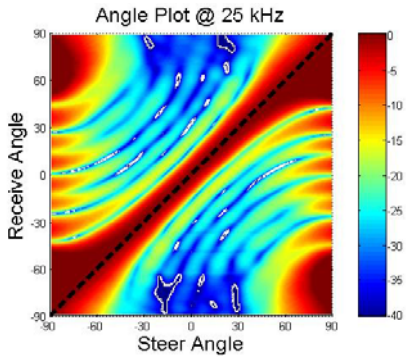

Fig. E.37. Measured receive angle versus steer angle directivity pattern surface plot at 25 kHz from no-plate 52-element planar array data.

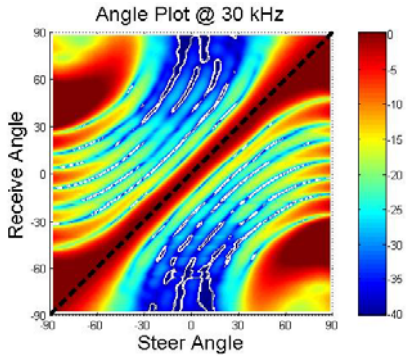

Fig. E.38. Measured receive angle versus steer angle directivity pattern surface plot at 30 kHz from no-plate 52-element planar array data.

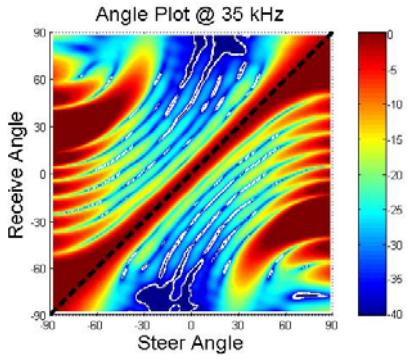

Fig. E.39. Measured receive angle versus steer angle directivity pattern surface plot at 35 kHz from no-plate 52-element planar array data.

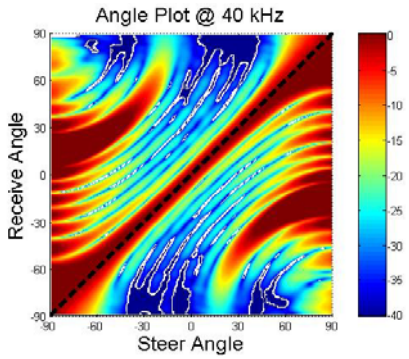

Fig. E.40. Measured receive angle versus steer angle directivity pattern surface plot at 40 kHz from no-plate 52-element planar array data.

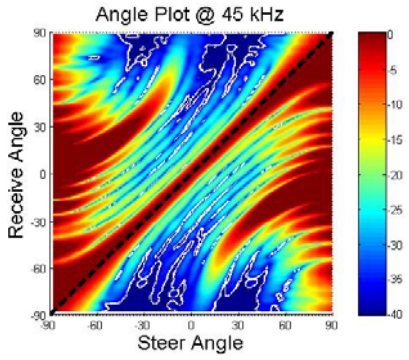

Fig. E.41. Measured receive angle versus steer angle directivity pattern surface plot at 45 kHz from no-plate 52-element planar array data.

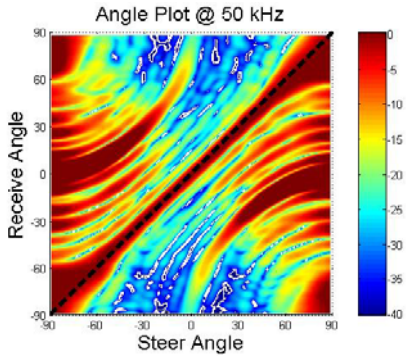

Fig. E.42. Measured receive angle versus steer angle directivity pattern surface plot at 50 kHz from no-plate 52-element planar array data.

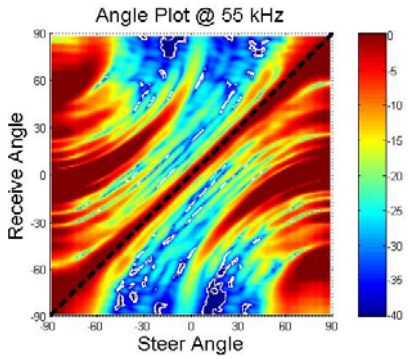

Fig. E.43. Measured receive angle versus steer angle directivity pattern surface plot at 55 kHz from no-plate 52-element planar array data.

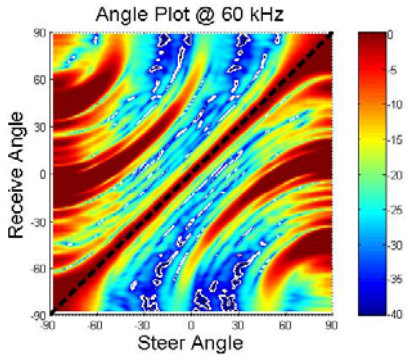

Fig. E.44. Measured receive angle versus steer angle directivity pattern surface plot at 60 kHz from no-plate 52-element planar array data.

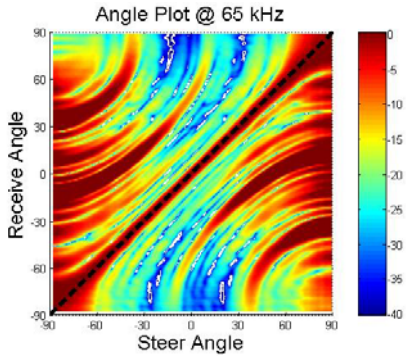

Fig. E.45. Measured receive angle versus steer angle directivity pattern surface plot at 65 kHz from no-plate 52-element planar array data.

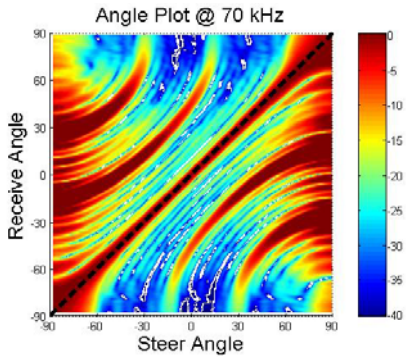

Fig. E.46. Measured receive angle versus steer angle directivity pattern surface plot at 70 kHz from no-plate 52-element planar array data.

E.6 Fifty-Two Element Planar Array – Aluminum Honeycomb Plate Measurements

Figures E.47-E.59 are measured directivity pattern surface plots, similar to those found in Section 6.8.2 at every 5 kHz multiple from 10 kHz to 70 kHz.

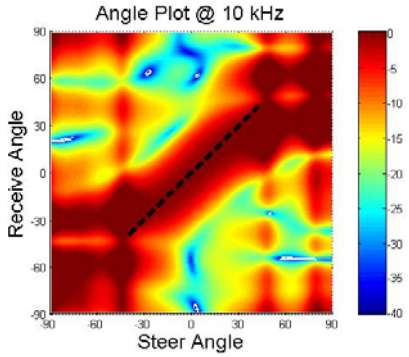

Fig. E.47. Measured receive angle versus steer angle directivity pattern surface plot at 10 kHz from aluminum honeycomb plate 52-element planar array data.

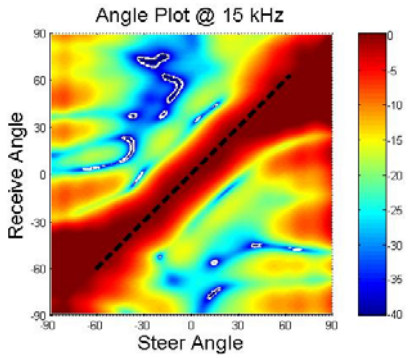

Fig. E.48. Measured receive angle versus steer angle directivity pattern surface plot at 15 kHz from aluminum honeycomb plate 52-element planar array data.

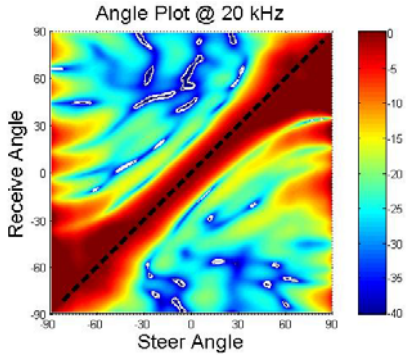

Fig. E.49. Measured receive angle versus steer angle directivity pattern surface plot at 20 kHz from aluminum honeycomb plate 52-element planar array data.

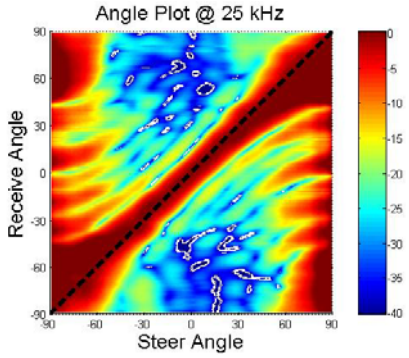

Fig. E.50. Measured receive angle versus steer angle directivity pattern surface plot at 25 kHz from aluminum honeycomb plate 52-element planar array data.

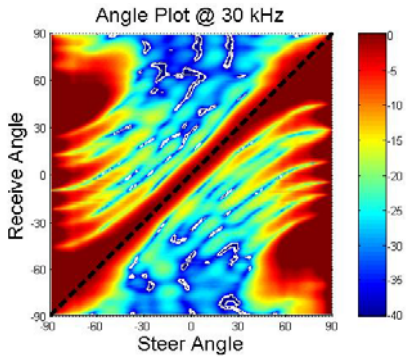

Fig. E.51. Measured receive angle versus steer angle directivity pattern surface plot at 30 kHz from aluminum honeycomb plate 52-element planar array data.

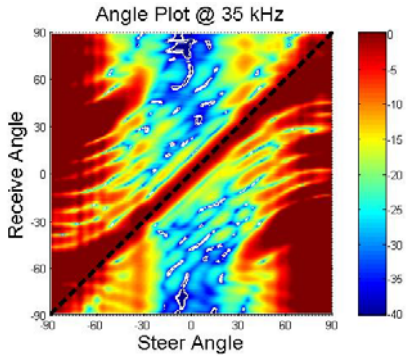

Fig. E.52. Measured receive angle versus steer angle directivity pattern surface plot at 35 kHz from aluminum honeycomb plate 52-element planar array data.

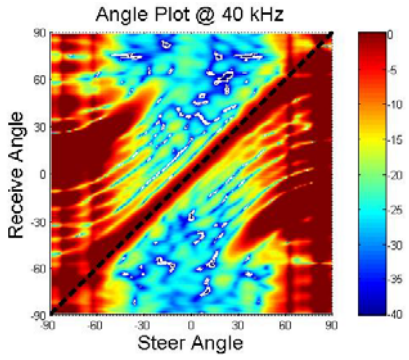

Fig. E.53. Measured receive angle versus steer angle directivity pattern surface plot at 40 kHz from aluminum honeycomb plate 52-element planar array data.

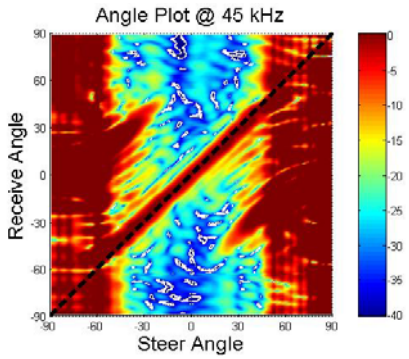

Fig. E.54. Measured receive angle versus steer angle directivity pattern surface plot at 45 kHz from aluminum honeycomb plate 52-element planar array data.

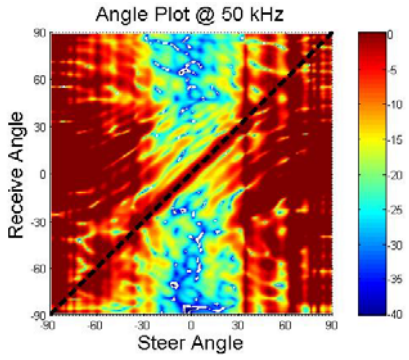

Fig. E.55. Measured receive angle versus steer angle directivity pattern surface plot at 50 kHz from aluminum honeycomb plate 52-element planar array data.

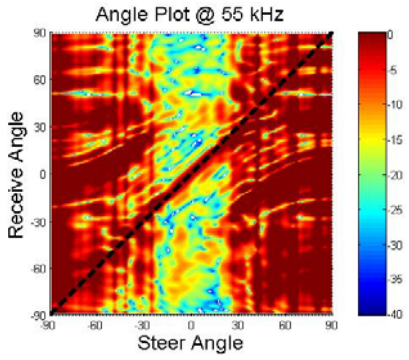

Fig. E.56. Measured receive angle versus steer angle directivity pattern surface plot at 55 kHz from aluminum honeycomb plate 52-element planar array data.

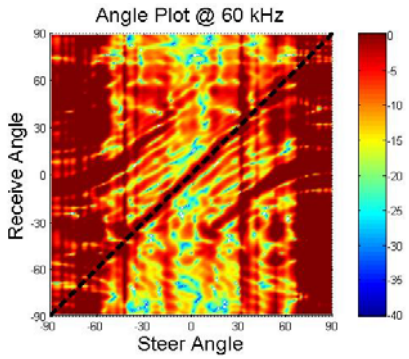

Fig. E.57. Measured receive angle versus steer angle directivity pattern surface plot at 60 kHz from aluminum honeycomb plate 52-element planar array data.

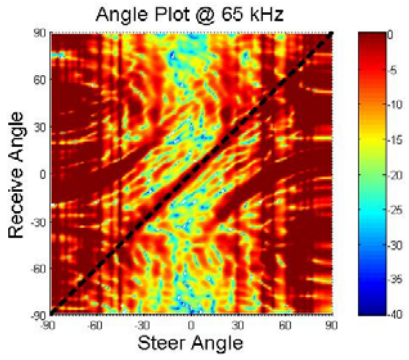

Fig. E.58. Measured receive angle versus steer angle directivity pattern surface plot at 65 kHz from aluminum honeycomb plate 52-element planar array data.

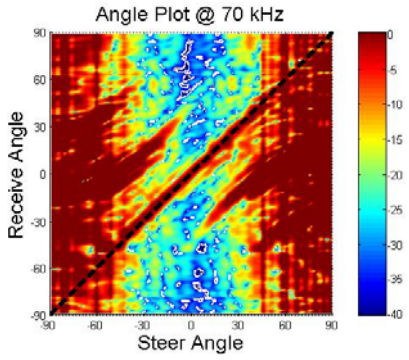

Fig. E.59. Measured receive angle versus steer angle directivity pattern surface plot at 70 kHz from aluminum honeycomb plate 52-element planar array data.

E.7 Eight Element Line Array – Alumina Bar Revisited Measurements

Figures E.60-E.61 are measured directivity pattern surface plots, similar to those found in Section 6.8.3 at 25 kHz, 40 kHz, and 50 kHz.

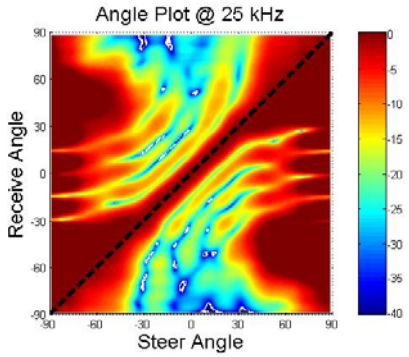

Fig. E.60. Measured receive angle versus steer angle directivity pattern surface plot at 25 kHz from the revisited alumina bar 8-element line array data.

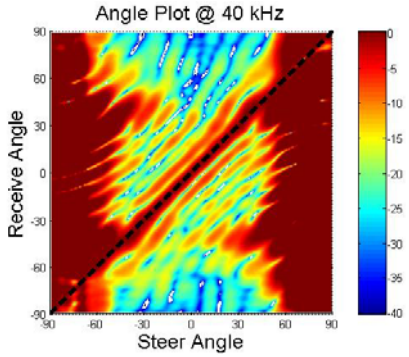

Fig. E.61. Measured receive angle versus steer angle directivity pattern surface plot at 40 kHz from the revisited alumina bar 8-element line array data.

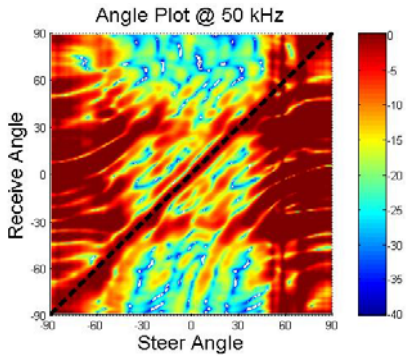

Fig. E.62. Measured receive angle versus steer angle directivity pattern surface plot at 50 kHz from the revisited alumina bar 8-element line array data.

E.8 Eight Element Line Array – Pine Bar Measurements

Figures E.63-E.68 are measured directivity pattern surface plots, similar to those found in Section 6.8.4 at 25 kHz and 5 kHz multiples from 40 kHz to 50 kHz.

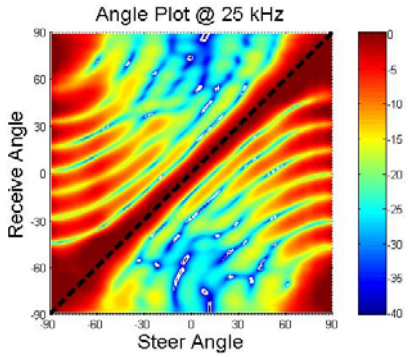

Fig. E.63. Measured receive angle versus steer angle directivity pattern surface plot at 25 kHz from the R-direction pine bar 8-element line array data.

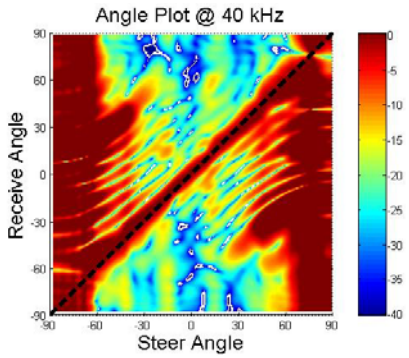

Fig. E.64. Measured receive angle versus steer angle directivity pattern surface plot at 40 kHz from the R-direction pine bar 8-element line array data.

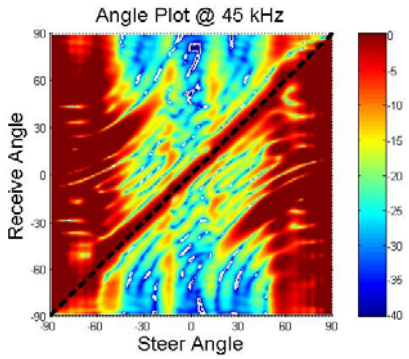

Fig. E.65. Measured receive angle versus steer angle directivity pattern surface plot at 45 kHz from the R-direction pine bar 8-element line array data.

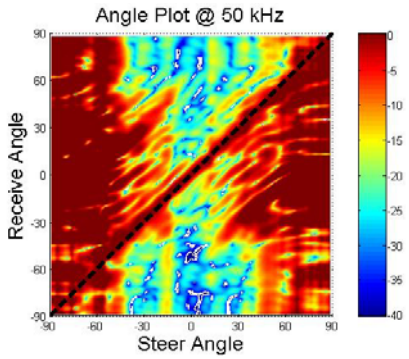

Fig. E.66. Measured receive angle versus steer angle directivity pattern surface plot at 50 kHz from the R-direction pine bar 8-element line array data.

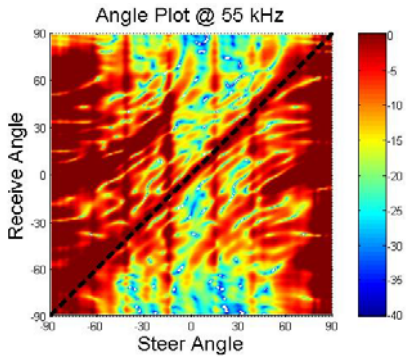

Fig. E.67. Measured receive angle versus steer angle directivity pattern surface plot at 55 kHz from the R-direction pine bar 8-element line array data.

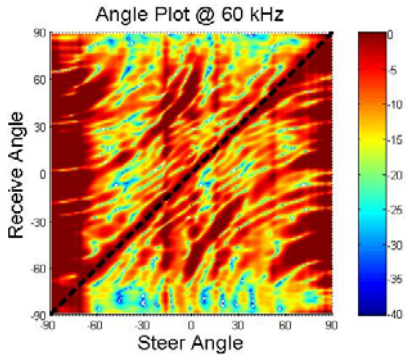

Fig. E.68. Measured receive angle versus steer angle directivity pattern surface plot at 60 kHz from the R-direction pine bar 8-element line array data.

E.9 Additional Bars and Plates Tested

An additional pine bar was tested, using the same mounting techniques as for the R-direction pine bar, with it's thickness in the T-direction (see Fig. 6.25). The results from measurements made using this bar were very similar to the results for the R-

direction pine bar and therefore were not included in this thesis. The T-direction bar had the same thickness and about the same stiffness to mass ratio.

A carbon fiber plate was manufactured for experimental testing as well. This plate was made with the same radius as the aluminum honeycomb plate with a half inch thickness. The plate was purposefully manufactured to possess a high Young's modulus in one planar direction ($E = 127\,\text{GPa}$) and a low modulus in the other planar direction ($E = 1\text{GPa}$). Unfortunately the results from measurement made with this plate provided almost no comparison with theory. These results were not included in this thesis since the data was assumed to be incorrect due to some unknown perturbation relative to other measurements.

A 0.75 inch thick aluminum bar was also measured, using the same mounting techniques as for the pine bars, and it also provided almost no comparison with theory. These results were also not included in this thesis since the data was assumed to be incorrect due to some unknown perturbation relative to other measurements.

Appendix F

Additional Filter Shapes for the Alumina Bar Line Array

This appendix contains filter shapes for the original alumina bar line array at every 5 kHz multiple from 25 to 70 kHz. The filter shapes are normalized in a similar fashion as was outlined for the right hand plots of the figures contained in Section 7.3. The theoretical filter shapes are based upon the expression given in Eq. (3.32) using the material properties of alumina ($E = 391\text{GPa}$, $\rho_P = 3956\,\text{kg}/\text{m}^3$, $\sigma = 0.22$, and $\eta = 0$) along with a bar thickness of 0.4 inches as specified in Table 3.2. The theoretical filter shapes were then normalized such that their normal incidence levels were set equal to 0 dB. The experimentally obtained filter shapes were generated using the same procedure outlined in Section 7.3. The experimental filter shapes were also normalized such that their pass band levels were set equal to zero. While this normalization procedure eliminates the offset difference information, it is extremely useful in angular dependence comparisons, just as it is useful to normalize directivity patterns for comparison purposes. However, amplitude offset information may be obtained from the difference between the equivalent circuit modeling and experimental results for the normal incidence transmission loss (see Fig. 7.21). Figure 7.21 has been reproduced as Fig. F.1 in this appendix to allow the reader to determine what the actual differences between normal incidence values are. Figures F.2-F.3 display the filter shapes described above for the frequencies indicated in the upper right corner of each subplot.

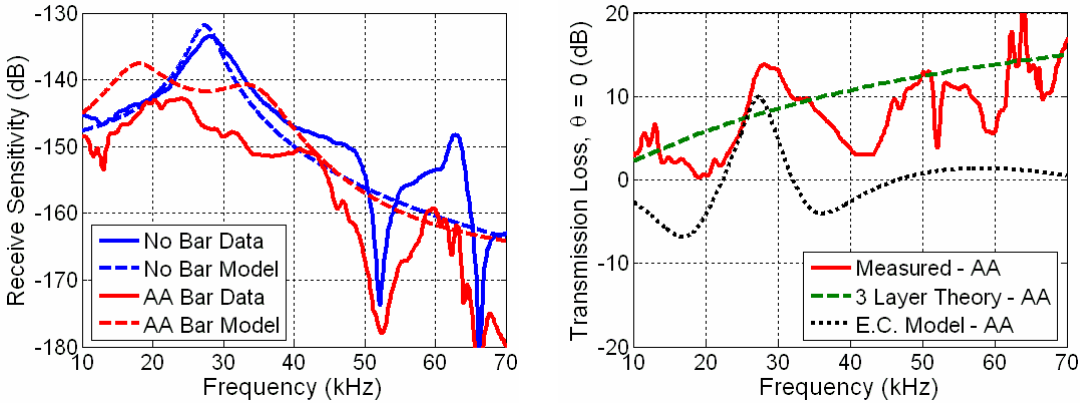

Fig. F.1. Alumina bar measured and modeled frequency responses for no-bar and with-bar conditions, from the no-bar data and the revisited alumina bar data (left subplot). Measured, theory, and modeled normal incidence transmission loss plots from the revisited alumina bar data (right subplot). Theory refers to the 3 layer transmission loss model and E. C. Model refers to the equivalent circuit model. This figure is a reproduction of Fig. 7.21.

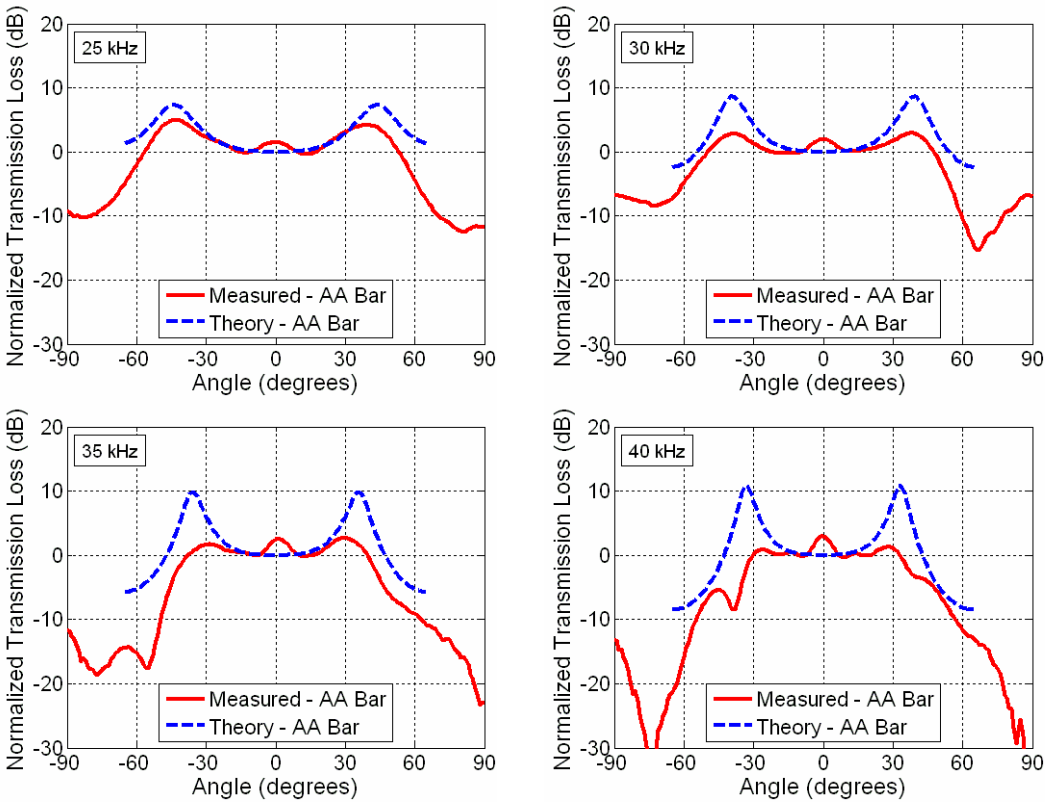

Fig. F.2. Normalized filter shapes for the alumina bar determined from theory and from the 8-element alumina bar array data. Normalization refers to setting each pass band level to 0 dB.

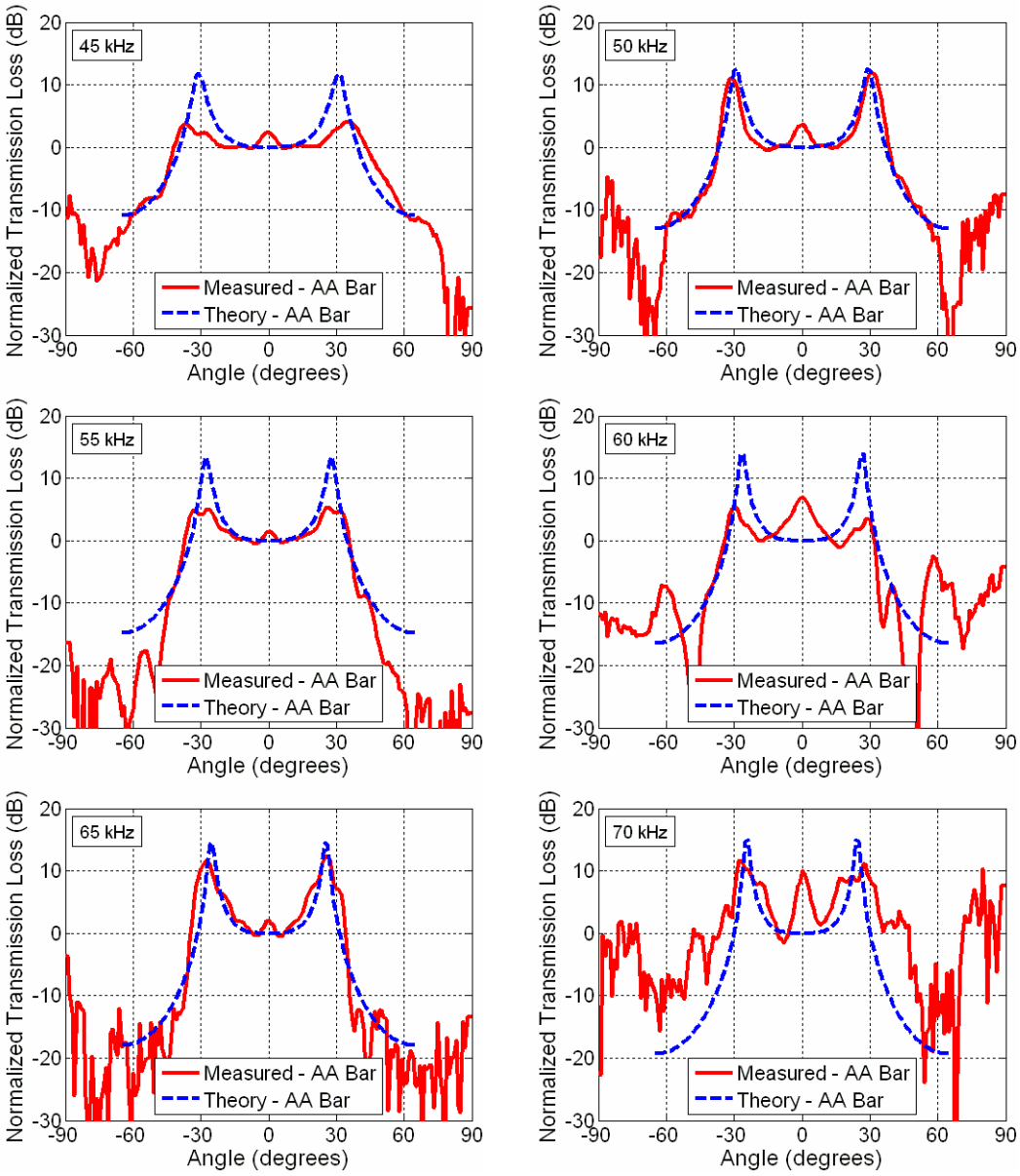

Fig. F.3. Additional normalized filter shapes for the alumina bar determined from theory and from the 8-element alumina bar array data. Normalization refers to setting each pass band level to 0 dB.

VITA

Brian Eric Anderson

Brian E. Anderson was born on August 27, 1977 to Vance N. Anderson and Carla D. Peterson Anderson in Santa Clara, California. Brian married Angela Pippin on August 10, 2001, has a two year old son named Travis, and will have another boy in December 2006. He earned a Bachelor of Science Degree in General Physics from Brigham Young University. He then earned a Master of Science Degree in Physics (Acoustics Emphasis) from Brigham Young University. This dissertation has been submitted as part of the requirements for the Doctor of Philosophy Degree in Acoustics from The Pennsylvania State University. While at Penn State, Brian was awarded a University Graduate Research Fellowship, a College of Engineering Fellowship, and an Audio Engineering Society Educational Foundation Award. Brian served as an officer in the Society of Physics Students (SPS) in the BYU student chapter. He has worked on the technical support staff at Larson Davis, Inc. in Provo, UT. As a graduate student at BYU, Brian also worked on research projects in the areas of Musical Acoustics, Noise Control, and Architectural Acoustics. He was the chairman of the Brigham Young University student section of the Audio Engineering Society. Brian served as a member of the Student Council for the Acoustical Society of America representing the Technical Committee on Noise Acoustics. Currently, Brian is working as a post-doctoral research associate in the Geophysics Group at the Los Alamos National Laboratory.